Contribution of volatile organic compounds (VOCs) from vehicle emissions to secondary organic aerosol (SOA) and urban pollution

Alvaro Martinez

N°d'ordre NNT : 2019LYSE1041

THESE de DOCTORAT DE L'UNIVERSITE DE LYON
opérée au sein de
l'Université Claude Bernard Lyon 1

Ecole Doctorale N° 206
(Ecole Doctorale de Chimie de Lyon)

Spécialité de doctorat : **Chimie**
Discipline : **Chimie de l'environnement**

Soutenue publiquement le 29/03/2019, par :
Alvaro Martinez

Contribution des composés organiques volatils (COVs) provenant des émissions des véhicules aux aérosols organiques secondaires (AOS) et à la pollution urbaine

---

Devant le jury composé de :

Giroir-Fendler, Anne	Directrice de recherche, CNRS Lyon	Presidente
Sartelet, Karine	Directrice de recherche, CEREA Paris	Rapporteure
Astorga, Covadonga	Scientific officer, EC-JRC Ispra, Italie	Rapporteure
Chovelon, Jean Marc	Professeur, Université Lyon 1	Examinateur
Sleiman, Mohamad	Maître de conférences, ICCF	Examinateur
Temime-Roussel, Brice	Ingénieur Recherche, CNRS Marseille	Examinateur
D'Anna, Barbara	Directrice de recherche, CNRS Marseille	Directrice de thèse
Ferronato, Corinne	Maître de conférences	Co-directrice de thèse

UNIVERSITE CLAUDE BERNARD – LYON 1

Président de l'Université	**M. le Professeur Frédéric FLEURY**
Président du Conseil Académique	M. le Professeur Hamda BEN HADID
Vice-président du Conseil d'Administration	M. le Professeur Didier REVEL
Vice-président du Conseil Formation et Vie Universitaire	M. le Professeur Philippe CHEVALIER
Vice-président de la Commission Recherche	M. Fabrice VALLÉE
Directrice Générale des Services	Mme Dominique MARCHAND

COMPOSANTES SANTE

Faculté de Médecine Lyon Est – Claude Bernard	Directeur : M. le Professeur G.RODE
Faculté de Médecine et de Maïeutique Lyon Sud – Charles Mérieux	Directeur : Mme la Professeure C. BURILLON
Faculté d'Odontologie	Directeur : M. le Professeur D. BOURGEOIS
Institut des Sciences Pharmaceutiques et Biologiques	Directeur : Mme la Professeure C. VINCIGUERRA
Institut des Sciences et Techniques de la Réadaptation	Directeur : M. X. PERROT
Département de formation et Centre de Recherche en Biologie Humaine	Directeur : Mme la Professeure A-M. SCHOTT

COMPOSANTES ET DEPARTEMENTS DE SCIENCES ET TECHNOLOGIE

Faculté des Sciences et Technologies	Directeur : M. F. DE MARCHI
Département Biologie	Directeur : M. le Professeur F. THEVENARD
Département Chimie Biochimie	Directeur : Mme C. FELIX
Département GEP	Directeur : M. Hassan HAMMOURI
Département Informatique	Directeur : M. le Professeur S. AKKOUCHE
Département Mathématiques	Directeur : M. le Professeur G. TOMANOV
Département Mécanique	Directeur : M. le Professeur H. BEN HADID
Département Physique	Directeur : M. le Professeur J-C PLENET
UFR Sciences et Techniques des Activités Physiques et Sportives	Directeur : M. Y.VANPOULLE
Observatoire des Sciences de l'Univers de Lyon	Directeur : M. B. GUIDERDONI
Polytech Lyon	Directeur : M. le Professeur E.PERRIN
Ecole Supérieure de Chimie Physique Electronique	Directeur : M. G. PIGNAULT
Institut Universitaire de Technologie de Lyon 1	Directeur : M. le Professeur C. VITON
Ecole Supérieure du Professorat et de l'Education	Directeur : M. le Professeur A. MOUGNIOTTE
Institut de Science Financière et d'Assurances	Directeur : M. N. LEBOISNE

Remerciements

Je tiens à tout d'abord remercier l'Agence de l'Environnement et de la Maitrise de l'Energie (ADEME) pour avoir financé le projet CAPVeREA dans lequel s'inscrit cette thèse. Merci aux gens de l'IFSTTAR pour être des collaborateurs et pour son aide continue.

Je souhaite tout particulièrement remercier Catherine Pinel, directrice de l'Institut de Recherches sur la Catalyse et l'Environnement de Lyon (IRCELYON), pour m'avoir permis d'effectuer mes travaux de thèse au sein de son établissement.

Merci à Karine Sartelet, Covadonga Astorga pour avoir accepté d'être les rapporteuses de cette thèse. Je remercie également Mohamad Sleiman, Brice Temime-Roussel, Anne Giroir-Fendler et Jean Marc Chovelon pour leur participation à mon jury de thèse.

Merci beaucoup à toutes les personnes qui composent le groupe Ircelyon, aux membres du laboratoire, aux services techniques et aux services administratifs pour leur aide toujours importante et leur dévouement constant. Un merci spécial aux membres des groupes CARE et ATARI pour m'avoir accueilli dans leurs rangs en tant que membre de plus. Un grand remerciement à Corinne pour être là chaque fois que j'en avais besoin et pour son guidage pendant cette étape.

Merci à mes amis du laboratoire qui m'ont soutenu jour après jour. Pour toutes les fêtes ensemble, les repas et les éclats de rire qui on rendu inoubliable le temps passé ici.

Un merci spécial à Marc, avec qui j'ai partagé tous les bons et les mauvais côtés de la thèse. Merci pour ton aide, pour ta patience avec mon anglais, pour ta sympathie et pour les pauses café qui m'ont fait découvrir les chocolats Raffaello.

Un grand merci à toutes les personnes du laboratoire LCE à Marseille pour leur sympathie dès le premier moment avec un étudiant perdu et stressé. Merci surtout à Brice pour son aide constante et sa bonne prédisposition. Merci également à tous les étudiants du laboratoire pour leurs conversations scientifiques et moins scientifiques chez Berthoms et chez Sylvain. Merci également à tous les grands amis faites à Marseille. Merci d'avoir rendu mes trois mois là-bas beaucoup plus supportables et de trouver une deuxième maison en France.

Un merci spécial à Badr, ma première aide toujours, à Lyon et à Marseille. Merci pour ta compréhension, ta tranquillité et votre savoir-être, les discussions scientifiques et ton excellent thé.

Un grand merci aux gens d'Innsbruck-Oslo. Spécialement Philipp et Markus pour m'avoir accepté lors de mon séjour en Autriche et pour leur source inépuisable de connaissances grâce auxquelles j'ai tant appris. Merci pour les bons moments passes en Innsbruck, Lyon et Valencia et pour les discussions scientifiques.

Un merci infini à Barbara, la personne qui m'a fait confiance dès le premier instant et m'a conduit à être docteur. Merci pour ton aide quotidienne, même depuis loin, pour ton énorme patience, pour tout le travail et dévouement envers moi qui a rendu possible la réalisation de cette thèse. Mais merci surtout pour me faire grandir, mûrir et affronter la vie ; et grâce a tes conseils, lesquelles j'ai toujours entendus, même si cela ne semblait pas être le cas.

Gracias a todo el grupo de Españoles que he tenido la suerte de conocer aquí. Por todas las fiestas, cumpleaños y cremaillere vividos y los buenos momentos pasados. Gracias por Agadir, Copenhague y Cracovia. Mención especial a Edgar, que me ha aguantado todo este tiempo a pesar de mi humor de la meseta y a Jordi, gracias al cual todos hemos abierto un poco los ojos y descubierto la verdad 

Gracias a Natalia, por ser mí mejor amiga en Lyon. Por los domingos de sushi y hacerme parte siempre de su emocionantísima vida.

Mil gracias a mis guepardos: Al granadino peor hablado de Andalucía, el cual ni los andaluces entienden. Por su alegría innata y por ser mi recuerdo diario a mi tierra. También a su compañera, loca de los gatos, gracias a la cual he "aprendido portugués". A mi bailador favorito, por todos los cafés diarios, todas nuestras historias vividas y por iniciarme al maravilloso mundo del baile. A mi Puca, compañero inquebrantable de fatigas, viernes tras viernes y sábado tras sábado, sin flaquear. Por todas nuestras noches de intelectuales, por su optimismo, su eterno apoyo y por los incontables viajes a Boston y Sevilla.

A mis amigos de España, gente que hace que siempre quiera volver a mi tierra y con la cual el tiempo siempre pasa demasiado rápido. Por Mojacar, Portugal, por hinojosas…días que hacen olvidar todos los problemas. Un gracias especial a Calero, por los viajes pasados y futuros, por los audios reconfortantes, consejos y en resumen por ser mi mejor amigo desde tiempos inmemoriales.

Mil gracias a mi familia, por su continuo apoyo y hacerme sentir siempre cerca de ellos, por muy lejos que estuviese. Por las locas comidas familiares, los aperitivos y las tardes alrededor del brasero, y por todos los malos momentos superados juntos. Gracias a los que estuvieron, están y a los que están por venir.

Nunca podre agradecer suficiente a mis padres, los verdaderos artífices de que haya llegado hasta aquí. Gracias por todos los valores que me habéis transmitido a lo largo de mi vida, por todo el apoyo recibido y por todos los mensajes de ánimo. Siempre una sonrisa en la cara, incluso cuando no había nada por lo que sonreír. Esta tésis es un poco vuestra también.

MERCI, GRACIAS, THANKS

Et maintenant, accrochez-vous à votre siège, le bon commence…

CONTENTS

Abstract/Résumé

Figures and Tables captions

List of Abbreviations

Publication List

Oral Communications

Poster Communications

CHAPTER I: Context and State of the art 1

1.1. Road Transport Production and Evolution 3

1.2. Primary emissions from road-transport 4

1.2.1. Particles 5

1.2.2. Gaseous Pollutants 7

1.3. Regulation and Control Strategies 12

1.3.1. Air Quality Regulations and European Emissions Standards 12

1.3.2. Vehicle Emission Control 15

1.3.3. Emission models and inventories 20

1.4. Impacts of road transport emissions 21

1.4.1. Air quality, environmental and ecosystem impacts 21

1.4.2. Climate impacts 22

1.4.3. Health impacts 24

1.4.4. Economic impacts 26

1.5. Secondary pollutants 27

1.5.1. Ozone and SOA formation 27

1.5.2. Influence of Atmospheric Parameters for SOA formation 31

1.5.3. Gas-particle partitioning theory 32

1.5.4. The Volatility Basis Set (VBS) approach 34

1.5.5. The Master Chemical Mechanism (MCM) model 35

1.5.6. The GECKO-A model 36

1.5.7. SOA Formation from Road-transport 37

1.6. Challenges and Remaining Questions 44

1.7. Thesis Objectives 46

CHAPTER II: Materials and methods 61

2.1. Emission Studies 63
2.1.1. Chassis dynamometer 63
2.1.2. Dilution systems 64
2.1.3. Driving cycles 66
2.1.4. Particle Measurement 68
2.1.5. Tested vehicles and experimental conditions 68
2.1.6. Emission factors 70
2.2. Experimental set up for SOA studies 70
2.2.1. Aerosol Flow Tube 71
2.2.2. Seed Particles 74
2.2.3. Selected Volatile Organic Compounds 74
2.2.4. Hydroxy radical precursor 76
2.3. Instrumentation 77
2.3.1. Gas phase chemical composition 77
2.3.2. Aerosol chemical composition 84
2.3.3. Monitors 89
CHAPTER III: Primary emissions from diesel and gasoline light duty vehicles 97
3.1. Particle Emission Study 100
3.1.1. Impact of dilution system for particle measurements 100
3.1.2. Gasoline Particle Emission 101
3.1.3. Diesel Particle Emission 109
3.1.4 Emission Factor of Particle Phase 114
3.2. Regulated Gas Phase Pollutants 119
3.2.1. Transient Profiles of Gaseous Pollutants 119
3.2.2. Emission Factor of Gaseous Pollutants 122
3.3. Non Regulated Gas Phase Pollutants 125
3.3.1. Transient Profiles of Gaseous Pollutants 125
3.3.2. Speciation of Organic Compounds 126
3.4. Conclusions 131
CHAPTER IV: SOA formation and on-line chemical analysis 137
4.1. Toluene photoxidation 140
4.1.1. Influence of parameters for SOA formation 141
4.1.2. Gas and particle phase carbon distribution 143
4.1.3. Gas and particle phase analysis 144
4.1.4. Gas/Particle phase partitioning analysis 147
4.2. Naphthalene photoxidation 148
4.2.1. Influence of parameters for SOA formation 148

4.2.2. Gas and particle phase carbon distribution 149
4.2.3. Gas and particle phase analysis 151
4.2.4. Gas/particle phase partitioning analysis 153
4.3. Cyclohexane photoxidation 154
4.3.1. Influence of parameters for SOA formation 155
4.3.2. Gas and particle phase carbon distribution 155
4.3.3. Gas and particle phase analysis 156
4.4. Nonane photoxidation 158
4.4.1. Influence of parameters for SOA formation 159
4.4.2. Gas and particle phase carbon distribution 160
4.4.3. Gas and particle phase analysis 160
4.5. SOA from nonane-toluene 163
4.6. General trends in SOA formation 165
4.7. Photoxidation of real vehicle emissions 167
4.7.1 Primary VOC emissions speciation 167
4.7.2. SOA formation from VOC photoxidation 169
4.7.3. Gas and particle phase carbon distribution 170
4.8. Conclusions 172
CHAPTER V: General conclusions and perspectives 178
ANNEXES 185
Annex I 186
Annex II 187
Annex III 191
Annex IV 194
Annex V 195
Annex VI 217
Annex VII 218

Summary

The transport sector is fundamental to the economic development of a country and to ensure communication and a good quality of life. However, road transport contributes significantly to global warming and leads to serious degradation of the air quality. Among all pollutants, fine and ultrafine particles, emitted by vehicles but also formed in the atmosphere via the atmospheric oxidation of volatile organic compounds (VOCs) or intermediate-volatiles (IVOCs), are considered as potentially toxic. Many toxicological and epidemiological studies show that chronic exposure to fine particles promotes the development of respiratory and cardiovascular diseases. Thus, according to Santé Publique France, 43,000 premature deaths (or 9% of total deaths) are caused in France by fine particles and more than 47 million people are exposed to annual average concentrations of $PM_{2.5}$ exceeding the World Health Organization (WHO) guideline value (annual average of 10 µg m^{-3}). The main gaseous precursors, the atmospheric chemical pathways as well as the chemical composition and the physical transformations that secondary organic aerosol (SOA) undergo in the atmosphere, remain poorly understood. Despite recent research efforts and a considerable progress in the past 15 years, the SOA remains the least understood aerosol species.

The main aim of this work was on one side to improve the knowledge about primary pollutants emitted from Euro 5 and Euro 6 diesel and gasoline passenger cars and on the other side to investigate the photochemical transformations of the VOCs/IVOCs emitted from these cars. Passenger car emissions have been evaluated on a chassis dynamometer test bench at the IFSTTAR laboratory. Regulated and non-regulated emissions have been investigated during WLTC and Artemis driving cycles. Measurements intercomparison at the Constant Volume Sampler (CVS) and at the tailpipe (equipped with FPS-4000 dilution system) indicated that particle number concentration and size distribution were clearly affected by measurements bias at the CVS due to cold and variable dilutions which promoted both nucleation and condensation processes. These bias were particularly important for gasoline DI passenger cars.

Particle number measurements were carried out directly at the tailpipe. For GDI vehicles $PN_{0.23}$ (< 23 nm) represented on average 20 -30 % of total particle number emitted, while for diesel cars, this fraction was considerably lower (≈10-15%). During high speed regimes (Artemis motorway) of diesel passenger cars Diesel Particulate Filter (DPF) passive regeneration was observed. These periods were characterized by a high particle number concentration; their composition was mainly soot, bisulfate and some organic material. During WLTC cycle, Diesel car showed in general, very low Black Carbon (BC) emissions. PM emitted from gasoline DI passenger cars was mainly composed by BC in form of chains or/and agglomerates by some organic droplets containing traces of sulfur, phosphorous, alkaline elements or heavy metals. During cold start GDI cars do emit important concentrations of BC and organic material. The

organic fraction was mainly composed of unburned fuel and Polycyclic Aromatic Hydrocarbons (PAHs).

Emission of hydrocarbons has also been investigated. Gasoline DI emitted important concentration of THCs during cold start. GC-MS analysis revealed that linear and branched alkane/alkenes and BTEX were among the major emitted HCs with EFs reaching 10^4µg/Km and 3×10^3 µg/Km, respectively. While diesel passenger cars were characterized by important emissions of cyclic compounds up to $3x10^5$ µg/km for, followed by oxygenated compounds and alkanes/alkenes $4x10^4$ µg/km. Among the aliphatic compounds, families until C_{15} have been identified, confirming emission of heavier HCs from diesel cars.

The second aim of this work was the study of atmospheric degradation of selected VOCs emitted from Euro 5 and Euro 6 vehicles and to determine the SOA formation potential of these compounds under different environmental conditions. Among the measured HCs we selected one compound as "model compound" for each chemical family: for example toluene for the monoaromatics; naphthalene for the light PAHs; cyclohexane as cycloalkane and nonane as model aliphatic alkane. The choice of the model compounds was supported by our own measurements and previous literature on hydrocarbons speciation and quantification of car exhaust. The chosen compounds have been photoxidized (alone and in mixture) in an Aerosol Flow Tube (AFT) reactor in order to simulate VOCs atmospheric aging. The results suggest: (1) aromatic and PAHs compounds, own highest potential to form SOA; (2) the temperature has an important impact on SOA formation and yield; (3) the presence of pre-existing seed particles has, in general, a positive effect on SOA formation and (4) NOx has been found to negatively affect SOA formation; (5) SOA potential formation of VOC mixtures is highly influenced by the fraction of aromatics. The gas and particle phase reaction products have been investigated. Some of the products identified in the particle phase have never been previously reported. Degradation of aromatic compounds under medium NOx regime produced nitro-aromatic compounds identified both in the gas and particle phase. Those compounds are known to be toxic and harmful for human health. Finally the partitioning coefficients and the volatility of the major particle components have been evaluated at 7, 12 and 21 °C. A last series of experiments consisted on real GDI exhaust emission photoxidation have been carried out. Results suggest a quickly formation of SOA, accounting for a third of total OA after few •OH exposure hours.

This PhD contributes to enrich the primary emissions database, still limited for Euro 5 and Euro 6 recent vehicles. The studies developed also confirm problem that can arise from a bad sampling and measurement protocol (CVS-non PMP) and investigate aerosol emission from a physical and chemical point of view. Speciation of non-regulated compound, especially those that own large SOA formation potential, as aromatic or IVOCs, will help to better understand atmospheric SOA budget. By last, the photoxidation study of primary VOCs (alone, mixture and

full emissions) will lead to a better comprehension of SOA formation, favorable conditions and main VOC precursors. Chemical speciation of both gas and particle phase and the fact that some toxic and carcinogenic compounds have been found put in evidence up to what level road transport affects human health.

Key words: Emissions, Euro 5, Euro 6, gasoline, diesel, Particle matter, Volatile Organic Compounds, Photoxidation, Secondary Organic Aerosol

Résumé

Le secteur des transports est fondamental pour le développement économique d'un pays et pour assurer la communication et une bonne qualité de vie. Cependant, le transport routier contribue largement au réchauffement de la planète et conduit à une grave dégradation de la qualité de l'air. Parmi tous les polluants, les particules fines et ultrafines, émises par les véhicules mais également formées dans l'atmosphère via l'oxydation atmosphérique de composés organiques volatils (COV) ou de volatilité intermédiaire (COVI), sont considérées comme potentiellement toxiques. De nombreuses études toxicologiques et épidémiologiques montrent que l'exposition chronique aux particules fines favorise le développement de pathologies respiratoires et cardiovasculaires. Ainsi, d'après Santé Publique France, 43000 décès prématurés (soit 9% des décès totaux) sont provoqués en France, par les particules fines et plus de 47 millions de personnes sont exposées à des concentrations moyennes annuelles de $PM_{2,5}$ dépassant la valeur guide de l'Organisation Mondiale de la Santé (OMS) (moyenne annuelle de 10 µg m^{-3}). Les précurseurs gazeux, les principaux mécanismes réactionnels ainsi que les transformations physiques que les Aérosol Organiques Secondaires (AOS) subit dans l'atmosphère restent incertains et sont à l'origine de sérieuses lacunes dans la compréhension et dans l'évaluation des impacts de l'AOS. Malgré les efforts consentis au cours de la dernière décennie, l'AOS demeure la fraction de l'aérosol la moins bien connue.

La présente étude porte principalement sur la caractérisation des polluants primaires émis par les échappements automobiles et les transformations photochimiques des COV / COVI. Les émissions des voitures ont été évaluées à l'aide d'un banc à rouleau au laboratoire de l'IFSTTAR. Les émissions réglementées et non réglementées ont été étudiées au cours des cycles de conduite WLTC et Artemis. Les mesures d'intercomparaison au niveau du Constant Volume Sampler (CVS) et de l'échappement (équipé du système de dilution FPS-4000) montre que dans les CVS, en raison d'une dilution froide et avec des taux variables, des processus de nucléation et de condensation on été observés. Ce biais était particulièrement important pour les voitures à essence. Les mesures du nombre de particules ont été effectuées directement au niveau de l'échappement. Pour les véhicules GDI, $PN_{0.23}$ (<23 nm) représentait en moyenne 20-30% du nombre total de particules émises, alors que pour les voitures diesel, cette fraction était bien inférieure (≈10-15%). Lors des régimes à grande vitesse (autoroutier Artemis) des véhicules diesel, une régénération passive de Filtre à Particules (FAP) a été observée. La composition chimique et la morphologie des particules ont été étudiées en combinant les résultats de spectrométrie de masse d'aérosol et de microscopie électronique à transmission. Au cours de la régénération passive, les particules émises étaient principalement constituées de suie, de bisulfate et de matière organique. Au cours du cycle WLTC, de faibles émissions de carbone suie ont été observés pour le véhicule diesel.

Les particules émises par les voitures essence à injection directe étaient principalement composées de Black Carbon (BC) sous forme de chaînes et/ou d'agglomérats et de gouttelettes organiques contenant des traces de soufre, de phosphore, d'éléments alcalins ou de métaux lourds. Pendant le démarrage à froid, les voitures GDI émettent des concentrations importantes de BC et de matière organique. La fraction organique était principalement composée de combustible non brûlé et d'Hydrocarbures aromatiques polycycliques (HAPs).

Les émissions d'hydrocarbures ont également été étudiées. Les véhicules GDI ont émis des concentrations importantes de THC lors du démarrage à froid. L'analyse des cartouches par GC-MS a montre que les alcanes/alcènes linéaires et ramifiés et que le BTEX figuraient parmi les principaux HC émis. Les facteurs d'émission (EF) atteignant respectivement 10^4 µg/km et 3×10^3 µg/km. Alors que les voitures diesel étaient caractérisées par des émissions importantes de composés cycliques allant jusqu'à $3x10^5$ µg/km, suivies des composés oxygénés et des alcanes/alcènes autour de $4x10^4$ µg/km. Parmi les composés aliphatiques, des composés jusqu'à la C_{15} ont été identifiés, confirmant l'émission d'hydrocarbures plus lourds par les voitures diesel.

La deuxième partie de ce travail consistait à étudier la transformation atmosphérique de certains COV émis par les véhicules Euro 5 et Euro 6 et à déterminer le potentiel de formation de AOS de ces composés. Parmi les hydrocarbures mesurés, nous avons sélectionné un "composé modèle" pour chaque famille chimique: le toluène pour les monoaromatiques; le naphtalène pour les HAP légers; le phénol en tant que produit d'oxydation de première génération des composes monoaromatiques; le cyclohexane pour les cycloalcanes et le nonane parmi les alcanes aliphatiques. Le choix des composés modèles a été supporté par nos propres mesures et par la littérature précédente. Les composés choisis ont été photo-oxydés (seuls et en mélange) dans un réacteur à tube à flux d'aérosol (AFT) afin de simuler le vieillissement atmosphérique des COV.

Les résultats majeurs suggèrent: (1) des composés aromatiques et des HAP représentent les composés avec le plus fort potentiel de formation d'AOS ; (2) la température a un impact important sur la formation et le rendement d'AOS ; (3) la présence de particules préexistantes a un effet positif sur la formation d'AOS; (4) il a été constaté que la présence des NOx affectaient négativement la formation d'AOS ; (5) la formation d'AOS de mélanges de COV est fortement influencée par la fraction de composé aromatique. Les produits de réaction en phase gazeuse et particulaire ont été étudiés. Certains des produits identifiés dans la phase particulaire n'ont jamais été signalés auparavant. La dégradation des composés aromatiques en régime de NOx moyen a produit des composés nitro-aromatiques identifiés à la fois en phase gazeuse et en phase particulaire. Ces composés sont connus pour être toxiques et nocifs pour la santé humaine. Enfin, les coefficients de partage et la volatilité des principaux composants des particules ont été évalués à 7, 12 et 21 °C. Une dernière série d'expériences sur la

photoxydation des émissions réelles GDI ont été réalisées. Les résultats suggèrent une formation rapide d'AOS, représentant un tiers du total de l'AO après quelques heures d'exposition à l'˙OH.

Cette thèse contribue à enrichir la base de données d'émissions primaires, encore limitée aux véhicules récents Euro 5 et Euro 6. Les études développées confirment les problèmes pouvant résulter d'un protocole d'échantillonnage et de mesure incorrect (CVS-non PMP). La spéciation des composés non réglementés, en particulier ceux qui possèdent un grand potentiel de formation d'AOS, comme les aromatiques ou les AOS intermédiaires, aidera à mieux comprendre le budget atmosphérique d'AOS. Enfin, l'étude de photoxydation de COV primaires (seuls, mélange et émissions complètes) conduira à une meilleure compréhension de la formation d'AOS, des conditions favorables et des principaux précurseurs COV. La spéciation chimique à la fois des phases gazeuse et particulaire et le fait que certains composés toxiques et cancérogènes ont été découverts ont mis en évidence jusqu'à quel point le transport routier affectait la santé humaine.

Mots clés: Emissions, Euro 5, Euro 6, essence, diesel, matière particulaire, composés organiques volatiles, photoxydation, aérosols secondaires organiques

Figures and Tables captions

Figure 1.1. *World passenger car production, source : ACEA, 2018.* **3**

Figure 1.2. *Passenger car in use.Source: ACEA pocket guide 2017-2018.* **4**

Figure 1.3. *Emission of the main pollutants by sector group in Europe in 2016 (source: EEA, 2018).* **5**

Figure 1.4. *Formation of nucleation, Aitken and accumulation particles mode during vehicle exhaust emissions (source: Kittelson, 1998).* **6**

Figure 1.5. *Different steps in soot particle formation process. Source: combustion.mie.utoronto.ca.* **7**

Figure 1.6. *Nucleation and growth processes for sulfuric acid and water from clusters to droplets. (Source: Curtius, 2006).* **9**

Figure 1.7. *Chemical composition of diesel and gasoline fuel by carbon number. (Source : Gentner, 2012)* **10**

Figure 1.8. *Volatility/carbon number of n-alkanes for a typical (a) gasoline (b) diesel vehicles using quartz filter, Tenax tubes and Tedlar bag. The red dashed lines indicate the particle fraction assuming C_{OA} of 10 µg/m^3 and 298K. (Source: Lu, 2018).* **11**

Figure 1.9. *Working principle of a DOC. Source: Gil, 2015.* **16**

Figure 1.10. *Schematic DPF working principle. Source: Vauxhall.* **16**

Figure 1.11. *Working principle of the urea SCR system. Source: www.doosanequipment.com* **17**

Figure 1.12. *Schematic working principle of NOx trap. Source: www.cjcatal.org* **18**

Figure 1.13. *Working principle of a TWC (left) and NOx, CO and HC conversion on TWC depending on air to fuel ratio (right). Source: www. ac.umicore.com/en/technologies/three-way-catalyst/; http://www.meca.org/resources/featured-article* **19**

Figure 1.14. *Difference between a haze and clean day for Paris city. (Source: Guay et Tribouillard, AFP).* **21**

Figure 1.15. *Radiative forcing in 2011, source: IPCC, 2013 (Values are global average radiative forcing. The best estimates of the net radiative forcing are shown as black diamonds with corresponding uncertainty intervals; the numerical values are provided on the right of the figure, together with the confidence level in the net forcing (VH - very high, H - high, M - medium, L - low, VL - very low).* **23**

Figure 1.16. *Interaction between solar radiation and particles.* **24**

Figure 1.17. *Airway macrophages from healthy schoolchildren in Leicester, UK; a) non-affected by particle inhalation, b) affected by particle inhalation. (Source: Kulkarni, 2016).* **25**

Figure 1.18. *Schematic overview of the particle size and related body affection Source: SCOR, 2018.* **26**

Figure 1.19. *Simplified scheme for VOCs degradation. (Source: Hallquist, 2009)* **28**

Figure 1.20. *Ozone production potential for gasoline, diesel and non-tailpipe gasoline. (Source : Gentner, 2013).* **30**

Figure 1.21. *Simulated annual mean surface concentration of (a) anthropogenic VOCs and (b) isoprene. (Source: Spracklen, 2011)* **31**

Figure 1.22. *Effect of total organic mass (C_{OA}) over condensed fraction (φ) of a specie i, as a function of the partition coefficient ($K_{p,i}$). (Source : Aladro, 2013)* **33**

Figure 1.23. *Framework of the 2-D VBS, where the OA composition is described as a function of the degree of the OA oxygenation and the saturation concentration. The black lines denote the number of the carbons, while the green lines correspond to the oxygen number. The experimental ambient oxygenated organic aerosol (OOA) is in the dashed area in the upper corner.* **35**

Figure 1.24. *Flow chart for the reactions and chemical products of the MCM model. (Source: Saunders, 2003)*..... **36**

Figure 1.25. *Comparison mechanism for n-heptane oxidation. Solid lines GECKO-A model, dashed lines: MCM v3 model. Shaded area represents ±20% deviation.* **37**

Figure 1.26. *Potential SOA yield as sum of SOA contribution for gasoline and diesel fuel as a function of carbon number. (Source: Gentner, 2012)*..... **38**

Figure 1.27. *Time series of ammonium, sulfate, organics and nitrate for a PAM experiment as a function of photochemical age. Shaded periods represent non-photoxidation periods. Equivalent atmospheric oxidation (i.e, "1 day" at [$^{\bullet}$OH] = 3x10^{6} molec/cm^{3}). (Source: Tkacik, 2014)* **39**

Figure 1.28. *Influence of cold/hot start conditions for SOA formation. GDI Euro 5 vehicle emissions were oxidized in an oxidation flow reactor (OFR). Vehicle emissions were injected during a WLTC run. Source: Pieber, 2018*..... **40**

Figure 1.29. *Predicted aromatics versus observed SOA for a smog chamber experiment during aging of emissions from Euro 5 gasoline light-duty vehicle. (Source: Platt, 2013)* **41**

Figure 1.30. *SOA and OA from diesel cars a) influence of driving conditions and DPF for diesel vehicles; b) averaged POA and fractional predicted SOA after 2 days of photoxidation. (Source: Zhao, 2015)*..... **42**

Figure 1.31. *a) Measured AMS PMF factor concentration as function of photochemical age; b) OA/ΔCO evolution for weekdays and weekend as function of photochemical age; c) OOA/ΔCO evolution for weekdays and weekend as function of photochemical age. (Source: Ensberg, 2014)* **44**

Figure 2.1. *IFSTTAR schematic diagram of the experimental set up.* **63**

Figure 2.2. *Chassis dynamometer forces, source : http://howstuffworks.* **64**

Figure 2.3. *Chassis dynamometer device: a) screen; b) fan; c) roller bench system.* **64**

Figure 2.4. *FPS setup and working principle where a) is the exhaust gas enter, b) is the diluted exhaust gas outlet, c) is the primary dilution air enter and d) is the second dilution air enter.* **65**

Figure 2.5. *VKL dilution system working principle.* **65**

Figure 2.6. *Speed profile of transient cycles : a) WLTC, b) Artemis urban, c) Artemis road and d) Artemis motorway.* **67**

Figure 2.7. *Aerosol flow tube schematic setup.* **72**

Figure 2.8. *a) AFT view with case to protect from UV lights, b) detailed cone inlet and Teflon piece, c) cross-sectional view for the arrangement of lamps and water jacket around the flow reactor, d) seed inlet, e) humidity inlet, f) air inlet, g) IPN inlet, h) Primary VOC inlet, i) Secondary VOC inlet (if necessary), j) by-pass reactor line, k) humidity sensor at reactor outlet, l) three-way valve for bypass/reactor measurements, m) HEPA bypass line, n) Splitter for measurement lines, o) flow controller box and flow controllers set, p) permeation oven n°1.*..... **73**

Figure 2.9. *Schematic diagram of a Michelson interferometer, configured for FTIR.*..... **78**

Figure 2.10. *Schematic diagram for Flame Ionization Detection (FID).* **79**

Figure 2.11. *PTRMS working principle.* **79**

Figure 2.12. *Time of flight principle.* **81**

Figure 2.13. *TD-GC-MS analytic system, a) sample changer, b) thermo-desorber, c) air server, d) mass spectrometer, e) gas phase chromatograph.* **82**

Figure 2.14. *a) general scheme of c-ToF-AMS b) working principle of aerodynamic lens in HR-ToF-AMS through FLUENT software simulation and c) working principle of thermal vaporization and electron impact ionization. (Source : Drewnick, 2005 ; Jayne, 2000 and Alfarra, 2004)* ... **85**

Figure 2.15. *CHARON inlet configuration. (Source: Eichler, 2015)* **86**

Figure 2.16. *a)Comparison of measured and injected acetone for removing efficiency of GPD. b) Transmission efficiency of the GPD for size selected particles generated from ammonium nitrate (AN), ammonium sulfate (AS), glutaric acid (GA) and methylglyoxal (MG). (Source: Eichler, 2015)* **87**

Figure 2.17. *Enrichment factor of the ADL for ammonium nitrate (AN), ammonium sulphate (AS) and dimethylaminium nitrate (DMAN) particles in the 200-750nm size range. (Source: Eichler, 2015)* **88**

Figure 2.18. *TEM grid sampling.* **89**

Figure 2.19. *SMPS operating principle with detail working principle of impactor, DMA and CPC. (Source: Hinds, 1999 and Kim, 2009)* **90**

Figure 2.20. *FMPS operating principle. Source: dieselnet.com* **91**

Figure 2.21. *Faraday cup electrometer operating principle. Source: grimm-aerosol.de* **92**

Figure 2.22. *Aethalometer working principle.* **93**

Figure 2.23. *Nitrogen oxides analyzer scheme. Source: www.Ecophysics-us.com)* **93**

Figure 3.1. *Particle number concentration for gasoline DI Euro 6 (GDI2) vehicle during WLTC cold start cycle, sampled after tailpipe (a) and after CVS dilution system (b).* **100**

Figure 3.2. *Time series of organic, water, NO_3^-, PAHs, BC particles and particle distribution during a WLTC cold start cycle (a, b) and WLTC hot start (c, d) for GDI 3 Euro 5 gasoline vehicle.* **102**

Figure 3.3. *Mass spectra of the organics and PAHs fraction and related size distribution during the first minutes of a WLTC cold start for GDI3 Euro 5 vehicle.* **103**

Figure 3.4. *Size distribution of the organic fraction during a WLTC cold cycle for GDI3 vehicle.* **104**

Figure 3.5. *BC concentration and particle size distribution (5-60 nm) for Euro 5 GDI1 vehicle during Artemis urban cold start (cycle n°1) and Artemis motorway (cycle n°2-5).* **104**

Figure 3.6. *TEM analysis during Artemis Urban cold start sampled in the first 120 seconds for GDI2 vehicle.* **105**

Figure 3.7. *TEM analysis during WLTC cycles for Euro 6 GDI2 vehicle: a, b and c sampled during the first two minutes of the cycle and d, e and f sampled at the end of the cycle (from the 26th to 29th minute).* **106**

Figure 3.8. *TEM analysis during cold start Artemis Urban cycle for a Euro 5 GDI1 vehicle (sampled after CVS, first 120 seconds).* **108**

Figure 3.9. *TEM analysis during Artemis Motorway cycle for Euro 5 GDI1 vehicle (after CVS, first 7 minutes of cycle).* **109**

Figure 3.10. *Time series concentration of organic, SO_4^{2-}, NO_3^-, NH_4^+, PN and particle size distribution during WLTC cold/hot start for a Euro 5 D3 diesel.* **110**

Figure 3.11. *Time series concentration of organic, water, BC and PN during Artemis urban cold start cycle for a Euro 5 D1 diesel vehicle.* **111**

Figure 3.12. *TEM analysis during Artemis urban cold start period for Euro 5 diesel D1 vehicle.* **112**

Figure 3.13. *Time series concentration of organic, water, NO_3^-, NH_4^+, BC, PN and particle distribution under Artemis Motorway cycle for Euro 5 D1 diesel vehicle.* **113**

Figure 3.14. *TEM analysis during Artemis Motorway cycle for Euro 5 D1 vehicle (after CVS).* **114**

Figure 3.15. *Percentage of 14< PN ≤ 23 nm compared to total particle number emission factors for four vehicles and during different cycles. C: cold, H: hot* **116**

Figure 3.16. *EFs of a) BC for three GDI vehicles during Artemis and WLTC cycles, b) BC for three diesel vehicles during Artemis and WLTC cycles, c) organic and inorganic fraction for Euro 5 diesel D3 vehicle during WLTC cycle, d) organic and inorganic fraction for D1 vehicle during WLTC cycle and e) organic and inorganic fraction for GDI3 vehicle during WLTC cycle.* **118**

Figure 3.17. *CO time series emission during WLTC (cold and hot start) for a) GDI3 and b) D3.* **119**

Figure 3.18.*THC time series emission during WLTC (cold and hot start) for a) Euro 5 GDI3 and b) Euro 5 D3.* **120**

Figure 3.19. *NOx time series emission during WLTC (cold and hot start) for a) Euro 5 GDI3 and b) Euro 5 D3.* **121**

Figure 3.20. *CO_2 time series emission during WLTC (cold and hot start) for a) Euro 5 GDI3 and b) Euro 5 D3.* **121**

Figure 3.21. *EFs of CO, CO_2, NOx and THC for three GDI and three diesel (Euro 5 and Euro 6) vehicles. Error bars have been determinate from repeatability of EFs obtained during cycles.* **123**

Figure 3.22. *Time series profile of benzene under WLTC cold start for Euro 5 (a) GDI3 and (b) D3 and time series profile of ammonia under WLTC cold start for Euro 5 (c) GDI3 and (d) D3.* **125**

Figure 3.23. *Emission Factors of gaseous compounds for GDI3 vehicle during WLTC cycle.* .. **127**

Figure 3.24. *Emission Factors of gaseous compound for D3 vehicle during WLTC cycle.* **128**

Figure 3.25. *Mass speciation of compounds based on family for GDI3 and D3vehicles during WLTC cold and hot start cycle.* **128**

Figure 3.26. *Emission Factors of BTEX compounds for GDI3 vehicle during WLTC cycle.* **129**

Figure 3.27. *Emission Factors of BTEX compounds for D3 vehicle.* **129**

Figure 3.28. *EF for linear/branched aliphatic compounds up to C_{15} emitted for the GDI3 vehicle during WLTC cycle.* **130**

Figure 3.29. *EF for linear/branched aliphatic compounds up to C_{15} emitted for the D3 vehicle during WLTC cycle.* **131**

Figure 4.1. *Comparison between SOA measured using AMS and CHARON.* **140**

Figure 4.2. *Comparison between measured particle phase using AMS and SMPS.* **140**

Figure 4.3. *Time series of sulfate, ammonium, nitrate, organic SOA mass concentrations as measured by the AMS and organic SOA mass concentration as sampled by CHARON-PTR-ToF-MS during two toluene photo-oxidation experiments. The AMS mass concentrations have been corrected for the CE, while the CHARON-PTR-ToF-MS organic mass concentration has been corrected for transmission efficiency. In both cases the initial toluene concentration was approximately 131 ppb and the RH was around 32%.* **141**

Figure 4.4. *SOA yield as a function of* (a) *formed organic aerosol; (b) seed concentration.* . **142**

Figure 4.5. *SOA yield comparison with Ng et al. 2007 and Hildebrandt et al. 2009 toluene SOA experiments.* **142**

Figure 4.6. *Gas phase carbon number distribution of toluene degradation products a) as a function of oxygen at 7°C, b) as a function of oxygen at 21°C, c) as a function of nitrogen at 7°C, d) as a function of nitrogen at 21°C.* **143**

Figure 4.7. *Particle phase carbon number distribution of toluene degradation products a) as a function of oxygen at 7°C, b) as a function of oxygen at 21°C, c) as a function of nitrogen at 7°C, d) as a function of nitrogen at 21°C.* **144**

Figure 4.8. *Experimental K_p values of m/z's for toluene photoxidation, where a unique compound or a set of isomers compounds were assigned. The error bars correspond to the one standard deviation of the average.* **147**

Figure 4.9. *O:C ratios versus the saturation concentration in terms of $log_{10}C^*$ for the species indentified in both gas and particle phase. The size of the dots denotes the oxygen atom number of each species. The error bars correspond to logarithmic values of the minimum and maximum K_p values shown in Figures 4.6. and AV.2.* **148**

Figure 4.10. *Influence of Temperature and initial VOC concentration for naphthalene experiments.* **149**

Figure 4.11. *Gas phase carbon number distribution with addition of 200 ppb of NOx a) as a function of oxygen at 21°C b) as a function of nitrogen at 21°C c) as a function of oxygen at 7°C d) as a function of nitrogen at 7°C* **150**

Figure 4.12. *Particle phase carbon number distribution with addition of 200 ppb of NOx at 7°C a) as a function of oxygen b) as a function of nitrogen.* **151**

Figure 4.13. *Experimental K_p values of m/z's for naphthalene photoxidation, where a unique compound or a set of isomers compounds were assigned. The error bars correspond to the one standard deviation of the average.* **153**

Figure 4.14. *O:C ratios versus the saturation concentration in terms of $log_{10}C^*$ for the species indentified in both gas and particle phase. The size of the dots denotes the oxygen atom number of each species. The error bars correspond to logarithmic values of the minimum and maximum K_p values shown in Figures 4.12.* **154**

Figure 4.15. *SOA yield versus SOA concentration as a function of temperature and initial cyclohexane concentration.* **155**

Figure 4.16. Average oxygen number as a function of carbon number product distribution at 7°C for: gas phase experiment (a), gas phase experiment with NOx addition (b), particle phase experiment (c), particle phase experiment with NOx addition(d). **156**

Figure 4.17. *O:C ratios versus the saturation concentration in terms of $log_{10}C^*$ for the species indentified in particle phase. The size of the dots denotes the oxygen atom number of each species.* **158**

Figure 4.18. SOA *yield versus SOA formation as a function of different temperatures and initial concentrations of nonane.* **159**

Figure 4.19. *Average oxygen number as a function of carbon number product distribution for: gas phase experiment at 21°C (a) , for gas phase experiment at 7°C (b) for particle phase experiment at 21°C (c) and for particle phase experiment at 7°C (d).* **160**

Figure 4.20. *Simplified linear alkane degradation mechanism at low NOx regime, adapted from Yee et al, 2013*..... **162**

Figure 4.21. SOA *yield versus SOA formation as a function of different temperatures, VOC concentrations and NOx concentrations.*..... **163**

Figure 4.22. carbon number distribution as a function of oxygen number distribution for: gas phase experiments at 16°C (a), particle phase experiments at 7°C (b), gas phase experiments at 16°C (c) and particle phase experiments at 7° C (d). **164**

Figure 4.23. *SOA formed as a function of ammonium sulfate seed for individual VOC and mixtures.* **165**

Figure 4.24. *SOA formed as a function of temperature for individual VOC and mixtures.*... **165**

Figure 4.25. *Normalized SOA for some VOC and mixtures.* **166**

Figure 4.26. *Comparison of normalized SOA yield for experiment with/without addition of NOx.* **167**

Figure 4.27. *Averaged primary VOC concentration as a function of carbon number for different families of compounds.* **168**

Figure 4.28. *Averaged VOC concentration over mass spectrum distributed by families for GDI Euro 5 vehicle for first 7 minutes of WLTC cold cycle.* **168**

Figure 4.29. *Organic, nitrate, sulfate and PAHs time series profiles for AFT photoxidation of GDI emissions.* **169**

Figure 4.30. *Gas phase carbon number distribution as a function of oxygen (a) and nitrogen (b) for GDI exhaust photoxidation.* **170**

Figure 4.31. *Particle phase carbon number distribution as a function of oxygen (a) and nitrogen (b) for GDI exhaust photoxidation.* **171**

Figure AIV.1. *m/z for first minute of Artemis urban cold start cycle for D1 diesel Euro 5 vehicle.* **194**

Figure AIV.2. *Particle size distribution for a) GDI2 during Artemis urban cold start cycle, b) Diesel D2 during Artemis urban cold start cycle , c) GDI2 during Artemis Motorway cycle and d) Diesel D2 during Artemis Motorway cycle*..... **194**

Figure AV.1. *Proposed first generation products and tentative further products for toluene photoxidation based on experimental analysis and previous literature.*..... **199**

Figure AV.2. Experimental K_p values of m/z's, where a unique compound or a set of isomers compounds were assigned. The error bars correspond to the one standard deviation of the average. **204**

Figure AV.3. *Simplified naphthalene degradation mechanism, adapted from Kautzman et al.2010.* **204**

Figure AV.4. *Possible mechanism for the formation of C_7 and C_9 compounds. Source: Kautzman et al. 2010.*..... **205**

Figure AV.5. *Simplified cyclohexane degradation mechanism and first generation product formation, adapted from Alam et al., 2011 and Lim and Ziemann, 2009* **208**

Figure AV.6. *Possible route to formic acid formation from cyclohexoxy radical. Source: Orlando et al.,2000* **208**

Figure AV 7. *Proposed mechanism for first generation product formation from phenol photoxidation. Source: Olariu et al., 2002* **213**

Figure AV.8. *Formation mechanism of maleic anhydride from catechol. Source: Turpin et al., 2005* **213**

Table 1.1. *Air quality standards under the Air Quality Directive, and WHO air quality guidelines*..... **13**

Table 1.2. *Evolution of emission limits for light passenger cars approved in Europe*. **14**

Table 2.1. *Technical characteristic of used cycles*..... **68**

Table 2.2. *Characteristics of tested vehicles*. **69**

Table 2.3. *Vapor pressure of used compounds (in mmHg) at 30, 60 and 90°C*. **75**

Table 2.4. *Rate constants for selected VOCs with •OH radical oxidant and corresponding lifetimes*. **76**

Table 2.5. *Values of proton affinity for some typical VOCs*..... **80**

Table 2.6. *ATD-GC-MS conditions* **83**

Table 3.1. *Relation of vehicles used for each study*. **99**

Table 3.2. *Particle composition by EDX in mass % analysis for GDI2 vehicle*. **107**

Table 3.3. *Main characteristics and dilution conditions for vehicle and experiments carried out for particle number study*. **115**

Table 4.1. *Gas and particle phase products quantification (ppbC) during the toluene photoxidation for experiments carried out at 7°C and 21°C. In bold are the identified products upon comparison with pure reference compounds*. **145**

Table 4.2. *Gas and particle phase products quantification (ppbC) found in naphthalene photoxidation for experiments at 7°C and 21°C*. **152**

Table 4.3. *Gas and particle phase products quantification (ppbC) found in cyclohexane photoxidation for experiments at 7°C without and with NOx addition*. **157**

Table 4.4. *Gas and particle phase products quantification (ppbC) found in nonane photoxidation for experiments at 7°C and 21°C*. **161**

Table 4.5. Gas and particle mass fraction of product regarding parent VOC. **164**

Table 4.6. *Nitro-products found in gas and particle phase of GDI exhaust photoxidation*.... **172**

Table 4. 7. *Maximun and minimum consumed VOC fraction (%) and identified product fractions (%) in gas and particle phase for tested VOCs at different temperatures.* **173**

Table AI.1. *Fuel composition for tested vehicles.* **186**

Table AII.1. *Experiment conditions using for D1 Euro 5 diesel vehicle.* **187**
Table AII.2. *Experiment conditions using for D3 Euro 5 diesel vehicle.* **187**
Table AII.3. *Experiment conditions using D2 Euro 6b diesel vehicle.* **188**
Table AII.4. *Experiment conditions using for GDI1 Euro 5 gasoline vehicle.* **189**
Table AII.5. *Experiment conditions using for GDI3 Euro 5 gasoline vehicle.* **189**
Table AII.6. *Experiment conditions using for GDI2 Euro 6b gasoline vehicle.* **190**

Table AIII.1. *Experimental conditions for toluene experiments.* **191**
Table AIII.2. *Experimental conditions for nonane experiments.* **192**
Table AIII.3. *Experimental conditions for cyclohexane experiments.* **192**
Table AIII.4. *Experimental conditions for naphthalene experiments*..... **192**
Table AIII.5. *Experimental conditions for naphthalene experiments*..... **193**
Table AIII.6. *Experimental conditions for naphthalene experiments*..... **193**

Table AV.1. *Gas and particle phase main products (concentration of product/concentration total product (ppbC/ppbC)) found in toluene photoxidation for experiments at 21°C*..... **195**
Table AV.2. *Gas and particle phase main products (concentration of product/concentration total product found (ppbC/ppbC)) found in toluene photoxidation for experiments at 7°C.* **196**
Table AV.3. *Gas and particle phase main products (concentration of product/consumed VOC (ppbC/ppbC)) found in toluene photoxidation for experiments at 7°C.* **197**
Table AV.4. *Gas and particle phase main products (concentration of product/consumed VOC (ppbC/ppbC)) found in toluene photoxidation for experiments at 21°C.* **198**
Table AV.5. *Gas and particle phase products (concentration of product/concentration total product formed (ppbC/ppbC)) found in naphthalene photoxidation for experiments at 7°C.* **200**
Table AV.6. *Gas phase main products (concentration of product/concentration total product (ppbC/ppbC)) found in naphthalene photoxidation for experiments at 21°C.* **201**
Table AV.7. *Gas phase main products (concentration of product/consumed VOC (ppbC/ppbC)) found in naphthalene photoxidation for experiments at 7°C.* **202**
Table AV.8. *Gas phase main products (concentration of product/consumed VOC (ppbC/ppbC)) found in naphthalene photoxidation for experiments at 21°C*..... **203**
Table AV.9. *Gas and particle phase products (concentration of product/concentration total product formed (ppbC/ppbC)) found in cyclohexane photoxidation for experiments at 7°C without NOx addition*..... **205**

Table AV.10. *Gas and particle phase main products (concentration of product/concentration total product (ppbC/ppbC)) found in cyclohexane photoxidation for experiments at 7°C with NOx addition.* **206**
Table AV.11. *Gas and particle phase main products (concentration of product/consumed VOC (ppbC/ppbC)) found in cyclohexane photoxidation for experiments at 7°C without NOx addition.* **206**
Table AV.12. *Gas and particle phase main products (concentration of product/consumed VOC (ppbC/ppbC)) found in cyclohexane photoxidation for experiments at 7°C with NOx addition.* **207**
Table AV.13. Gas and *particle phase main products (concentration of product/concentration total product (ppbC/ppbC)) found in nonane photoxidation for experiments at 7°C.* **209**
Table AV.14. Gas and *particle phase main products (concentration of product/concentration total product (ppbC/ppbC)) found in nonane photoxidation for experiments at 21°C.* **210**
Table AV.15. Gas and *particle phase main products (concentration of product/consumed VOC (ppbC/ppbC)) found in nonane photoxidation for experiments at 7°C.* **211**
Table AV.16. Gas and *particle phase main products (concentration of product/consumed VOC (ppbC/ppbC)) found in nonane photoxidation for experiments at 21°C.* **212**
Table AV.17. *K rate (x10^{-9} cm s^{-1}) used for detected mass during PTRMS/CHARON analysis. Rests of masses have a k rate of 3.2 by default.* **214**
Table AV.18. *References of pure compounds (>99 %, Sigma-Aldrich) for PTRMS gas phase and CHARON particulate phase. PTRMS configuration was: Pdrift 2.075 mbar; Tdrift= 120°C; Udrift= 395 V; E/N= 114 Td (PTRMS) ; E/N =108 Td (CHARON). For CHARON references, pure compound were used. The compounds were dissolved in water (if soluble). Some compounds was not detected in the particle phase probably for the reduced solubility.* **215**

Table VI.1. *Response factors (counts/ng) for VOCs used for ATD-GC-MS calibration* **217**

Table AVII.1. *AMS and CHARON SOA formed intercomparison.* **218**

List of Abbreviations

ACEA: *European Automobile Manufacturers Association*

ADEME: *Agence de l'Environnement et de la Maîtrise de l'Energie*

ADL: *Aerodynamic Lens*

AEIG: *Atmospheric Emission Inventory Guidebook*

AFT: *Aerosol Flow Tube*

AMS: *Aerosol Mass Spectrometer*

AN: *Ammonium Nitrate*

AS: *Ammonium Sulphate*

ATD-GC MS: *Automated Thermo desorption gas chromatograph*

BC: *Black Carbon*

BrC: *Brown Carbon*

BTEX: *Benzene-Toluene-Ethylbenzene-Xylene*

CADC: *Common Artemis Driving Cycles*

CaPVeREA: *Caractérisation des Particules des Véhicules Récents et leur Évolution Atmosphérique*

CCFA: *Comité des Constructeurs Français d'Automobiles*

CCN: *Cloud condensation nuclei*

CFC: *Chlorofluorocarbon*

CH_4: *Methane*

CHARON: *CHemical Analysis of aeRosol ON-line*

CIMS: *Chemical Ionisation Mass Spectrometer*

CIOA: *Cooking-Influenced Organic Aerosol*

CO: *Carbon monoxide*

CO_2: *Carbon dioxide*

CPC: *Condensation Particle Counter*

CVS: *Constant Volume Sampler*

DHF: *Dihydrofuran*

DMA: *Differenctial Mobility Analyzer*

DNPH: *Dinitrophenylhydrazine*

DOC: *Diesel Oxydation Catalyst*

DPF: *Diesel Particulate Filter*

DR: *Dilution Ratio*

EC: *Elemental Carbon*

EDX: *Energy Dispersive X-ray spectroscopy*

EEA: *European Environment Agency*

EF: *Emission Factor*

***ELPI**: Electrical Low Pressure Impactor*

***ELVOC**: Extremely Low Volatility Organic compound*

***EPA**: United States Environmental Protection Agency*

***ERMES**: the European Research group on Mobile Emission Sources*

***EU**: European Union*

***FBC**: Fuel Borne Catalyst*

***FID**: Flame Ionization Detection*

***FIDMS**: Flame Ionization Detector Mass Spectrometer*

***FMPS**: Fast Mobility Particle Sizer*

***FPS**: Fast Particle Sampler*

***FTIR**: Fourier Transform Infrared Spectroscopy*

***GA**: Glutaric Acid*

***GBD**: Global Burden of Disease*

***GDI**: Gasoline Direct Injection*

***GDP**: Gross Domestic Product*

***GECKO-A**: Generator of Explicit Chemistry and Kinetics of Organics in the Atmosphere*

***GHG**: Greenhouse Gases*

***GIEC**: Groupe d'experts intergouvernemental sur l'évolution du climat*

***GPD**: Gas Phase Denuder*

***GPF**: Gasoline Particulate Filter*

***H_2O**: Water/ vapour water*

***HBEFA**: HandBook Emission Factor for Road Transport*

***HCl**: Hydrogen Chloride*

***HCN**: Hydrogen Cyanide*

***HCs**: Hydrocarbons*

***HEI**: Health Effects Institute*

***HEPA**: High Efficiency Particulate Air*

***HF**: Hydrogen Fluoride*

***HM**: Heavy Metals*

***HNCO**: Isocyaniric acid*

***HOA**: Hydrocarbon-like Organic Aerosol*

***HONO**: Nitrous acid*

***IARC**: International Agency for Research on Cancer*

***IE**: Ionization Efficiency*

***IFSTTAR**: French Institute of Science and Technology for Transport, Spatial Planning, Development and Networks*

***IHME**: Institute for Health Metrics and Evaluation*

***IPCC**: Intergovernmental Panel on Climate Change*

***IPN**: Isopropyl Nitrite*

***IR**: Infrared*

***ITS**: Intelligent Transport Systems*

***IVOC**: Intermediate Volatile Organic Compounds*

***LOA**: Local organic Aerosol*

***LVOC**: Low volatility Organic compounds*

***LVOOA**: Low Volatility Oxygenated Organic Aerosol*

***MAAP**: MultIAngle Absorption Photometer*

***MCM**: Master Chemical Mechanism*

***MCP**: Micro Channel Plates*

***MG**: Methylglyoxal*

***MW**: Molecular Weight*

***N_2O**: Nitrous oxide*

***NEDC**: New European Driving Cycle*

***NH_3**: Ammonia*

***NH_4^+**: Ammonium*

***NMOG**: Non Methane Organic Gas*

***NMVOC**: Non-Methane Volatile Organic Compound*

***NO**: Nitrogen monoxide*

***NO_2**: Nitrogen dioxide*

***NO_3^-**: Nitrate*

***NOx**: Nitrogen oxides*

***O_2**: Oxygen*

***O_3**: Ozone*

***OA**: Organic Aerosol*

***OC**: Organic Carbon*

***OECD**: Organization for Economic Cooperation and Development*

***$^{\bullet}OH$**: Hydroxyl radical*

***OM**: Organic Matter*

***OPP**; Ozone Production Potential*

***PA**: Proton Affinity*

***PAHs**: Polycyclic Aromatic Hydrocarbons*

***PAM**: Potential Aerosol Mass*

***PAN**: Peroxyacyl Nitrates*

***PEMS**: Portable Emission Measurement System*

***PFI**: Port Fuel Injection*

***PM**: Particle Matter*

***PMF**: Positive Matrix Factorization*

***PMP**: Particle Measurement Programme*

***PN**: Particle Number*

***PNC**: Particle Number Concentration*

***POA**: Primary Organic Aerosol*

***PTRMS**: Proton Transfer Reaction Mass Spectrometer*

***RDE**: Real Driving Emission*

***RF**: radiative forcing*

***RH**: Relative Humidity*

***$RO^{\bullet}$**: Alkoxy radical*

***$RO_2^{\bullet}$** alkylperoxy radical*

***SCR**: Selective Catalytic Reduction*

***SMPS**: Scanning Mobility Particle Sizer*

***SO_2**: Sulfur dioxide*

***SO_4^{2-}**: Sulphate*

***SOA**: Secondary Organic Aerosol*

***SOx**: Sulfur oxides*

***SULEV**: Super Ultra-Low Emission Vehicle*

***SVOC**: Semi Volatile Organic Compounds*

***SVOOA**: Semi Volatile Oxygenated Organic Aerosol*

***TDC**: Time-to-Digital Converter*

***TDU**: Thermo Desorption Unit*

***TEM**: Transmission Electron Microscopy*

***THCs**: Total Hydrocarbons*

***ToF**: Time of Flight*

***TSP** total suspended particles*

***TWC**: Three Way Catalyst*

***UNO**: United Nation Organization*

***UV**: Ultraviolet*

***VBS**: Volatility Basis Set*

***VOC**: Volatile Organic Compound*

***WHO**: World Health Organization*

***WLTC**: Worldwide Harmonized Light Vehicles Test Cycle*

***WLTP**: Worldwide Harmonized Light-Duty Vehicles Test Procedure*

Publication List

Louis, C., Liu Y., Martinet, S., D'Anna, B., Martinez-Valiente, A., Boreave, A., R'Mili, B., Tassel, P., Perret, P., André, M. Dilution effects on ultrafine particle emissions from Euro 5 and Euro 6 diesel and gasoline vehicles. *Atmospheric Environment*. 169, 80-88, 2017. doi:10.1016/j.atmosenv.2017.09.007

A. Martinez-Valiente, M. Müller, P. Eichler, B. Temime-Roussel, E. Kostenidou' A. Wisthaler B. D'Anna, OH-initiated degradation of toluene: novel insight into the gas and particle phase chemical composition and partitioning, submission march/april 2019

A. Martinez-Valiente, E. Kostenidou; L. Fine, P. Eichler , F. Piel, C. Ferronato,' A. Wisthaler, B. D'Anna, Euro 5 unregulated pollutant characterization : particles and gaseous pollutants, submission 2019

A. Martinez-Valiente, E. Kostenidou; L. Fine, C. Ferronato,' B. D'Anna, Novel insight into the gas and particle phase chemical composition and partitioning of SOA produced by nonane, cyclohexane, naphthalene and phenol, submission 2019

P. Eichler, F. Piel, M. Müller, A. Martinez-Valiente, B. D'Anna, A. Wisthaler, Transient emissions of aromatics from modern GDI cars, article in preparation

F. Piel, M. Müller, P. Eichler, A. Martinez-Valiente, B. D'Anna, A. Wisthaler, Transient emissions of intermediate-volatility organic compounds from Euro 6 passenger cars, article in preparation

Oral Communications

A. Martinez Valiente, C. Louis, S. Martinet, P. Eichler, M. Müller, B. R'mili, P. Tassel, P. Perret, A. Wisthaler, M. André, Y.Liu, B. D'Anna « Regulated and unregulated emissions from Euro 6 DI gasoline vehices », *Atmos'fair : Pollution de l'air extérieur et intérieur, Sources, Impacts, Diagnostics & Solutions*. Lyon, France. 10-11 Octobre 2017.

A. Martinez Valiente, M. Müller, P. Eichler, W. Tan, B. Temime-Roussel, E. Kostenidou, A. Wisthaler, B. D'Anna, *"Secondary Organic Aerosol formation from toluene photoxidation using a new method for online submicron aerosol characterization", Conference Aerosol Technology* 2018. Bilbao, Espagne. 18-20 Juin 2018

Poster Presentations

A. Martinez-Valiente, C. Louis , A. Boreave, B. R'Mili, P. Tassel, P. Perret, M. Andre, B. D'Anna, Y. Liu. *'Emissions particulaires des véhicules Diesel et essence Euro 5 sur banc rouleau et effet de la dilution des échappements'*. 3ème réunion plénière du GDR Suie et journée « la suie dans l'atmosphère », Orléans 2016

A. Martinez-Valiente, B. R'Mili, A. Boreave, D. Lopez-Gonzalez, P. Vernoux, S. Perrier, C. Ferronato, L. Fine, C. George, T. Mikoviny, L. Zhou, M. Leblanc, S. Raux, A. Wisthaler and B. D'Anna, *"Impact of Diesel Particulate Filter (DFP) regeneration on primary emissions and secondary aerosol formation : preliminary results of laboratory study"* 3ème réunion plénière du GDR Suie et journée « la suie dans l'atmosphère ». Orleans, France. 10-13 Octobre 2016

A. Martinez-Valiente, B. R'Mili, A. Boreave, D. Lopez-Gonzalez, P. Vernoux, M. Leblanc, S. Raux and B. D'Anna, *"Emissions study during regeneration of diesel particulate filters (DPF) and their potential contribution to the formation of secondary organic aerosols (SOA)"* XXXVIème édition du colloque annuel du groupe français de cinétique et de photochimie » Reims, France. 31-01 juin 2016

CHAPTER I:

Context and State of the art

1.1. Road Transport Production and Evolution

The transport sector is fundamental to the economic development of a country and also allows better communication between people, favoring their quality of life.[1] The passenger car represents the most used displacement mean through the world. The worldwide production of passenger cars accounted for approximately 50 million vehicles in the 90's and exceeded the threshold of 78 million vehicles in 2016, [2] see figure 1.1. The monotonic growth was slowed down in 2008 and 2009 as a consequence of the financial crisis. A part from those years and average growth in car production of 3-4 % is observed. Looking more in details regional differences are important: China and South Asia show growth more than Europe and South America.

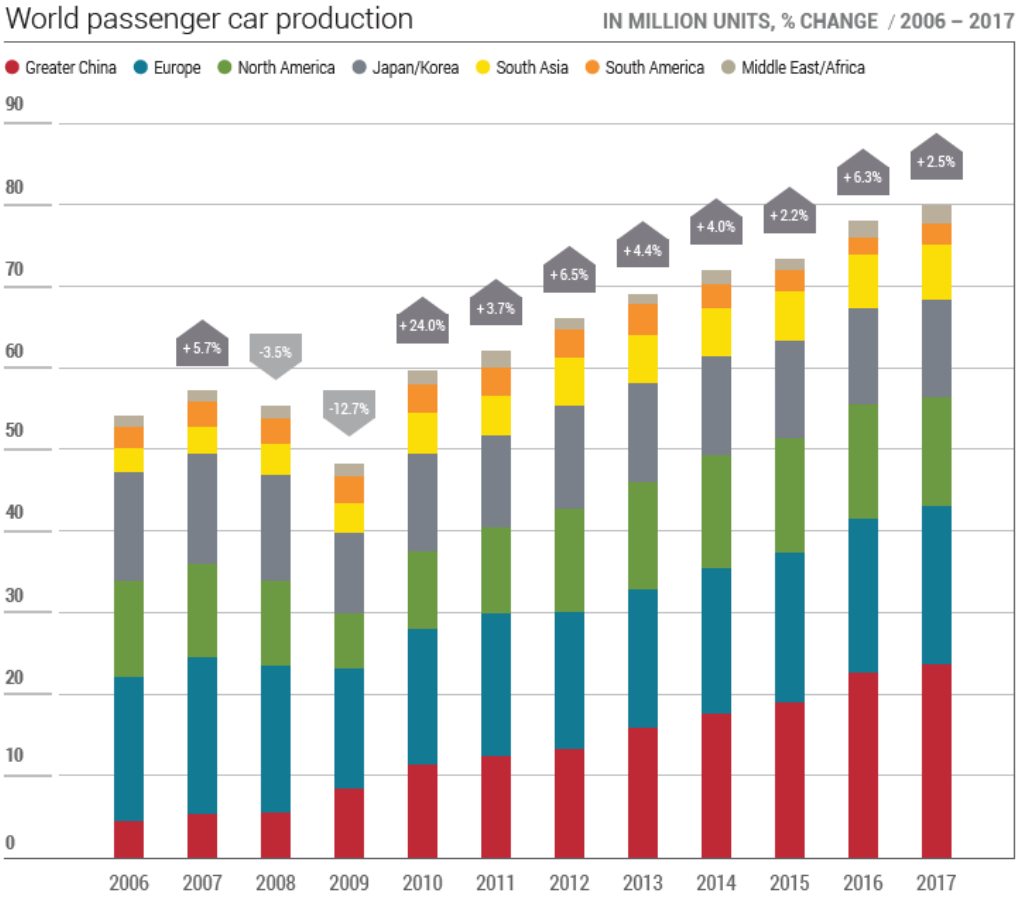

Figure 1.1. *World passenger car production, source : ACEA, 2018.*

Figure 1.2. shows the importance of in use passenger cars in Europe with respect to other countries. West European countries show higher motorization than in East European countries where passenger cars older than 10 years account for 43% of the fleet in 2016.[2] In 2016 in France, more than 2 million of vehicles were registered.[2] In Europe, petrol vehicles

already dominate market share over diesel in 2017 (49.4% vs. 44.8%).[3] Electric vehicles account for approximately 1.8% of the market share. Registration have doubled (38.000 vehicles) in last 3 years.[4] Despite the effort of some European cities as Oslo, Madrid or London to reduce traffic by limiting car access to downtown, road transport continues to be a major source of pollutants in urban areas around the world.[5]

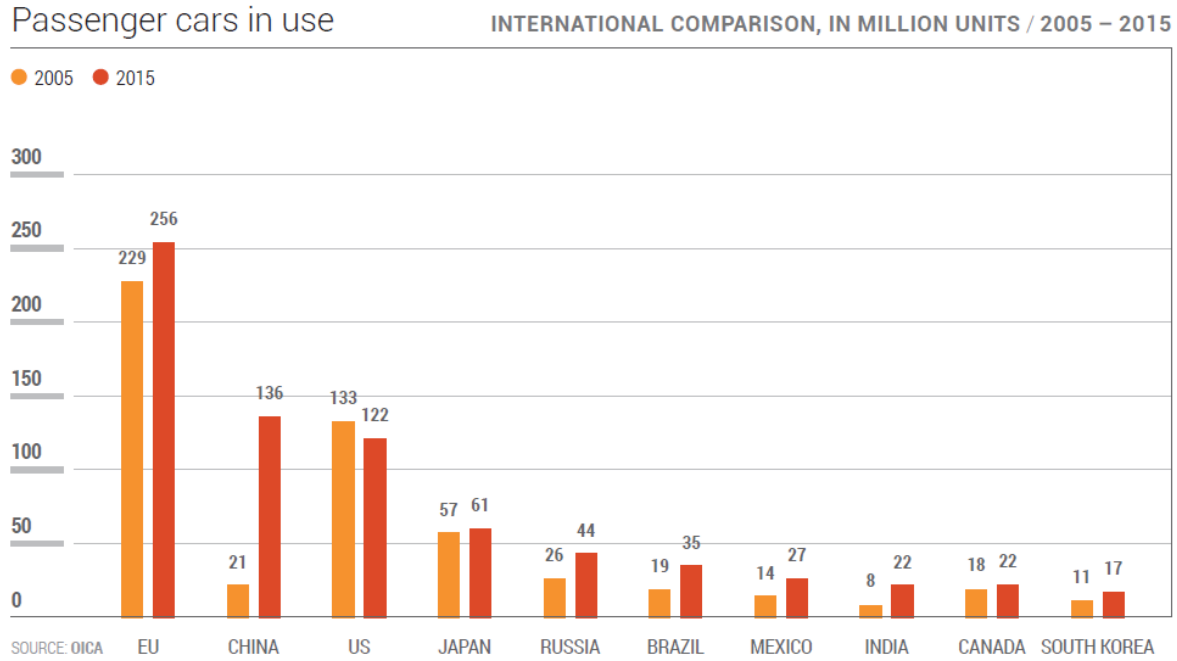

Figure 1.2. *Passenger car in use.Source: ACEA pocket guide 2017-2018.*

1.2. Primary emissions from road-transport

Emissions from road transport are particularly important in urban environment and along some commercial axis where the number of vehicles is extremely high and pollutants can be accumulated. These pollutants highly impact local and regional air quality and affect human health. Figure 1.3. shows the contribution to main pollutants by anthropogenic sources in Europe in 2016.[6] Road traffic emissions represent around the 40% of total Nitrogen Oxides (NOx) emissions, 10% of total Non Methane Volatile Organic Compounds (NMVOC), 20% of total Carbon Oxide (CO), 29% of total Black Carbon (BC) and 11% of Particle Matter below 2.5 μm (PM2.5). In addition, vehicle emissions highly contribute to the increase of greenhouse gases (GHGs). Some toxic species as metals (Pb and Cd) or Polycyclic Aromatic Hydrocarbons (PAHs) are also emitted. The important reduction in vehicle exhaust emissions achieved in the last two decades is offset between the growth in traffic fleet and the introduction of aftertreatment devices together with improvement of engines efficiency and use of cleaner fuels. Thus, a reduction of approximately 80% is achieved for CO and NMVOC and around 50% for particles and NOx. Nevertheless, Carbon dioxide (CO_2) emissions from transport have increased by 17%

between 1990 and 2014.[7] The next sections will be devoted to a detailed description of road transport emissions.

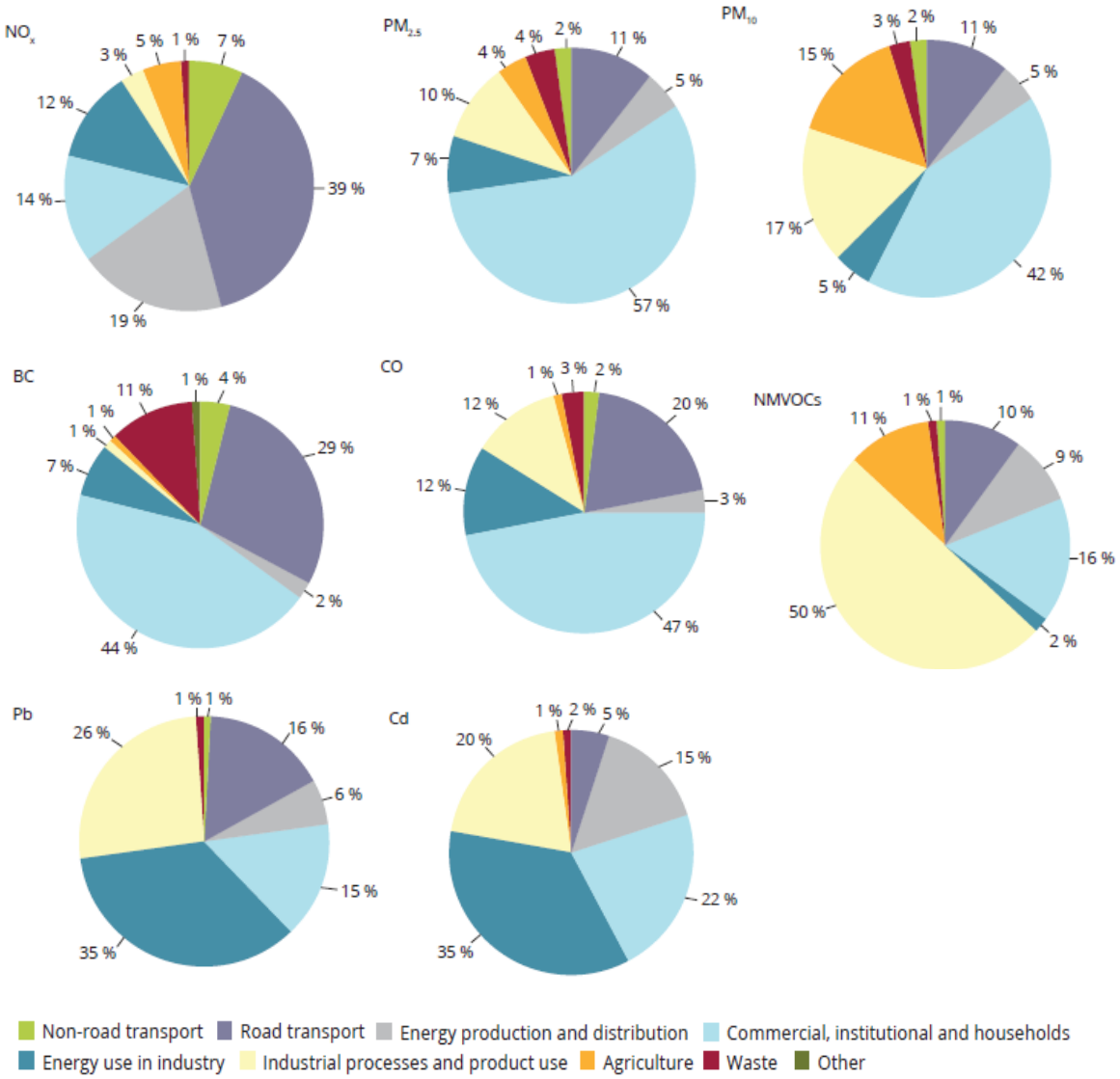

Figure 1.3. *Emission of the main pollutants by sector group in Europe in 2016 (source: EEA, 2018).*

1.2.1. Particles

Road transport is estimated to be responsible for up to approximately 11% of primary emitted PM2.5 in Europe,[6] and can reach 25% in urban areas.[8] Soot is a major component of particle matter emitted from vehicles, coming from incomplete combustion. In an ideal case, engine combustion will lead to the formation of water vapor and CO_2 only. In reality, unburned carbon is also formed. PM emitted from road transport presents three main distribution modes: nucleation, Aitken and accumulation. Formation of different modes is described in figure 1.4.

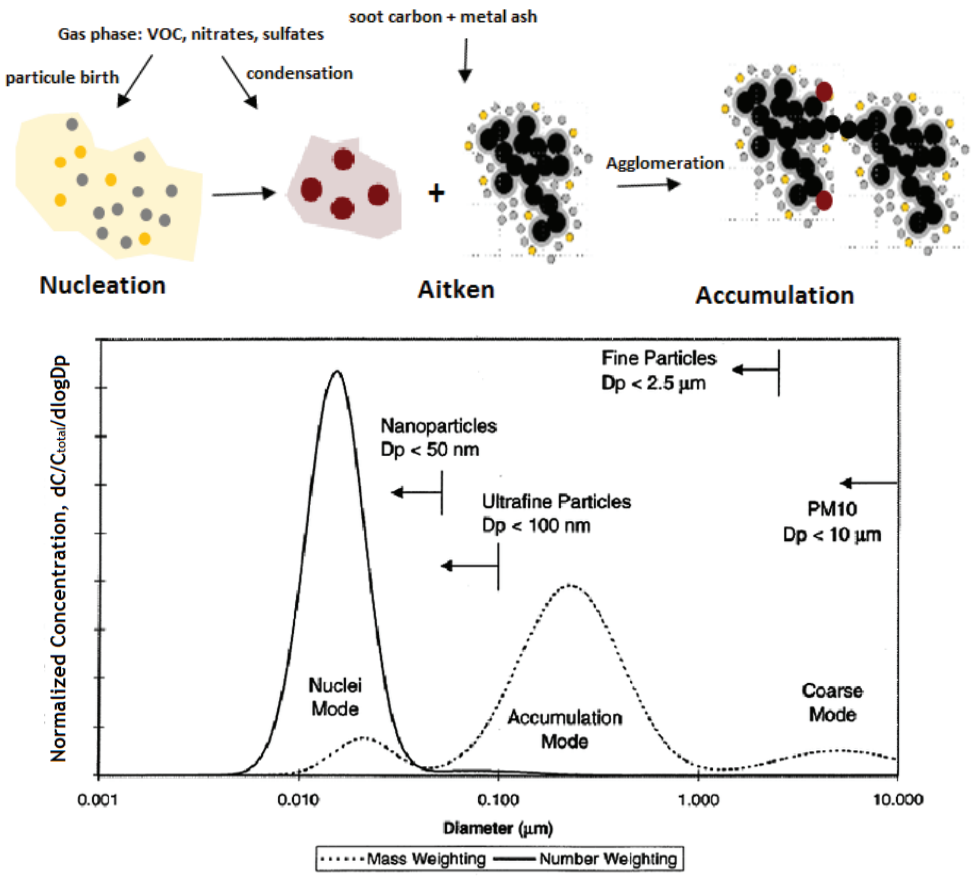

Figure 1.4. *Formation of nucleation, Aitken and accumulation particles mode during vehicle exhaust emissions (source: Kittelson, 1998).*

A first nucleation mode below 20 nm is typically formed by condensable material as organic compounds and/or sulphates during dilution and cooling of the exhaust. The second mode is around 60-100 nm, the so-called Aitken mode. This mode comprises fractal-like soot particles and condensable material. The accumulation mode, with particles around 100-500 nm, can also be observed and comprises carbonaceous soot agglomerates and lubricant oil droplets.

Road transport contributes to approximately 30% of the total BC emitted (figure 1.3.). Both Gasoline Direct Injection (GDI) engines and Diesel cold start and regeneration periods can emit a high fraction of soot.[9, 10] The formation process of soot particles is shown in figure 1.5. Soot formation can be regarded as a transition from the gas phase to the solid phase.[11] Firstly, molecules as acetylene, single aromatics or PAHs are formed from fuel through a pyrolysis process. Dimmers and tetramers provide next step in soot formation from PAHs. Further process of nucleation and coagulation will form finest particles.[12] After that, the soot concentration increases as a result of adsorption of PAHs and as a result of particle surface reaction (hydrogen detachment, carbon attachment), leading to a surface growth.[13] Finally, primary particles around 20-30 nm coagulate into large aggregates.

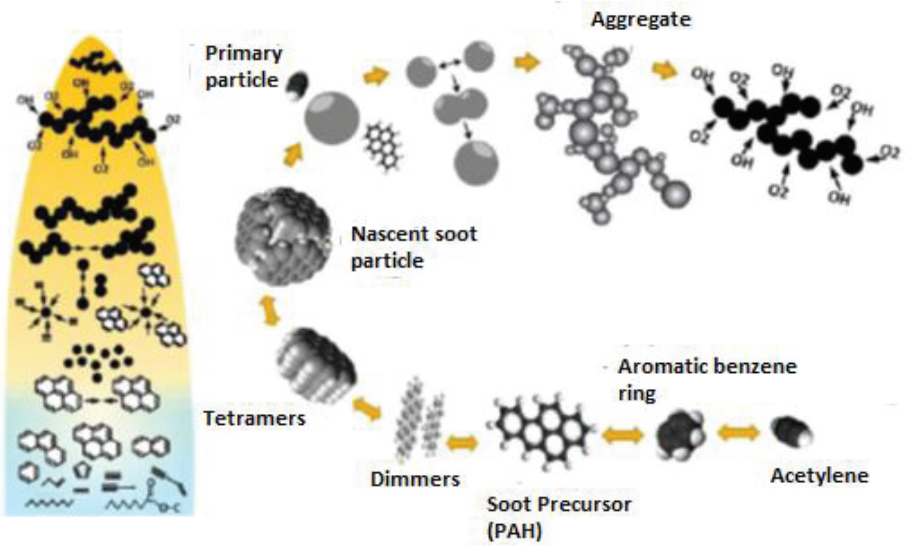

Figure 1.5. *Different steps in soot particle formation process. Source: combustion.mie. utoronto.ca.*

Soot is defined as a complex mixture of elemental carbon (EC) and organic carbon (OC),[14] literature usually attributes the term soot or black carbon (BC) to elemental carbon only.[15] In this manuscript I will use the terms soot or BC indiscriminately. EC is characterized by non-functionalized and highly polymerized carbon atoms and it is considered to be refractory (operationally it does not evaporate at temperatures around 700°C). The remaining fraction is called organic carbon (OC), and evaporates at those temperatures or even lower. The "Organic Matter" (OM) is defined by the sum of the OC fraction associated with heteroatom as O, N, H… This latter can also be defined as Primary Organic Aerosol (POA). It is emitted from both gasoline and diesel cars and it is thought to arise mainly from lubricants motor oils [16, 17] and unburnt fuel components.[18-20]

In addition to the EC and OM, the particles emitted from vehicles may contain inorganic species as sulphate (SO_4^{-2}), nitrate (NO_3^-) and ammonium (NH_4^+) that can be in the nucleation mode or in the accumulation mode or in agglomerates. Metals as nickel (Ni), zinc (Zn), cooper (Cu), aluminium (Al), iron (Fe), sodium (Na) or potassium (K) can also been found in car exhaust PM. Engine wear and lubricant oils/fuels are major sources of them.[21-24] After-treatment system and exhaust line abrasion could be also an emission source.[25, 26]

1.2.2. Gaseous Pollutants

1.2.2.1. Carbon monoxide and dioxide

Carbon dioxide is the most emitted GHG accounting for 35.8 Gt in 2016 [27] and represents 75% of the total GHG emissions.[28] Major contributors are road transport, biomass burning, house heating or electricity transformations. Transport is the only sector for which CO_2 emissions have grown since 1990.[29] Nowadays, road transport is the largest source of CO_2

emissions in Europe, accounting for 1.200 Mt [30] which correspond to 73% of the total CO_2 emitted from transport, while aviation and maritime transport account for 13% each, respectively. At global scale, road transport represents 20% of total CO_2 emissions.[31]

The EU community aims at an average emission of CO_2 for light duty passenger cars of 95 g/km per vehicle for 2020, in agreement with the framework of the Horizon 2020 program. Average emission of CO_2 from new passenger cars in 2016 was around 160 g/km (120 g/km in laboratory test), still far of desired target.[4] CO_2 emission is directly proportional to the amount of fuel consumed by the engine. Thus, improvements in reducing CO_2 levels are related with upgrades in engine efficiency, which is not an easy task; or by using renewable, low-CO_2 fuels (with low carbon footprint).[32, 33]

CO is a highly undesirable co-product in the combustion process due to its toxicity. [34] As for the CO_2, improving efficiency in engine will lead to its reduction. CO is formed mainly in engines during low load of fuel and excess of air (incomplete combustion) and cases with a rich mixture (leading to bad mixture of air and fuel). Other minor cases that entail formation of CO are the extinguishing of the flame by contact with cold surfaces as cylinder walls or the thermal decomposition of CO_2 at high temperatures inside the engine.[35, 36]

1.2.2.2. Nitrogen oxides

NOx are major pollutants from combustion sources and as seen in figure 1.3. the road transport contributes to approximately 40% of the emissions. In 2014, global annual emission of NOx from combustion and industrial sources was 129 Tg, 160% more than in 1960.[37] NOx are produced in the engine from the oxidation of nitrogen present in the air at high temperatures. As a result, nitrogen dioxide, nitric oxide and nitrous oxide are formed. Diesel is known to produce higher amount of NOx since these engines work at higher compression rates and combustion chamber temperature than gasoline engines.[36] NO is formed through the reaction between nitrogen and oxygen by the mechanism proposed by Zeldovich. Once NO is formed it can be oxidized to NO_2 which participate to the photochemical smog, ozone formation, and to secondary particle formation via conversion to nitric acid and hence, acid rain.[38] Nitrous oxide (N_2O) is emitted by vehicles as well. It has a global warming potential 296 times higher than the CO_2.

1.2.2.3. Sulphur dioxide

Sulphur dioxides (SO_2) is emitted from vehicles upon oxidation of sulphur additives containing in the fuels and the lubricant oils. Since diesel fuels generally present higher sulphur content than the gasoline ones, diesel vehicles present higher SO_2 emissions.[39] The European Union (EU) has regulated the maximum % of sulphur in fuels to 10 ppm since 2009 [40] with an consequent efficient and drastic reduction of road-transport contribution to SO_2 emissions. It is

estimated that sulphur emission from road transport has been reduced by 95% since the year 2000 in Europe.[6] Sulphur may poison the catalyst and cause its malfunctioning.[41-43] Sulphates can also be adsorbed onto the Diesel Particulate Filter (DPFs) and then be re-emitted during the regeneration process.[9]

Nucleation is the dominant source of ultrafine Particle Number (PN) in the atmosphere.[44] Nucleation occurs when a gaseous specie own a low vapour pressure at atmospheric temperatures.[45] Such molecule can easily condense over pre-existing surfaces (heterogeneous nucleation) or form clusters with other molecules (homogenous nucleation). Figure 1.6. summarizes the nucleation and the growth steps for sulphuric acid and water.

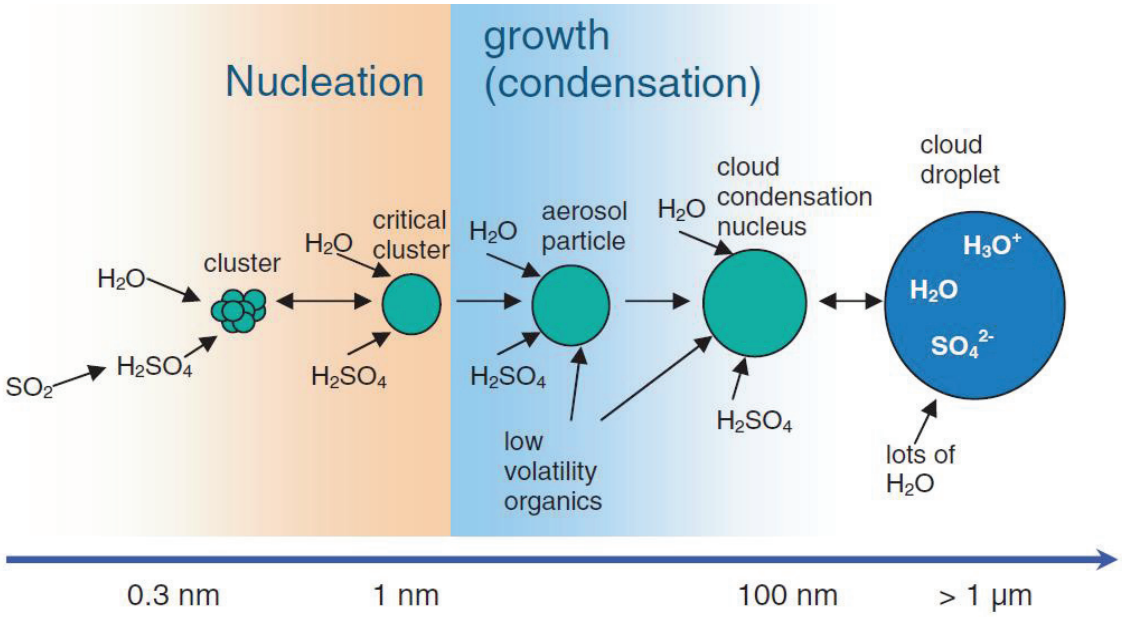

Figure 1.6. *Nucleation and growth processes for sulfuric acid and water from clusters to droplets. (Source: Curtius, 2006)*

The SO_2 is the most important precursor of particles in the atmosphere through oxidation to sulphuric acid. Sulphuric acid is highly hygroscopic and readily forms adducts with water vapour molecules (and if available ammonia) which may form clusters of 1-2 nm.[46] The clusters may overcome the nucleation barrier and finally form nucleating particles.[47] Sulphuric acid can also undergo uptake into cloud droplets and contribute to acid rain.[48, 49]

1.2.2.4. Organic Compounds

Organic compounds are also emitted during combustion. Generally, vehicle emissions related literature uses the term hydrocarbons (HCs) refers to molecules containing only C and H; the term Volatile Organic Compounds (VOCs), often used in atmospheric context, defines volatile organic compounds containing C, H and heteroatoms as O and N. In this manuscript we will use most of this terminology. The organic compounds are formed in the engines by several processes: incomplete combustion, flame extinguishing on the walls, insufficient evaporation of

fuel, short-circuiting of fresh load, inadequate fuel/air mixture or leakage.[36] Since the introduction of the oxidation catalyst in the exhaust line, the contribution of road transport to THCs has been constantly reduced.

Figure 1.7. shows the chemical composition of diesel and gasoline fuel. As observed, alkanes, cycloalkanes and aromatics largely contribute to the gasoline fuel mass speciation while longer chain compounds including byclycloalkanes, trycycloalkanes, aromatics, branched alkanes and some PAHs contribute to diesel fuel composition. These differences may have an important impact in HCs emissions from the two engine types.

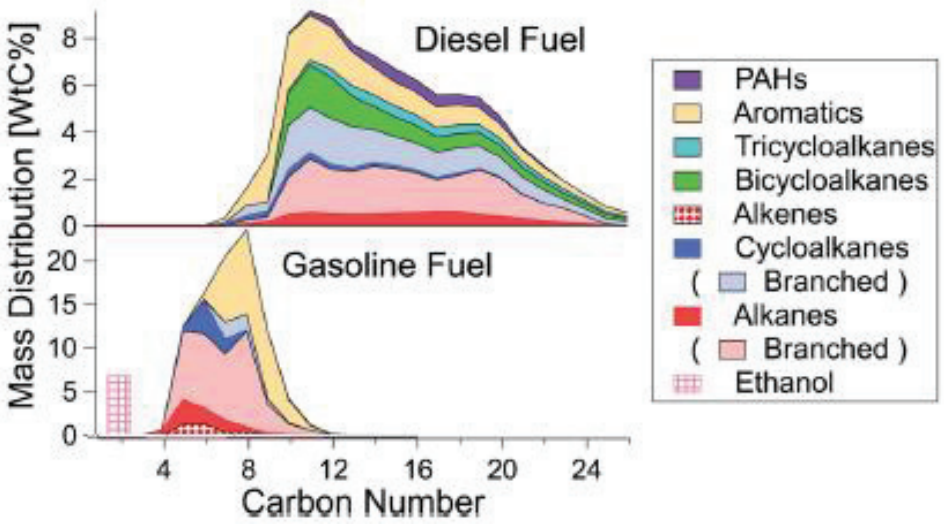

Figure 1.7. *Chemical composition of diesel and gasoline fuel by carbon number. (Source : Gentner, 2012)*

Alves et al. [50] reported THCs EFs in the range of 80-100 mg/km for Euro 3-4 and 20 mg/km for Euro 5 diesel vehicles during Artemis Urban cycles.[50] The same authors reported THCs EFs below 20 µg/Km for Euro 3-5 gasoline passenger cars. Fontaras et al.[51] reported THCs EFs emissions for Euro 5 gasoline cars: in general during New European Driving Cycle (NEDC) cycles all vehicles satisfied the regulation and showed emissions below 100mg/km, but for Artemis Urban cycles one of the Gasoline Direct Injection (GDI) passenger cars reached 150 mg/km. Euro 5 diesel cars were also tested and THCs EFs were always below 20 mg/km.[51] Ko et al.[52] tested Euro 6 diesel passenger cars and reported THCs EFs below 70 mg/km at different ambient temperatures. For Euro 5 GDI vehicles, Köhler et al.[53] reported THCs of 24 mg/km in average during Worldwide harmonized Light vehicle Test Cycle (WLTC).

A complete assessment of organic compounds contributing to the total HCs emission is a difficult task due to the large variety of species emitted. Ensberg et al.[54] provided emission evaluation based on California fuel-sale data (13% diesel, 87% gasoline) and they reported branched alkanes as the largest emitted family (37.3%) followed by single ring aromatics (27.4%) and straight alkanes (7.6%). Alves et al.[50] reported emissions of linear alkanes up to C_{11} and aromatic compounds for Euro 4 and Euro 5 gasoline and diesel vehicles. For diesel

vehicles they found alkanes in a percentage of 38-46% while the aromatic compounds represented 53-61% during cold start cycles and for vehicles with/without DPF.[50] For gasoline Euro 5 vehicles, same authors reported that aromatic compounds represent the largest family with 69-73% of the measured THCs emissions. Alkanes represent 23-27% while the oxygenated compounds account for a small fraction (3%) during both cold and hot start cycles.[50]

Lu et al.[55] recently published comprehensive organic emission profiles for mobile sources by integrating tedlar bags, tenax tubes and quartz filters measurements of emissions from recent vehicles. Figure 1.8. shows the volatility distribution (see section 1.5.3.) and the carbon number of n-alkanes organic emissions for (a) gasoline (b) diesel vehicles.[55] The authors suggest the importance of aromatic compounds together with n/b-alkanes and alkenes in the C_5-C_{10} range for gasoline cars emissions, while for diesel vehicles small carbonyl compounds and C_8-C_{20} seems to be the highly emitted. The measurements also indicate the presence of long chains reaching C_{30} in diesel vehicles emissions.[55] Dunmore et al.[56] recently reported an increase from 23% to 61% of diesel-related HCs in wintertime when considering hydrocarbons above C_{13}.

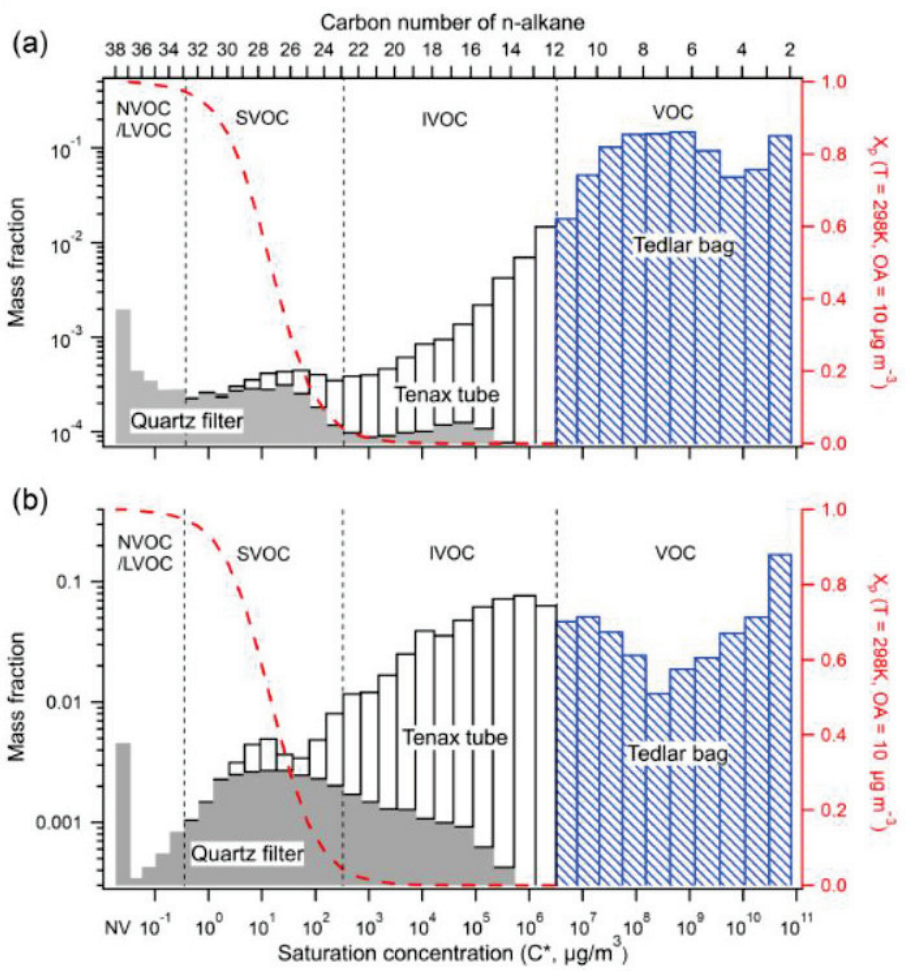

Figure 1.8. *Volatility/carbon number of n-alkanes for a typical (a) gasoline (b) diesel vehicles using quartz filter, Tenax tubes and Tedlar bag. The red dashed lines indicate the particle fraction assuming C_{OA} of 10 µg/m^3 and 298K. (Source: Lu, 2018)*

Regarding gasoline emissions, two families of compounds have received a special attention: the aromatics and the PAHs.[50, 57, 58] Aromatic compounds are highly reactive and are known to highly contribute to the formation of secondary aerosols and ozone.[54, 59] The BTEX (Benzene, Toluene, Ethylbenzene, Xylenes) is a sub-group of the aromatic compounds often measured in fuels and car exhaust. The PAHs are aromatic compounds with more than one benzenic ring and are found in fuels or can be formed during the combustion through the HACA mechanism (H-abstraction + C_2H_2 addition).[60] The lightest are often present in the gas phase emissions (as naphthalene) while the heaviest are present mainly in the particle phase.

Other compounds emitted from modern gasoline and diesel passenger cars are small oxygenated compounds. Martinet et al.[57] reported emissions for acetaldehyde and formaldehyde of approximately 0.1 mg/km for recent diesel vehicles. Suarez-Bertoa et al.[61] reported emissions in the range 0.2-1 mg/km for acetaldehyde and formaldehyde during WLTC tests for flex-fuel vehicles. Emission of these pollutants was found to be mainly linked to the cold start of the cycle. Clairotte et al.[62] found important concentrations of formaldehyde, acetaldehyde, ethanol, ethylene or hydrogen cyanide during NEDC cycle and they report higher emissions when tests were performed at low temperature (-7°C).

By last, other compounds containing nitrogen atoms as ammonia (up to 165 mg/km), isocyanic acid (up to 90 mg/kg fuel), nitromethane (up to 12 mg/km) or hydrogen cyanide (up to 5.6 mg/km) have been measured in vehicle emission studies of recent gasoline and diesel vehicles.[62-68] Such compounds are thought to come from secondary reactions involving NOx species in the aftertreatment devices.[65] Some of them as ammonia poses serious issues, being an important precursor of new particle (nucleation together with sulphuric acid and water) and being also toxic for human health.[65]

1.3. Regulation and Control Strategies

1.3.1. Air Quality Regulations and European Emissions Standards

Air quality refers to the condition of the air within our surrounding. Good air quality relates to the degree which the air is clean, clear and free from pollutants. Air quality is determined by assessing a variety of pollution indicators. Since the 70's, European Union has developed policies and standards in order to improve air quality. At the same time, the World Health Organization recommends some air quality guidelines in order to assess the pollution limits that ensure people health. Table 1.1. shows the Air quality standards under the Air Quality Directive, and WHO air quality guidelines.

Table 1.1. *Air quality standards under the Air Quality Directive, and WHO air quality guidelines.*

Pollutant	Averaging period	Objective	Comments	WHO objective
PM2.5	One day			25 μg/m^3
PM2.5	Calendar year	Limit value, 25 μg/m^3		10 μg/m^3
PM10	One day	Limit value, 50 μg/m^3	Not to be exceeded for more than 35 days per year	50 μg/m^3
PM10	Calendar year	Limit value, 40 μg/m^3		20 μg/m^3
O_3	Maximum daily 8h mean	Target value, 120 μg/m^3	Not to be exceeded for more than 25 days per year, averaged over three years	100 μg/m^3
NO_2	One hour	Limit value, 200 μg/m^3	Not to be exceeded more than 18 times during a calendar year	200 μg/m^3
NO_2	Calendar year	Limit value, 40 μg/m^3		40 μg/m^3

The EU regulations contributed to relevant reduction of air pollutants between 1990 and 2015. Nevertheless, some air pollutants concentration is still high in urban environments. In the period 2006 - 2015, between 8-16% of urban population in Europe has been exposed to PM2.5 values exceeding EU limitations, while 82-97% of the population was exposed to concentrations above the WHO guidelines values.[69] For some pollutants as ozone, NOx and fine PM, the expected reduction in air ambient concentration has been below expectations.

Regulation of secondary pollutants, as it is the case for ozone and fine PM, is not straightforward since a large fraction of the PM2.5 is produced via atmospheric processing of reactive volatile and semi-volatile organic compounds ultimately forming secondary organic aerosol (SOA).[54, 70, 71]

In order to reduce pollutant emissions from diesel and gasoline vehicles, European Union introduced the so-called “Euro” standards. These legislations limit the emission of tailpipe pollutants and from other sources on the vehicle, as evaporative emissions from the fuelling system. Table 1.2. summarizes the European standards emission limits since 1993.

Table 1.2. *Evolution of emission limits for light passenger cars approved in Europe.*

Standard		Euro 1	Euro 2	Euro 3	Euro 4	Euro 5	Euro 6b	Euro 6c	Euro 6d
Year		1993	1996	2001	2006	2011	2015	2018	2019
Driving test		NEDC	NEDC	NEDC	NEDC	NEDC	NEDC	WLTC	WLTC
DIESEL									
Emission limits	RDE compliance factor (NOx)	-	-	-	-	-	-	-	2.1
	NOx	-	-	500	250	180	80	80	80
	CO	2720	1000	640	500	500	500	500	500
	HC	-	-	-	-	-	-	-	-
	HC+ NOx	970	900	560	300	230	170	170	170
	Particle mass	140	100	50	25	5	4.5	4.5	4.5
	Particle number	-	-	-	-	$6x10^{11}$	$6x10^{11}$	$6x10^{11}$	$6x10^{11}$
GASOLINE									
Emission limits	RDE compliance factor (NOx)	-	-	-	-	-	-	2.1	2.1
	NOx	-	-	150	80	60	60	60	60
	CO	2720	2200	2200	1000	1000	1000	1000	1000
	HC	-	-	200	100	100	100	100	100
	Particle mass	-	-	-	-	5	4.5	4.5	4.5
	Particle number	-	-	-	-	-	$6x10^{12}$	$6x10^{11}$	$6x10^{11}$

*All emissions limits are set in mg/km except the particle number which is set in #/km

Euro standards define the maximum emission values allowed for each pollutant per kilometer under the official driving cycle and provide guidelines about the good conditions for an appropriate measure of the pollutants. The Euro 1 standard sets the emission limits for CO, particle mass and NOx + HCs for diesel cars and CO in case of gasoline vehicles. Since Euro 1, others Euro standards have been introduced. Further Euro standards have led to further reduction of allowed pollutants emission as well as the regulation of new pollutants. Thus, nowadays, NOx, CO, HCs, particle mass and particle number are regulated. The current standard is the Euro 6c standard, applied since September 2018. The emission limit values set for Euro 6c: 80 mg/km for NOx, 500 mg/km for CO and 170 mg/km for HCs+NOx for diesel passenger cars and 60 mg/km, 1000 mg/km for CO and 100 mg/km for HC for gasoline passenger cars. Diesel and gasoline vehicles have the same limitation with respect particle mass (4.5 mg/km) and particle number concentration ($6x10^{11}$ particles/km).

In addition, the latest legislation defines new measurement methods via (1) the introduction of new Worldwide harmonized Light vehicle Test Cycle (WLTC) in substitution of

the New European Driving Cycle (NEDC) and (2) the introduction of a regulated protocol for Real Driving Emission (RDE) tests for NOx emissions only.[7, 72] In addition to Euro 6 standards, manufacturers are required to achieve the average fleet target of 95 g/km of CO_2 for new passenger cars sold from 2021. The measure reliability and implementation of other compounds as NO_2, N_2O, NH_3, ethanol, formaldehyde and acetaldehyde has been tested by the United Nation Organization commission.[73] Therefore, the possible introduction of these pollutants in further EU standards has to be considered.

1.3.2. Vehicle Emission Control

The reduction of emissions from road transport is clearly one of the priorities for governments, which progressively introduced more restrictive regulations for emissions. Car manufacturers have responded by introducing a series of in-engine modifications and exhaust after treatment technologies, e.g. the Diesel Particulate Filter (DPF), Three Way Catalyst (TWC) and NOx trap devices. However, recent cars are still poorly characterized, especially in view of recently discovered manipulation practices. In-use aftertreatment technologies for diesel and gasoline vehicles are described in this section.

Diesel vehicles are now equipped with a Diesel Oxidation Catalyst (DOC), a Diesel Particulate Filter (DPF) and a NOx catalytic unit (Selective Catalytic Reduction (SCR) or NOx Trap). All diesel vehicles own the direct injection system, what leads to higher combustion performance but high particle emissions.[74-77] Gasoline passenger cars are equipped with a three-way oxidation catalyst (TWC) and new vehicles may own also a gasoline particle filter (GPF) since particle number for gasoline cars has been regulated in the last Euro standards update. The introduction of the particle number limits for gasoline vehicle is motivated by the spread use of gasoline direct injection (GDI) engines, who leads to a higher number of particle emitted than conventional gasoline cars.[10, 78, 79]

1.3.2.1. Diesel Oxidation Catalyst

This device is equipped with a two-way oxidation catalyst with the goal of reducing CO and unburned HC emissions from diesel engines. Noble metals as Pt, Pd and Rh are generally used as active phase of the catalyst deposited on an oxide mixture of Al_2O_3 or CeO_2.[80-82] Figure 1.9. shows a scheme of the DOC.

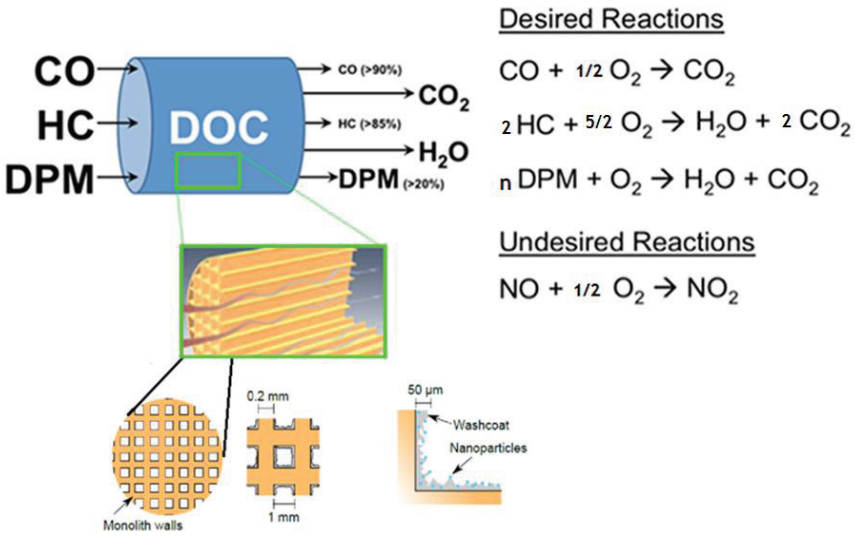

Figure 1.9. *Working principle of a DOC. Source: Gil, 2015*

In addition, the DOC system leads to the reduction of particulate matter by oxidizing a part of the organic fraction present on soot particles.[83] The DOC effectiveness in oxidizing CO and HCs can be observed at temperatures above ‘‘light-off’’ for the catalytic activity. Light-off temperature is defined as the temperature at which the reaction starts in the catalyst and varies depending on exhaust composition, flow velocity and catalyst composition. Another inconvenient of the DOC is that the traces of sulphur coming from engine can be oxidized to sulphur oxides and further sulphuric acid.[84]

1.3.2.2. Diesel Particulate Filter

The main goal of the diesel particulate filter (DPF) is the removal of particle matter by filtration. Figure 1.10. shows a scheme of working principle.

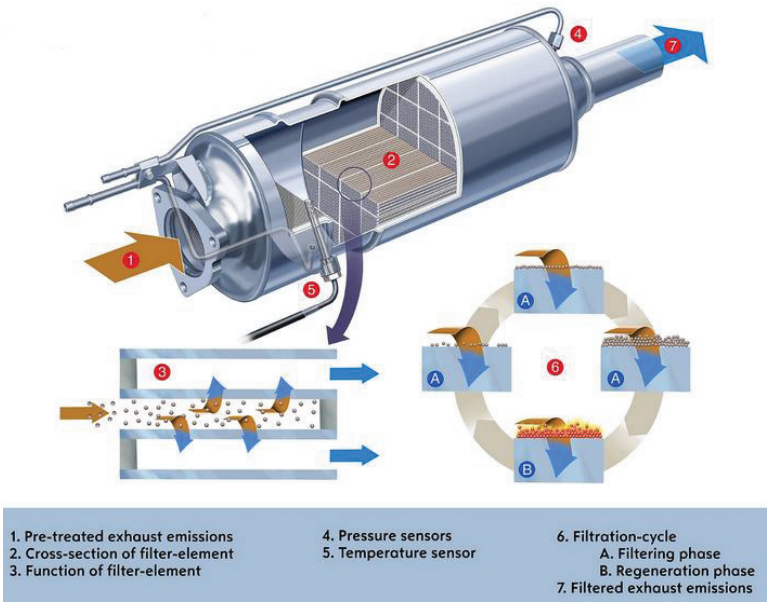

Figure 1.10. *Schematic DPF working principle. Source: Vauxhall.*

The filter consists of ceramic honeycombs, generally made on silicon carbide or cordierite, whose pores are alternately clogged. Thus, the gas exhaust is forced to pass through the channel walls while particles are retained there. The DPF can efficiently remove more than 95% of the PM.[9, 85-87] Continuous soot deposition on the DPF's walls forms a deep-bed "soot-cake", which significantly improves filtration efficiency.[88] This can build up the pressure leading to problems as loss of power, increase of fuel consumption, engine failure and stress on the filter.[89, 90] To avoid excessive back pressure on the engine, regeneration of the accumulated soot is periodically required, and it is commonly accomplished by an exothermic reaction. The so-called "active regeneration" is initiated by the post-injection in the engine's cylinders during the late expansion stroke or directly in the exhaust line in order to generate exothermic energy across the DOC.[91-93]

Combustion of soot by oxygen requires temperatures above 600°C which are rarely achieved in the exhaust of Diesel vehicles. DPF regeneration by decreasing temperature below to 600°C is called "passive regeneration". Soot combustion temperature can be reduced by a catalytic washcoat deposited at inlet channels of the DPF to boost NO oxidation reaction into NO_2 which can oxidize soot, called catalyzed DPF (cDPF).[94, 95] Another common system, called Fuel Borne Catalyst (FBC), is based on the addition of metallic salts or organometallic compounds into the engine combustion chamber.[96-98] Upon combustion, the additive produces nanoparticles of metal oxides which are intimately mixed with soot particles and stored on the DPF walls. As the regeneration process starts and the temperature rises, the oxygen of the metal oxide catalyses the oxidation of the soot layer from around 550°C instead of 650-700°C without any catalysts.

1.3.2.3. Selective Catalyst Reduction

The Selective Catalyst Reduction system has for objective the reduction of NOx in diesel vehicles exhaust. Figure 1.11. shows the working principle of the urea SCR system.

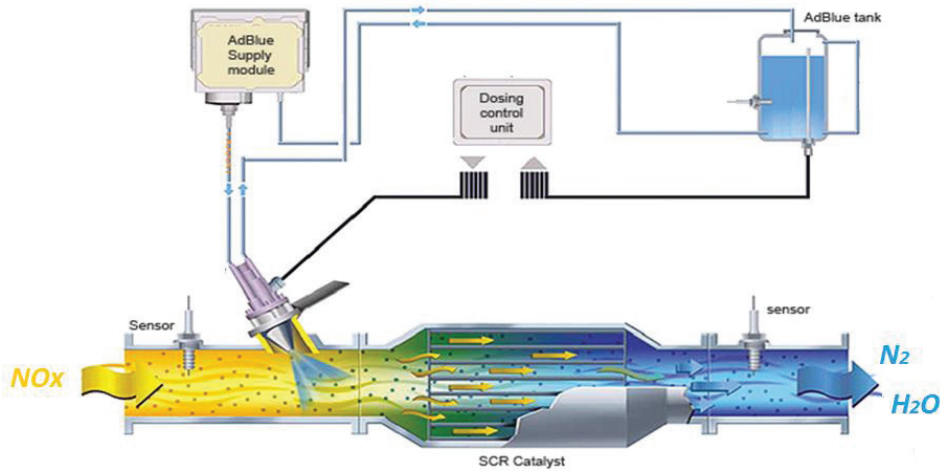

Figure 1.11. *Working principle of the urea SCR system. Source: www.doosanequipment.com*

Urea (NH_2-CO-NH_2) is commonly used as ammonia source, which is the reducing agent that converts NO_X to N_2 and water. Urea is used since the direct use of ammonia presents some problems related to storage and since ammonia is toxic and corrosive.[99] However, in working conditions, isocyanic acid (HNCO) can be formed from urea. Increase of HNCO means less ammonia formation and reduced NOx conversion, [100, 101] and also ammonia emissions have been reported in the literature during cold start and DPF regeneration.[9]

The SCR technology presents a high efficiency and selectivity in the reduction of NOx in atmospheres rich in oxygen, reaching values higher than 90% of conversion.[102, 103] However, at low temperature, the removal of NO can be associated to the generation of other nitrogen products as N_2O or to the emission of ammonia not used in the catalyst.[104, 105] Other secondary reactions leading to formation of ammonium sulfate and ammonium nitrate can occur in the SCR, producing catalyst deactivation.[106, 107]

1.3.2.4. NOx trap

Figure 1.12. shows the NOx trap working principle. In this device, the adsorbers, which are incorporated into the catalyst washcoat, chemically bind NOx during lean engine operation.

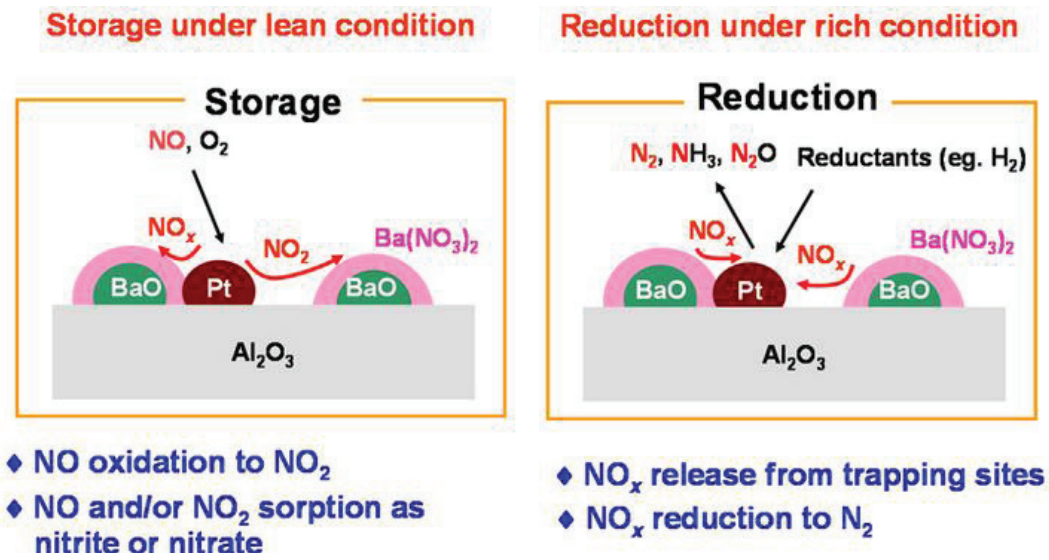

Figure 1.12. *Schematic working principle of NOx trap. Source: www.cjcatal.org*

Then, NO is oxidized to NO_2, which further reacts to form barium nitrate. When the adsorber capacity is saturated, the system is regenerated during a period of rich engine operation, and released NOx is catalytically reduced to nitrogen. NOx adsorbers also require periodic desulfation, to remove sulfur stored in their washcoat.

1.3.2.5. Three Way Catalyst

The main goal of the three way catalyst (TWC) is the removal of CO, HCs and NOx from gasoline exhaust. The system is mainly formed by two sections, the first dedicated to reduction reactions, the second to oxidation. In total, three major reaction pathways occur in the three way catalyst: oxidation of CO to produce CO_2; oxidation of HCs to produce CO_2 and water vapour; and reduction of NOx to form molecular nitrogen (N_2). Figure 1.13. shows a scheme of the three ways catalyst.

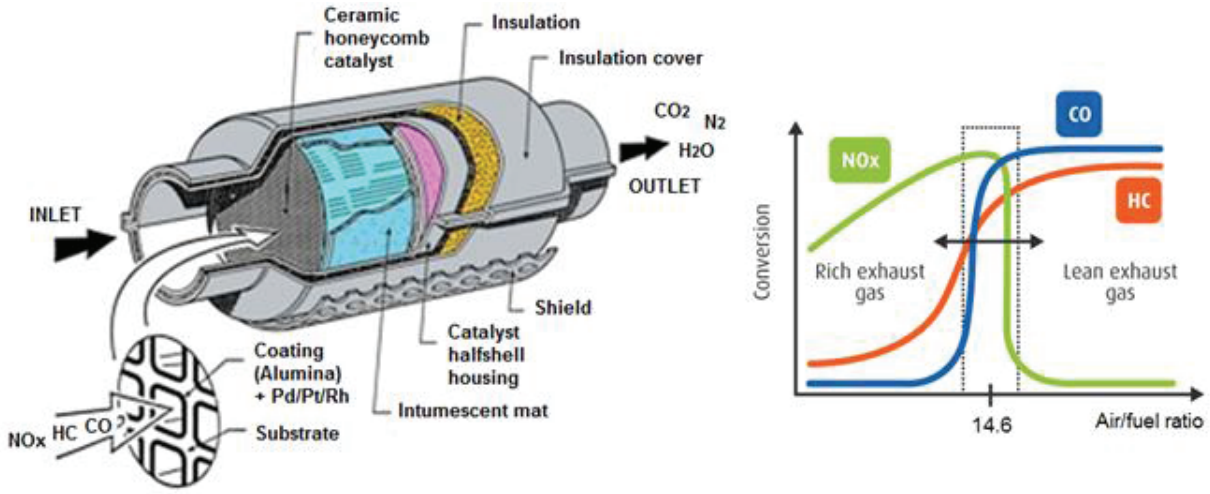

Figure 1.13. *Working principle of a TWC (left) and NOx, CO and HC conversion on TWC depending on air to fuel ratio (right). Source: www. ac.umicore.com/en/technologies/three-way-catalyst/; http://www.meca.org/resources/featured-article*

The catalytic rack consists of ceramic honeycomb monoliths. Surface of coating layer is composed of noble metals (Pd,Pt,Rh) while walls are coated with aluminium and ceria oxides. [108] In order to achieve a good conversion, the exhaust gases must be always very close to stoichiometric conditions for combustion reaction (ideally 14.6) (Figure 1.13.).[108] If air/fuel ratio is much higher (lean conditions), NOx removal efficiency decreases. On the other hand, ratios lower than 14.7 (rich conditions) leads to low oxidation efficiency, thus, poor conversion of CO and HCs.[109] Secondary reactions in the reduction catalyst lead to formation of ammonia and N_2O. High conversion efficiency in the TWC is achieved after warm up phases of the engine, therefore under cold conditions, important emission of pollutants is observed.[72, 110]

1.3.2.6. Gasoline Particulate Filter

One of the reasons to limit gasoline vehicles PM emissions is the market large number of gasoline vehicles owning the Direct Injection (GDI). GDI engines have higher fuel economy compared to the port fuel injection (PFI) engines.[78, 111, 112] As a result, GDI sales highly increased in the last years, reaching 50% of the gasoline sales in 2017.[113, 114] However, GDI vehicles do emit higher particle concentrations than the traditional PFI vehicles.[115, 116]

In the GDI engines, the injection is located at the top of the cylinder right at the combustion chamber, while the injection in the PFI engines takes place right at the manifold runners before the valves. The direct injection leads to an incomplete fuel volatilization, partially fuel rich zones, and impregnation of fuel to piston and cylinder surfaces. All these issues favor the increase of particulate emission.[117-119] Generally, GDI passenger cars do not respect the particle number limitation imposed by Euro 6.[87] As a consequence, car manufacturers have been forced to introduce a gasoline particule filter (GPF). The filter will be essentially passive.[120] Thereby, the risk of uncontrolled rise of temperature is very low. Generally, GPFs are made of cordierite, the same material as the three-way catalysts and diesel oxidation catalysts, which is a lighter and cheaper material than the silicon carbide, generally used for particulate filters Diesel.[121-123]

1.3.3. Emission models and inventories

Models for predicting emissions represent a cost effective alternative to direct measurements.[124] Emission models are based on empirical emission data, and they provide an ensemble of emission factors (EFs). To accurately reflect real world emissions, it is important to take into account vehicles type and driving conditions. In order to get a permanent network of mobile emissions and inventories, the European Research group on Mobile Emission Sources (ERMES) was founded in 2009. ERMES is composed by stakeholders that include laboratories, vehicle emission modelers, industry representatives and European commission. ERMES organization developed two major models leading emissions in Europe: COPERT and Handbook Emission Factor for Road Transport (HBEFA).

COPERT model [125] is the main road transport emissions model of the Atmospheric Emission Inventory Guidebook (AEIG) and it is used by several European members state to compile their official national inventories of emissions. Estimation of emissions is divided in three sections: emissions produced during thermally stabilized engine operation (hot conditions), excess emissions occurring during engine start from ambient temperature (cold-start and warming-up effect) and non-methane volatile organic compound (NMVOC) emissions due to fuel evaporation. Total emissions are calculated as the combination of vehicle fleet and activity data selected by the user and the libraries of emissions factors included in the models.[126] HBEFA model is used at low scales compared to COPERT, and requires more detailed traffic data inputs. The emission factors depend on “traffic situations” while in COPERT are related to speed. Both models account for an extensive amount of vehicle emission tests, and they provide emission factors for a comprehensive set of vehicle categories.

1.4. Impacts of road transport emissions

The impacts of pollution from road transport can span different spatial scales. Local and regional scale is usually related to pollutants with short lifetime and close to the sources.[127] The minimization or reduction of these impacts can be carried out in the short term with the appropriate local reduction measures.[128] Worldwide impacts are produced by pollutants with long lifetime that accumulate in the atmosphere. The mitigation of such impacts must be considered in the medium-long term with policies and measures at global scale.

1.4.1. Air quality, environmental and ecosystem impacts

Human health, plants, animals and natural resources are threatened when pollution in the air reaches high concentrations. Air pollution is often associated to haze or photochemical smog produced by a mixture of both primary and secondary pollutants.[129, 130] Figure 1.14. shows the decrease of visibility in Paris during an episode of photochemical smog. The reduction of visibility occurs when sunlight hits particles.[131, 132] Under high humidity and weak wind conditions, fine droplets can be formed and low visibility episodes can remain for days.[133, 134]

Figure 1.14. *Difference between a haze and clean day for Paris city. (Source: Guay et Tribouillard, AFP)*

Formation of ozone and secondary particles will be further developed in section 1.5., briefly, reactions involving HCs, NO, NO_2 leads to an increase of O_3 levels and secondary particles formation. Especially worrying is the situation of cities in valleys where the pollution builds up during weak wind conditions.[135]

In urban environments, some compounds can alter materials and degrade monuments.[135] Sulfuric acid, formed upon oxidation of SO_2, corrodes and blackens buildings [135] and participate to the formation of acid rain, which produces acidification of forest and watercourses.[135] Even if the acid rain issue has been solved in Western Europe and USA; it is still an important environmental problem in many countries as China and India.[135]

Plants are also affected by air pollution. Necrosis, impaired growth or diminished resistance are some of the derived issues.[136, 137] Tropospheric ozone causes risk to food production through crop damages.[138] Emission of nitrogen oxides and further transfer to the aquatic ecosystem produces eutrophication.[139, 140] This high-level of nutrients increases the algae bloom, affecting the ecosystem.[141] Wildlife is also affected by toxic pollutants. Thus, animals can suffer of health problems due to long exposition of pollutants, leading to birth defects, reproductive failure and various diseases.[142] Finally, deposition of pollutants as metals on vegetation, soil or water surfaces produces biomagnification. This process often refers to the build-up of toxic substances such as pesticides or heavy metals into lakes, rivers and the ocean, and then move up into the food chain in progressively greater concentrations as the substances are incorporated into the diet of aquatic organisms such zooplankton, which in turn are eaten by fish, which then may be eaten by bigger fish, large birds, animals, or humans. The substances become increasingly concentrated in tissues or internal organs as they move up the chain.

1.4.2. Climate impacts

Radiative forcing or climate forcing is defined as the difference between the solar radiative energy absorbed by the Earth and energy radiated back to space. A positive radiative forcing is characterized by a global heating of the atmospheric system while a negative radiative forcing means a global cooling of the atmospheric system. The natural equilibrium between incoming/outcoming radiation allowed life on Earth by stabilizing an average temperature around 15°C. Figure 1.15. shows the contribution of individual pollutants to the global radiative balance since pre-industrial times.

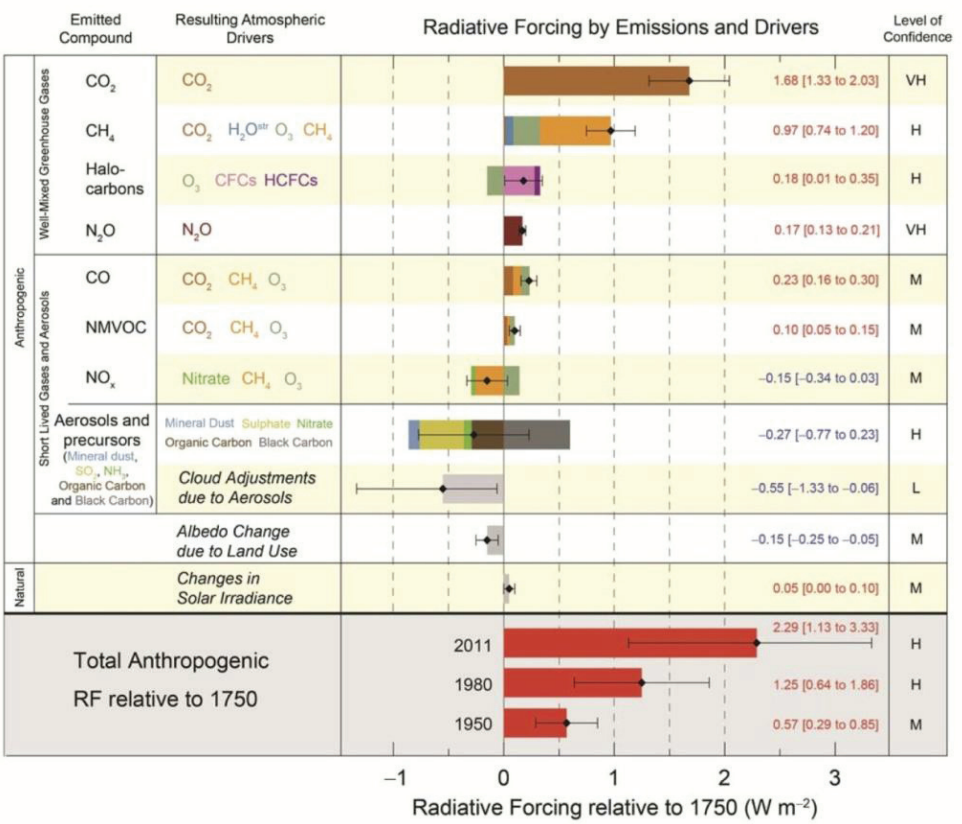

Figure 1.15. *Radiative forcing in 2011, source: IPCC, 2013 (Values are global average radiative forcing. The best estimates of the net radiative forcing are shown as black diamonds with corresponding uncertainty intervals; the numerical values are provided on the right of the figure, together with the confidence level in the net forcing (VH - very high, H - high, M - medium, L - low, VL - very low).*

Anthropogenic activities contribute to a considerable increase of greenhouse gases (GHGs) as CO_2, CH_4, N_2O and ozone. CO_2 alone contributes to a positive radiative forcing (RF) of 1.7 W/m^2, methane follows with a contribution of almost 1 W/m^2, while N_2O and CO are associated to a RF of 0.2 and 0.25 W/m^2, respectively. The emissions of NOx are rather related to a negative RF of -0.24 W/m^2 due to the formation of nitrate particles. Atmospheric particles and clouds also play an important role in the terrestrial climate system. A schematic representation of the radiative interaction particle-cloud with solar radiation is presented in figure 1.16.

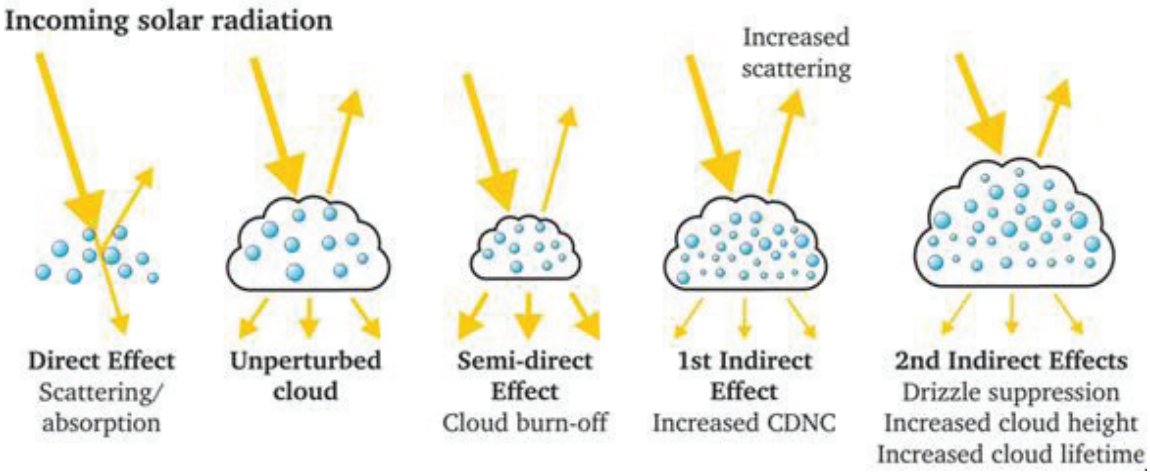

Figure 1.16. *Interaction between solar radiation and particles.*

Atmospheric particles and clouds also play an important role in the terrestrial climate system. A schematic representation of the radiative interaction particle-cloud with solar radiation is presented in figure 1.16. Aerosols can directly interact with the incoming solar radiation (direct effect) and depending on their optical properties they can diffuse the radiation back to the atmosphere (cooling effect) and/or absorb the incoming radiation (heating effect) as it is the case of BC particles. Reflection and absorption of solar radiation by particles strongly depends on their composition, shape and concentration. The direct effect accounts for -0.9 W/m^2. Particles can modify the physicochemical properties of clouds acting as cloud condensation nuclei (CCN) onto which water droplets are formed. Hygroscopy particles, as sulfates or sea salt may be good CNN precursors. But if a polluted atmosphere contains light absorbing particles (as soot) which enter the cloud, local heating may occur and partial evaporation of the cloud is observed (semi-direct effect).

The increase CCN number in a polluted atmosphere can lead to the formation of a high number of cloud droplets of smaller size (since the water vapor available is unchanged). This will increase cloud scattering and finally leads to a cooling effect.[143] (1st indirect effect). A second indirect effect is linked to the increased lifetime of the cloud and reduced precipitation for clouds containing a high number of CCN and small cloud droplets. The aerosol-cloud interaction contributes to the RF with approximately -0.5 W/m^2 but remains nowadays the most uncertain contribution to the global radiative balance of the planet.

1.4.3. Health impacts

One of the biggest issue related with road transport is its contribution to air pollution in urban environments. Air pollution is one of the first five likely causes of mortality in Europe [144, 145] and among all pollutants in the urban atmosphere, particulate matter (PM) below 10 µm presents high toxicity.[29] Health impacts can vary from irritation of eyes, respiratory problems, asthma or cardiovascular issues to cancer. Many epidemiologic studies have already

demonstrated the relationship between particle matter exposure and appearance of diseases at short and long term.[146-150] Other studies have also shown that people living in polluted locations die prematurely, compared with those people living in areas with low levels of pollution.[144] Kampa et al.[151] reported that 80% of premature deaths due to particle exposure are caused by cardiovascular problems. Other diseases leading to premature death are stroke, chronic obstructive pulmonary disease, lung cancer or acute respiratory infections in children. According to a recent study, 9% of premature deaths in France are linked to fine particles, the third leading cause of death behind smoking and alcoholism.[152] The Global Burden of Disease (GBD) estimates the number of premature death by PM2.5 exposure in 4.2 millions in 2015.

New information about adverse health effects associated with particle exposure comes to light every year: Jedrychowski et al.[153] reported impact during pregnancy affecting fetal growth, the WHO report effects on the newborns health, and a limited development of cognitive abilities;[154] Carré et al.[155] and Frutos et al.[156] alerted about the effect of fertility caused by fine particle exposure, while another work related fine PM to the increase of diabetes,[157, 158] and asthma during childhood and adolescence.[159, 160] Other diseases and problems as DNA damage, oxidative stress, Alzheimer, lung tissue or brain damage are also associated to particle exposure.[161-167] The International Agency for Research on Cancer (IARC) has classified air pollution as carcinogenic to humans since 2013. Diesel engine emissions were evaluated separately and were also classified as carcinogenic due to its high risk of lung cancer in 2012.[168, 169] Figure 1.17. shows an example of alteration in children lung's (airways macrophages) when affected by particle inhalation.

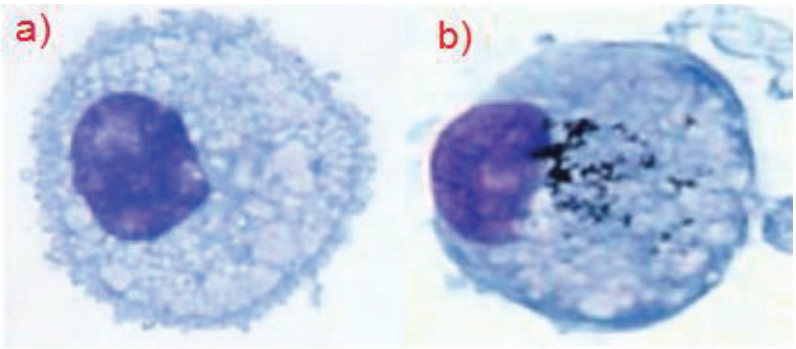

Figure 1.17. *Airway macrophages from healthy schoolchildren in Leicester, UK; a) non-affected by particle inhalation, b) affected by particle inhalation. (Source: Kulkarni, 2016).*

Health issues related to PM inhalation depend on several parameters as exposure time, particle size and particle composition. Particle size is a key parameter because it governs the deposition within the respiratory system and because size is directly linked to chemical composition and source.[170] Figure 1.18. shows which part of the human body is affected by particle inhalation depending on PM size.

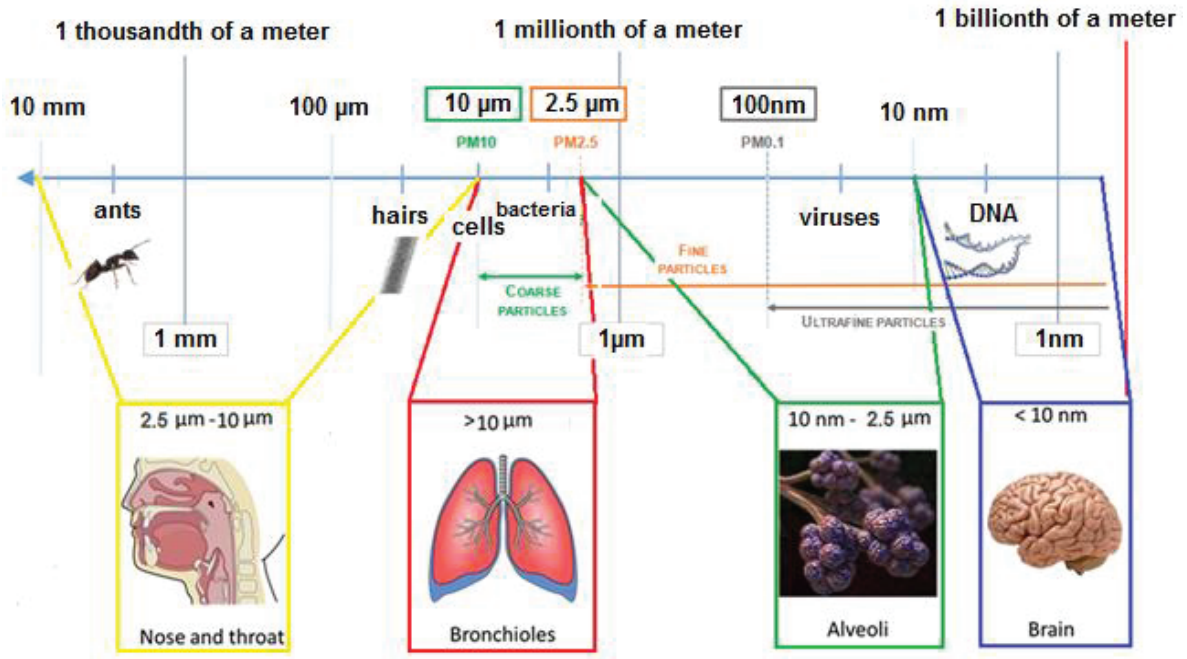

Figure 1.18. *Schematic overview of the particle size and related body affection Source: SCOR, 2018.*

Largest particles, up to 10 µm are blocked by the respiratory human system, and cannot pass beyond the nose and throat. Particles from 2.5 µm to 10 nm reach the deep levels of pulmonary system and are deposited on the alveoli where the lifetime could be even one month.[171, 172] The ultrafine particles, PM below <100 nm, have the ability to cross the biological barriers, and pass into the bloodstream and be distributed around the body, reaching also the brain.[165, 173-175] Some metals presented in PM from traffic emissions as zinc, cadmium or nickel are toxic, and can affect the nervous and immune systems, and ultimately, induce cancer.[176, 177]

Apart from PM, some of the gaseous pollutants emitted from vehicles affect human health. CO cause impaired oxygen delivery. Inhalation can cause coma or death.[178] NO and NOx are irritating for respiratory tracts, both gases have been associated with respiratory diseases.[179] SO_2 causes respiratory problems [151] and can induce cancer.[180] In addition, some of the emitted VOCs are considered carcinogenic, like formaldehyde [181] or benzene [182] while toluene produce irritant effect on the skin, eyes and respiratory system. Some PAHs are considered carcinogenic as well.[183] They can cause decrease in the level of red blood cells, damage to bone marrow, haemorrhages and damages to the immunitary system as well.[184-186] By last, some of the oxidized products from primary VOCs are carcinogenic as well, as for example some nitro aromatic compounds.[187, 188]

1.4.4. Economic impacts

Atmospheric pollution entails significant economic costs to the society as a result of the health impacts on humans and the productivity losses. As previously seen, pollution can also

affect the productivity of crops, reduce the number and size of forests or change the natural ecosystems through acid rain or global warming processes, which leads to economic impacts as well. Due to the difficulty to account for direct and indirect costs caused by air pollution, many costs are still unacknowledged, unaccounted, non monetised and remain outside the domain of public policies evaluation.[189] Estimations based in a market-based model from the Organization for Economic Cooperation and Development (OECD) set the costs associated to air pollution to a 1% of the total European Gross Domestic Product (GDP) for the year 2060, what means around 185 billion of euros.[190] This model takes into account lost of labour productivity, health costs and diminished agricultural yields.

1.5. Secondary pollutants

Apart from the direct impacts derived from primary pollutants emitted from road-transport, some compounds can participate to a complex interplay of chemical and physical processes resulting in the formation of secondary pollutants. NOx and VOCs are precursors of ozone and secondary organic aerosol (SOA). While ozone formation is in general well understood, formation of secondary aerosol remains unclear. The influence of atmospheric parameters on reaction mechanisms that involve the generation of particles still presents some uncertainties leading to inaccurate estimation of SOA budget in atmospheric models.

1.5.1. Ozone and SOA formation

Formation of tropospheric ozone occurs in the presence of NO_2 and VOCs. Firstly, NOx photolysis forms ozone that can further photolyse and form the $^{\bullet}OH$ radicals. The main reactions involved are listed below.

$$NO_2 + h\upsilon\ (300 < \lambda < 420nm) \rightarrow NO + O^{\bullet}(^3P) \quad [1.1]$$

$$O^{\bullet}(^3P) + O_2 + M \rightarrow O_3 + M \quad [1.2]$$

$$O_3 + NO \rightarrow NO_2 + O_2 \quad [1.3]$$

$$O_3 + h\upsilon\ (\lambda < 310nm) \rightarrow O^{\bullet}(^1D) + O_2(^1\Delta g) \quad [1.4]$$

$$O^{\bullet}(^1D) + H_2O \rightarrow 2\ {}^{\bullet}OH \quad [1.5]$$

Ozone can also reacts with NO to form again NO_2.[191] The cycle described from equations 1.1. to 1.5. is null and no net ozone is formed. In the presence of VOCs, however, NO preferably reacts with $RO_2^{\bullet}$ radicals (formed from VOCs) rather than ozone (equation 1.8.) leading to NO_2 formation and then ozone.[192, 193] In polluted areas (high NOx) the titration of NO_2 by the hydroxyl radical becomes competitive and forms HNO_3. This reaction can therefore

remove the main ozone precursors from the environment. This is why in areas with very high NOx emission ozone is often lower than in areas of lower NOx level.

The hydroxy radical reaction determines the gas phase oxidation occurring in the troposphere, both in clean and polluted areas. The •OH concentration is highly variable and depends strongly on the solar flux, ozone and HONO concentrations and the levels of hydrocarbon species.[194, 195] The overall photo-oxidation sequence of a VOC with •OH radicals is illustrated in Figure 1.19.

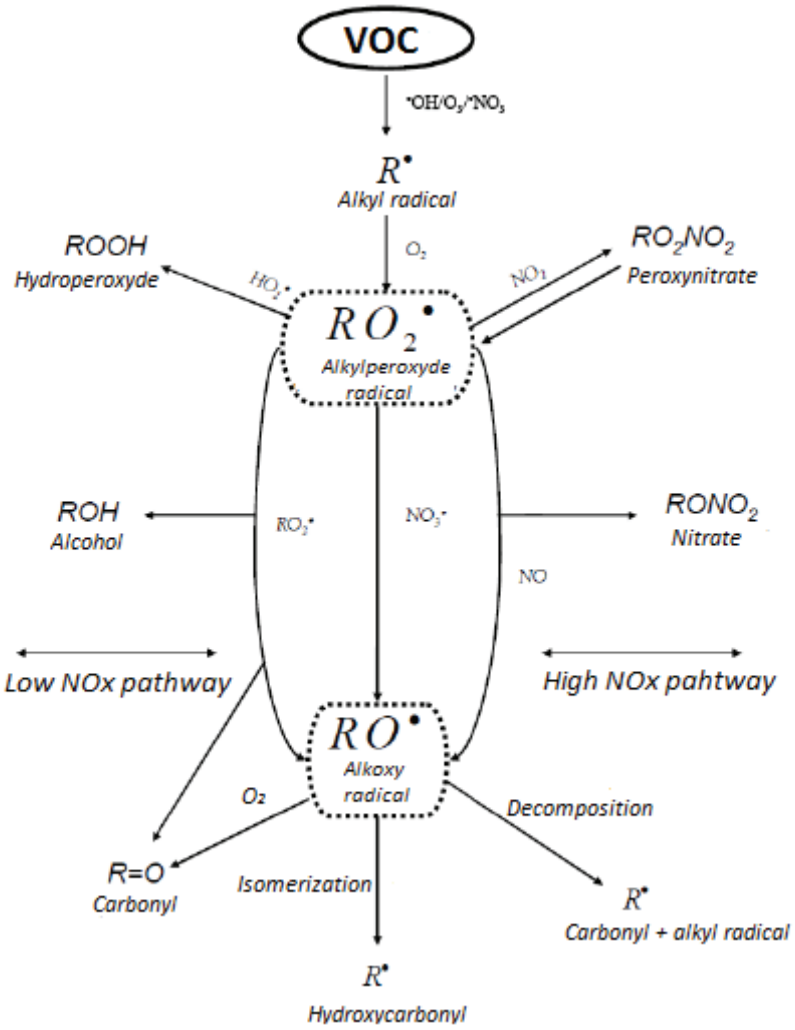

Figure 1.1. *Simplified scheme for VOCs degradation. (Source: Hallquist, 2009)*

The reaction mechanism occurs via H-abstraction (saturated compound) or OH-addition (double bond or aromatic compounds) and leads to the formation of an alkyl radical that rapidly reacts with atmospheric oxygen to form an alkylperoxy radical ($RO_2^{\bullet}$).

$$RH + OH^{\bullet} \rightarrow R^{\bullet} + H_2O \quad [1.6]$$

$$R^{\bullet} + O_2 \rightarrow RO_2^{\bullet} \quad [1.7]$$

The $RO_2^{\bullet}$ radical can undergo different reactions depending on the amount of NOx present in the atmosphere. Generally, we refer to low NOx regime when VOC/NOx ratio is higher than 8 and high NOx regime when VOC/NOx ratio is lower than 8.[191] The NOx regime will determine the mechanism of VOCs removal as shown in figure 1.19. Under high NOx conditions formation of alkoxy radical is favored.

$$RO_2^{\bullet} + NO \rightarrow RO^{\bullet} + NO_2 \quad [1.8]$$

$$RO_2^{\bullet} + NO \rightarrow RONO_2 \quad [1.9]$$

Then, the alkoxy radical can further react with O_2 to form a carbonyl compounds, it can decomposes by breaking of the C-C bond which produces smaller alkyl radicals and carbonyls or it can isomerizes by internal H-rearrangement forming hydroxy-carbonyl compounds.[196, 197] This last pathway generates polyfunctional products of lower volatility than the parent compound.

If the VOCs degradation takes place in low NOx atmosphere, the alkylperoxy radical mainly reacts with $HO_2^{\bullet}$ radical or with another $RO_2^{\bullet}$ radical:

$$RO_2^{\bullet} + HO_2^{\bullet} \rightarrow ROOH + O_2 \quad [1.10]$$

$$RO_2^{\bullet} + RO_2^{\bullet} \rightarrow RO^{\bullet} + RO^{\bullet} + O_2 \quad [1.11]$$

First reaction leads to formation of hydroperoxyde (which can readily photolyse) while the second leads to formation of alkoxy radicals, and further formation of alcohols (ROH) and carbonyls compounds (RO) (figure 1.19.).

The hydrocarbons can be compared in terms of Ozone Production Potential (OPP), defined as the change in photochemical ozone production due to a change in concentration of a particular VOC. The OPP evaluation is complex, it may be determined by photochemical model calculations or/and by laboratory experiments. Different photochemical model calculations indicate that substantial reduction of VOCs and NO_x emissions (more than 50%) are necessary, in order to achieve significant ozone reduction.[198-200] As road transport simultaneously emits VOCs and NOx, it is considered an important source of ozone.

Wood et al.[201] investigated ozone formation in gasoline vehicle and reported a contribution of ozone formed for each family species: 39% from alkenes, 24% from aromatics, 20% from alkanes, 10% from oxygenated and 7% from carbon monoxide. Figure 1.20. shows the OPP modeled for gasoline, diesel and non-tailpipe gasoline.

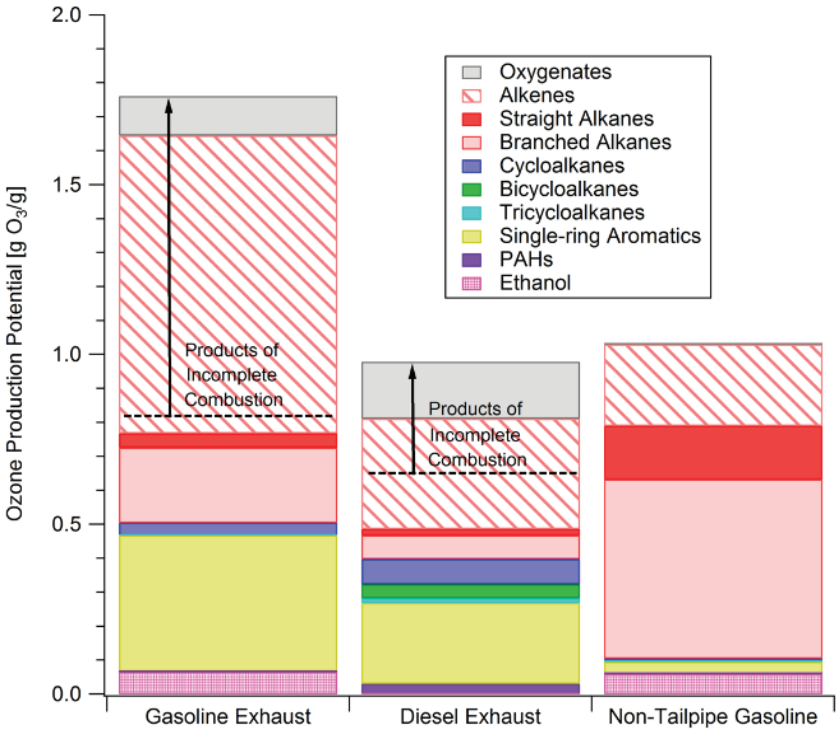

Figure 1.2. *Ozone production potential for gasoline, diesel and non-tailpipe gasoline. (Source : Gentner, 2013)*

Gentner et al.[71] modeled the OPP using the SAPRC-07 chemical mechanism and the speciated composition of the fuel and reported highest OPP for gasoline followed by non tailpipe gasoline emissions and diesel exhaust. For gasoline and diesel exhaust, alkenes, followed by single aromatic ring show the highest OPP, while branched alkanes have the highest OPP for non-tailpipe gasoline emissions.

During the atmospheric aging (figure 1.19.), VOCs are oxidized leading to molecules with higher oxygen content and lower volatility (isomerization and oxygen addition of alkoxy radical pathways). Therefore, the initial VOCs are progressively converted to Semi Volatile Organic Compounds (SVOCs), Low Volatility Organic Compounds (LVOCs) and Extremely Low Volatile Organic Compounds (ELVOCs) that can then partition on pre-existing particles forming SOA. The oxidation processes occurring on secondary and tertiary reaction products are key steps in the understating of SOA formation.[202]

SOA represents an important fraction of the total OA.[203, 204] At global scale, secondary organic aerosols are formed from a variety of VOCs coming from both natural and anthropogenic sources. In troposphere, biogenic species as isoprene and terpenes (limonene, pinene…) represent more than two third of total emitted VOCs.[205] Figure 1.21. shows the simulated worldwide concentration of isoprene and anthropogenic VOCs.

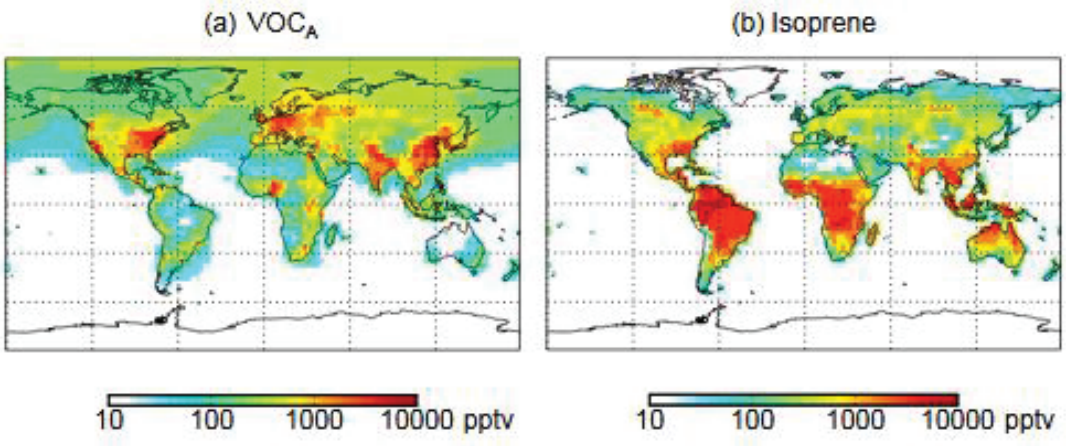

Figure 1.3. *Simulated annual mean surface concentration of (a) anthropogenic VOCs and (b) isoprene. (Source: Spracklen, 2011)*

It is therefore expected that SOA from biogenic compounds will dominated over SOA derived from anthropogenic precursors.[206] Although in highly polluted areas, anthropogenic emissions mostly due to combustion process (road traffic, industrial production and biomass burning), may overcome biogenic emissions, at least in some period of the year. And contrary to what was thought a couple of decades ago, secondary particles formed in the atmosphere through physical and chemical processes dominated the fine fraction of the aerosol in urban and polluted environments.[54, 78, 207-210]

1.5.2. Influence of Atmospheric Parameters for SOA formation

Formation of secondary organic particles depends on several parameters as the VOC, the type of oxidant and the meteorological conditions as humidity and temperature. The ability of a precursor to form SOA is usually described by a fractional aerosol mass yield, which is the product of the mass of aerosol formed divided by the mass of VOC reacted.[211]

$$SOA\ Yield\ (\%) = \frac{C_{OA}}{\Delta VOC} \cdot 100 \qquad [1.12]$$

where C_{OA} represents the concentration of SOA formed (μg/m^3) and ΔVOC represents the consumed VOC (μg/m^3). Temperature, humidity, NOx concentration or seed surface will affect the amount of secondary particle formed. SOA yield has been the main focus for many studies in the last 10 years, presenting values that widely vary for the same VOC depending on the chosen experimental conditions.

The temperature is considered an important parameter during SOA formation process, driving important changes in aerosol mass loading for small temperature variations.[212, 213] However, most simulation chambers present difficulties to perform temperature dependence studies. Thus, temperature sensitivity has received less attention that what it deserved. In general higher SOA yields are reported at lower temperature for toluene, m-xylene and 1,2,4-

trimethylbenzene, as well as for n-undecane, n-dodecane and alpha-pinene.[214, 215] A decrease of a factor 2-3 in SOA yield is reported when temperature increases from 283 K to 303 K.[214] During toluene photoxidation, a SOA yield 80-120% higher for experiments at 11°C compared to the ones at 32°C has been reported.[216] Temperature largely affects gas/particle partitioning [211] (see further details in chapter IV).

The influence of seeds has also been widely investigated.[217-225] In general, all studies agree that the presence of seed favors condensation of the gas phase, and hence, increases the SOA mass loading. Ng et al.[226] did not found any evidence of increased SOA for acidic seeds. A recent work carried out experiments at high and low NOx levels and reported that acidity of seed strongly enhanced SOA formation at high NOx but had little or no effect at low NOx.[227] All studies agree that SOA yields are higher at low NOx regime,[216, 218, 219, 228-230] suggesting that reaction products formed in these conditions are less volatile than those formed under high NOx conditions.

Relative humidity (RH) seems to be another important parameter for secondary organic aerosol formation in atmosphere. The RH determines the amount of water present in the system and could influence some heterogeneous on bulk reactions during SOA growth.[231-233] A recent toluene photoxydation experiment investigated SOA yield and its chemical composition varying humidity from 2% to 75%.[234] The results indicated a significant reduction in the mass of SOA and in the fraction of oligomers present in the particles for high RH.[234] But in general, for monoaromatic VOCs, in the presence of hygroscopic seeds, SOA yield increased at high RH conditions [221, 235-238] due to the fact that some low volatile compounds, as functionalized aldehydes, can easily partition into deliquescent seeds and react with water forming gem-diols.[239] Faust et al.[237] used ammonium sulfate effloresced seed (water content ≈ 0.2 μg/m^3) and deliquesced seed (water content ≈ 20 μg/m^3) and found 13% and 19% enhancement of SOA yield in the case of deliquesced seed for alpha-pinene and toluene photoxydation, respectively.

1.5.3. Gas-particle partitioning theory

The theoretical fundaments that describe the partitioning of organic compounds between gas and particle phase was developed first by Pankow [240] and then extended by Odum et al.[211] The equilibrium between the two phases is described by a partition coefficient, $K_{p,i}$ (m^3/μg):

$$K_{p,i} = \frac{C_{p,i}}{C_{g,i} \cdot C_{TSP}} \qquad [1.13]$$

Where $C_{p,i}$ and $C_{g,i}$ are the particle and gas phase mass concentrations, of an organic compound i respectively and C_{TSP} is the total suspended particulate mass concentration. The three parameters are expressed in μg/m^3. Odum et al.[211] show that the mass transfer from the

gas to the particle phase for a determinated compound increases with the total aerosol mass concentration. The mass fraction φ of a compound i in the aerosol phase is given by:

$$\varphi_i = \frac{C_{p,i}}{C_{p,i} + C_{g,i}} = \frac{K_{p,i} \cdot C_{TSP}}{1 + K_{p,i} \cdot C_{TSP}} \quad [1.14]$$

Figure 1.22. shows the evolution of the mass fraction φ_i as a function of K_{pi} for different concentrations of the organic aerosol.

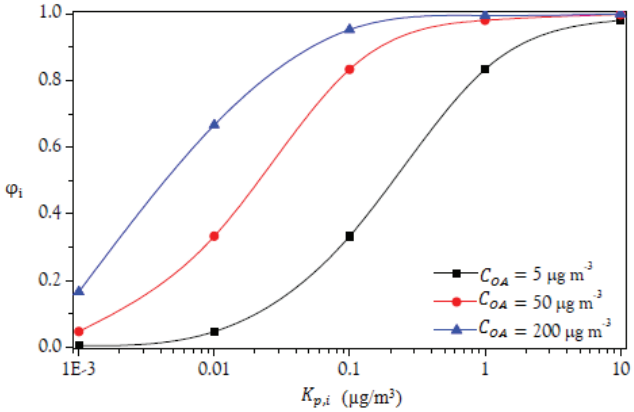

Figure 1.4. *Effect of total organic mass (C_{OA}) over condensed fraction (φ) of a specie i, as a function of the partition coefficient ($K_{p,i}$). (Source : Aladro, 2013)*

The partitioning coefficient, K_p, is linked to the vapor pressure through the equation below [240]:

$$K_{p,i} = \frac{760 \cdot R \cdot T}{10^6 \cdot \chi_i \cdot P_{i,sat} \cdot M_{W,av}} \quad [1.15]$$

where R is the perfect gas constant (8.2 x 10^{-5} atm m^3 / mol K), T is the temperature (K), $P_{i,sat}$ is the saturate vapor pressure of species i, (Torr), χ_i the activity coefficient of particle phase and $M_{w,av}$ is the average molecular weight of the organic aerosol (g/mol). As observed, the partitioning coefficient depends directly on the temperature. There is also an indirect relationship with the saturated vapor pressure, which is related to the temperature by the Clausius-Clapeyron equation:

$$P_{i,sat}(T) = P_{i,sat}(T_{ref}) \cdot exp\left[\frac{-\Delta H_{vap,i}}{R} \cdot \left(\frac{1}{T} - \frac{1}{T_{ref}}\right)\right] \quad [1.16]$$

where $\Delta H_{vap,i}$ is the vaporization enthalpy of species i , namely, the amount of energy needed to evaporate a substance from a temperature T_{ref} to a temperature T. The equations above show that the gas/particle partitioning depends also on the physical and thermodynamic properties of the species, as the molecular weight and the vaporization enthalpy.

The volatility of a chemical species is often expressed through the saturation concentration, C_i^*(µg/m^3) [241], defined as the inverse of the partition coefficient:

$$C_i^* = \frac{1}{K_{p,i}} \quad [1.17]$$

Based on this saturation concentration, a standard nomenclature has been developed [242] and five volatility ranges has been established. Looking at the saturation concentration (C_i^*), Extremely Low Volatile Organic Compounds (ELVOCs) are characterized by C_i^* lower than 3.2 x 10^{-4} μg/m^3 and are present only in the condensed phase under atmospheric conditions. Low Volatile Organic Compounds (LVOCs) have C_i^* values between 3.2 x 10^{-4} and 3.2 x 10^{-1} μg/m^3; Semi Volatile Organic Compounds (SVOCs) have C_i^* between 3.2 x 10^{-1} and 3.2 x 10^2 μg/m^3; Intermediate Volatile Organic Compounds (IVOCs) have C_i^* values between 3.2 x 10^2 and 3.2 x 10^6 μg/m^3 and for C_i^*larger than 3.2 x 10^6 μg/m^3, the compound is consider as a Volatile Organic Compound (VOCs).

One of the first models based on laboratory experiments was the so-called "two products".[211] The model links the partitioning theory of Pankow with the SOA yield (Y) and SOA mass formed (C_{OA}). For different conditions, the representation of the SOA yield values versus SOA masses formed is known as "SOA formation yield curve" (Y vs C_{OA}). Using the partitioning theory, the model is able to adjust the final yields from two hypothetical semivolatile products according to the following expression:

$$Y = C_{OA} \cdot \left[\frac{\alpha_1 \cdot K_{p,1}}{1 + K_{p,1} \cdot C_{0A}} + \frac{\alpha_2 \cdot K_{p,2}}{1 + K_{p,2} \cdot C_{0A}} \right] \quad [1.18]$$

Being *a* and *K* the stoichiometric and partitioning coefficients, respectively, for hypothetical products 1 and 2. The formation of the two semivolatile species ($SVOC_1$ and $SVOC_2$), depends on their stoichiometric coefficients α_i and the further condensation onto the particle phase, governed by the partition coefficients ($K_{p,i}$).

Using experimental Y and C_{OA} data, it is possible to adjust the four parameters in order to represent SOA formation. The addition of more products did not improve the fit to the yield obtained experimentally. The "two product" model has been used by many authors in laboratory and model works.[211, 218, 243, 244] The model, nevertheless, does not take into account the kinetics of both gas and/or aerosol phase processes, that involve reactions in condensed phase and/or second generation products formation. Another limitation is that the model could find problems to properly represent real atmospheric conditions, as example, temperature or C_{OA} sometimes are far from the chamber conditions on which model are based.

1.5.4. The Volatility Basis Set (VBS) approach

More recently, the Volatility Basis Set (VBS) approach was developed by Donahue et al.[241] in order to reduce the limitations presented in the "two products" model. In this case the volatility is represented as a distribution discretized into logarithmically spaced bins based

on the saturation concentration (C^*) covering a range between 10^{-4} to 10^5 μg/m^3. The C^* of a compound is the concentration above which it is transferred from the gas to the particle phase. For example, if a compound has a value of C*=50 μg/m^3, it means that it must reach a concentration of 50 μg/m^3 in order to start condensing on the particulate phase. The saturation concentration is defined as the inverse of the partitioning coefficient.

The 2-dimension VBS (2D-VBS) proposed by Donahue et al.[245, 246] was later introduced in order to describe the volatility, the thermodynamics and the chemical evolution of the organic aerosol as a function of the saturation concentration and the degree of oxygenation (Figure 1.23). This framework was then applied to the available experimental data in order to explain fundamental insights regarding the organic aerosol chemistry.

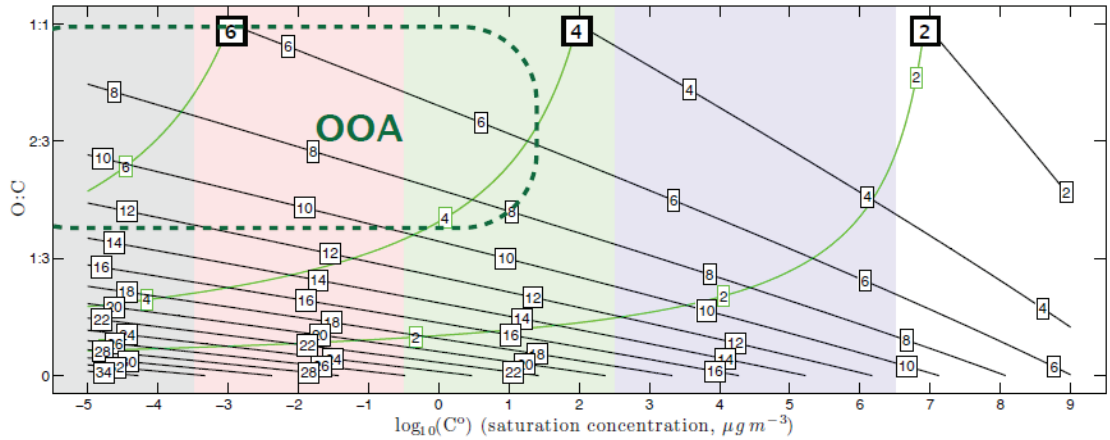

Figure 1.23. *Framework of the 2-D VBS, where the OA composition is described as a function of the degree of the OA oxygenation and the saturation concentration. The black lines denote the number of the carbons, while the green lines correspond to the oxygen number. The experimental ambient oxygenated organic aerosol (OOA) is in the dashed area in the upper corner.*

1.5.5. The Master Chemical Mechanism (MCM) model

One of the most used explicit models in the atmospheric chemistry community is the Master Chemical Mechanism (MCM) [247, 248] and further updates.[202, 248-251] The MCM is a near-explicit chemical mechanism that provides a detailed description of degradation mechanism in gas phase for a series of VOCs. The fundamental assumption is that the kinetics and products of a large number of unstudied chemical reactions can be defined on the basis of the known reactions of a comparatively small number of similar chemical species, by analogy and with the use of structure-reactivity correlations.[248] Currently, the degradation of methane and 142 VOCs are included in the model (www.mcm.leeds.ac.uk/MCM/). These VOCs comprise aromatics, alkanes, alkynes, alkenes, aldehydes, ketones, alcohols, glycols, ethers, glycoethers, carboxylic acids, esters and chlorine contained hydrocarbons.

The mechanism nowadays account for around 17000 reactions and 6700 compounds.[250] Even like this, plenty of minority reactions are not taken into account. Some approaches have

been developed in order to extend the MCM to the particle phase. Jenkin et al.[249] used a representation of gas-to-aerosol transfer of semivolatile and non-volatile oxygenated products to predict SOA formation from alpha and beta pinene ozonolysis. Camredon et al.[252] developed an explicit model based on the coupling of gas-phase oxidation schemes with a thermodynamic condensation module to study oxidation of 1-octene. However, results are not as good as expected and SOA formed is overestimated in models by a factor of 2. Li et al.[240] included an equilibrium partitioning module, based on Pankow's absorption-partitioning theory; and reactive surface uptake processes coupled to the Community Multiscale Air Quality model (CMAQ).[253] Figure 1.24. summarizes the flow chart for reactions and products simulated by the model.

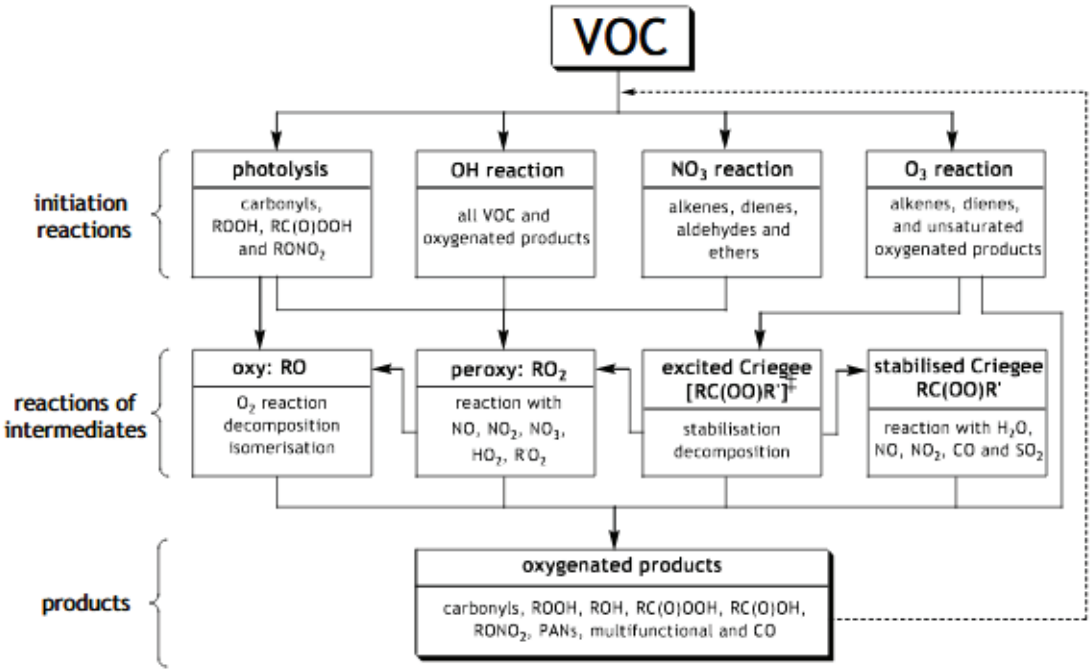

Figure 1.24. *Flow chart for the reactions and chemical products of the MCM model. (Source: Saunders, 2003)*

The generator steps can be summarized as follow : an initial reaction between a VOC and an oxidant to form the organic peroxy radical (RO_2); the peroxy radical reaction with NO, NO_2, NO_3^-, $HO_2^\bullet$ or $RO_2^\bullet$ to form secondary stable species or an alkoxy radical ($RO^\bullet$). As some degradation pathway can lead to very large mechanism, especially for heavy VOCs, some simplifications are required. These simplifications disregard channels of low probability or minor compounds.[247]

1.5.6. The GECKO-A model

The Generator of Explicit Chemistry and Kinetics of Organics in the Atmosphere (GECKO-A) [252, 254] is able to generate an explicit and complete chemical degradation mechanism whatever is the VOC. Mechanisms include species as linear and branched alkanes, alkenes, cyclics, ethers, esters, alcohols, carbonyls, nitrates, peroxyacylnitrates, carboxylic

acids, peracids, hydroperoxides, alkyl radicals, peroxy radicals and alkoxy radicals. The model proposes a fully develop mechanism including all intermediate compounds, radicals and oxidation pathways from the initial VOC to the final oxidation products as CO, CO_2 and water. The model accounts for around 10^5 species and 10^6 reactions.[254] Figure 1.25. presents a comparison for some species involved in the degradation of n-heptane between MCM v3 (dashed lines) and the GECKO-A models (solid lines).

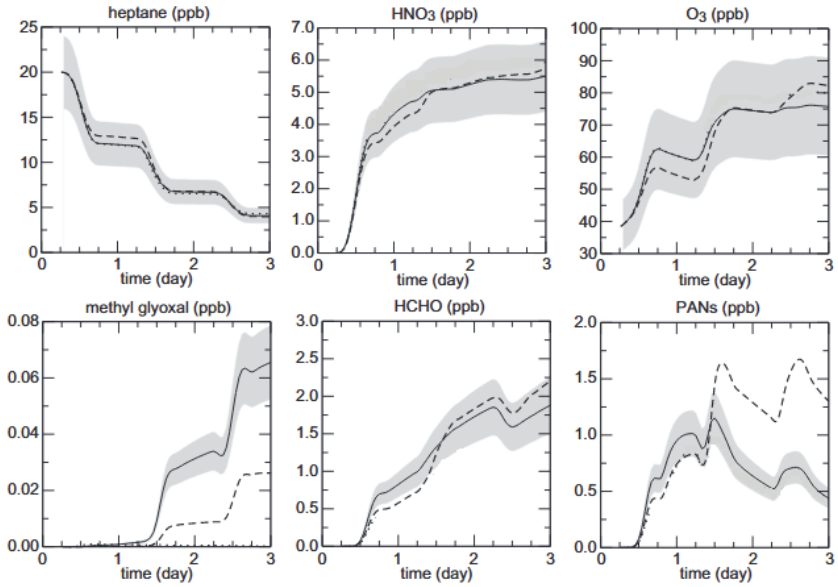

Figure 1.25. *Comparison mechanism for n-heptane oxidation. Solid lines GECKO-A model, dashed lines: MCM v3 model. Shaded area represents ±20% deviation.*

The two models seem to agree reasonably well for some species (n-heptane, ozone or HNO_3). Further generation products present unclear trend, whit large discrepancies for methyl glyoxal and Peroxyacyl Nitrates (PANs) but an excellent agreement for formaldehyde. A thermodynamic condensation module has been developed and coupled to the gas-phase oxidation mechanism in order to simulate SOA formation and speciation.[252] The SOA formation module is based on the absorption mechanism and follows the gas-particle partitioning theory.[240] The model shows factor 3-4 overestimation for the alpha-pinene modeled SOA compared with experimental laboratory data.[255] A possible explanation is that model does not take into account wall losses of the semivolatile species. In more recent studies where wall losses have been taken into account, an improvement of the modeling estimation compared to the experimental data is achieved.[256]

1.5.7. SOA Formation from Road-transport

Literature work suggests that vehicular emissions highly contribute to the total PM on urban areas through primary particles and SOA precursor emissions.[257] Composition and emission rates of SOA precursors widely vary depending on vehicle type, size, fuel or post-

treatment devices. Potential SOA formation from vehicle can be estimated by measuring traffic areas and elucidating sources of emission by tracers (top-down methods) or by investigating fuel/oils/emissions from an individual car under controlled conditions (bottom-up methods).

1.5.7.1 Bottom-up methods

The bottom-up approach uses fuel chemical mass balance or single car emissions to elucidate the relative contribution to SOA.[71, 258] Fuel composition data have been used to estimate SOA formation from exhaust.[207, 257] The total SOA yield is reported as the sum of the estimated SOA yield contributions for each individual compound of the fuel. Some of these individual SOA yields contribution can be estimated from real laboratory tests. For estimation of SOA yield from non-tested compounds, theoretical approaches based in partitioning theory and models described above have been used.[259, 260]

Some previous work estimated an effective SOA yield larger for diesel fuel than for gasoline fuel.[207, 261] However, introduction of DFP and DOC may shift major SOA production to gasoline vehicles.[262] Figure 1.26. shows SOA Yield estimated as a sum of SOA contributions from different chemical families as a function of the carbon number for different fuels.

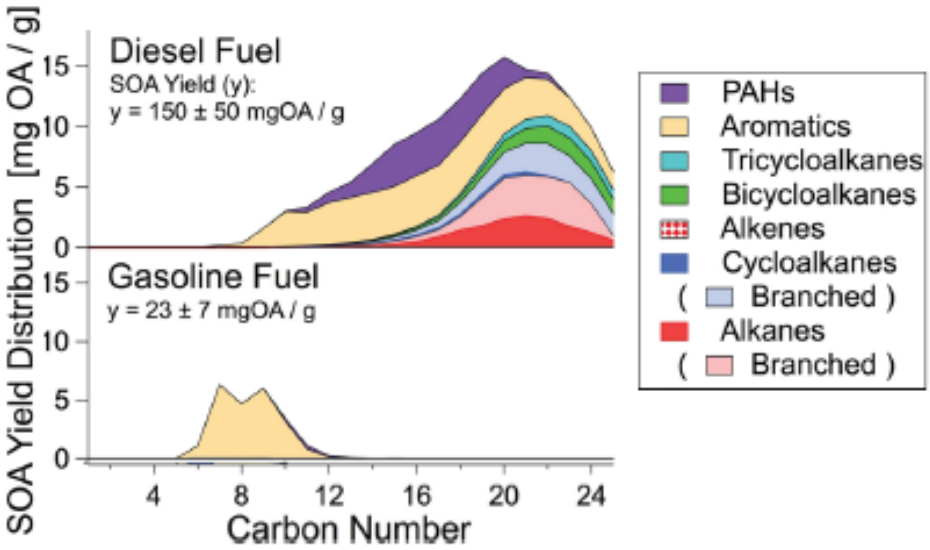

Figure 1.26. *Potential SOA yield as sum of SOA contribution for gasoline and diesel fuel as a function of carbon number. (Source: Gentner, 2012)*

SOA from gasoline fuel arises almost exclusively from aromatic compounds, while for diesel fuel the situation is more complex as many chemical families do participate to the SOA formation. First observation is that heavier compounds from C_8 to C_{24} are involved in diesel SOA formation; then the alkanes families together are responsible for 47% of the SOA yield, followed by the aromatics (36%) and the PAHs (17%). Miracolo et al.[263] showed that reduction of aromatic compounds from the Fischer-Tropsch synthetic jet fuel highly reduced the SOA formation. While other authors [19, 20] did not report any observable reduction of formed SOA by

using biodiesel fuel. The influence of ethanol content in gasoline fuel (10% , 85% and 100%) was investigated by Timonen et al.[264] who observed a clear decrease in SOA formation as ethanol content increased in the blend. The use of fuel speciation as tool for the determination of SOA has some limitations. This method assumes that products coming from lubricant oils present little contribution to the SOA budget, and this could not be the case.

Another experimental method to determine SOA formation consists on the oxidation of primary emissions from cars in a reactor tube or simulation chamber. This approach provides a more realistic view of SOA formation from vehicles. As drawback, reactor and chamber experiments are limited to a reduced number of vehicles, limiting the possibility to get information for the whole fleet.[265, 266]

Several experiments suggest that SOA mass does not need long photo-oxidation times (or $^{\bullet}OH$ exposure) to exceed POA mass for both gasoline and diesel vehicles [20, 267-270] despite the probably loss of some fraction of IVOCs or SVOCs in the lines or exhaust dilution manifolds. Thereby, taking into account those losses, SOA concentration would be even higher than experimentally determined.[271, 272] The SOA/POA ratio widely varies depending on many factor related to the driving conditions, type of vehicle (cycle, fuel load, fuel type…) and with experimental conditions (dilution, $^{\bullet}OH$ exposure, NOx level…). Figure 1.27. shows the time series of organic, nitrate, sulfate and ammonium formed in a Potential Aerosol Mass (PAM) chamber experiment from primary emission sampled in a highway tunnel.[267]

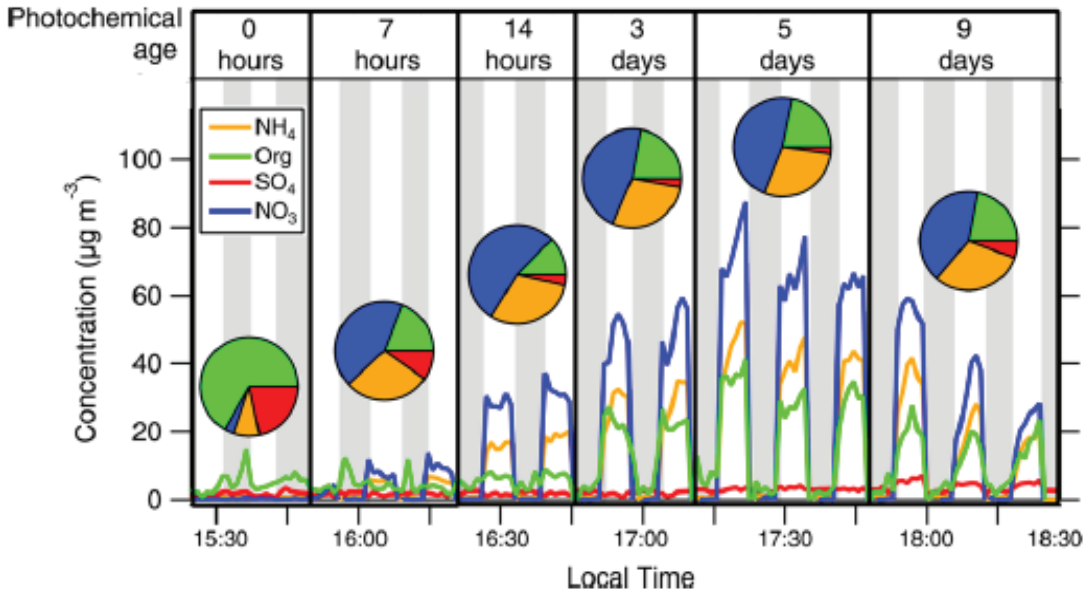

Figure 1.27. *Time series of ammonium, sulfate, organics and nitrate for a PAM experiment as a function of photochemical age. Shaded periods represent non-photoxidation periods. Equivalent atmospheric oxidation (i.e, "1 day" at [$^{\bullet}OH$] = 3x10^{6} molec/cm^{3}). (Source: Tkacik, 2014)*

The shaded periods are without photochemistry while during the white portions, the air from the tunnel is exposed to different levels of oxidants which give rise to the formation of

ammonium nitrate (orange and blue) and SOA (green). The SOA mass loading exceeds the POA for photochemical ages of 14 hours. The maximum values of secondary generated particles are observed for a photochemical age of 5 days. The significant formation of ammonium nitrate is due to oxidation of NO_2 to HNO_3 and further neutralization by the ammonia emitted.[64, 273, 274] Platt et al.[270] performed photoxydation experiment on Euro 5 gasoline emissions and found a SOA/POA ratio of 9-15 after aging.

Other authors,[78, 208] compared the SOA formation from GDI and PFI vehicles and reported little difference between the two technologies. Pieber et al.[268] reported higher SOA formation during cold start regime due to higher VOCs emission. Figure 1.28. shows the comparison on SOA formation (green) due to cold and hot start upon oxidation in a flow reactor of emissions from a GDI Euro 5 exhaust.

The POA is represented by the dashed lines, BC by the black line and nitrate by the blue line. At cold start, SOA mass loading rapidly overcomes POA leading to a SOA/POA ratio >>>10. The ratio SOA/BC remains around 1 during the whole cycle. At hot start, SOA reaches same values than POA.

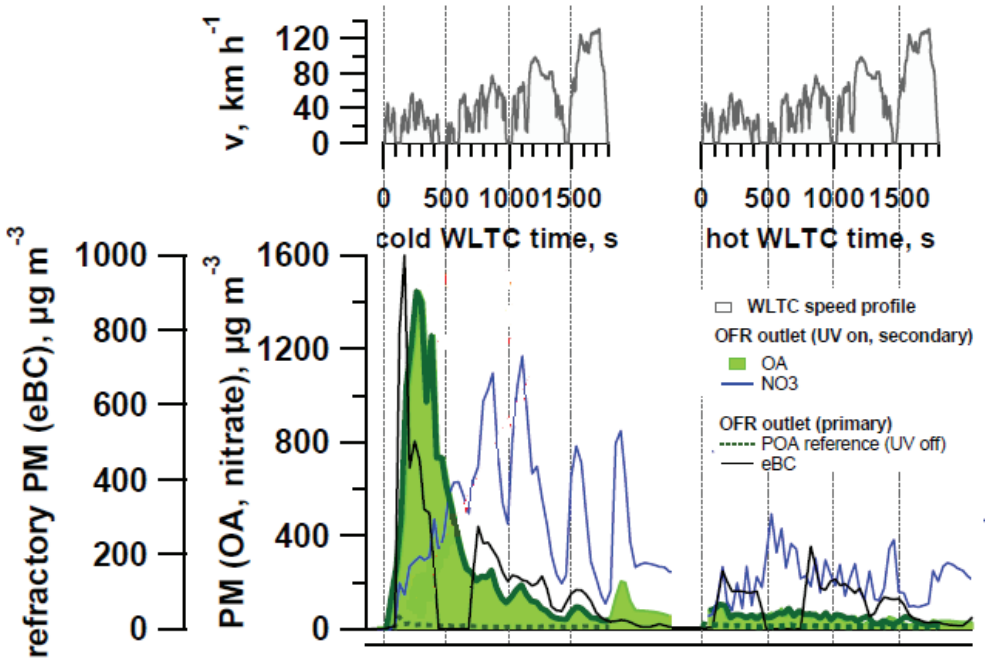

Figure 1.28. *Influence of cold/hot start conditions for SOA formation. GDI Euro 5 vehicle emissions were oxidized in an oxidation flow reactor (OFR). Vehicle emissions were injected during a WLTC run. Source: Pieber, 2018*

Platt et al.[262] also studied the influence of driving car temperature (22°C and -7°C) on SOA formation for gasoline Euro 5 emissions and reported a dramatically increase of POA and VOCs and hence SOA formation for experiments performed at-7°C. Pieber et al.[275] reported an increase of SOA of a factor 3 when increasing relative humidity from 40% to 90%. Recently, Drozd et al.[276] and Zhao et al.[277] estimated the SOA formation for a large fleet of gasoline

vehicles in the U.S. They found an important decrease of emitted VOCs and hence, reduction in SOA formed for modern vehicles (SULEV standards) compared to older ones.

Traditionally, aromatic compounds were considered the most efficient SOA precursors.[191, 278] However, comparison between observed and predicted SOA taking into account aromatics, suggest that SOA cannot be explained by this class of compounds alone.[279, 280] Figure 1.29. shows the predicted SOA contribution of the most abundant aromatic species based on experimental measurements in comparison with total observed SOA from a smog chamber experiment of a Euro 5 gasoline car. Predicted SOA for each aromatic has been calculated by multiplying measured VOC consumption and individual SOA yields reported previously in literature. As observed, aromatics only account for a small fraction of the formed SOA. Thus, focus has been shifted to other families of compounds that potentially could contribute to the observed SOA.

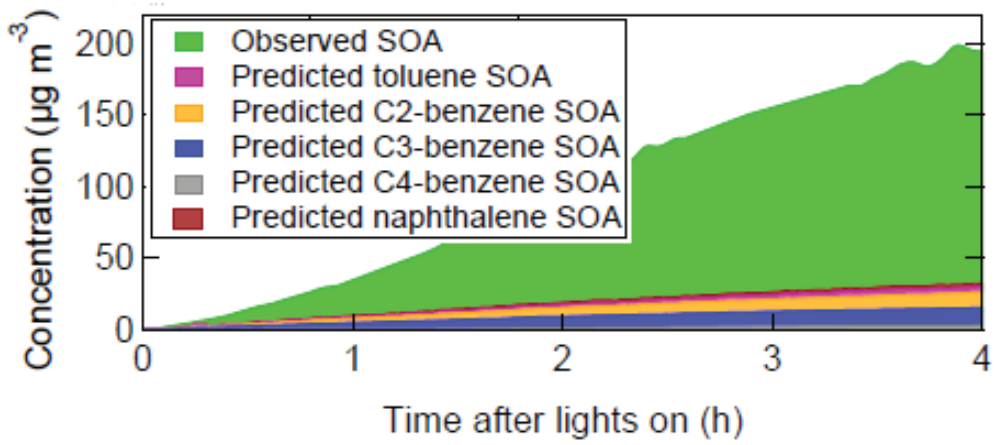

Figure 1.29. *Predicted aromatics versus observed SOA for a smog chamber experiment during aging of emissions from Euro 5 gasoline light-duty vehicle. (Source: Platt, 2013)*

More recently, IVOCs (roughly C_{12}-C_{22} n-alkanes/alkenes) and heavier alkanes/alkenes (SVOCs) have been reported as effective SOA precursors.[257, 281, 282] These compounds are thought to have an important SOA potential formation even if atmospheric concentrations are lower than those of smaller VOCs.[283, 284] Zhao et al.[285] estimated SOA formation from IVOCs 5 times higher that produced from single-ring aromatics during ambient measurements during a field campaign in Pasadena (CA). The authors indicated the IVOCs as a major contributor (57%) to SOA formed in urban areas.

Same authors [286] reported emissions studies of recent GDI vehicles and simulate potential contribution to SOA formation of each family. Average EFs for single ring aromatics was 5 times higher than IVOCs EFs. However, single ring aromatic accounted by 50% of predicted formed mass, and IVOCs accounted for the remaining mass fraction. Platt et al.[270] also performed photoxidation experiment to Euro 5 gasoline vehicles and suggested that large

part of formed SOA is derived by IVOCs. By taking into account IVOCs emissions and chemical regime variations, Sartelet et al.[287] were able to correctly reproduce Platt's observations.[270]

Diesel passenger cars may also produce SOA and many studies have been devoted to the investigation of primary and secondary OA from diesel. Several studies focused on old diesel vehicles without aftertreatment devices and reported efficient formation of SOA.[281, 288-290] The introduction of aftertreatment devices for diesel vehicles (DOC, DPF) provided an efficient way to reduce PN and VOCs precursors, leading to drastically reduction of SOA production.[20, 291-293] Chirico et al.[293] measured primary emissions and SOA formation from three diesel vehicles (one without abatement technologies, other with DOC and other with DOC+DPF). The highest reduction in SOA formation was reported for the vehicles equipped with DOC+DPF, but the DOC was also able to reduce of SOA formation, by removal of gaseous precursors.[293] The authors attributed a large fraction of SOA to IVOCs and SVOCs species while a very little fraction was explained by traditionally SOA precursors as aromatics. Jathar et al.[19] suggested that the combination of aftertreatment systems and higher engine loads reduced POA EFs by an order of magnitude and SOA production by a factor of 2-10. Gordon et al.[20] reported very little primary PM from diesel equipped with DFP. As a result, no SOA was formed. Platt et al.[262] studied the influence of driving car temperature (22°C and -7°C) on SOA formation for diesel Euro 5 emissions. The authors reported no influence of the temperature for diesel vehicles, where total PM was dominated by primary emissions.

Figure 1.30. shows the average POA and predicted SOA contribution for different families of organic compounds after 48h of photoxidation.

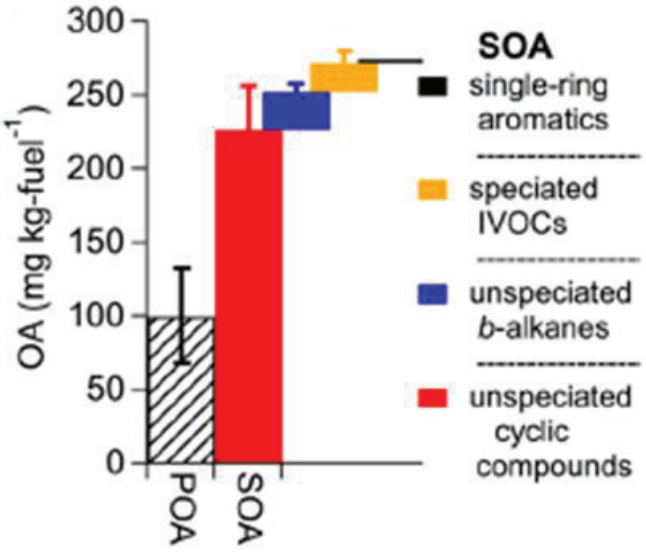

Figure 1.30. *SOA and OA from diesel cars a) influence of driving conditions and DPF for diesel vehicles; b) averaged POA and fractional predicted SOA after 2 days of photoxidation. (Source: Zhao, 2015)*

SOA/POA ratio was set approximately 2.5. Predicted SOA was due to IVOCs containing compounds from C_{12} to C_{22}. It accounts for a small fraction of speciated IVOCs, unspeciated b-

alkanes and cyclic compounds which represent the dominant fraction, while the contribution of single ring aromatic compounds to SOA formation resulted to be negligible.

These results suggest that IVOCs (accounting for 60% of NMHC) are responsible for more than 95% of total SOA formed.[294] In general, SOA produced in smog chamber and PAM as results of exhaust photoxidation could not be explained by the oxidation of VOCs precursors included in traditional models.[20, 270, 295] IVOCs could potentially fill this gap in the case of diesel vehicles.

1.5.7.2 Top-down methods

Top-down methods based on ambient measurements is another option to determine SOA potential formation from passenger car emissions. Chemical composition of ambient OA is measured and separate in emission sources through apportionment analysis.[296, 297] However, due to the high complexity of the total OA bulk, speciation is limited and only a small fraction of the aerosol can be assigned to its source.[298, 299] Some well-known SOA products have been used as proxies from a chemical compound family, but SOA assessment from a specific source remains unclear.[300, 301] Therefore, it is not an easy task to separate vehicle emissions from other sources and even the separation from gasoline from diesel vehicles is challenging since compounds as, for example aromatics, are emitted from gasoline and diesel vehicle and also for other sources.[257, 302] The main drawback of the top-down methods is the initial assumption that SOA formation in urban areas is dominated by vehicle emitted SOA precursors. Even if in urban areas road transport accounts for a high VOCs fraction, there is always the possibility of undefined SOA precursors for other sources.[257] Thereby, Ensberg et al.[54] and Zotter et al.[303] estimated the contribution to SOA formation of traffic emissions of 50% and 75%, respectively.

The figure 1.31.a shows a Positive Matrix Factorization (PMF) analysis based on Aerosol Mass Spectrometer (AMS) data for speciation of anthropogenic sources.[54] As observed, organic aerosol (OA) categories assumed as primary emission tracers (Hydrocarbon-like OA, (HOA); Cooking-influenced OA, (CIOA) or Local OA, (LOA)) present a plateau or even a decrease as photoxidation time increases. These sources have been described as a surrogate for primary combustion, cooking and other SOA contribution sources around the area, respectively. SOA formation surrogates (Semi-Volatile Oxygenated OA, (SVOOA) and Low Volatility Oxygenated OA, (LVOOA)) present a growing trend as photochemistry goes on.

Measured AMS PMF factor concentrations normalized by CO variation as a function of the photochemical age during weekdays, saturdays and sundays is shown in figures 1.31.b and 1.31.c[54] The OOA factor corresponds to the sum of the secondary factors (SVOOA+LVOOA) while the figure 1.31.b shows the sum of the primary and oxidized surrogates (OA). It is possible to observe how OA/ΔCO ratio is higher during weekdays rather than weekends due to the higher contribution of traffic sources to OA during weekdays. Contrary, oxidized surrogate

OOA/ΔCO does increase during weekends. Some authors suggested that the lower NOx emissions during weekends will increase the VOC/NOx ratio and hence enhance SOA formation.[304, 305]

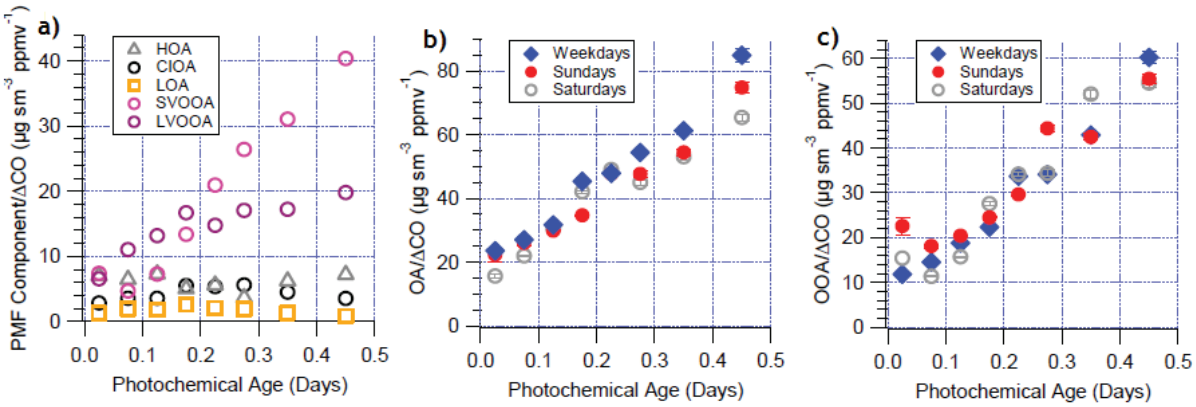

Figure 1.31. *a) Measured AMS PMF factor concentration as function of photochemical age; b) OA/ΔCO evolution for weekdays and weekend as function of photochemical age; c) OOA/ΔCO evolution for weekdays and weekend as function of photochemical age. (Source: Ensberg, 2014)*

The higher presence of vehicles during weekdays with respect to weekends urban areas can be used to assess SOA formation from traffic sources by observing increase/decrease of specific tracers. Some authors pointed out that in L.A. basin, BC or NOx concentration (as vehicle tracer) clearly followed weekday/weekend dependence and therefore the reduction of primary emissions will lead to higher values of secondary product during weekend, as ozone or SOA.[306-308]

In air quality models, the introduction of IVOCs has lead to a better estimation of SOA budget.[309, 310] Jathar et al.[311] used the CMAQ model in California and found that half of the mobile source SOA was explained by IVOCs oxidation products. In Europe (diesel dominance), Ots et al.[312] reported an emission ratio IVOCs/VOCs of 2.3. Thus, the introduction of these inputs in the ACTM model indicated that diesel-related IVOCs were responsible up to 30% of annual SOA formed in and around London. Sartelet et al.[287] performed the Polyphemus/Polair3D transport model and reported a small contribution to SOA formation for VOCs over Greater Paris. However, contribution to SOA formation from low volatility species (IVOCs, SVOCs…), the so-called $POA_{vapor,}$ is quite high. They reported lower organic aerosol concentration when POA_{vapor} emissions are estimated from VOCs rather than POA emissions.

1.6. Challenges and Remaining Questions

Relevant progress has been achieved over the last 20 years in the understanding of SOA formation, establishing main SOA precursors and the VOCs degradation pathways.[19, 218, 267, 278, 313, 314] Based on this information, models have been developed in order to simulate SOA

formation yield, degradation products and ultimately, establish SOA budget at local and regional scale and built better climate models. However both global and air quality models poorly represent the SOA, particularly in urban environments, where anthropogenic activities and transport are a major source of pollutants.[209, 287, 315, 316] Possible reasons have been indicated in several papers: omission of key precursors in the models, vapor pressure assignment based on estimations, not fully developed chemical mechanisms for IVOCs and SVOCs coming from vehicles emission.[317-319] In addition road transport fleet is in constant evolution via fleet renewal and technology shifts (as from PFI to GDI vehicles) which adds on to new fuel composition (biofuels): all these factors will influence car emissions and consequently SOA budget.

Several are the remaining questions related to the environmental impacts of vehicle emissions. While regulated pollutants are more or less well characterized, non-regulated pollutants (as IVOCs, ammonia, metals, particle below 23 nm) are poorly investigated despite their potential key role in air quality and health related issues. One important question is related to the Particle Measurement Programme (PMP) protocol and the lack of knowledge on condensable species of emitted PM and, another issue, is related to particles below 23 nm. These latter represent, during specific driving conditions, an important fraction of total emitted Particle Number (PN) and do negatively affect human health, air quality and climate. Another issue is related to the IVOCs/SVOCs, which have recently been indicated as key precursors of SOA.[287, 294, 316, 320] A major uncertainty in the models rises from poor emission inventory and their atmospheric processing. These compounds are difficult to measure, which is why they are usually assumed to be emitted proportionally to primary organic aerosol mass or VOCs.[210] Nevertheless, their estimation does not seem to be enough to explain the SOA formation.[310, 321] To reduce this gap it is important to improve the analytical techniques and therefore better determines IVOCs/SVOCs inventory. Another future step will be to identified, understand and quantified low volatility products from other sources as biomass burning, oil production or oil sands; which have been already reported in literature.[55, 322, 323]

The SOA composition remains, up to now, a big analytical challenge. Firstly due to the myriad of compounds found in SOA at trace levels. Traditionally the identification of the organic compounds in SOA was performed using off-line method which implies PM collection on filters followed by extraction and analysis. Several derivatization methods have been developed in order to identify and quantify functionalized compounds (as hydroxyl, carbonyl, carboxylic, and nitro or nitroso compounds) found in the particles.[239, 324] Nevertheless, these methods pose some withdraws, as they focus on a limited number of compounds, they are costly and time consuming, and finally they provide information on a small fraction of the total SOA.[325, 326] In the last 15 years on-line methods for chemical analysis (as the High-Resolution Time-of-Flight Aerosol Mass Spectrometer (HR-ToF-AMS) Aerodyne) have been successfully

applied to the study of PM.[327] However, the AMS ionization method, based on electron impact at 70eV, leads to a severe fragmentation, which does not allow the identification of the individual organic molecules of the SOA. Despite this limitation, source apportionment analysis applied to the AMS mass spectra was able to separate the OA into different source components such as POA related to vehicle emissions, cooking preparation, biomass burning etc. and SOA.

This approach sums up all SOA without being able to distinguish between the various sources. Therefore, new instrumentations and methods are required. Very recent techniques open new possibilities to the identification of SOA components at molecular level and high time resolution. Some new techniques apply chemical ionization mass spectrometry to particulate matter.[326, 328, 329] These analytical developments led to the quantification of the large fraction of carboxylic acids in SOA produced in forested environments.[329] A very recent work quantified high levels of levoglucosan, an important tracer of wood burning, in several European cities during winter time.[330] The identification of individual components in SOA remains one of the biggest challenge in organic aerosol research. Detailed information on chemical composition will allow, on one side, the identification of the main precursors of the SOA from road transport, and on the other side, to establish a more direct link to the adverse health effect of SOA. On the basis of that knowledge better emission regulations can therefore be designed.

1.7. Thesis Objectives

Significant controversy exists nowadays over the contribution of vehicles emissions to ambient pollution and to SOA formation. These open questions are linked to the limited identification of key precursors and poor understanding of chemical and physical processing of these latter in the atmosphere. This PhD was supported by the project CaPVeREA (ADEME CORTEA) which proposed a comprehensive study of both modern vehicle emissions and their chemical transformations in the atmosphere. The research focused on two major objectives:

1) To investigate primary emissions of gasoline GDI and diesel Euro 5 and Euro 6 passenger cars and implement European databases. For all vehicles regulated and non-regulated pollutants have been measured. Special attention has been devoted to the development of a methodology for tailpipe measurements using multi stage dilution systems. Our main focus was the identification and quantification of non-regulated pollutants. In particular we investigated the chemical composition of primary emitted particles focusing on the condensable fraction using state-of-the art on line instrumentation. Furthermore morphology and elemental composition was determined by using TEM grids coupled to EDX analysis. Then we investigated the emission of particles below 23 nm diameter. The ensemble of the chemical species that compose PM as well as the size distribution can affect air quality

and human health. Then we focused on the speciation of VOCs and IVOCs for both gasoline and diesel vehicles. The study allowed the development of a new methodology for IVOCs sampling aiming at reducing measurements bias due to condensational losses. Emission studies were undertaken at the IFSTTAR facility and emissions were measured using WLTC or Artemis cycles, under cold and hot start conditions.

2) A second and extensive part of my PhD focused on SOA formation studies. The work is mainly based on laboratory investigations (aerosol flow tube) where VOCs emitted from Euro5 and Euro6 vehicles were oxidized under different simulated atmospheric conditions. This work was based on the oxidation of individual VOCs. The aim was to determine SOA yield, chemical composition of both gas and particle phase, key parameters controlling SOA formation (as temperature, type and quantity of VOC, pre-existing seed particles). Then experiments were repeated using a mixture of the selected VOCs. The new developed Chemical Analysis of aerosol on-line (CHARON) inlet coupled to PTRMS was deployed for the speciation of the organics in the particle phase. Few photoxidation experiments of car exhaust were performed using an aerosol flow tube to determine major SOA constituents and SOA potential formation.

The PhD manuscript is organized as follows:

- Chapter I addresses the context and state of the art of my study introducing vehicle emissions and SOA formation in the atmosphere;
- Chapter II is dedicated to the description of the IFSTTAR facility for emission measurements, the aerosol flow tube used for photochemical studies and all analytical and instrumental tools deployed in the project;
- Chapter III is dedicated to the first objectives and present results from the vehicle emissions studies (both gaseous and particle pollutants);
- Chapter IV presents the results of the photo-oxidation of toluene, naphthalene, cyclohexane, nonane and mixtures of them; and the SOA study from real car exhaust. Potential SOA formation and chemical speciation of degradation product is presented.
- Chapter V finished with some general conclusions and future perspectives.

References:

1. EEA. Transitions towards a more sustainable mobility system.Transport indicators tracking progress towards environmental targets in Europe. In: EEA Report No 34/2016 . 2016.
2. CCFA. L'industrie automobile française. Analyse et statistiques. In: Comité des Constructeurs Français d'Automobiles, CCFA; 2017.
3. ACEA. The automobile industry pocket guide. In. European Automobile Manufacturers Association; 2018.
4. ICCT. CO2 emissions from new passenger cars in the UE: Car manufacturer's performance in 2017. In: The International Council of Clean Transportation; 2018.
5. Zhang K, Batterman S. Air pollution and health risks due to vehicle traffic. The Science of the total environment 2013; 450-451:307-316.
6. EEA. Emissions of the main air pollutants in Europe. In. Environmental European Agency; 2018.
7. Hooftman N, Messagie M, Van Mierlo J, Coosemans T. A review of the European passenger car regulations – Real driving emissions vs local air quality. Renewable and Sustainable Energy Reviews 2018; 86:1-21.
8. Karagulian F, Belis CA, Dora CFC, Prüss-Ustün AM, Bonjour S, Adair-Rohani H, et al. Contributions to cities' ambient particulate matter (PM): A systematic review of local source contributions at global level. Atmospheric Environment 2015; 120:475-483.
9. R'Mili B, Boréave A, Meme A, Vernoux P, Leblanc M, Noël L, et al. Physico-Chemical Characterization of Fine and Ultrafine Particles Emitted during Diesel Particulate Filter Active Regeneration of Euro5 Diesel Vehicles. Environmental Science & Technology 2018; 52(5):3312-3319.
10. Karjalainen P, Pirjola L, Heikkilä J, Lähde T, Tzamkiozis T, Ntziachristos L, et al. Exhaust particles of modern gasoline vehicles: A laboratory and an on-road study. Atmospheric Environment 2014; 97:262-270.
11. Haynes BS, Wagner HG. Soot formation. Progress in Energy and Combustion Science 1981; 7(4):229-273.
12. Glassman I. Soot formation in combustion processes. Symposium (International) on Combustion 1989; 22(1):295-311.
13. Mansurov ZA. Soot Formation in Combustion Processes (Review). Combustion, Explosion and Shock Waves 2005; 41(6):727.
14. Bertrand A. Vieillissement atmosphérique de l'aérosol de combustion de biomasse: du potentiel de formation d'aérosol organique secondaire à la modification de l'empreinte chimique à l'échelle moléculaire. In. Thése, Universite d'Aix-Marseille, Laboratoire chimie de l'environnement; 2017.
15. Andreae MO, Gelencsér A. Black carbon or brown carbon? The nature of light-absorbing carbonaceous aerosols. Atmos Chem Phys 2006; 6(10):3131-3148.
16. Worton DR, Isaacman G, Gentner DR, Dallmann TR, Chan AWH, Ruehl C, et al. Lubricating Oil Dominates Primary Organic Aerosol Emissions from Motor Vehicles. Environmental Science & Technology 2014; 48(7):3698-3706.
17. Alam MS, Zeraati-Rezaei S, Liang Z, Stark C, Xu H, MacKenzie AR, et al. Mapping and quantifying isomer sets of hydrocarbons (≥ C12) in diesel exhaust, lubricating oil and diesel fuel samples using GC × GC-ToF-MS. Atmos Meas Tech 2018; 11(5):3047-3058.
18. Kuwayama T, Collier S, Forestieri S, Brady JM, Bertram TH, Cappa CD, et al. Volatility of primary organic aerosol emitted from light duty gasoline vehicles. Environ Sci Technol 2015; 49(3):1569-1577.
19. Jathar SH, Friedman B, Galang AA, Link MF, Brophy P, Volckens J, et al. Linking Load, Fuel, and Emission Controls to Photochemical Production of Secondary Organic Aerosol from a Diesel Engine. Environmental Science & Technology 2017; 51(3):1377-1386.
20. Gordon TD, Presto AA, Nguyen NT, Robertson WH, Na K, Sahay KN, et al. Secondary organic aerosol production from diesel vehicle exhaust: impact of aftertreatment, fuel chemistry and driving cycle. Atmospheric Chemistry and Physics 2014; 14(9):4643-4659.
21. Pulles T, Denier van der Gon H, Appelman W, Verheul M. Emission factors for heavy metals from diesel and petrol used in European vehicles. Atmospheric Environment 2012; 61:641-651.
22. Adamiec E, Jarosz-Krzemińska E, Wieszała R. Heavy metals from non-exhaust vehicle emissions in urban and motorway road dusts. Environmental monitoring and assessment 2016; 188(6):369-369.
23. Johansson C, Norman M, Burman L. Road traffic emission factors for heavy metals. Atmospheric Environment 2009; 43(31):4681-4688.
24. Cheung KL, Ntziachristos L, Tzamkiozis T, Schauer JJ, Samaras Z, Moore KF, et al. Emissions of Particulate Trace Elements, Metals and Organic Species from Gasoline, Diesel, and Biodiesel Passenger Vehicles and Their Relation to Oxidative Potential. Aerosol Science and Technology 2010; 44(7):500-513.
25. Liati A, Schreiber D, Dimopoulos Eggenschwiler P, Arroyo Rojas Dasilva Y. Metal Particle Emissions in the Exhaust Stream of Diesel Engines: An Electron Microscope Study. Environmental Science & Technology 2013; 47(24):14495-14501.
26. Lough GC, Schauer JJ, Park J-S, Shafer MM, DeMinter JT, Weinstein JP. Emissions of Metals Associated with Motor Vehicle Roadways. Environmental Science & Technology 2005; 39(3):826-836.
27. Olivier JC, Schure KM, Peter JA. Trends in global CO2 and total greenhouse emissions. In: PBL, Netherlands Environmental Assenssment Agency; 2017.
28. IPCC. Fifth Assessment Report: Climate Change 2013: The Physical Science Basis, Contribution of Working Group I to the Fifth Assessment Report of the Intergovernmental Panel on Climate Change. In.

doi:10.1017/CBO9781107415324.016 ed: edited by: Stocker, T. F., Qin, D., Plattner, G.K., Tignor, M., Allen, S. K., Doschung, J., Nauels, A., Xia,Y., Bex, V., and Midgley, P. M.; 2013.
29. EEA. Air quality in Europe. In: EEA; 2017.
30. Grelier F. CO2 emissions from car: the facts. In. European Federation for Transport and Environment; 2018.
31. TERM. Fundamental changes needed for sustainable mobility. In: Transport and Environment Reporting Mechanism (TERM), European Environmental Agency; 2016.
32. Lackner KS, Brennan S, Matter JM, Park AHA, Wright A, van der Zwaan B. The urgency of the development of CO₂ capture from ambient air. Proceedings of the National Academy of Sciences 2012; 109(33):13156.
33. Graves C, Ebbesen SD, Mogensen M, Lackner KS. Sustainable hydrocarbon fuels by recycling CO2 and H2O with renewable or nuclear energy. Renewable and Sustainable Energy Reviews 2011; 15(1):1-23.
34. Rose JJ, Wang L, Xu Q, McTiernan CF, Shiva S, Tejero J, et al. Carbon Monoxide Poisoning: Pathogenesis, Management, and Future Directions of Therapy. American Journal of Respiratory and Critical Care Medicine 2016; 195(5):596-606.
35. Reşitoğlu İA, Altinişik K, Keskin A. The pollutant emissions from diesel-engine vehicles and exhaust aftertreatment systems. Clean Technologies and Environmental Policy 2015; 17(1):15-27.
36. Heywood J. Internal Combustion Fundamentals. In: McGraw-Hill; ISBN 0-07-100499-8; 1988.
37. Huang T, Zhu X, Zhong Q, Yun X, Meng W, Li B, et al. Spatial and Temporal Trends in Global Emissions of Nitrogen Oxides from 1960 to 2014. Environ Sci Technol 2017; 51(14):7992-8000.
38. Parungo F, Nagamoto C, Maddl R. A Study of the Mechanisms of Acid Rain Formation. Journal of the Atmospheric Sciences 1987; 44(21):3162-3174.
39. Olatunji SO, Fakinle BS, Jimoda LA, Adeniran JA, Adesanmi AJ. Air Emissions of Sulphur Dioxide From Gasoline and Diesel Consumption in the Southwestern States of Nigeria. Petroleum Science and Technology 2015; 33(6):678-685.
40. 2009/30/EC D. Directive 2009/30/EC of the European Parliament and of the Council of 23 April 2009 amending Directive 98/70/EC as regards the specification of petrol, diesel and gas-oil and introducing a mechanism to monitor and reduce greenhouse gas emissions and amending Council Directive 1999/32/EC as regards the specification of fuel used by inland waterway vessels and repealing Directive 93/12/EEC. In. Official Journal of the European Union; 2009.
41. Beck DD. Impact of sulfur on three-way automotive catalyst performance and catalyst diagnostics. In: Studies in Surface Science and Catalysis. Bartholomew CH, Fuentes GA (editors): Elsevier; 1997. pp. 21-38.
42. Truex TJ. Interaction of Sulfur with Automotive Catalysts and the Impact on Vehicle Emissions-A Review. SAE Transactions 1999; 108:1192-1206.
43. Summers JC, Skowron JF, Williamson WB, Mitchell KI. Fuel Sulfur Effects on Automotive Catalyst Performance. In: SAE International; 1992.
44. Yu F, Luo G. Simulation of particle size distribution with a global aerosol model: contribution of nucleation to aerosol and CCN number concentrations. Atmos Chem Phys 2009; 9(20):7691-7710.
45. Ayers GP, Gillett RW, Gras JL. On the vapor pressure of sulfuric acid. Geophysical Research Letters 1980; 7(6):433-436.
46. Kulmala M, Korhonen P, Napari I, Karlsson A, Berresheim H, O'Dowd CD. Aerosol formation during PARFORCE: Ternary nucleation of H2SO4, NH3, and H2O. Journal of Geophysical Research-Atmospheres 2002; 107(D19):11.
47. Curtius J. Nucleation of atmospheric aerosol particles. Comptes Rendus Physique 2006; 7(9):1027-1045.
48. Likens GE, Bormann FH. Acid Rain: A Serious Regional Environmental Problem. Science 1974; 184(4142):1176.
49. Menz FC, Seip HM. Acid rain in Europe and the United States: an update. Environmental Science & Policy 2004; 7(4):253-265.
50. Alves CA, Lopes DJ, Calvo AI, Evtyugina M, Rocha S, Nunes T. Emissions from Light-Duty Diesel and Gasoline In-Use Vehicles Measured on Chassis Dynamometer Test Cycles. Aerosol and Air Quality Research 2015; 15(1):99-116.
51. Fontaras G, Franco V, Dilara P, Martini G, Manfredi U. Development and review of Euro 5 passenger car emission factors based on experimental results over various driving cycles. Science of the Total Environment 2014; 468:1034-1042.
52. Ko J, Jin D, Jang W, Myung CL, Kwon S, Park S. Comparative investigation of NOx emission characteristics from a Euro 6-compliant diesel passenger car over the NEDC and WLTC at various ambient temperatures. Applied Energy 2017; 187:652-662.
53. Köhler F. Testing of particulate emissions from positive ignition vehicles with direct fuel injection system. In. Technical Report, Institut für Fahrzeugtechnik und Mobilität; 2013.
54. Ensberg JJ, Hayes PL, Jimenez JL, Gilman JB, Kuster WC, de Gouw JA, et al. Emission factor ratios, SOA mass yields, and the impact of vehicular emissions on SOA formation. Atmos Chem Phys 2014; 14(5):2383-2397.
55. Lu Q, Zhao Y, Robinson AL. Comprehensive organic emission profiles for gasoline, diesel, and gas-turbine engines including intermediate and semi-volatile organic compound emissions. Atmos Chem Phys 2018; 18(23):17637-17654.

56. Dunmore RE, Hopkins JR, Lidster RT, Lee JD, Evans MJ, Rickard AR, et al. Diesel-related hydrocarbons can dominate gas phase reactive carbon in megacities. Atmospheric Chemistry and Physics 2015; 15(17):9983-9996.
57. Martinet S, Liu Y, Louis C, Tassel P, Perret P, Chaumond A, et al. Euro 6 Unregulated Pollutant Characterization and Statistical Analysis of After-Treatment Device and Driving-Condition Impact on Recent Passenger-Car Emissions. Environmental Science & Technology 2017; 51(10):5847-5855.
58. Pang YB, Fuentes M, Rieger P. Trends in the emissions of Volatile Organic Compounds (VOCs) from light-duty gasoline vehicles tested on chassis dynamometers in Southern California. Atmospheric Environment 2014; 83:127-135.
59. Vlachokostas C, Chourdakis E, Michalidou AV, Moussiopoulos N, Kelessis A, Petrakakis M. Establishing relationships between chemical health stressors in urban traffic environments: Prediction of toluene concentration levels in European cities. Atmospheric Environment 2012; 55:299-310.
60. Kislov VV, Sadovnikov AI, Mebel AM. Formation Mechanism of Polycyclic Aromatic Hydrocarbons beyond the Second Aromatic Ring. The Journal of Physical Chemistry A 2013; 117(23):4794-4816.
61. Suarez-Bertoa R, Zardini AA, Keuken H, Astorga C. Impact of ethanol containing gasoline blends on emissions from a flex-fuel vehicle tested over the Worldwide Harmonized Light duty Test Cycle (WLTC). Fuel 2015; 143:173-182.
62. Clairotte M, Adam TW, Zardini AA, Manfredi U, Martini G, Krasenbrink A, et al. Effects of low temperature on the cold start gaseous emissions from light duty vehicles fuelled by ethanol-blended gasoline. Applied Energy 2013; 102:44-54.
63. Suarez-Bertoa R, Zardini AA, Lilova V, Meyer D, Nakatani S, Hibel F, et al. Intercomparison of real-time tailpipe ammonia measurements from vehicles tested over the new world-harmonized light-duty vehicle test cycle (WLTC). Environmental Science and Pollution Research 2015; 22(10):7450-7460.
64. Suarez-Bertoa R, Astorga C. Isocyanic acid and ammonia in vehicle emissions. Transportation Research Part D-Transport and Environment 2016; 49:259-270.
65. Sekimoto K, Inomata S, Tanimoto H, Fushimi A, Fujitani Y, Sato K, et al. Characterization of nitromethane emission from automotive exhaust. Atmospheric Environment 2013; 81:523-531.
66. Sun K, Tao L, Miller DJ, Pan D, Golston LM, Zondlo MA, et al. Vehicle Emissions as an Important Urban Ammonia Source in the United States and China. Environmental Science & Technology 2017; 51(4):2472-2481.
67. Borsari V, Assunção JVd. Ammonia emissions from a light-duty vehicle. Transportation Research Part D: Transport and Environment 2017; 51:53-61.
68. Moussa SG, Leithead A, Li S-M, Chan TW, Wentzell JJB, Stroud C, et al. Emissions of hydrogen cyanide from on-road gasoline and diesel vehicles. Atmospheric Environment 2016; 131:185-195.
69. EEA. Outdoor air quality in urban areas. In. Environmental European Agency; 2017.
70. Lee PK, Brook JR, Dabek-Zlotorzynska E, Mabury SA. Identification of the major sources contributing to PM2.5 observed in Toronto. Environ Sci Technol 2003; 37(21):4831-4840.
71. Gentner DR, Worton DR, Isaacman G, Davis LC, Dallmann TR, Wood EC, et al. Chemical Composition of Gas-Phase Organic Carbon Emissions from Motor Vehicles and Implications for Ozone Production. Environmental Science & Technology 2013; 47(20):11837-11848.
72. Suarez-Bertoa R, Astorga C. Impact of cold temperature on Euro 6 passenger car emissions. Environmental Pollution 2018; 234:318-329.
73. ECE. WLTP. In: ECE/TRANS/WP.29/2016/69; 2016.
74. Gelso ER, Dahl J. Diesel Engine Control with Exhaust Aftertreatment Constraints. IFAC-PapersOnLine 2017; 50(1):8921-8926.
75. Yu RC, Cole AS, Stroia BJ, Huang SC, Howden K, Chalk S. Development of Diesel Exhaust Aftertreatment System for Tier II Emissions. In: SAE International; 2002.
76. Lox ES, Engler BH, Koberstein E. Diesel Emission Control. In: Studies in Surface Science and Catalysis. Crucq A (editor): Elsevier; 1991. pp. 291-321.
77. Bugarski AD, Schnakenberg JGH, Hummer JA, Cauda E, Janisko SJ, Patts LD. Effects of Diesel Exhaust Aftertreatment Devices on Concentrations and Size Distribution of Aerosols in Underground Mine Air. Environmental Science & Technology 2009; 43(17):6737-6743.
78. Saliba G, Saleh R, Zhao YL, Presto AA, Larnbe AT, Frodin B, et al. Comparison of Gasoline Direct-Injection (GDI) and Port Fuel Injection (PFI) Vehicle Emissions: Emission Certification Standards, Cold-Start, Secondary Organic Aerosol Formation Potential, and Potential Climate Impacts. Environmental Science & Technology 2017; 51(11):6542-6552.
79. Kim Y, Kim Y, Jun S, Lee KH, Rew S, Lee D, et al. Strategies for Particle Emissions Reduction from GDI Engines. In: SAE International; 2013.
80. Wiebenga MH, Kim CH, Schmieg SJ, Oh SH, Brown DB, Kim DH, et al. Deactivation mechanisms of Pt/Pd-based diesel oxidation catalysts. Catalysis Today 2012; 184(1):197-204.
81. Nagai YFNaTHaSYaHTaKDaTNaY. Study of coordination environments around Pd and Pt in a Pd-core Pt-shell nanoparticle during heating. Journal of Physics: Conference Series 2016; 712(1):012067.
82. Nishimura YF, Hamaguchi T, Yamaguchi S, Takagi H, Dohmae K, Nonaka T, et al. Study of coordination environments around Pd and Pt in a Pd-core Pt-shell nanoparticle during heating. Journal of Physics: Conference Series 2016; 712(1):012067.
83. Wang TJ, Baek SW, Lee J-H. Kinetic Parameter Estimation of a Diesel Oxidation Catalyst under Actual Vehicle Operating Conditions. Industrial & Engineering Chemistry Research 2008; 47(8):2528-2537.

84. Zhu L, Cheung CS, Zhang WG, Fang JH, Huang Z. Effects of ethanol–biodiesel blends and diesel oxidation catalyst (DOC) on particulate and unregulated emissions. Fuel 2013; 113:690-696.
85. Geller MD, Ntziachristos L, Mamakos A, Samaras Z, Schmitz DA, Froines JR, et al. Physicochemical and redox characteristics of particulate matter (PM) emitted from gasoline and diesel passenger cars. Atmospheric Environment 2006; 40(36):6988-7004.
86. Beatrice C, Iorio SD, Guido C, Napolitano P. Detailed characterization of particulate emissions of an automotive catalyzed DPF using actual regeneration strategies. Experimental Thermal and Fluid Science 2012; 39:45-53.
87. Köhler F. Testing of particulate emissions from positive ignition vehicles with direct fuel injection system, technical report. In: www.transportenvironment.org; 2013.
88. Choi S, Oh K-C, Lee C-B. The effects of filter porosity and flow conditions on soot deposition/oxidation and pressure drop in particulate filters. Energy 2014; 77:327-337.
89. Mokhri MA, Abdullah NR, Abdullah SA, Kasalong S, Mamat R. Soot Filtration Recent Simulation Analysis in Diesel Particulate Filter (DPF). Procedia Engineering 2012; 41:1750-1755.
90. Sappok A, Wong V. Ash Effects on Diesel Particulate Filter Pressure Drop Sensitivity to Soot and Implications for Regeneration Frequency and DPF Control. SAE International Journal of Fuels and Lubricants 2010; 3(1):380-396.
91. Fino D, Specchia V. Open issues in oxidative catalysis for diesel particulate abatement. Powder Technology 2008; 180(1):64-73.
92. Di Sarli V, Di Benedetto A. Modeling and simulation of soot combustion dynamics in a catalytic diesel particulate filter. Chemical Engineering Science 2015; 137:69-78.
93. van Setten BAAL, Makkee M, Moulijn JA. Science and technology of catalytic diesel particulate filters. Catalysis Reviews 2001; 43(4):489-564.
94. Twigg MV, A.J.J. Wilkins, N.S. Will Emission Control. In. US6294141 (B1); 2001.
95. Setiabudi A, Makkee M, Moulijn JA. The role of NO2 and O2 in the accelerated combustion of soot in diesel exhaust gases. Applied Catalysis B: Environmental 2004; 50(3):185-194.
96. Majewski WA, Khair MK. Diesel emissions and their control. In: SAE Technical Paper; 2006.
97. Song J, Wang J, Boehman AL. The role of fuel-borne catalyst in diesel particulate oxidation behavior. Combust Flame 2006; 146(1–2):73-84.
98. Ntziachristos L, Samaras Z, Zervas E, Dorlhène P. Effects of a catalysed and an additized particle filter on the emissions of a diesel passenger car operating on low sulphur fuels. Atmos Environ 2005; 39(27):4925-4936.
99. König A, Herding G, Hupfeld B, Richter T, Weidmann K. Current Tasks and Challenges for Exhaust Aftertreatment Research. A Viewpoint from the Automotive Industry. Topics in Catalysis 2001; 16(1):23-31.
100. Piazzesi G, Krocher O, Elsener M, Wokaun A. Adsorption and hydrolysis of isocyanic acid on TiO2. Applied Catalysis B-Environmental 2006; 65(1-2):55-61.
101. Yim SD, Kim SJ, Baik JH, Nam IS, Mok YS, Lee J-H, et al. Decomposition of Urea into NH3 for the SCR Process. Industrial & Engineering Chemistry Research 2004; 43(16):4856-4863.
102. Pieterse JAZ, Top H, Vollink F, Hoving K, van den Brink RW. Selective catalytic reduction of NOx in real exhaust gas of gas engines using unburned gas: Catalyst deactivation and advances toward long-term stability. Chemical Engineering Journal 2006; 120(1):17-23.
103. Sala MBaR. A study on the indirect urea dosing method in the Selective Catalytic Reduction system. IOP Conference Series: Materials Science and Engineering 2016; 148(1):012062.
104. Johnson TV. Review of Vehicular Emissions Trends. SAE Int J Engines 2015; 8(3):1152-1167.
105. Kondratenko VA, Baerns M. Mechanistic insights into the formation of N2O and N2 in NO reduction by NH3 over a polycrystalline platinum catalyst. Applied Catalysis B: Environmental 2007; 70(1):111-118.
106. Zhu Y, Hou Q, Shreka M, Yuan L, Zhou S, Feng Y, et al. Ammonium-salt formation and catalyst deactivation in the SCR system for a marine diesel engine. In: Catalysts; 2018.
107. Falk C. Ammonium Sulphate Deactivation of SCR DeNOx Catalysts. In: Department of Chemical Engineering, Lund Institute of Technology; 2007.
108. Guillén Hurtado N, Rico Pérez V, Garcia-Garcia A, Lozano Castelló D, Bueno López A. Three-way catalysts: past, present and future.
109. Yan S, Song T, Liu T. A Study of Three-Way Catalyst Deterioration Monitoring. In: Proceedings of SAE-China Congress 2016: Selected Papers. Singapore: Springer Singapore; 2017. pp. 637-646.
110. Bielaczyc P, Szczotka A, Woodburn J. The effect of a low ambient temperature on the cold-start emissions and fuel consumption of passenger cars. Proceedings of the Institution of Mechanical Engineers, Part D: Journal of Automobile Engineering 2011; 225(9):1253-1264.
111. Zhu R, Hu J, Bao X, He L, Zu L. Effects of aromatics, olefins and distillation temperatures (T50 & T90) on particle mass and number emissions from gasoline direct injection (GDI) vehicles. Energy Policy 2017; 101:185-193.
112. Chincholkar SP, Suryawanshi JG. Gasoline Direct Injection: An Efficient Technology. Energy Procedia 2016; 90:666-672.
113. Zhang S, McMahon W. Particulate Emissions for LEV II Light-Duty Gasoline Direct Injection Vehicles. SAE Int J Fuels Lubr 2012; 5(2):637-646.

114. Zimmerman N, Wang JM, Jeong C-H, Ramos M, Hilker N, Healy RM, et al. Field Measurements of Gasoline Direct Injection Emission Factors: Spatial and Seasonal Variability. Environmental Science & Technology 2016; 50(4):2035-2043.
115. Mohr M, Forss AM, Lehmann U. Particle emissions from diesel passenger cars equipped with a particle trap in comparison to other technologies. Environmental Science & Technology 2006; 40(7):2375-2383.
116. Zervas E, Dorlhène P, Daviau R, Dionnet B. Repeatability of Fine Particle Measurement of Diesel and Gasoline Vehicles Exhaust Gas. In: SAE International; 2004.
117. Sementa P, Maria Vaglieco B, Catapano F. Thermodynamic and optical characterizations of a high performance GDI engine operating in homogeneous and stratified charge mixture conditions fueled with gasoline and bio-ethanol. Fuel 2012; 96:204-219.
118. Maricq MM, Podsiadlik DH, Chase RE. Examination of the Size-Resolved and Transient Nature of Motor Vehicle Particle Emissions. Environmental Science & Technology 1999; 33(10):1618-1626.
119. Bonandrini G, Di Gioia R, Papaleo D, Venturoli L. Numerical Study on Multiple Injection Strategies in DISI Engines for Particulate Emission Control. In: SAE International; 2012.
120. Chen LF, Liang ZR, Zhang X, Shuai SJ. Characterizing particulate matter emissions from GDI and PFI vehicles under transient and cold start conditions. Fuel 2017; 189:131-140.
121. Lambert C, Chanko T, Dobson D, Liu X, Pakko J. Gasoline Particle Filter Development. Emission Control Science and Technology 2017; 3(1):105-111.
122. Hashimoto S, Miyairi Y, Hamanaka T, Matsubara R, Harada T, Miwa S. SiC and Cordierite Diesel Particulate Filters Designed for Low Pressure Drop and Catalyzed, Uncatalyzed Systems. In: SAE International; 2002.
123. Andreata M, Millo F, Mallamo F, Mercuri D, Pozzi C. Experimental Investigation on Three Different Ceramic Substrate Materials for a Diesel Particulate Filter. In: SAE International; 2013.
124. Esteves-Booth A, Muneer T, Kubie J, Kirby H. A review of vehicular emission models and driving cycles. Proceedings of the Institution of Mechanical Engineers, Part C: Journal of Mechanical Engineering Science 2002; 216(8):777-797.
125. Gkatzoflias D, Kouridis C, Ntziachristos L, Samaras Z. COPERT 4: Computer programme to calculate emissions from road transport. In: European Environment Agency; 2006.
126. Franco Garcia V. Evaluation and improvements of road vehicle pollutant emission factors based on instantaneous emissions data processing. In: School of Technology and Experimental Sciences-Jaume I university; 2014.
127. Levy H, Moxim WJ. Examining the Global Impact of Local/Regional Air Pollution: The Role of Global Chemical Transport Models. In: Air Pollution Modeling and Its Application VII. van Dop H (editor). Boston, MA: Springer US; 1989. pp. 139-157.
128. Thunis P, Miranda A, Baldasano JM, Blond N, Douros J, Graff A, et al. Overview of current regional and local scale air quality modelling practices: Assessment and planning tools in the EU. Environmental Science & Policy 2016; 65:13-21.
129. EPA. Photochemical smog: what it means for us. In: Environmental Protection Authority; 2004.
130. White WH. Reduction of visibility by sulphates in photochemical smog. Nature 1976; 264:735.
131. Moussiopoulos N, Sahm P, Kessler C. Numerical simulation of photochemical smog formation in Athens, Greece—A case study. Atmospheric Environment 1995; 29(24):3619-3632.
132. Wang J, Zhang J-s, Liu Z-j, Wu J-h, Zhang Y-f, Han S-q, et al. Characterization of chemical compositions in size-segregated atmospheric particles during severe haze episodes in three mega-cities of China. Atmospheric Research 2017; 187:138-146.
133. Deng H, Tan H, Li F, Cai M, Chan PW, Xu H, et al. Impact of relative humidity on visibility degradation during a haze event: A case study. Sci Total Environ 2016; 569-570:1149-1158.
134. Ma N, Zhao C, Chen J, Xu W, Yan P, Zhou X. A novel method for distinguishing fog and haze based on PM2.5, visibility, and relative humidity. Science China Earth Sciences 2014; 57(9):2156-2164.
135. Collins CO, Scott SL. Air Pollution in the Valley of Mexico. Geographical Review 1993; 83(2):119-133.
136. Gupta A. Effect of Air Pollutants on Plant Gaseous Exchange Process: Effect on Stomata and Respiration. In: Plant Responses to Air Pollution. Kulshrestha U, Saxena P (editors). Singapore: Springer Singapore; 2016. pp. 85-92.
137. Janhäll S. Review on urban vegetation and particle air pollution – Deposition and dispersion. Atmospheric Environment 2015; 105:130-137.
138. Rai R, Agrawal M. Impact of Tropospheric Ozone on Crop Plants. Proceedings of the National Academy of Sciences, India Section B: Biological Sciences 2012; 82(2):241-257.
139. EEA. Eutrophication of terrestrial ecosystems due to air pollution. In: European Environmental Agency; 2017.
140. Bouwman AF, Van Vuuren DP, Derwent RG, Posch M. A Global Analysis of Acidification and Eutrophication of Terrestrial Ecosystems. Water, Air, and Soil Pollution 2002; 141(1):349-382.
141. Smith VH, Tilman GD, Nekola JC. Eutrophication: impacts of excess nutrient inputs on freshwater, marine, and terrestrial ecosystems. Environmental Pollution 1999; 100(1):179-196.
142. Hippeli S, Elstner EF. Effects of air pollutants on man, animals, plants and buildings: mechanisms and dose-response effects. In: Studies in Environmental Science. Vernet JP (editor): Elsevier; 1993. pp. 13-22.
143. Twomey S. Pollution and the planetary albedo. Atmospheric Environment (1967) 1974; 8(12):1251-1256.
144. IHME H. State of global air. In; 2017.
145. SCOR. Health impact of air pollution. In: SCOR global life; 2018.

146. Pope CA. Epidemiology of fine particulate air pollution and human health: Biologic mechanisms and who's at risk? Environmental Health Perspectives 2000; 108:713-723.
147. Pope CA, Burnett RT, Thun MJ, Calle EE, Krewski D, Ito K, et al. Lung cancer, cardiopulmonary mortality, and long-term exposure to fine particulate air pollution. Jama-Journal of the American Medical Association 2002; 287(9):1132-1141.
148. Sun H, Shamy M., Kluz T, Mu ñ oz AB, Zhong M, Laulicht F, et al. Gene expression profiling and pathway analysis of human bronchial epithelial cells exposed to airborne particulate matter collected from Saudi Arabia. In: Toxicology and Applied Pharmacology; 2012. pp. 147-157.
149. Kelly FJ, Fussel JC. Size, source and chemical composition as determinants of toxicity attributable to ambient particulate matter. In: Atmospheric Environment; 2012. pp. 504-526.
150. Merbitz H, Buttstädt M, Michael S., Dott W, Schneider C. GIS-based identification of spatial variables enhancing heat and poor air quality in urban areas. In: Applied Geography; 2012. pp. 94-106.
151. Kampa M, Castanas E. Human health effects of air pollution. Environmental Pollution 2008; 151(2):362-367.
152. Medina, S., Pascal M, Tillier C. Impacts de l'exposition chronique aux particules fines sur la mortalité en France continentale et analyse des gains en santé de plusieurs scénarios de réduction de la pollution atmosphérique. In: S.-M. S. p. France, p. p.12; 2016.
153. Jedrychowski, Wieslaw, Ivona Bendkowska, Elzbieta Flak, Agnieszka Penar, Ryszard Jacek, et al. Estimated Risk for Altered Fetal Growth Resulting from Exposure to Fine Particles during Pregnancy: An Epidemiologic Prospective Cohort Study in Poland. In: Environmental Health Perspectives; 2004. pp. 1398-1402.
154. WHO. Review of evidence on health aspects of air pollution. In. Copenhagen ed. RE-VIHAAP Project: World Health Organisation, WHO RegionalOffice for Europe,; 2013.
155. Carré J, Gatimel N, Moreau J, Parinaud J, Léandri R. Does air pollution play a role in infertility?: a systematic review. Environmental Health 2017; 16(1):82.
156. Frutos V, Gonzalez-Comadran M, Sola I, Jacquermin B, Carreras R., Checa Vizcaino MA. Impact of air pollution on fertility: a systematic review. In: Gynecological Endocrinology; 2014.
157. Bowe B, Xie Y, Li T, Yan Y, Xian H, Al-Aly Z. The Lancet Planetary Health 2018; 2(7):e301-e312.
158. Dzhambov AM. Ambient air pollution and diabetes in China. The Lancet Planetary Health 2018; 2(2):e52-e53.
159. Sonnenschein-van der Voort AMM, Arends LR, de Jongste JC, Annesi-Maesano I, Arshad SH, Barros H, et al. Preterm birth, infant weight gain, and childhood asthma risk: A meta-analysis of 147,000 European children. The Journal of Allergy and Clinical Immunology 2014; 133(5):1317-1329.
160. Gehring U, Wijga AH, Hoek G, Bellander T, Berdel D, Brüske I, et al. Exposure to air pollution and development of asthma and rhinoconjunctivitis throughout childhood and adolescence: a population-based birth cohort study. The Lancet Respiratory Medicine 2015; 3(12):933-942.
161. Risom L, Moller P, Loft S. Oxidative stress-induced DNA damage by particulate air pollution. Mutat Res 2005; 592(1-2):119-137.
162. Bräuner EV, Forchhammer L, Møller P, Simonsen J, Glasius M, Wåhlin P, et al. Exposure to Ultrafine Particles from Ambient Air and Oxidative Stress–Induced DNA Damage. Environmental Health Perspectives 2007; 115(8):1177-1182.
163. Vaiserman A. Epidemiologic evidence for association between adverse environmental exposures in early life and epigenetic variation: a potential link to disease susceptibility? Clinical Epigenetics 2015; 7(1):96.
164. Cantone L, Iodice S, Tarantini L, Albetti B, Restelli I, Vigna L, et al. Particulate matter exposure is associated with inflammatory gene methylation in obese subjects. Environmental Research 2017; 152:478-484.
165. Underwood E. The polluted brain. Science 2017; 355(6323):342-345.
166. Künzi L, Krapf M, Daher N, Dommen J, Jeannet N, Schneider S, et al. Toxicity of aged gasoline exhaust particles to normal and diseased airway epithelia. Scientific Reports 2015; 5:11801.
167. Calderón-Garcidueñas L, Villarreal-Ríos R. Living close to heavy traffic roads, air pollution, and dementia. The Lancet 2017; 389(10070):675-677.
168. Silverman DT, Samanic CM, Lubin JH, Blair AE, Stewart PA, Vermeulen R, et al. The Diesel Exhaust in Miners study: a nested case-control study of lung cancer and diesel exhaust. J Natl Cancer Inst 2012; 104(11):855-868.
169. McClellan RO. Re: The diesel exhaust in miners study: a nested case-control study of lung cancer and diesel exhaust, a cohort mortality study with emphasis on lung cancer, and the problem with diesel. In: J Natl Cancer Inst. United States; 2012. pp. 1843-1845; author reply 1847-1849.
170. WHO. Air quality guidelines. In: World Health Organization; 2000.
171. Churg A, Brauer M, del Carmen Avila-Casado M, Fortoul TI, Wright JL. Chronic exposure to high levels of particulate air pollution and small airway remodeling. Environmental Health Perspectives 2003; 111(5):714-718.
172. Sturm R. Total deposition of ultrafine particles in the lungs of healthy men and women: experimental and theoretical results. Annals of translational medicine 2016; 4(12):234-234.
173. Elder A, Oberdorster G. Translocation and effects of ultrafine particles outside of the lung. Clin Occup Environ Med 2006; 5(4):785-796.
174. Oberdorster G, Sharp Z, Atudorei V, Elder A, Gelein R, Kreyling W, et al. Translocation of inhaled ultrafine particles to the brain. Inhal Toxicol 2004; 16(6-7):437-445.

175. Peters A, Veronesi B, Calderón-Garcidueñas L, Gehr P, Chen LC, Geiser M, et al. Translocation and potential neurological effects of fine and ultrafine particles a critical update. Particle and Fibre Toxicology 2006; 3:13-13.
176. HEI. Characterization of Metals Emitted from Motor Vehicles. In. HEI, research report 133; 2006.
177. WHO. Health Risks of Heavy Metals from Long range Transboundary Air Pollution. In. WHO Regional Office for Europe, Copenhagen, Denmark, ISBN 978 92 890 7179 6.; 2007.
178. Gozubuyuk AA, Dag H, Kacar A, Karakurt Y, Arica V. Epidemiology, pathophysiology, clinical evaluation, and treatment of carbon monoxide poisoning in child, infant, and fetus. Northern clinics of Istanbul 2017; 4(1):100-107.
179. César ACG, Carvalho JA, Jr., Nascimento LFC. Association between NOx exposure and deaths caused by respiratory diseases in a medium-sized Brazilian city. Brazilian journal of medical and biological research = Revista brasileira de pesquisas medicas e biologicas 2015; 48(12):1130-1135.
180. Munawer ME. Human health and environmental impacts of coal combustion and post-combustion wastes. Journal of Sustainable Mining 2018; 17(2):87-96.
181. IARC. IARC classifies formaldehyde as carcinogenic to humans. In. Press release: International Agency for Research on Cancer; 2004.
182. IARC. Benzene. In. Press release: IARC monographs; 2012.
183. Goriaux M. Étude des artefacts de prélèvement et de la distribution gaz-particules des HAP. In: Océan, Atmosphère. Université de Provence - Aix-Marseille I; 2006.
184. Tongo I, Ogbeide O, Ezemonye L. Human health risk assessment of polycyclic aromatic hydrocarbons (PAHs) in smoked fish species from markets in Southern Nigeria. Toxicology reports 2016; 4:55-61.
185. Franco SS, Nardocci AC, Gunther WM. PAH biomarkers for human health risk assessment: a review of the state-of-the-art. Cad Saude Publica 2008; 24 Suppl 4:s569-580.
186. Wang C, Zhou S, Song J, Wu S. Human health risks of polycyclic aromatic hydrocarbons in the urban soils of Nanjing, China. Sci Total Environ 2018; 612:750-757.
187. Kovacic P, Somanathan R. Nitroaromatic compounds: Environmental toxicity, carcinogenicity, mutagenicity, therapy and mechanism. J Appl Toxicol 2014; 34(8):810-824.
188. Isayev O, Rasulev B, Gorb L, Leszczynski J. Structure-toxicity relationships of nitroaromatic compounds. Mol Divers 2006; 10(2):233-245.
189. UNO. Towards a pollution-free planet. In: UNO environment assembly; 2017.
190. OCDE. Les conséquences économiques de la pollution de l'air extérieur. In: OCDE; 2016.
191. Seinfeld J, Pandis S. Atmospheric Chemistry and Physics: From Air Pollution to Climate Change. In. New York: Wiley; 1998.
192. Chameides WL, Fehsenfeld F, Rodgers MO, Cardelino C, Martinez J, Parrish D, et al. Ozone precursor relationships in the ambient atmosphere. Journal of Geophysical Research: Atmospheres 1992; 97(D5):6037-6055.
193. Parrish DD, Trainer M, Williams EJ, Fahey DW, Hübler G, Eubank CS, et al. Measurements of the NO x -O3 photostationary state at Niwot Ridge, Colorado. Journal of Geophysical Research: Atmospheres 1986; 91(D5):5361-5370.
194. Zhang N, Zhou X, Bertman S, Tang D, Alaghmand M, Shepson PB, et al. Measurements of ambient HONO concentrations and vertical HONO flux above a northern Michigan forest canopy. Atmos Chem Phys 2012; 12(17):8285-8296.
195. Acker K, Möller D, Wieprecht W, Meixner FX, Bohn B, Gilge S, et al. Strong daytime production of OH from HNO2 at a rural mountain site. Geophysical Research Letters 2006; 33(2).
196. Orlando JJ, Tyndall GS, Wallington TJ. The Atmospheric Chemistry of Alkoxy Radicals. Chemical Reviews 2003; 103(12):4657-4690.
197. Atkinson R, Arey J. Atmospheric degradation of volatile organic compounds. Chemical Reviews 2003; 103(12):4605-4638.
198. Vinciguerra T, Bull E, Canty T, He H, Zalewsky E, Woodman M, et al. Expected ozone benefits of reducing nitrogen oxide (NOx) emissions from coal-fired electricity generating units in the eastern United States. Journal of the Air & Waste Management Association 2017; 67(3):279-291.
199. Hidy GM, Blanchard CL. Precursor reductions and ground-level ozone in the Continental United States. J Air Waste Manag Assoc 2015; 65(10):1261-1282.
200. Jhang S-R, Chen K-S, Lin S-L, Lin Y-C, Amesho KTT, Chen C-B. Evaluation of the reduction in carbonyl emissions and ozone formation potential from the exhaust of a heavy-duty diesel engine by hydrogen-diesel dual fuel combustion. Applied Thermal Engineering 2018; 132:586-594.
201. Wood EC, Canagaratna MR, Herndon SC, Onasch TB, Kolb CE, Worsnop DR, et al. Investigation of the correlation between odd oxygen and secondary organic aerosol in Mexico City and Houston. Atmos Chem Phys 2010; 10(18):8947-8968.
202. Wagner V, Jenkin ME, Saunders SM, Stanton J, Wirtz K, Pilling MJ. Modelling of the photooxidation of toluene: conceptual ideas for validating detailed mechanisms. Atmospheric Chemistry and Physics 2003; 3:89-106.
203. Zhang Q, Jimenez JL, Canagaratna MR, Ulbrich IM, Ng NL, Worsnop DR, et al. Understanding atmospheric organic aerosols via factor analysis of aerosol mass spectrometry: a review. Analytical and Bioanalytical Chemistry 2011; 401(10):3045-3067.
204. Jimenez JL, Canagaratna MR, Donahue NM, Prevot ASH, Zhang Q, Kroll JH, et al. Evolution of Organic Aerosols in the Atmosphere. Science 2009; 326(5959):1525.

205. Guenther A, Karl T, Harley P, Wiedinmyer C, Palmer PI, Geron C. Estimates of global terrestrial isoprene emissions using MEGAN (Model of Emissions of Gases and Aerosols from Nature). Atmospheric Chemistry and Physics 2006; 6:3181-3210.
206. Tsigaridis K, Kanakidou M. Secondary organic aerosol importance in the future atmosphere. Atmospheric Environment 2007; 41(22):4682-4692.
207. Gentner DR, Isaacman G, Worton DR, Chan AWH, Dallmann TR, Davis L, et al. Elucidating secondary organic aerosol from diesel and gasoline vehicles through detailed characterization of organic carbon emissions. Proceedings of the National Academy of Sciences 2012; 109(45):18318.
208. Zhao Y, Lambe AT, Saleh R, Saliba G, Robinson AL. Secondary Organic Aerosol Production from Gasoline Vehicle Exhaust: Effects of Engine Technology, Cold Start, and Emission Certification Standard. Environmental Science & Technology 2018; 52(3):1253-1261.
209. Tsigaridis K, Daskalakis N, Kanakidou M, Adams PJ, Artaxo P, Bahadur R, et al. The AeroCom evaluation and intercomparison of organic aerosol in global models. Atmos Chem Phys 2014; 14(19):10845-10895.
210. Bergström R, Denier van der Gon HAC, Prévôt ASH, Yttri KE, Simpson D. Modelling of organic aerosols over Europe (2002–2007) using a volatility basis set (VBS) framework: application of different assumptions regarding the formation of secondary organic aerosol. Atmos Chem Phys 2012; 12(18):8499-8527.
211. Odum JR, Hoffmann T, Bowman F, Collins D, Flagan RC, Seinfeld JH. Gas/particle partitioning and secondary organic aerosol yields. Environmental Science & Technology 1996; 30(8):2580-2585.
212. Huang W, Saathoff H, Pajunoja A, Shen XL, Naumann KH, Wagner R, et al. alpha-Pinene secondary organic aerosol at low temperature: chemical composition and implications for particle viscosity. Atmospheric Chemistry and Physics 2018; 18(4):2883-2898.
213. Kristensen K, Jensen LN, Glasius M, Bilde M. The effect of sub-zero temperature on the formation and composition of secondary organic aerosol from ozonolysis of alpha-pinene. Environmental Science-Processes & Impacts 2017; 19(10):1220-1234.
214. Takekawa H, Minoura H, Yamazaki S. Temperature dependence of secondary organic aerosol formation by photo-oxidation of hydrocarbons. Atmospheric Environment 2003; 37(24):3413-3424.
215. Lamkaddam H, Gratien A, Pangui E, Cazaunau M, Picquet-Varrault B, Doussin J-F. High-NOx Photooxidation of n-Dodecane: Temperature Dependence of SOA Formation. Environmental Science & Technology 2017; 51(1):192-201.
216. Hildebrandt L, Donahue NM, Pandis SN. High formation of secondary organic aerosol from the photo-oxidation of toluene. Atmospheric Chemistry and Physics 2009; 9(9):2973-2986.
217. Cao G, Jang M. Effects of particle acidity and UV light on secondary organic aerosol formation from oxidation of aromatics in the absence of NOx. Atmospheric Environment 2007; 41(35):7603-7613.
218. Ng NL, Chhabra PS, Chan AWH, Surratt JD, Kroll JH, Kwan AJ, et al. Effect of NOx level on secondary organic aerosol (SOA) formation from the photooxidation of terpenes. Atmospheric Chemistry and Physics 2007; 7(19):5159-5174.
219. Kroll JH, Chan AWH, Ng NL, Flagan RC, Seinfeld JH. Reactions of semivolatile organics and their effects on secondary organic aerosol formation. Environmental Science & Technology 2007; 41(10):3545-3550.
220. Hao LQ, Wang ZY, Huang MQ, Fang L, Zhang WJ. Effects of seed aerosols on the growth of secondary organic aerosols from the photooxidation of toluene. Journal of Environmental Sciences 2007; 19(6):704-708.
221. Kamens RM, Zhang HF, Chen EH, Zhou Y, Parikh HM, Wilson RL, et al. Secondary organic aerosol formation from toluene in an atmospheric hydrocarbon mixture: Water and particle seed effects. Atmospheric Environment 2011; 45(13):2324-2334.
222. Huang MQ, Hao LQ, Gu XJ, Hu CJ, Zhao WX, Wang ZY, et al. Effects of inorganic seed aerosols on the growth and chemical composition of secondary organic aerosol formed from OH-initiated oxidation of toluene. Journal of Atmospheric Chemistry 2013; 70(2):151-164.
223. Ge S, Xu Y, Jia L. Effects of inorganic seeds on secondary organic aerosol formation from photochemical oxidation of acetone in a chamber. Atmospheric Environment 2017; 170:205-215.
224. Beardsley RL, Jang M. Simulating the SOA formation of isoprene from partitioning and aerosol phase reactions in the presence of inorganics. Atmos Chem Phys 2016; 16(9):5993-6009.
225. Iinuma Y, Böge O, Gnauk T, Herrmann H. Aerosol-chamber study of the α-pinene/O3 reaction: influence of particle acidity on aerosol yields and products. Atmospheric Environment 2004; 38(5):761-773.
226. Ng NL, Kroll JH, Chan AWH, Chhabra PS, Flagan RC, Seinfeld JH. Secondary organic aerosol formation from m-xylene, toluene, and benzene. Atmospheric Chemistry and Physics 2007; 7(14):3909-3922.
227. Han Y, Stroud CA, Liggio J, Li SM. The effect of particle acidity on secondary organic aerosol formation from α-pinene photooxidation under atmospherically relevant conditions. Atmos Chem Phys 2016; 16(21):13929-13944.
228. Hurley MD, Sokolov O, Wallington TJ, Takekawa H, Karasawa M, Klotz B, et al. Organic aerosol formation during the atmospheric degradation of toluene. Environmental Science & Technology 2001; 35(7):1358-1366.
229. Stirnweis L, Marcolli C, Dommen J, Barmet P, Frege C, Platt SM, et al. Assessing the influence of NOx concentrations and relative humidity on secondary organic aerosol yields from α-pinene photo-oxidation through smog chamber experiments and modelling calculations. Atmos Chem Phys 2017; 17(8):5035-5061.
230. Presto AA, Huff Hartz KE, Donahue NM. Secondary Organic Aerosol Production from Terpene Ozonolysis. 2. Effect of NOx Concentration. Environmental Science & Technology 2005; 39(18):7046-7054.

231. Finlayson-Pitts BJ, Pitts Jr. JN. Chapter 6-Rates and Mechanisms of Gas-Phase Reaction in Irradiated Organic-NOx-Air Mixtures, in: Chemistry of the Upper and Lower Atmosphere. In. San Diego: Academic Press; 2000. pp. 179-263.
232. Ervens B, Turpin BJ, Weber RJ. Secondary organic aerosol formation in cloud droplets and aqueous particles (aqSOA): a review of laboratory, field and model studies. Atmos Chem Phys 2011; 11(21):11069-11102.
233. Jang M, Czoschke NM, Lee S, Kamens RM. Heterogeneous Atmospheric Aerosol Production by Acid-Catalyzed Particle-Phase Reactions. Science 2002; 298(5594):814.
234. Hinks ML, Montoya-Aguilera J, Ellison L, Lin P, Laskin A, Laskin J, et al. Effect of relative humidity on the composition of secondary organic aerosol from the oxidation of toluene. Atmospheric Chemistry and Physics 2018; 18(3):1643-1652.
235. Liu T, Huang DD, Li Z, Liu Q, Chan M, Chan CK. Comparison of secondary organic aerosol formation from toluene on initially wet and dry ammonium sulfate particles at moderate relative humidity. Atmos Chem Phys 2018; 18(8):5677-5689.
236. Jia L, Xu Y. Different roles of water in secondary organic aerosol formation from toluene and isoprene. Atmos Chem Phys 2018; 18(11):8137-8154.
237. Faust JA, Wong JPS, Lee AKY, Abbatt JPD. Role of Aerosol Liquid Water in Secondary Organic Aerosol Formation from Volatile Organic Compounds. Environmental Science & Technology 2017; 51(3):1405-1413.
238. Zhou Y, Zhang HF, Parikh HM, Chen EH, Rattanavaraha W, Rosen EP, et al. Secondary organic aerosol formation from xylenes and mixtures of toluene and xylenes in an atmospheric urban hydrocarbon mixture: Water and particle seed effects (II). Atmospheric Environment 2011; 45(23):3882-3890.
239. Jang MS, Kamens RM. Characterization of secondary aerosol from the photooxidation of toluene in the presence of NOx and 1-propene. Environmental Science & Technology 2001; 35(18):3626-3639.
240. Pankow JF. An absorption model of the gas/aerosol partitioning involved in the formation of secondary organic aerosol. Atmospheric Environment 1994; 28(2):189-193.
241. Donahue NM, Robinson AL, Stanier CO, Pandis SN. Coupled Partitioning, Dilution, and Chemical Aging of Semivolatile Organics. Environmental Science & Technology 2006; 40(8):2635-2643.
242. Murphy BN, Donahue NM, Robinson AL, Pandis SN. A naming convention for atmospheric organic aerosol. Atmos Chem Phys 2014; 14(11):5825-5839.
243. Kanakidou M, Seinfeld JH, Pandis SN, Barnes I, Dentener FJ, Facchini MC, et al. Organic aerosol and global climate modelling: a review. Atmos Chem Phys 2005; 5(4):1053-1123.
244. Seinfeld JH, Pankow JF. Organic atmospheric particulate material. Annu Rev Phys Chem 2003; 54:121-140.
245. Donahue NM, Kroll JH, Pandis SN, Robinson AL. A two-dimensional volatility basis set – Part 2: Diagnostics of organic-aerosol evolution. Atmos Chem Phys 2012; 12(2):615-634.
246. Donahue NM, Epstein SA, Pandis SN, Robinson AL. A two-dimensional volatility basis set: 1. organic-aerosol mixing thermodynamics. Atmos Chem Phys 2011; 11(7):3303-3318.
247. Jenkin ME, Saunders SM, Pilling MJ. The tropospheric degradation of volatile organic compounds: a protocol for mechanism development. Atmospheric Environment 1997; 31(1):81-104.
248. Saunders SM, Jenkin ME, Derwent RG, Pilling MJ. Protocol for the development of the Master Chemical Mechanism, MCM v3 (Part A): tropospheric degradation of non-aromatic volatile organic compounds. Atmos Chem Phys 2003; 3(1):161-180.
249. Jenkin ME. Modelling the formation and composition of secondary organic aerosol from α- and ß-pinene ozonolysis using MCM v3. Atmos Chem Phys 2004; 4(7):1741-1757.
250. Jenkin ME, Young JC, Rickard AR. The MCM v3.3.1 degradation scheme for isoprene. Atmos Chem Phys 2015; 15(20):11433-11459.
251. Bloss C, Wagner V, Jenkin ME, Volkamer R, Bloss WJ, Lee JD, et al. Development of a detailed chemical mechanism (MCMv3.1) for the atmospheric oxidation of aromatic hydrocarbons. Atmospheric Chemistry and Physics 2005; 5:641-664.
252. Camredon M, Aumont B, Lee-Taylor J, Madronich S. The SOA/VOC/NO_x system: an explicit model of secondary organic aerosol formation. Atmos Chem Phys 2007; 7(21):5599-5610.
253. Li J, Cleveland M, Ziemba LD, Griffin RJ, Barsanti KC, Pankow JF, et al. Modeling regional secondary organic aerosol using the Master Chemical Mechanism. Atmospheric Environment 2015; 102:52-61.
254. Aumont B, Szopa S, Madronich S. Modelling the evolution of organic carbon during its gas-phase tropospheric oxidation: development of an explicit model based on a self generating approach. Atmos Chem Phys 2005; 5(9):2497-2517.
255. Valorso R, Aumont B, Camredon M, Raventos-Duran T, Mouchel-Vallon C, Ng NL, et al. Explicit modelling of SOA formation from α-pinene photooxidation: sensitivity to vapour pressure estimation. Atmos Chem Phys 2011; 11(14):6895-6910.
256. La YS, Camredon M, Ziemann PJ, Valorso R, Matsunaga A, Lannuque V, et al. Impact of chamber wall loss of gaseous organic compounds on secondary organic aerosol formation: explicit modeling of SOA formation from alkane and alkene oxidation. Atmos Chem Phys 2016; 16(3):1417-1431.
257. Gentner DR, Jathar SH, Gordon TD, Bahreini R, Day DA, El Haddad I, et al. Review of Urban Secondary Organic Aerosol Formation from Gasoline and Diesel Motor Vehicle Emissions. Environmental Science & Technology 2017; 51(3):1074-1093.
258. Kirchstetter TW, Singer BC, Harley RA, Kendall GR, Hesson JM. Impact of California Reformulated Gasoline on Motor Vehicle Emissions. 2. Volatile Organic Compound Speciation and Reactivity. Environmental Science & Technology 1999; 33(2):329-336.

259. Hunter JF, Carrasquillo AJ, Daumit KE, Kroll JH. Secondary Organic Aerosol Formation from Acyclic, Monocyclic, and Polycyclic Alkanes. Environmental Science & Technology 2014; 48(17):10227-10234.
260. Aumont B, Camredon M, Mouchel-Vallon C, La S, Ouzebidour F, Valorso R, et al. Modeling the influence of alkane molecular structure on secondary organic aerosol formation. Faraday Discussions 2013; 165:105-122.
261. Jathar SH, Miracolo MA, Tkacik DS, Donahue NM, Adams PJ, Robinson AL. Secondary Organic Aerosol Formation from Photo-Oxidation of Unburned Fuel: Experimental Results and Implications for Aerosol Formation from Combustion Emissions. Environmental Science & Technology 2013; 47(22):12886-12893.
262. Platt SM, El Haddad I, Pieber SM, Zardini AA, Suarez-Bertoa R, Clairotte M, et al. Gasoline cars produce more carbonaceous particulate matter than modern filter-equipped diesel cars. Scientific Reports 2017; 7(1):4926.
263. Miracolo MA, Drozd GT, Jathar SH, Presto AA, Lipsky EM, Corporan E, et al. Fuel Composition and Secondary Organic Aerosol Formation: Gas-Turbine Exhaust and Alternative Aviation Fuels. Environmental Science & Technology 2012; 46(15):8493-8501.
264. Timonen H, Karjalainen P, Saukko E, Saarikoski S, Aakko-Saksa P, Simonen P, et al. Influence of fuel ethanol content on primary emissions and secondary aerosol formation potential for a modern flex-fuel gasoline vehicle. Atmos Chem Phys 2017; 17(8):5311-5329.
265. McDonald BC, Gentner DR, Goldstein AH, Harley RA. Long-Term Trends in Motor Vehicle Emissions in U.S. Urban Areas. Environmental Science & Technology 2013; 47(17):10022-10031.
266. Park SS, Kozawa K, Fruin S, Mara S, Hsu Y-K, Jakober C, et al. Emission Factors for High-Emitting Vehicles Based on On-Road Measurements of Individual Vehicle Exhaust with a Mobile Measurement Platform. Journal of the Air & Waste Management Association 2011; 61(10):1046-1056.
267. Tkacik DS, Lambe AT, Jathar S, Li X, Presto AA, Zhao Y, et al. Secondary Organic Aerosol Formation from in-Use Motor Vehicle Emissions Using a Potential Aerosol Mass Reactor. Environmental Science & Technology 2014; 48(19):11235-11242.
268. Pieber SM, Kumar NK, Klein F, Comte P, Bhattu D, Dommen J, et al. Gas-phase composition and secondary organic aerosol formation from standard and particle filter-retrofitted gasoline direct injection vehicles investigated in a batch and flow reactor. Atmos Chem Phys 2018; 18(13):9929-9954.
269. Nordin EZ, Eriksson AC, Roldin P, Nilsson PT, Carlsson JE, Kajos MK, et al. Secondary organic aerosol formation from idling gasoline passenger vehicle emissions investigated in a smog chamber. Atmos Chem Phys 2013; 13(12):6101-6116.
270. Platt SM, El Haddad I, Zardini AA, Clairotte M, Astorga C, Wolf R, et al. Secondary organic aerosol formation from gasoline vehicle emissions in a new mobile environmental reaction chamber. Atmos Chem Phys 2013; 13(18):9141-9158.
271. Krechmer JE, Pagonis D, Ziemann PJ, Jimenez JL. Quantification of Gas-Wall Partitioning in Teflon Environmental Chambers Using Rapid Bursts of Low-Volatility Oxidized Species Generated in Situ. Environmental Science & Technology 2016; 50(11):5757-5765.
272. Zhang X, Cappa CD, Jathar SH, McVay RC, Ensberg JJ, Kleeman MJ, et al. Influence of vapor wall loss in laboratory chambers on yields of secondary organic aerosol. Proceedings of the National Academy of Sciences 2014; 111(16):5802.
273. Durbin TD, Wilson RD, Norbeck JM, Miller JW, Huai T, Rhee SH. Estimates of the emission rates of ammonia from light-duty vehicles using standard chassis dynamometer test cycles. Atmospheric Environment 2002; 36(9):1475-1482.
274. Kean AJ, Littlejohn D, Ban-Weiss GA, Harley RA, Kirchstetter TW, Lunden MM. Trends in on-road vehicle emissions of ammonia. Atmospheric Environment 2009; 43(8):1565-1570.
275. S.M. Pieber, S.M. Platt, I. El Haddad, A.A. Zardini, R, Suarez-Bertoa, et al. Primary and secondary organic aerosol from vehicle engines. In; 2018.
276. Drozd GT, Zhao Y, Saliba G, Frodin B, Maddox C, Oliver Chang MC, et al. Detailed Speciation of Intermediate Volatility and Semivolatile Organic Compound Emissions from Gasoline Vehicles: Effects of Cold-Starts and Implications for Secondary Organic Aerosol Formation. Environmental Science & Technology 2018.
277. Zhao Y, Saleh R, Saliba G, Presto AA, Gordon TD, Drozd GT, et al. Reducing secondary organic aerosol formation from gasoline vehicle exhaust. Proceedings of the National Academy of Sciences 2017; 114(27):6984.
278. Calvert JG, Atkinson R, Becker KH, Kamens RM, Seinfeld JH, Wallington TJ, et al. The mechanisms of Atmospheric Oxidation of Aromatic Hydrocarbons. In. New York: Oxford University Press; 2002.
279. Henze DK, Seinfeld JH, Ng NL, Kroll JH, Fu TM, Jacob DJ, et al. Global modeling of secondary organic aerosol formation from aromatic hydrocarbons: high- vs. low-yield pathways. Atmos Chem Phys 2008; 8(9):2405-2420.
280. Johnson D, Jenkin ME, Wirtz K, Martin-Reviejo M. Simulating the Formation of Secondary Organic Aerosol from the Photooxidation of Aromatic Hydrocarbons. Environmental Chemistry 2005; 2(1):35-48.
281. Robinson AL, Donahue NM, Shrivastava MK, Weitkamp EA, Sage AM, Grieshop AP, et al. Rethinking organic aerosols: semivolatile emissions and photochemical aging. Science 2007; 315(5816):1259-1262.
282. Presto AA, Miracolo MA, Kroll JH, Worsnop DR, Robinson AL, Donahue NM. Intermediate-Volatility Organic Compounds: A Potential Source of Ambient Oxidized Organic Aerosol. Environmental Science & Technology 2009; 43(13):4744-4749.

283. Fraser MP, Cass GR, Simoneit BRT, Rasmussen RA. Air Quality Model Evaluation Data for Organics. 5. C6−C22 Nonpolar and Semipolar Aromatic Compounds. Environmental Science & Technology 1998; 32(12):1760-1770.
284. Ait-Helal W, Borbon A, Sauvage S, de Gouw JA, Colomb A, Gros V, et al. Volatile and intermediate volatility organic compounds in suburban Paris: variability, origin and importance for SOA formation. Atmospheric Chemistry and Physics 2014; 14(19):10439-10464.
285. Zhao YL, Hennigan CJ, May AA, Tkacik DS, de Gouw JA, Gilman JB, et al. Intermediate-Volatility Organic Compounds: A Large Source of Secondary Organic Aerosol. Environmental Science & Technology 2014; 48(23):13743-13750.
286. Zhao YL, Nguyen NT, Presto AA, Hennigan CJ, May AA, Robinson AL. Intermediate Volatility Organic Compound Emissions from On-Road Gasoline Vehicles and Small Off-Road Gasoline Engines. Environmental Science & Technology 2016; 50(8):4554-4563.
287. Sartelet K, Zhu S, Moukhtar S, André M, André JM, Gros V, et al. Emission of intermediate, semi and low volatile organic compounds from traffic and their impact on secondary organic aerosol concentrations over Greater Paris. Atmospheric Environment 2018; 180:126-137.
288. May AA, Presto AA, Hennigan CJ, Nguyen NT, Gordon TD, Robinson AL. Gas-Particle Partitioning of Primary Organic Aerosol Emissions: (2) Diesel Vehicles. Environmental Science & Technology 2013; 47(15):8288-8296.
289. Weitkamp EA, Sage AM, Pierce JR, Donahue NM, Robinson AL. Organic aerosol formation from photochemical oxidation of diesel exhaust in a smog chamber. Environmental Science & Technology 2007; 41(20):6969-6975.
290. Kim Y, Sartelet K, Seigneur C, Charron A, Besombes JL, Jaffrezo JL, et al. Effect of measurement protocol on organic aerosol measurements of exhaust emissions from gasoline and diesel vehicles. Atmos Environ 2016; 140:176-187.
291. Fino D. Diesel emission control: Catalytic filters for particulate removal. Science and Technology of Advanced Materials 2007; 8(1):93-100.
292. Walker AP. Controlling Particulate Emissions from Diesel Vehicles. Topics in Catalysis 2004; 28(1):165-170.
293. Chirico R, DeCarlo PF, Heringa MF, Tritscher T, Richter R, Prevot ASH, et al. Impact of aftertreatment devices on primary emissions and secondary organic aerosol formation potential from in-use diesel vehicles: results from smog chamber experiments. Atmos Chem Phys 2010; 10(23):11545-11563.
294. Zhao Y, Nguyen NT, Presto AA, Hennigan CJ, May AA, Robinson AL. Intermediate Volatility Organic Compound Emissions from On-Road Diesel Vehicles: Chemical Composition, Emission Factors, and Estimated Secondary Organic Aerosol Production. Environ Sci Technol 2015; 49(19):11516-11526.
295. Jathar SH, Donahue NM, Adams PJ, Robinson AL. Testing secondary organic aerosol models using smog chamber data for complex precursor mixtures: influence of precursor volatility and molecular structure. Atmospheric Chemistry and Physics 2014; 14(11):5771-5780.
296. Stone EA, Zhou J, Snyder DC, Rutter AP, Mieritz M, Schauer JJ. A Comparison of Summertime Secondary Organic Aerosol Source Contributions at Contrasting Urban Locations. Environmental Science & Technology 2009; 43(10):3448-3454.
297. Kleindienst TE, Jaoui M, Lewandowski M, Offenberg JH, Lewis CW, Bhave PV, et al. Estimates of the contributions of biogenic and anthropogenic hydrocarbons to secondary organic aerosol at a southeastern US location. Atmospheric Environment 2007; 41(37):8288-8300.
298. Williams BJ, Goldstein AH, Kreisberg NM, Hering SV, Worsnop DR, Ulbrich IM, et al. Major components of atmospheric organic aerosol in southern California as determined by hourly measurements of source marker compounds. Atmos Chem Phys 2010; 10(23):11577-11603.
299. Docherty KS, Stone EA, Ulbrich IM, DeCarlo PF, Snyder DC, Schauer JJ, et al. Apportionment of primary and secondary organic aerosols in southern California during the 2005 study of organic aerosols in riverside (SOAR-1). Environ Sci Technol 2008; 42(20):7655-7662.
300. Fahnestock KAS, Yee LD, Loza CL, Coggon MM, Schwantes R, Zhang X, et al. Secondary Organic Aerosol Composition from C-12 Alkanes. Journal of Physical Chemistry A 2015; 119(19):4281-4297.
301. Lewandowski M, Piletic IR, Kleindienst TE, Offenberg JH, Beaver MR, Jaoui M, et al. Secondary organic aerosol characterisation at field sites across the United States during the spring–summer period. International Journal of Environmental Analytical Chemistry 2013; 93(10):1084-1103.
302. Guzman-Morales J, Frossard AA, Corrigan AL, Russell LM, Liu S, Takahama S, et al. Estimated contributions of primary and secondary organic aerosol from fossil fuel combustion during the CalNex and Cal-Mex campaigns. Atmospheric Environment 2014; 88:330-340.
303. Zotter P, El-Haddad I, Zhang Y, Hayes PL, Zhang X, Lin Y-H, et al. Diurnal cycle of fossil and nonfossil carbon using radiocarbon analyses during CalNex. Journal of Geophysical Research: Atmospheres 2014; 119(11):6818-6835.
304. Turpin BJ, Huntzicker JJ. Identification of secondary organic aerosol episodes and quantitation of primary and secondary organic aerosol concentrations during SCAQS. Atmospheric Environment 1995; 29(23):3527-3544.
305. Warneke C, Gouw JA, Holloway JS, Peischl J, Ryerson TB, Atlas E, et al. Multiyear trends in volatile organic compounds in Los Angeles, California: Five decades of decreasing emissions. Journal of Geophysical Research: Atmospheres 2012; 117(D21).

306. Pollack IB, Ryerson TB, Trainer M, Parrish DD, Andrews AE, Atlas EL, et al. Airborne and ground-based observations of a weekend effect in ozone, precursors, and oxidation products in the California South Coast Air Basin. Journal of Geophysical Research: Atmospheres 2012; 117(D21).
307. Hayes PL, Ortega AM, Cubison MJ, Froyd KD, Zhao Y, Cliff SS, et al. Organic aerosol composition and sources in Pasadena, California, during the 2010 CalNex campaign. Journal of Geophysical Research: Atmospheres 2013; 118(16):9233-9257.
308. Bahreini R, Middlebrook AM, Gouw JA, Warneke C, Trainer M, Brock CA, et al. Gasoline emissions dominate over diesel in formation of secondary organic aerosol mass. Geophysical Research Letters 2012; 39(6).
309. Hayes PL, Carlton AG, Baker KR, Ahmadov R, Washenfelder RA, Alvarez S, et al. Modeling the formation and aging of secondary organic aerosols in Los Angeles during CalNex 2010. Atmos Chem Phys 2015; 15(10):5773-5801.
310. Woody MC, Baker KR, Hayes PL, Jimenez JL, Koo B, Pye HOT. Understanding sources of organic aerosol during CalNex-2010 using the CMAQ-VBS. Atmos Chem Phys 2016; 16(6):4081-4100.
311. Jathar SH, Woody M, Pye HOT, Baker KR, Robinson AL. Chemical transport model simulations of organic aerosol in southern California: model evaluation and gasoline and diesel source contributions. Atmos Chem Phys 2017; 17(6):4305-4318.
312. Ots R, Young DE, Vieno M, Xu L, Dunmore RE, Allan JD, et al. Simulating secondary organic aerosol from missing diesel-related intermediate-volatility organic compound emissions during the Clean Air for London (ClearfLo) campaign. Atmospheric Chemistry and Physics 2016; 16(10):6453-6473.
313. Lim YB, Ziemann PJ. Effects of Molecular Structure on Aerosol Yields from OH Radical-Initiated Reactions of Linear, Branched, and Cyclic Alkanes in the Presence of NOx. Environmental Science & Technology 2009; 43(7):2328-2334.
314. Hamilton JF, Lewis AC, Bloss C, Wagner V, Henderson AP, Golding BT, et al. Measurements of photo-oxidation products from the reaction of a series of alkyl-benzenes with hydroxyl radicals during EXACT using comprehensive gas chromatography. Atmospheric Chemistry and Physics 2003; 3:1999-2014.
315. Zhu S, Sartelet KN, Healy RM, Wenger JC. Simulation of particle diversity and mixing state over Greater Paris: a model–measurement inter-comparison. Faraday Discussions 2016; 189(0):547-566.
316. Eluri S, Cappa CD, Friedman B, Farmer DK, Jathar SH. Modeling the formation and composition of secondary organic aerosol from diesel exhaust using parameterized and semi-explicit chemistry and thermodynamic models. Atmos Chem Phys 2018; 18(19):13813-13838.
317. Hallquist M, Wenger JC, Baltensperger U, Rudich Y, Simpson D, Claeys M, et al. The formation, properties and impact of secondary organic aerosol: current and emerging issues. Atmospheric Chemistry and Physics 2009; 9(14):5155-5236.
318. Simpson D, Yttri KE, Klimont Z, Kupiainen K, Caseiro A, Gelencsér A, et al. Modeling carbonaceous aerosol over Europe: Analysis of the CARBOSOL and EMEP EC/OC campaigns. Journal of Geophysical Research: Atmospheres 2007; 112(D23).
319. Volkamer R, Jimenez JL, San Martini F, Dzepina K, Zhang Q, Salcedo D, et al. Secondary organic aerosol formation from anthropogenic air pollution: Rapid and higher than expected. Geophysical Research Letters 2006; 33(17):4.
320. Murphy BN, Woody MC, Jimenez JL, Carlton AMG, Hayes PL, Liu S, et al. Semivolatile POA and parameterized total combustion SOA in CMAQv5.2: impacts on source strength and partitioning. Atmos Chem Phys 2017; 17(18):11107-11133.
321. Hodzic A, Jimenez JL, Madronich S, Canagaratna MR, DeCarlo PF, Kleinman L, et al. Modeling organic aerosols in a megacity: potential contribution of semi-volatile and intermediate volatility primary organic compounds to secondary organic aerosol formation. Atmos Chem Phys 2010; 10(12):5491-5514.
322. Hatch LE, Yokelson RJ, Stockwell CE, Veres PR, Simpson IJ, Blake DR, et al. Multi-instrument comparison and compilation of non-methane organic gas emissions from biomass burning and implications for smoke-derived secondary organic aerosol precursors. Atmos Chem Phys 2017; 17(2):1471-1489.
323. Hunter JF, Day DA, Palm BB, Yatavelli RLN, Chan AWH, Kaser L, et al. Comprehensive characterization of atmospheric organic carbon at a forested site. Nature Geoscience 2017; 10:748.
324. Borras E, Tortajada-Genaro LA. Determination of oxygenated compounds in secondary organic aerosol from isoprene and toluene smog chamber experiments. International Journal of Environmental Analytical Chemistry 2012; 92(1):110-124.
325. Gkatzelis GI, Tillmann R, Hohaus T, Muller M, Eichler P, Xu KM, et al. Comparison of three aerosol chemical characterization techniques utilizing PTR-ToF-MS: a study on freshly formed and aged biogenic SOA. Atmospheric Measurement Techniques 2018; 11(3):1481-1500.
326. Eichler P, Muller M, D'Anna B, Wisthaler A. A novel inlet system for online chemical analysis of semi-volatile submicron particulate matter. Atmospheric Measurement Techniques 2015; 8(3):1353-1360.
327. DeCarlo PF, Kimmel JR, Trimborn A, Northway MJ, Jayne JT, Aiken AC, et al. Field-deployable, high-resolution, time-of-flight aerosol mass spectrometer. Analytical chemistry 2006; 78(24):8281-8289.
328. Lopez-Hilfiker FD, Mohr C, Ehn M, Rubach F, Kleist E, Wildt J, et al. A novel method for online analysis of gas and particle composition: description and evaluation of a Filter Inlet for Gases and AEROsols (FIGAERO). Atmos Meas Tech 2014; 7(4):983-1001.
329. Yatavelli RL, Mohr C, Stark H, Day DA, Thompson SL, Lopez-Hilfiker FD, et al. Estimating the contribution of organic acids to northern hemispheric continental organic aerosol. Geophysical Research Letters 2015; 42(14):6084-6090.

330. Müller M, Eichler P, D'Anna B, Tan W, Wisthaler A. Direct Sampling and Analysis of Atmospheric Particulate Organic Matter by Proton-Transfer-Reaction Mass Spectrometry. Anal Chem 2017; 89(20):10889-10897.

CHAPTER II:

Materials and methods

2.1. Emission Studies

Primary emissions from light duty gasoline and diesel vehicles have been investigated at the IFSTTAR infrastructure. The facility comprises a single roll bench chassis dynamometer device, different dilution methods as the Constant Volume Sampler (CVS) or the FPS-4000 and several instruments for gas and particles analysis. A scheme of the IFSSTAR facility including chassis dynamometer and dilution systems is presented in figure 2.1.

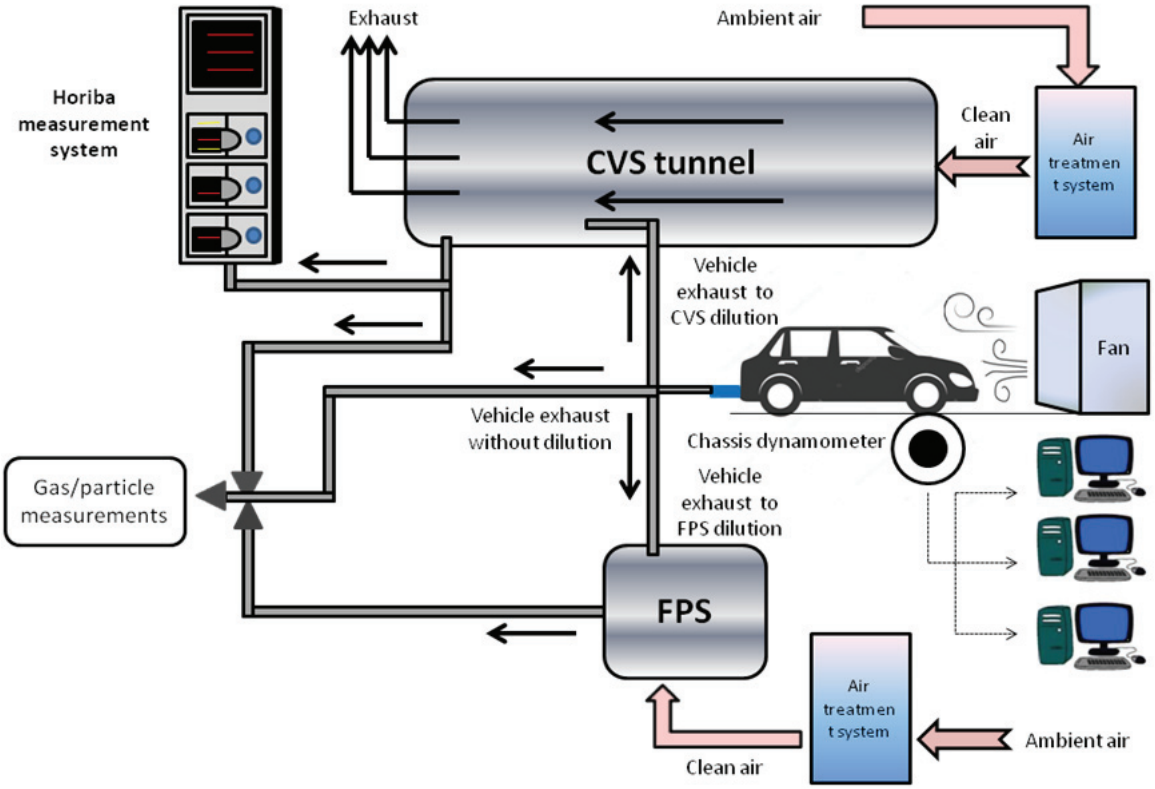

Figure 2.1. *IFSTTAR schematic diagram of the experimental set up.*

2.1.1. Chassis dynamometer

The chassis dynamometer device is a single roll bench for light duty vehicles. The drive wheels of the vehicle are placed on a 48 inch diameter roll. Once the vehicle starts to roll, the roller bench opposes a resistance to the vehicle similar to the one experienced in real driving by friction between wheels and surface. In order to move forwards, a vehicle has to generate a tractive force which compensates air resistance and rolling resistance. Software ensures the control and acquisition of the chassis parameters as power, acceleration, consume, distance, temperature or speed.[1, 2] Figure 2.2. shows a scheme of forces involving during chassis dynamometer test and figure 2.3. some images of the IFSTTAR installation.

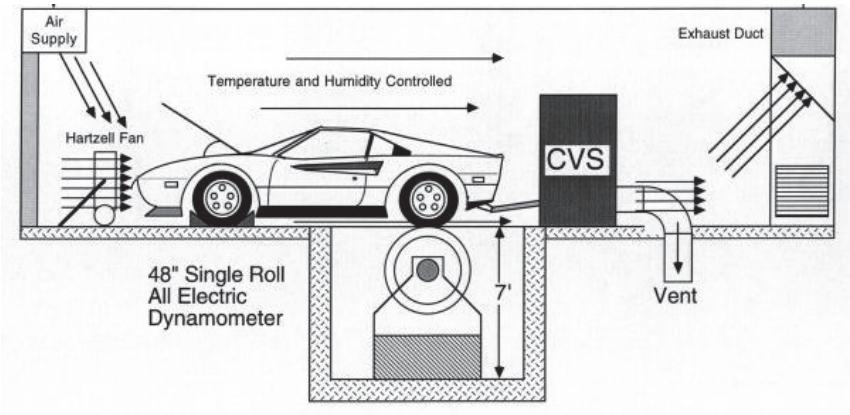

Figure 2.2. *Chassis dynamometer forces, source : http://howstuffworks.*

Figure 2.3. *Chassis dynamometer device: a) screen; b) fan; c) roller bench system.*

2.1.2. Dilution systems

During experiments at IFSTTAR, two dilution methods have been used: a Constant Volume Sampler (CVS) dilution tunnel and a second method based on direct dilution at the tailpipe. The latter method has been chosen in order to provide an alternative method to evaluate the condensable fraction of particulate matter.

For CVS measurements, the exhaust from the vehicle was diluted with conditioned and free particle clean air at 35°C. The dilution flow is adjusted to keep total flow at the end of the CVS constant. The dilution ratio of the CVS is therefore variable, depending on the vehicle and the driving cycle. For high speed cycles as Artemis Motorway, the total flow rate is set at 11 m^3/min while the total flow rate decreases to 9 m^3/min for the other cycles. Temperature gradient between diluted air and exhaust (35°C and approximately 200°C), together with possible turbulences inside the tunnel are the main drawbacks of the CVS. These parameters are very important in the framework of particle size and number concentration measurements. Phenomena as nucleation and condensation could occur during the dilution step inside the CVS (see section 2.1.4. Particle Measurements).

To investigate the condensable fraction of particles, relevant for environmental and health issues, most of experiments reported in this PhD thesis are based on particle measurements at the tailpipe using the Fine Particle Sampler (FPS 4000, Dekati Ltd). Figure 2.4. shows the FPS setup and it working principle. The FPS is a sampler /dilutor device with two dilution stages. Ambient dilution air is previously filtered by High Efficiency Particle Filters (HEPA), dehumidified and pressurized to 3.5 bar. The FPS allows a variable dilution ratio ranged between 10 and 150 times. The primary dilution is performed by a dilutor with a porous tube and the dilution is adjustable from room to 350°C. The second dilution is provided by an ejector dilutor at room temperature only. The difference of pressure created at the nozzle of the dilutor generates a proportional suction, causing the flow of diluted gas passing through the probe of the FPS-4000.

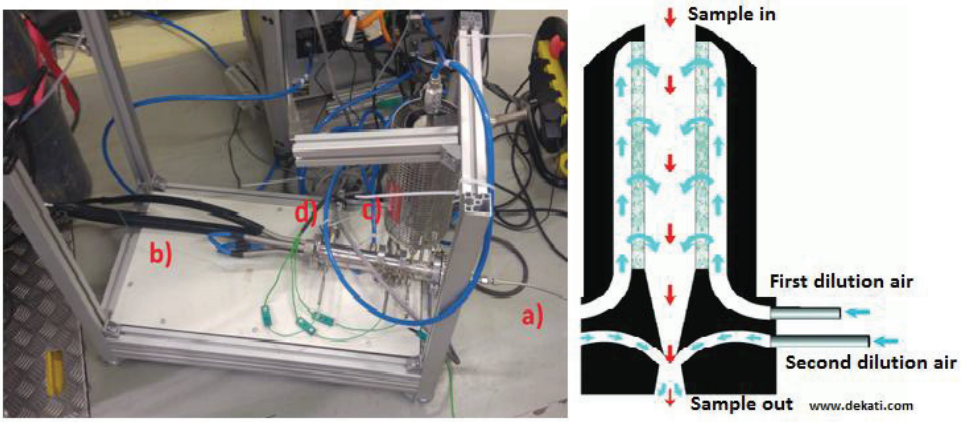

Figure 2.4. FPS setup and working principle where a) is the exhaust gas enter, b) is the diluted exhaust gas outlet, c) is the primary dilution air enter and d) is the second dilution air enter.

Sampling rate, primary dilution ratio, total dilution ratio and temperature can be continuously monitoring. Additional dilution systems VKL10 (PALAS) were used to achieve the higher dilution ratios (1000-4000). The VKL is a dilutor where zero air circulates through an annular passage around the suction nozzle. Then, clean air and exhaust are mixed in the internal chamber. Figure 2.5. shows the principle working of the VKL dilution system.

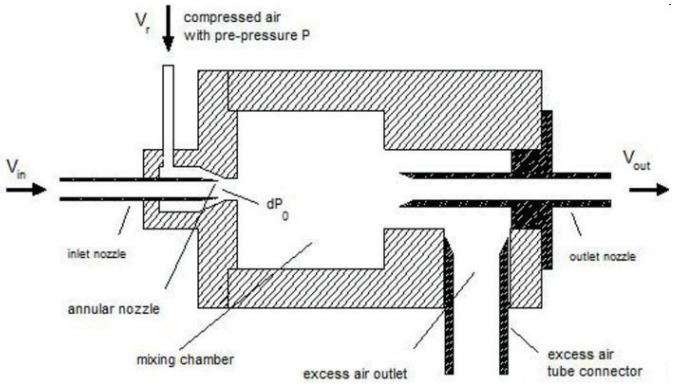

Figure 2.5. *VKL dilution system working principle.*

2.1.3. Driving cycles

Driving cycles are employed in chassis dynamometer studies to achieve reproducible and controlled tests. The driver follows the cycle using a driving system displayed on a screen. Several parameters as fuel consumption, regulated and unregulated emission can be investigated. Several cycles have been developed around the World even though most of the tests are carried out on a limited number of cycles, the ones established by the legislation. It has to be said that not all cycles reproduce realistic driving conditions but they have the advantage to be reproducible. In addition, most recent cycles (see figure 2.6.) do better simulate real driving conditions.

In Europe, since the first European standard (Euro 1) the selected driving cycle was the New European Driving Cycle (NEDC). This cycle presents periods of constant acceleration, deceleration and speed in the attempt to reproduce driving conditions. However, through the years, manufacturers have been able to adapt their vehicles to the NEDC cycle. As a result, cars that easily satisfied laboratory tests were found to emit much larger amount of pollutants during real driving condition tests.[3, 4] Recently a new driving cycle has been implemented as mandatory cycle since 2018 in the Euro 6c standard, the Worldwide Harmonized Light Vehicles Test Cycle (WLTC).[5-7] The WLTC is a 30-minute transient cycle and it is characterized by four sub-driving conditions: low speed, medium speed, high speed and extra high speed (see figure 2.6a). WLTC has been chosen as official test cycle due to its high accuracy to represent real driving conditions.[7, 8]

Another non official cycle widely used in laboratory studies is the Common Artemis Driving Cycles (CADC). The CADC procedures have been developed within the European Artemis (Assessment and Reliability of Transport Emission Models and Inventory Systems) project based on statistical analysis of a large database of European real world driving patterns and has also been used in this thesis. The Artemis urban is composed of the sections “urban dense”, “free-flow urban”, “congested-stops”, “congested-low speed” and “flowing-stable” while Artemis road and Artemis motorway are composed of the parts “unsteady speed” and steady speed” sub-driving parts.[9, 10] The profiles of WLTC and Artemis driving cycles are presented in figure 2.6. Technical details of the cycles used are presented in table 2.1.

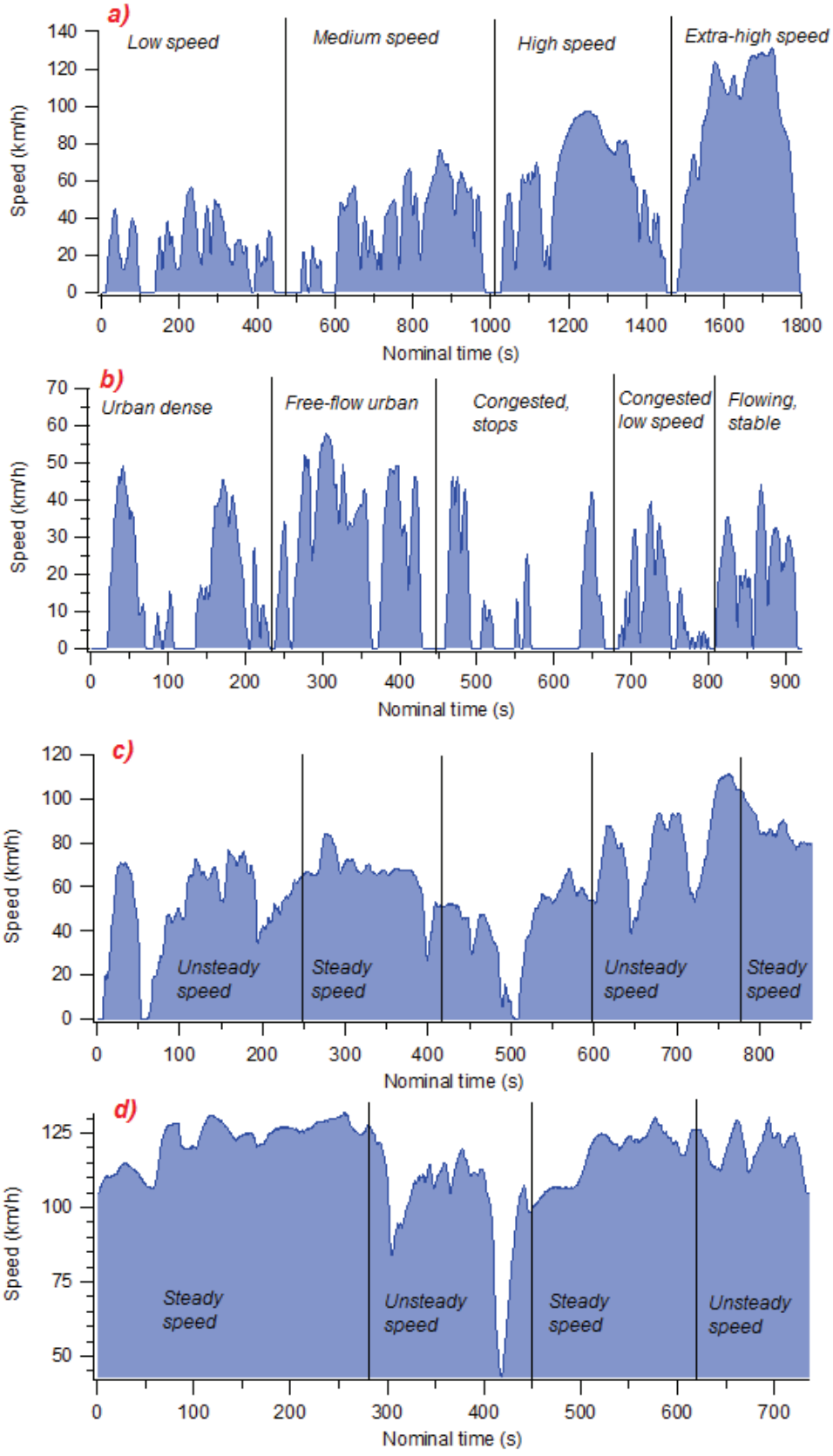

Figure 2.6. *Speed profile of transient cycles : a) WLTC, b) Artemis urban, c) Artemis road and d) Artemis motorway.*

Table 2.1. *Technical characteristic of used cycles.*

Cycle	start	mileage (km)	duration (s)	average speed (km/h)	CVS flow (m^3/min)
WLTC	cold/hot	23.25	1800	47	13
Artemis urban	cold/hot	4.47	921	17	9
Artemis road	hot	14.7	862	61	9
Artemis motorway	hot	23.7	736	116	13

2.1.4. Particle Measurement

Historically, only the particle mass was taken into account for European standards. Since 2011 for diesel, and since 2015 for gasoline vehicles, particle number regulation has been introduced (Euro 5 and Euro 6b, respectively). Particle number is now (Euro 6c) regulated for both diesel and gasoline passenger cars with a maximum concentration of $6x10^{11}$ particles/km.

The European regulation for Euro 5/6 light duty emissions introduced the measurement of non-volatile particles with diameter > 23 nm. In the frame of the Particle Measurement Program (PMP) the volatile fraction of particle is removed by using a heated dilution stage (150 °C) and a heated tube (at 300–400 °C).[11, 12]

The nucleation mode (< 30nm) accounts only for 0.1%-10% of total particle mass, but comprises up to 90% of total particle number [13] and nowadays several studies point out that 23 nm cut-off is not appropriate for the investigation of vehicle emissions.[14, 15] In addition, ultrafine particles have been related to serious environmental and health impacts and should therefore be more carefully investigated.[16-18] Actually, several research programs have investigated the implementation into the European standards emission of a lower cut-off for particle measurements (Down-To-Ten, PEMs4Nano and Sureal-23 projects). In the frame of this PhD, particle emission has been evaluated at the exhaust using FPS-4000 and VLK dilution systems without taking into account cut-off limitation at 23 nm. Dilution ratios ranged from 8 to 100 and dilution temperature ranged from 36°C to 150°C.

2.1.5. Tested vehicles and experimental conditions

A total of six (Euro 5 and Euro 6) vehicles have been tested in three different measurements campaigns at IFSTTAR laboratory. Specifications of the vehicles used are given in table 2.2. and include diesel cars equipped with DOC and PDF and three gasoline DI cars. The vehicles were borrowed or rent from individual owners and were considered representative of the French fleet. Renault Clio and Renault Twingo have been selected as they are in the top-ten ranking of most sold cars in France while the Skoda Octavia and Seat Altea were selected in order to increase representative sample of different technologies and brands.

The experiments were conducted using commercial fuel (sulfur content less than 10 ppm) pumped from the same service station to minimize the variability of fuel composition. Fuel composition can be found in annex I.

Table 2.2. *Characteristics of tested vehicles.*

Vehicule name	D1	D2	D3
Brand	Renault Clio III	Renault Clio	Skoda Octavia
Size class	1.5 DCI	1.5DCI	1.6TDI
Technology	Diesel	Diesel	Diesel
Standard	Euro 5	Euro 6b	Euro 5
Engine capacity (cm^3)	1461	1461	1598
Empty weight (kg)	1090	1087	1262
Mileage (Km)	87073	4700	78903
Gearbox type	Manual (5)	Manual (5)	Automatique (7)
Catalyst	DOC	DOC	DOC
Filter	Catalyzed DPF	Catalyzed DPF	Catalyzed DPF
NOx trap		NOx trap	-
Registration date	17/02/2012	31/12/2015	30/09/2016
Vehicule name	**GDI1**	**GDI2**	**GDI3**
Brand	**Seat Altea XL**	**Renault Twingo**	**Renault Clio**
Size class	1.2TSI	1Sce	0.9 TCE
Technology	Gasoline	Gasoline	Gasoline
Standard	Euro 5	Euro 6b	Euro 5
Engine capacity (cm^3)	1197	999	900
Empty weight (kg)	1320	864	1055
Mileage (Km)	25844	2164	9500
Gearbox type	Manual (5)	Manual (5)	Manual (5)
Catalyst	TWC	TWC	TWC
Registration date	27/02/2014	11/12/2015	30/09/2016

One of the aims of the research project CaPVeREA was to characterize the influence of sampling conditions (as dilution rate and temperature) on ultrafine particles, and to develop a suitable measurement methodology allowing a better quantification of the total number of emitted particles including also the condensable fraction. The results of this specific study can be found in the PhD manuscript of Cedric Louis and in a published paper. [19]

A total of 130 experiments have been carried out in three different field campaigns using 6 the selected gasoline and diesel vehicles. Tables AII.1-6. in annex II indicate the experimental conditions of each of them.

2.1.6. Emission factors

Vehicle emissions represent a particular challenge due to their dependence on many factors, as vehicle characteristics, emission control technology, fuel specifications and ambient and operation conditions.[20] Thus, emission inventories are needed in order to achieve an acceptable repeatability and avoid bias coming from single measurements. Emission inventories are based in Emission Factor (EF) database. The EF has been calculated following equation [2.1]

$$EF = \frac{C_{Average} \cdot 10^6 \cdot T_{Cycle} \cdot Q_{CVS} \cdot DR}{D} \quad [2.1]$$

where *EF* is the emission factor for a specific pollutant in µg/km or #/km depending on the pollutant, $C_{average}$ is the average concentration of specific pollutant along the cycle in µg/m^3 or #/cm^3, 10^6 represents the conversion factor from cm^3 to m^3, Q_{cvs} is the average flow in the CVS dilution system, in m^3/min, T_{cycle} is the duration of the cycle in minutes, *DR* is the external dilution ratio (if needed) and *D* is the distance along the cycle in kilometers. The equation [2.1] can be easily adapted for the cases where pollutant concentration is expressed in ppmv:

$$EF = \frac{C_{Average} \cdot T_{Cycle} \cdot Q_{CVS} \cdot DR}{D} \cdot \frac{M}{V_{mol} \cdot 10^3} \quad [2.2]$$

where *M* is the molecular mass of pollutant, in g/mol; V_{mol} is the molar volume of pollutant, in l/mol and 10^3 allows the conversion from mg to g. Thus EF is expressed in g/km in these cases. For tailpipe measurements, EF is expressed by the following equation [2.3]:

$$EF = \frac{C_{Average} \cdot 10^6 \cdot T_{Cycle} \cdot Q_{exh} \cdot DR}{D} \quad [2.3]$$

where Q_{exh} is the flow exhausted by the vehicle, in m^3/min and the pollutant is expressed in ppmv.

2.2. Experimental set up for SOA studies

An important part of my PhD was devoted to the study of secondary organic aerosol (SOA) formation from Volatile Organic Compounds (VOCs) found in vehicles exhaust. An aerosol flow tube has been deployed for this study. This type of tool has been chosen for different reasons:

1. the project CaPVeREA focused on the need to investigate SOA formation in the so called "champ proche" therefore close to source emission points. Shorter oxidation times were therefore requested.
2. the SOA yield was investigated as function of different environmental conditions (as temperature, $^{\bullet}OH$ concentration, VOC type and concentration). The SOA yield was calculated using the organic concentration detected by the AMS using an average density of 1.3 g/cm^3.

The temperature variations were achieved quite rapidly by a thermostated aerosol flow tube-reactor (AFT). For studies with variable temperature, the thermostated aerosol flow tube was considered to be more suitable than the smog chamber. In the following sections the experimental system will be described in detail.

2.2.1. Aerosol Flow Tube

Experiments were conducted at atmospheric pressure in a cylindrical aerosol flow tube (AFT) made of Pyrex (12 cm inner diameter, 152 cm of length). More details can be found in previous published work. [21, 22] Figure 2.7. shows a schematic diagram of the AFT setup while figure 2.8. shows some pictures of the different parts of the AFT system.

The reactor is surrounded by seven fluorescent lamps (Philips CLEO) with a continuous emission spectrum in the 310-420 nm wavelength range and a total irradiance of 2.7×10^{15} photons cm^{-2} s^{-1} which allows homogeneous irradiation of the reactants mixture. Inlet and outlet of the AFT tube are made of stainless steel cones of 14 cm length. The conic injector favored diffusion of mixtures along the cross section of reactor, minimizing as much as possible the formation of particle jets inside the rube. Teflon cylinders allow the connection of the cones and the inner part of the tube. The temperature into the AFT was controlled using a circulating water bath (Huber CC 405) through the outer jacket. Temperature ranged from 7°C to 22°C. The relative humidity (RH) inside the AFT was adjusted by bubbling from 100 up to 300 ml/min of N_2 (Air liquid, nitrogen 4.5) though ultrapure water and ranged from 24% to 50%. A humidity and temperature sensor was connected at the exit of the reactor allowing continuous monitoring of the experimental conditions (temperature and humidity). Clean zero air was used as gas carrier. In some experiments, NOx was added to the reactants mixture to vary the VOC/NOx ratio. Tables from AIII.2. to AIII.6 in annex III present the initial conditions for the each experiment.

Wall losses from parent VOCs were estimated by measuring concentration of VOCs before and after the AFT under dark conditions (lights-off). While wall losses from gas phase degradation products have not been evaluated and hence, not taken into account. Wall losses of seed particles of approximately 125-150 nm diameter have been evaluated measuring before

and after the AFT the concentration of ammonium sulfate. The losses were negligible (below 5%) for the residence times experiences by the particles in our experiments. The wall losses of the seeds coated with organic particles were also regarded as negligible since diameter ranged from 150-180 nm diameter and the residence times did not exceeded 13 minutes.

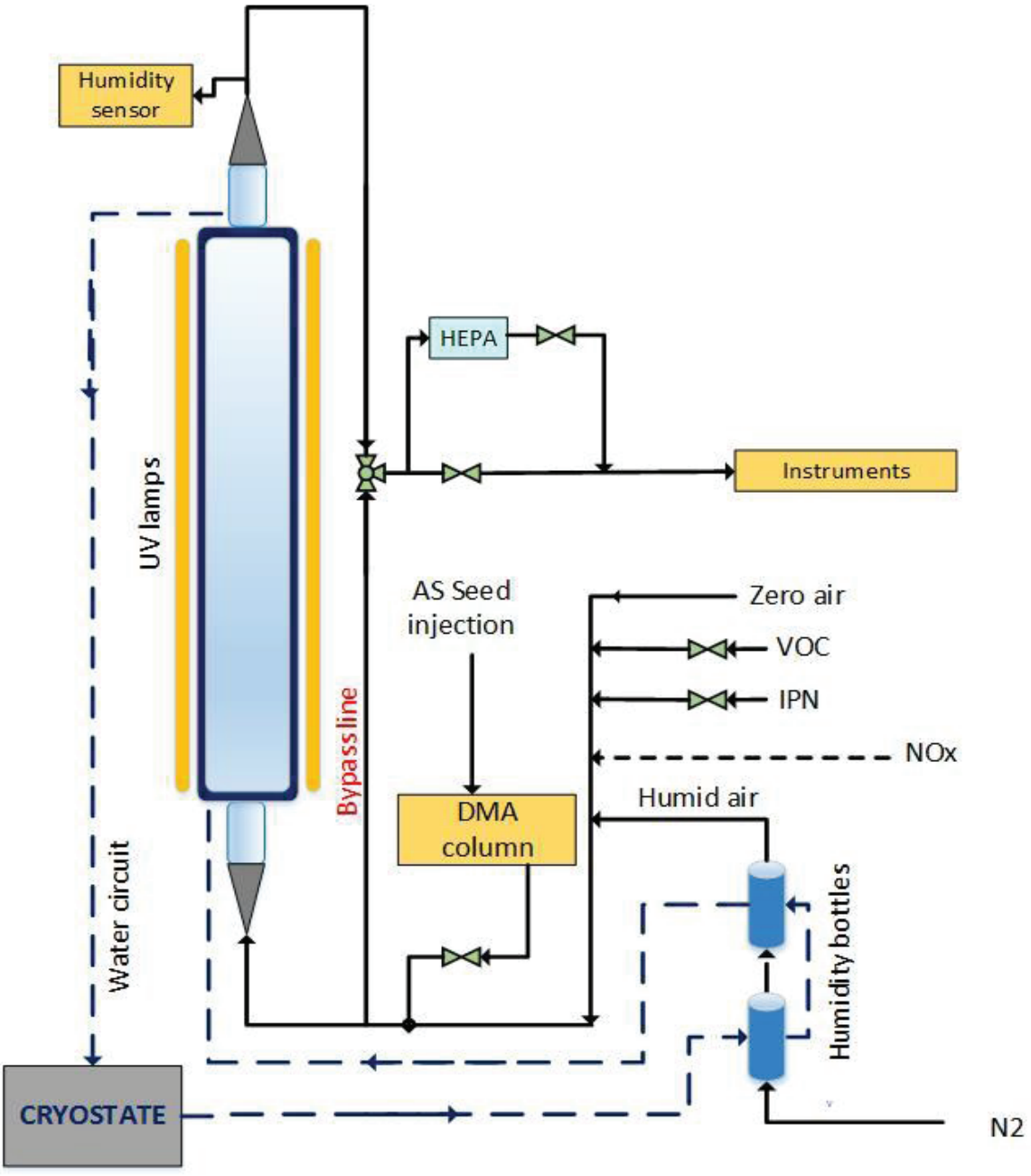

Figure 2.7. *Aerosol flow tube schematic setup.*

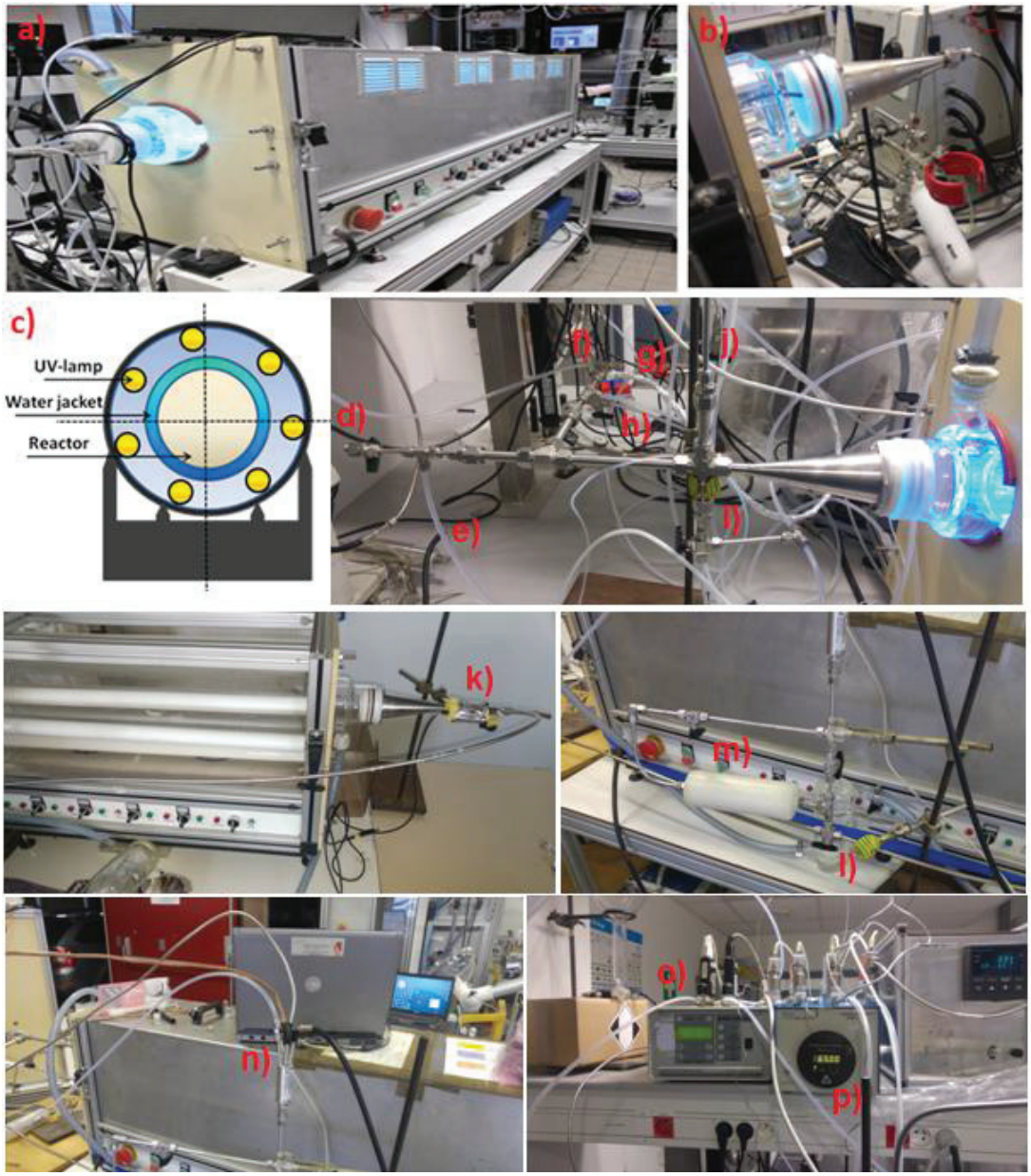

Figure 2.8. *a) AFT view with case to protect from UV lights, b) detailed cone inlet and Teflon piece, c) cross-sectional view for the arrangement of lamps and water jacket around the flow reactor, d) seed inlet, e) humidity inlet, f) air inlet, g) IPN inlet, h) Primary VOC inlet, i) Secondary VOC inlet (if necessary), j) by-pass reactor line, k) humidity sensor at reactor outlet, l) three-way valve for bypass/reactor measurements, m) HEPA bypass line, n) Splitter for measurement lines, o) flow controller box and flow controllers set, p) permeation oven n°1.*

The total flow through the AFT ranged from 1100-1400 cm^3/min for an experimental residence time of particles of 11-13 min. For a cylindrical tube, Reynolds number, the dimensionless number that characterize the movement of a fluid, is defined as the ratio of the inertial force (ρuL) and the viscous force (μ). Reynolds number can be expressed as:

$$Re = \frac{\rho \cdot u^2}{\mu \cdot u/D} = \frac{\rho \cdot u \cdot D}{\mu} \qquad [2.4]$$

where ρ is density (Kg/cm^3), u is flow speed (m/s), μ is the dynamic viscosity (Kg/m·s) and D is the internal diameter of the reactor (m). For Reynolds number (Re) below 2000, the

system is in a laminar regime, while above 4000 is in a turbulent regime. The air density was calculated using the ideal gas law. For 1atm and in temperature in the range 280K-294K, the density varied from 1.26 Kg/m^3 to 1.20 Kg/m^3. The dynamic viscosity in the cylindrical reactor was calculated using the Sutherland viscosity law:

$$\mu = \frac{C_1 . T^{3/2}}{T + C_2} \quad [2.5]$$

where μ is the viscosity at temperature T, μ_0 is the specific temperature and C_1 and C_2 are the Sutherland constant which linked temperature and viscosity. For an average temperature of 287 K, the dynamic viscosity of air is 1.78x10^{-5} Kg/m·s and 1.72x10^{-5} Kg/m·s for nitrogen. Therefore, taking into account the maximum flow rate used of 1400 ml/min and internal diameter of 12cm, the maximum speed can be calculated by:

$$u\,(^m/_s) = \frac{Q\,\left(^{m^3}/_s\right)}{A\,(m^2)} \quad [2.6]$$

where *Q* the volumetric flow and A the cross section of the tube. Thereby, the speed flow is equal to 2.06×10^{-3} m/s. Applying equation [2.4]; a Reynolds number of 17 was calculated. Under such conditions a laminar regime characterized the fluids in the AFT.

2.2.2. Seed Particles

Monodisperse ammonium sulfate particles (AS) were introduced into the AFT to provide a pre-existing surface onto which semi-volatile compounds would condense. The particles were generated from an aqueous solution of ammonium sulfate (reagent grade, Sigma Aldrich) and an aerosol generator 3076 (TSI). The polydisperse aerosol was first dried using silica diffusion driers and then passed though a long Differential Mobility Analyzer 3081, DMA (TSI) resulting in a monodisperse aerosol of a mean diameter between 120 and150 nm. Ammonium sulfate seeds concentration ranged from 3 to 13 μg/m^3 in order to mimic background particles concentration in EU cities.

Stability of the injected AS was tested at the exit of the first DMA column and due to high pressure system to generate the seed, around 10% variability was monitored in the scale of 2 hours. After, the AS alone were injected into the AFT and possible deposition losses were tested. The AS particles (120-150 nm) were not lost inside the AFT during experiment time (2-3 hours).

2.2.3. Selected Volatile Organic Compounds

The AFT experiments intended to mimic in a controlled and simplified system photo-oxidation of car exhaust in the first hours after emission ("champs proche"). Since experiments

were conducted in the laboratory the strategy adopted consisted in the selection of few keys compounds found in the car exhaust. The compounds have been chosen on the basis of primary VOCs emitted by diesel and gasoline vehicles from our own studies (see chapter III) and from the literature. Five compounds have been selected. Each compound is considered a "model molecule" of a family of pollutants. Among the mono-aromatic compounds, toluene was chosen since it was present in a fairly large amount and is less toxic than benzene. Among the cyclic compounds, cyclohexane (cyclic dominating diesel emissions) was chosen since was pretty abundant in car exhaust. Among the aliphatic, nonane was selected since present in emission exhaust from both gasoline and diesel vehicles in large amount. Among the light PAHs, naphthalene was selected. The pentadecane was also tentatively tested. But due to its low volatility ($4.92x10^{-3}$ mmHg at 25°C) the losses inside the AFT were very high and we could not investigate its photo-oxidation.

The selected VOCs (high purity Sigma Aldrich) were constantly introduced into the AFT through a permeation oven system: a 8cm length permeation Teflon tube filled with liquid VOC. The permeation tube was inserted in an oven at variable temperature depending on the VOC vapor pressure and then flushed with constant N_2 flow. In some cases, more than one VOC has been introduced in the AFT for the experiment. In those cases, two or even three permeation ovens were used, one for each VOC. Oven temperature and flushing flow are key parameters in determining the VOC concentration injected into the AFT. Naphthalene is a solid compound therefore another injection method has been deployed. The compound was weighted and inserted in a teflon tube, then it was located in a permeation oven. The injection was assured by passing a continuous flow of N_2 .

Typical flows coming out from permeation ovens ranged 5-20 cm^3/min. Temperature increase in the oven would induce higher vapor pressure and increase of the VOC concentration. Depending on the VOC, the temperatures ranged between 30 and 90°C. Table 2.3. shows the vapor pressure in mmHg for several compounds at 30, 60°C and 90°C.

Table 2.3. *Vapor pressure of used compounds (in mmHg) at 30, 60 and 90°C.*

Compound	Vap. Press. @ 30°C	Vap. Press. @ 60°C	Vap. press. @ 90°C
Toluene	40	150	400
Nonane	8	27	105
Cyclohexane	120	400	1000
Naphtalene	0	0	0.02

Wall losses of the injected VOCs have been evaluated. Cyclohexane did not show any wall loss. Toluene showed low losses of 1% at room temperature and up to 5 % at 7°C. Nonane showed a loss of 15% at 7°C. Naphthalene showed a loss of 10%. Such losses have been taking into account when interpreting the photoxydation results. For first, second and third generation products, the situation is more complicated and wall losses have not been evaluated

yet. Several reaction products are not commercially available but for other, commercially available, wall losses characterization is certainly needed and will be performed at the LCE in the near future.

2.2.4. Hydroxy radical precursor

The hydroxy radical (•OH) is the main atmospheric oxidation agent. The rate constants of the selected VOC with •OH radical oxidant are listed in table 2.4.

Table 2.4. *Rate constants for selected VOCs with •OH radical oxidant and corresponding lifetimes.*

	k rate •OH (cm^3/molecules·s)	Lifetime (h)
Toluene	$6x10^{-12}$	47
Nonane	$9x10^{-12}$	36
Cyclohexane	$6x10^{-12}$	64
Naphthalene	$2x10^{-11}$	5.8

Source: NIST Kinetics database

The •OH radical concentration was evaluated indirectly by the determination of the VOC decay following the procedure suggested by Barmet et al.[23] Using the initial and the final VOC concentration, the kinetic rate constant (k_{OH}) and the residence time, the •OH radical concentration is derived using the following equation.

$$\ln([VOC]_{t=end}) = (-k \cdot t \cdot [OH]) + \ln([VOC]_{t=0}) \qquad [2.7]$$

The so-called "OH-clock exposure" was calculated as suggested by Li et al. 2015 [24] This procedure allows to related the concentration of •OH radicals used during the laboratory experiment to an "OH exposure" that the VOC would experience under atmospheric conditions. Using an average daily atmospheric •OH exposure of 1.5×10^6 molecules/cm^3 [25] , the •OH exposure and the residence time in the AFT for each experiment (between 10 and 13 minutes), the corresponding OH-clock is calculated as follow:

$$OH\ clock\ \ (days) = \frac{OH\ exp\ in\ tube\ \left(\frac{molec}{cm^3}\right) \cdot residence\ time\ (seconds)}{average\ daily\ OH\ \left(\frac{molec}{cm^3}\right) \cdot 86400\ \left(\frac{seconds}{day}\right)} \qquad [2.8]$$

In AFT experiments the •OH radical concentration ranged from 5.9×10^7 to 3.8×10^8 molecules/cm^3 which corresponds to 8 and 28 hours of exposure to •OH radical respectively. During AFT experiments VOC reaction products of first, second and third generations were identified (see chapter IV).

Several •OH radical precursors can be used in experimental studies. The most common are nitrous acid (HONO), methyl nitrite (CH_3ONO) and isopropyl nitrite (IPN) or for chamber experiment with long residence time, also NO_2 can be used. The IPN was used as •OH radical

precursor in our experiments since it is a liquid and can be easily introduced in a controlled and constant amount using a permeation tube inserted in an oven at 35-40°C. The IPN was synthesized following the method described by Taylor et al.[26] by adding a cold mixture of 2-propanol (99.5%, Sigma Aldrich) and diluted hydrochloric acid (37%, Sigma Aldrich) to an aqueous solution of sodium nitrite (reagent grade, Sigma Aldrich). After synthesis, a saturated cold solution of sodium bicarbonate (reagent grade, Sigma Aldrich) was used to wash the IPN.

The IPN photolysis occurs inside the AFT once the UV-lights are switched on. This reaction starts with the decomposition of the IPN molecule to form nitrogen monoxide and alkoxy radical. This radical rapidly reacts with the oxygen present to form acetone and hydroperoxyl radical, which at the end reacts with the previously formed nitrogen monoxide to produce nitrogen dioxide and the desired $^{\bullet}OH$ radicals. At the end of the process, theoretically, one molecule of acetone, NO_2 and one of $^{\bullet}OH$ radical are formed.

$$C_3H_7NO_2 + h\upsilon \rightarrow C_3H_7O^{\bullet} + NO \quad [2.9]$$

$$C_3H_7O^{\bullet} + NO + O_2 \rightarrow C_3H_6O + HO_2^{\bullet} + NO \quad [2.10]$$

$$C_3H_6O + HO_2^{\bullet} + NO \rightarrow C_3H_6O + NO_2 + HO^{\bullet} \quad [2.11]$$

Formation of acetone as a co-product in the generation of $^{\bullet}OH$ radical could be a potential problem. Acetone can also react with the oxidant and be in competition with the VOC, especially for experiments where two permeation tubes of IPN were used in order to obtain a higher amount of $^{\bullet}OH$ radicals. However, the OH-rate constant of acetone is approximately 1.7×10^{-13} cm^3/molecules s, one or two order of magnitude lower than the rate constant between OH and the selected VOCs. In addition, the reaction products formed by acetone degradation have been properly identified and not taken into account for VOC degradation products study.

2.3. Instrumentation

2.3.1. Gas phase chemical composition

2.3.1.1. Horiba gas analysis system (IFSTTAR)

The HORIBA system was used for emission test only. The system provides real time measurement of carbon monoxide (CO), carbon dioxide (CO_2), total hydrocarbons (THC), nitrogen monoxide (NO), nitrogen oxides (NO_X) and methane (CH_4). Dry air dilution allowed partial removal of the water vapor in the sample.

The system measures the FTIR absorption spectrum of the CO and CO_2 in the range 400 - 4000cm^{-1} called Mid Infrared (MIR) domain. Molecules absorbing MIR radiation get changes in

their vibrational and roto-vibrational energy levels. In a conventional IR spectrophotomer, an IR beam is directed through the sample chamber and measured against a reference beam at each wavelength of the spectrum. The heart of an FTIR Spectrophotometer is a Michelson Interferometer, presented in figure 2.9.

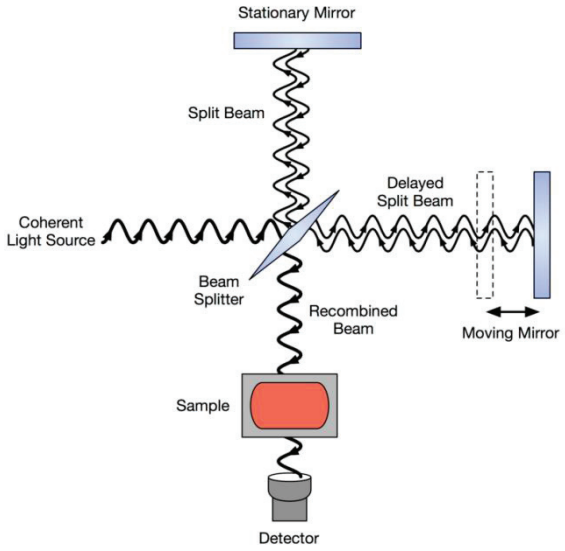

Figure 2.9. *Schematic diagram of a Michelson interferometer, configured for FTIR.*

Radiation from an IR source is directed through the sample cell to a beam splitter. Half of the radiation is reflected from a fixed mirror while the other half is reflected from a mirror which moved continuously over a distance of about 2.5 μm. When the two beams are recombined at the detector, an interference pattern is produced. A single scan of the entire distance takes about 2 seconds and is stored in the computer.

The NO and NOx are measured by chemiluminescence which is the emission of light of excited NO_2 generated by the reaction between NO and ozone. This NO_2 return to lower energy state by releasing photons of light.[27, 28] Emission of light is then measured by a photometer. Emission of light will be proportional to reacted NO. Before the measurement, the sample passes in a catalytic converter where NOx are transformed into NO. The concentration of NO_2 is determined by the subtraction NO_X-NO.

THCs and CH_4 are measured by Flame Ionization Detection (FID). The technique is based on the detection of ions formed during the combustion of organic compounds in a hydrogen flame. Ions are detected using a metal collector which is biased with a high DC voltage. The generated current from these ions is proportional to the concentration of analytes in the gas stream.[29, 30] The current is sensed by an electrometer, converted to digital form, and sent to output device. Working principle of FID technique is presented in figure 2.10.

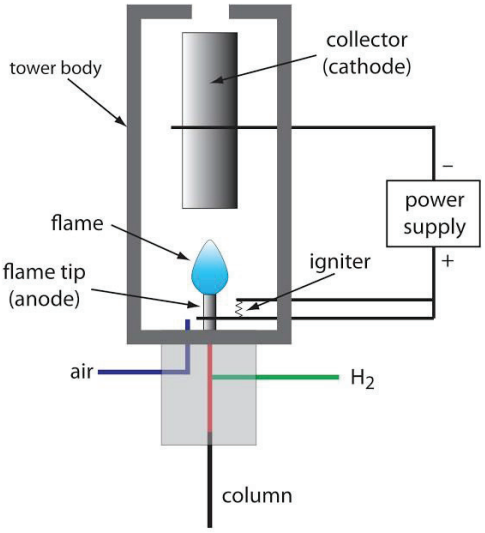

Figure 2.10. *Schematic diagram for Flame Ionization Detection (FID).*

The instrument measures the pollutant concentrations by two methods for each test. A first measurement is made continuously during the cycle and the analyzers give a concentration value in real time. The exhaust gases are then stored in Teflon bags that fill during the cycle. At the end of the cycle, the contents of the bags are re-injected into the analyzers, which measure the concentration of the average emissions of the cycle.

2.3.1.2. Proton Transfer Reaction Mass spectrometry

Concentration of VOCs were monitored by a Proton-Transfer-Reaction Time-of-Flight Mass Spectrometer (PTR-ToF-MS 8000, Ionicon Analytik GmbH, Austria). The PTR-ToF-MS principle of operation is described in detail elsewhere.[31, 32] A schema of the PTRMS working principle is showed in figure 2.11.

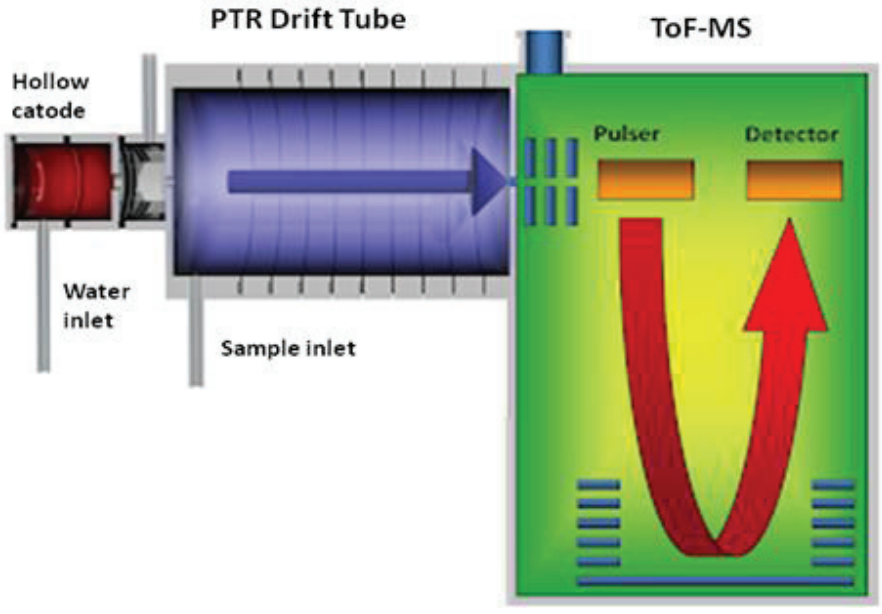

Figure 2.11. *PTRMS working principle.*

Briefly, a hollow cathode (ion source) forms hydronium primary ions (H_3O^+) from pure water vapor. The H_3O^+ ions act as proton donors to most organic analytes in an electrostatic drift tube that is constantly flushed with the analyte gas:[33, 34]

$$VOC + H_3O^+ \rightarrow VOCH^+ + H_2O \qquad [2.12]$$

Molecules and ions undergo many collisions at a drift tube pressure of 2 to 2.5 mbar which leads to high ionization efficiencies. The electric drift field prevents cluster formation. Mass spectrometric analysis is carried out in a medium-resolution ($m/\Delta m$ ~4000-5000) time-of-flight mass spectrometer. The main advantage of PTR-MS over other CIMS methods is its ability to quantitatively (±30%) detects almost all organic analytes (*i.e.* non-polar and polar) without external calibration. PTR-MS technique can produce a single analyte ion or minimal fragmentation, resulting in quite simplified mass spectra when compared with other techniques as electron impact mass spectrometry.

Proton transfer reaction can occur only if the proton affinity (PA) of the target VOCs is higher than that of the water (166 Kcal/mol). Most of the VOCs are ionized by H_3O^+, however, some compounds own lower PA than the water or in the same range, which makes very difficult or impossible to monitored them by this instrument. The PTR-MS technique is able to detect most of aldehydes, ketones, alcohols, acids, esters as well as many unsaturated and aromatic hydrocarbons.[35-37] Table 2.5. shows some PA values of typical VOCs in comparison with water.

Table 2.5. *Values of proton affinity for some typical VOCs.*

Compound	Formula	PA (Kcal/mol)	Mass (amu)
Water	H_2O	166	18.010
Ammonia	NH_3	203	17.026
Formaldehyde	CH_2O	171	30.01
Methanol	CH_4O	181	32.026
Acetaldehyde	C_2H_4O	186	44.026
Formic acid	CH_2O_2	178	46.005
Acetone	C_3H_6O	196	58.041
Glyoxal	$C_2H_2O_2$	161-165	58.005
Propanol	C_3H_8O	190	60.057
Cyclohexane	C_6H_{12}	164	84.093
Toluene	C_7H_8	187	92.062
Phenol	C_6H_6O	195	94.041
Naphthalene	$C_{10}H_8$	191	128.06
n-linear alkanes (C_6-C_{12})	C_9H_{20}	160-165	

Sources: NIST and Bôhme et al., 2017

The PTRMS is composed by an ion source for the production of the H_3O^+ ions, the reaction region where the proton transfer between the ions and the neutral analytes takes

place, and the mass analyzer where the detection of ionized analyte occurs. In the ion source, a high voltage is applied between the anode and the cathode through which a humid air flow (18 mΩ, ultrapure water) passes in order to generate the H_3O^+ ions. The generated ions are then introduced into a drift tube. Concentric rings arranged over the entire length of the reactor, mantain a gradual electric field, [38, 39] which accelerates the ions towards the time of flight mass spectrometer. The temperature can vary between 60 and 130°C, pressure is about 200 Pa and the reduced electric field chosen during the experiments was of 114 Td (1 Td = 10^{-17} V cm^2). Time of flight is composed of four regions, namely: the acceleration region (pulser), the steering plates, the field free flight tube and the detector. All components are under high vacuum (<10^{-6} mbar), as collisions with gas molecules will cause scattering of the ion beam and perturbation of the ions flight. Figure 2.12. illustrates the principle of the time of flight technique.

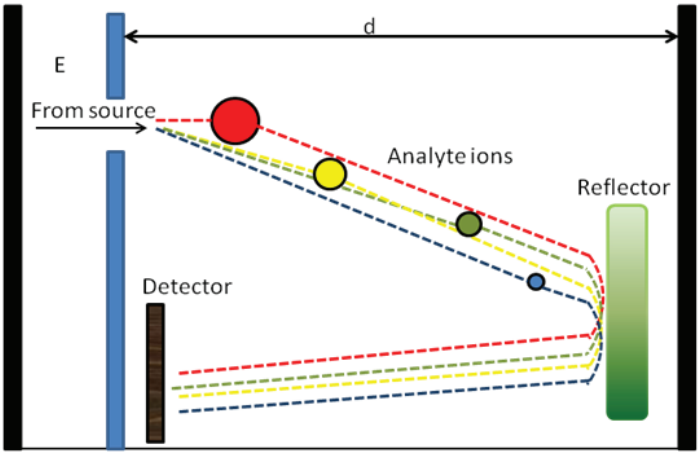

Figure 2.12. *Time of flight principle*.

In a ToF-MS, each ion is given an equal amount of kinetic energy by accelerating the ion pool over a finite distance. Thus, ions will travel with a terminal velocity proportional to their mass to charge ratio (m/z). Ions with lower mass will acquire greater velocity and will have a shorter time of flight to detector. If distance in the field free region is fixed and known, each ion of specific mass-to-charge ratio will have its own time-of-flight. [40-45] Consequently, the measurement of it is employed to determine its m/z, assuming that the potential energy of a charged particle in an electric field is converted into kinetic energy.

A reflector, composed of electrostatic mirrors, is placed upstream of the detector in order to optimize the collection of ions on the Micro Channel Plates (MCPs). The detector has a filter at its input to reduce the saturation due to the H_3O^+ ions. The output of the MCP is sent via a pre-amplifier to a time-to-digital converter (TDC). The TDC is responsible for triggering the pulsed extractor and recording ion arrival times at the detector. The measurements of ion signals provide a means for quantitative determination of the VOC concentration set as:

$$\frac{[VOCH^+]_t}{[H_3O^+]_O} = k \cdot [VOC] \cdot t \qquad [2.13]$$

If *k* and *t* are known, the concentration of specific analyte can be determined through the measurements of the $VOCH^+$/ H_3O^+ signal ratio.

PTRMS data were processed using Igor Pro 6.37. version (Wavemetrics, Inc.) coupled to standard PTR data analysis toolkits (Tofwerk Inc, Switzerland) version 2.5.10. and PTR-ToF-data-analyzer-toolbox v4 (Universität Innsbruck, Austria). Used *K* rate for each detected mass can be found in table AV.17. in the annex V.

2.3.1.3. Automatic Thermal Desorption Gas Chromatography Mass Spectrometry

For experiments where PTR-MS was not available for some VOCs, off-line analyses based on gas-chromatographic separation and mass spectrometry detection has been used. This analysis required a pre-concentration step to achieve the detection limits. In most of the cases, the pre-concentration step is combined with the sampling step. One of the widely used sampling techniques is the active sampling by enrichment on solid adsorbents. Active sampling of VOCs consists on pumping air through a tube filled with selected adsorbent. Tubes can be packed with one or more different adsorbents, depending on the wide volatility range of the compounds. Common adsorbents used are porous organic polymers such as Tenax TA (poly-(2,6-diphenyl-p-phenylenoxide) or graphitized carbon blacks (Carbotrap, Carbopack) or Carbone molecular sieves (Carbosieve, Carboxen ...). In case of these study, multibed-tubes containing Carbotrap C, Carbotrap and Carbosieve SIII were used for complete adsorption of VOCs of interest. The desorption of the analytes could be either done by solvent or thermal desorption. In this work, collected VOCs were further analyzed by automatic thermal desorption directly coupled with capillary gas chromatography with mass spectrometry. The analytical chain is presented in figure 2.13.

Figure 2.13. *TD-GC-MS analytic system, a) sample changer, b) thermo-desorber, c) air server, d) mass spectrometer, e) gas phase chromatograph.*

The thermo-desorption system (Markes International Limited, Llantrisand, UK) includes the sample charger (100 samples), model Series Ultra 2, including ten trays of ten tubes and the thermo-desorber, model Unity 1, including a thermo-desorption furnace, a cryogenic trap (adsorbing phase) cooled by Peltier effect and analyte transfer line to the chromatograph (temperature controlled, column disabled).

The gas chromatography mass spectrometry (GC-MS) system (Agilent Technologies Inc., Santa Clara, USA) includes a gas chromatograph, model 6890N and a mass spectrometer model 5973, having a quadrupole mass filter and an electronic impact source. The principle of the thermal desorption consists in a two-step desorption. The first one consists to transfer the VOCs trapped from the sampling tube to a thin cryogenic trap. This cold trap was then desorbed during the second desorption step by flash heating. The compounds were then injected into the GC and detected by mass spectrometry. The sampling and analytical conditions used in this work are indicated in Table 2.6.

Table 2.6. *ATD-GC-MS conditions*

Thermodesorption	
Injection mode	split
Split ratio	10/1
Purge duration	2 min
Primary desorption duration	8 min
Primary desorption temperature	300C
Desorption flow	35 mL/min
Cold trap temperature	-10°C
Inlet split	-
Secondary desorption duration	3 min
Secondary desorption temperature	310 °C
Outlet split	15 mL/min
Interface temperature	150°C
Gas chromatography	
Carrier gas	He
Flow rate	1.4 mL/min
Capillary column	DB-VRX 60 m, i.d 0.25 mm, film thickness 1.4 µm
Oven temperature	50°C (5 min), 5°C/min, 100°C, 15°C/min, 230°C
Mass spectrometry	
Ionization mode	Electronic impact
Electron energy	70eV
Scan	20-300 uma

Calibration of the system was performed by liquid doping of the adsorption tube. 1 µL of VOC solutions used as reference standards was injected in the sampling tube, using the

heated injector port of a conventional gas chromatograph set at 250°C and a flow of helium set at 60 mL/min over 4 min to evaporate the solvent and to ensure the repeatability of the injection.

Once prepared, the calibration tubes are analyzed by ATD-GC-MS as described earlier. As it was not possible to calibrate all the identified VOCs, the calibration curves were performed for only 22 compounds: benzene, toluene, ethylbenzene, m-xylene, 1,3,5 tri-methyl benzene, naphthalene, 1-butanol, propan-2-ol, heptanol, cyclohexane, dimethylpentane and linear alkanes from nonane to nonadecane. Response factor of named compounds can be found in table AVI.1 in annex VI The quantification of the non-calibrated compounds was performed using the response factor of the calibrated molecules of the family.

2.3.2. Aerosol chemical composition

2.3.2.1. Aerosol Mass Spectrometry

Aerosol composition of secondary organic aerosol from VOCs aging as well as primary emissions from vehicles has been measured by a Time-of-Flight-Aerosol-Mass-Spectrometry, ToF-AMS (Aerodyne Research Inc; Time-of-Flight MS, Tofwerk AG). The ToF-AMS allows real time and size-resolved analysis of non-refractory particles. The instrument can't analyze soot and metals. The ToF-AMS consists of three different sections: the aerosol sampling lens, a particle-sizing section and the particle detection and chemical analysis units.[46-50] A general scheme of AMS and the different parts are shown in figure 2.14.

The instrument samples continuously at atmospheric pressure with a flow rate of 80 cm^3/min through a critical orifice of 100 µm. 6 turbo pumps assure a progressive vacuum inside the instrument. Then, particles are guided through a five aerodynamic lenses system in the vacuum conditions (≈ 10^{-7} hPa) and focused into a narrow and collimated beam. These lenses own a circular aperture that sequentially decreases its internal diameter (from 5mm to 3mm). Transmission efficiency is function of the particle size. Thus, spherical particles in the range of 70 to 650 nm are transmitted with 100% efficiency. Smaller particles have too little inertia to be focused and the majority of them are removed by the first turbo pump. The supersonic expansion of the beam lens leads to a size-dependent particle velocity distribution, where small particles travel faster than larger ones. Particle velocity is then calculated by measuring the particle-time-of-flight over a known distance. Time of flight measure is possible through a "chopper" (rotating disc at 150 Hz with two slots positioned 180° apart), which determines a discontinuous flow of particle that will be able to be distributed into the vacuum chamber.

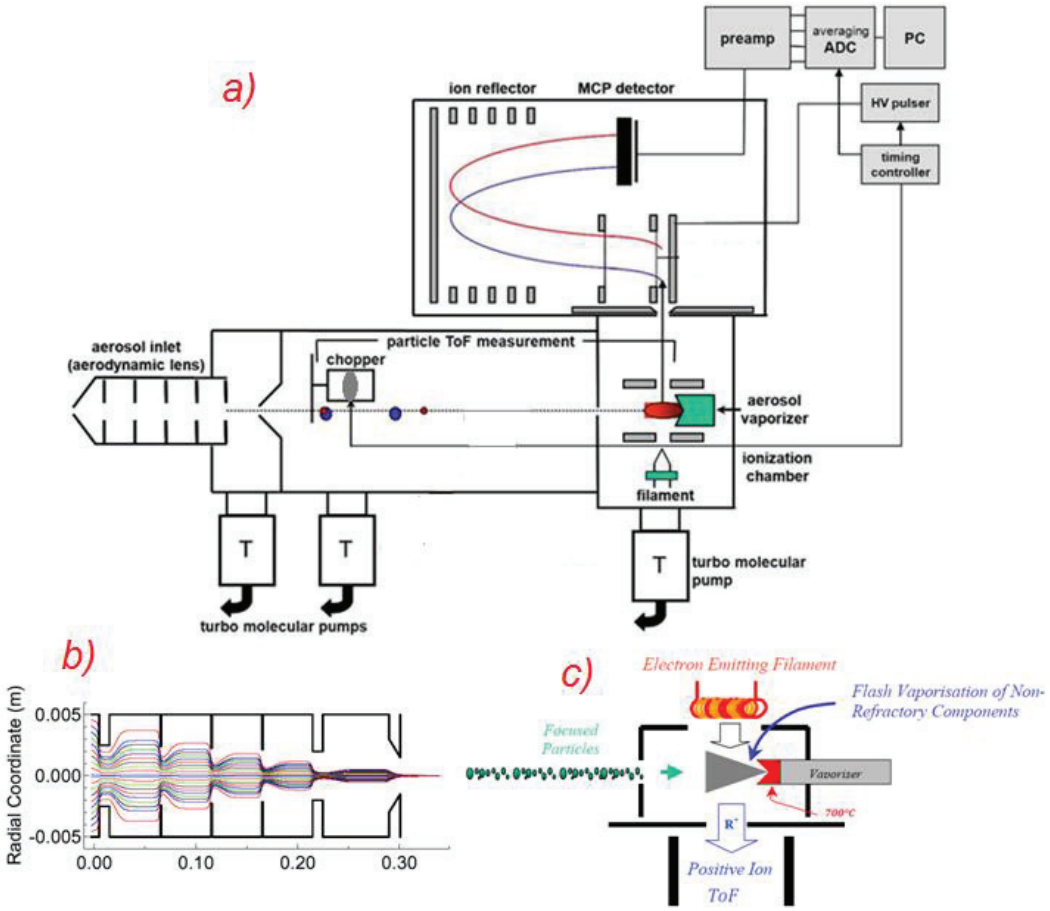

Figure 2.14. *a) general scheme of c-ToF-AMS b) working principle of aerodynamic lens in HR-ToF-AMS through FLUENT software simulation and c) working principle of thermal vaporization and electron impact ionization. (Source : Drewnick, 2005 ; Jayne, 2000 and Alfarra, 2004)*

Once the particle time of flight has been determinate, the vacuum aerodynamic diameter can be calculated.[51-53] Classical volume-equivalent and vacuum aerodynamic diameter are linked by equation below:

$$D_{va} = \frac{\rho_P}{\rho_0} \cdot \frac{D_v}{\chi_v} \qquad [2.14]$$

where D_{va} is the vacuum aerodynamic diameter, D_v is the classical volume-equivalent diameter, ρ_P is the density of the particle, ρ_0 is the unit density (1 g/cm^3) and χ_v is the dynamic shape factor (being 1 for spherical particles and less for ammonium nitrate or other salts).

Particles are then vaporized on a tungsten plate (vaporizer) heated to a temperature around 600-700°C. The non-refractory fraction of the particles, flash vaporizes upon contact with the surface on a time scale of few microseconds, and the gaseous molecular analytes are then ionized at 70 eV. Positive ions are directed in the Time-of-Flight module (see section 2.3.1.2.).

The detector is again a MCP detector (see section 2.3.1.2). A preamplifier is used then to convert the signal into voltage, which is sampled using National Instruments data acquisition

cards on the controlling computer.[54-57] The data acquisition software receives the voltage outputs from the preamplifier, which are directly proportional to the electrical current outputs of the electron multiplier detector. The latter are divided by the average single ion signal strength in order to be converted to detected ion rates.[53] Following the formula adapted from Jimenez et al.[49], it is possible to convert ion rate signal, *I*, to equivalent mass concentration, *C* in μg/m^3.

$$C = \frac{1}{IE} \cdot \frac{1}{Q} \cdot \frac{MW}{N_A} \cdot I \qquad [2.15]$$

where MW is the molecular weight, N_A is Avogadro's number, Q is volumetric flow into AMS and IE is the Ionisation Efficiency. IE is defined as the ratio of the number of ions detected by the electron multiplier to the number of available desorbed molecules of the parent chemical species.[53]

AMS data were processed using Igor Pro 6.37 version (Wavemetrics, Inc.) coupled to standard AMS data analysis toolkits "SQUIRREL" version 1.20A. Mass concentrations of total organics, sulfate, nitrate and ammonium are measured in HR-ToF-AMS and C-ToF-AMS. The single particle organic matter species detection limit is ≈40 ng/m^3 and the HR-ToF mass analyzer is able to resolve isobars up to *m*/*z* 400, which covers the usual *m*/*z*-range of the organic ionic fragments. The instrument has some drawbacks, since the electron impact lead to high fragmentation of the analyte ions.

2.3.2.2. Chemical Analysis of Aerosol Online

The sub-μm Organic Matter (OM) is composed of thousands of individual organic compounds. None of the currently available analytical techniques provides a comprehensive organic speciation of atmospheric PM. The chemical identity of particle species is needed for a better understanding of OM sources, processing and physical and chemical properties and health impacts. In this framework, the Chemical Analysis of Aerosol Online" (CHARON) inlet tool has been developed. [58] Figure 2.15. shows the configuration of CHARON inlet.[58]

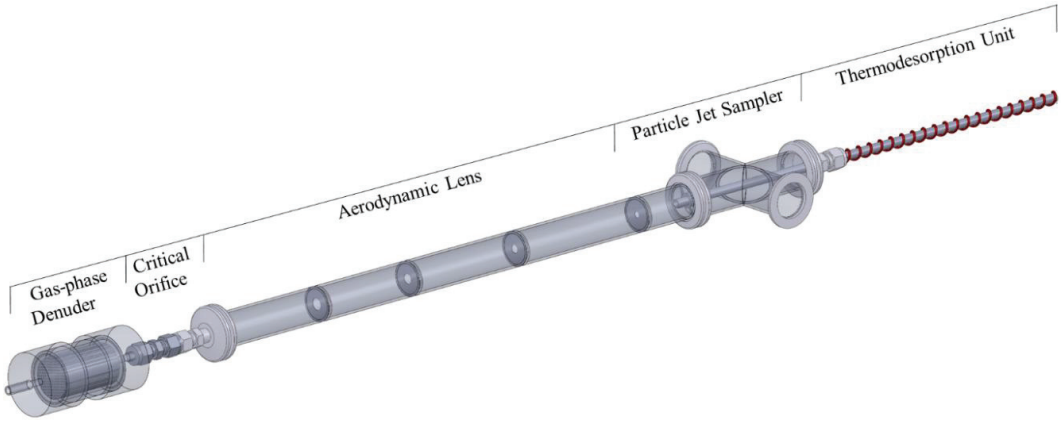

Figure 2.15. *CHARON inlet configuration. (Source: Eichler, 2015)*

CHARON inlet coupled to PTR-MS enables to sample and analyze submicron particle matter in-situ and real time resolution. The CHARON inlet is formed by a gas phase denuder (GPD) used for efficiently strip off the gas phase analytes. The GPD consist of a NovaCarb F activated charcoal monolith (Mast Carbon International Ltd., Guilford, UK) with a channel density of 210 channels per inch and an open cross section of 36%. The cylindrical denuder (L: 5cm, OD: 3cm) is mounted in a stainless steel housing sealed with Viton ® O-rings. In order to avoid particle losses through surface collisions, the flow through the GPD is kept laminar with a residence time of about one second. First, the GPD was able to remove with an efficiency of > 99.999% of various gas phases analytes injected in the ppbv concentration including (Figure 2.16.a).

In figure 2.16.b the transmission efficiency of particles through the GPD has been calculated for ammonium nitrate, ammonium sulphate, glutaric acid and methylglyoxal solution.[58] Thereby, particles below 50 nm are poorly transmitted (<20%), particles in the range of 50-150 nm progressively increase until reach the maximum value of transmission around 90% for particles between 150-750 nm.

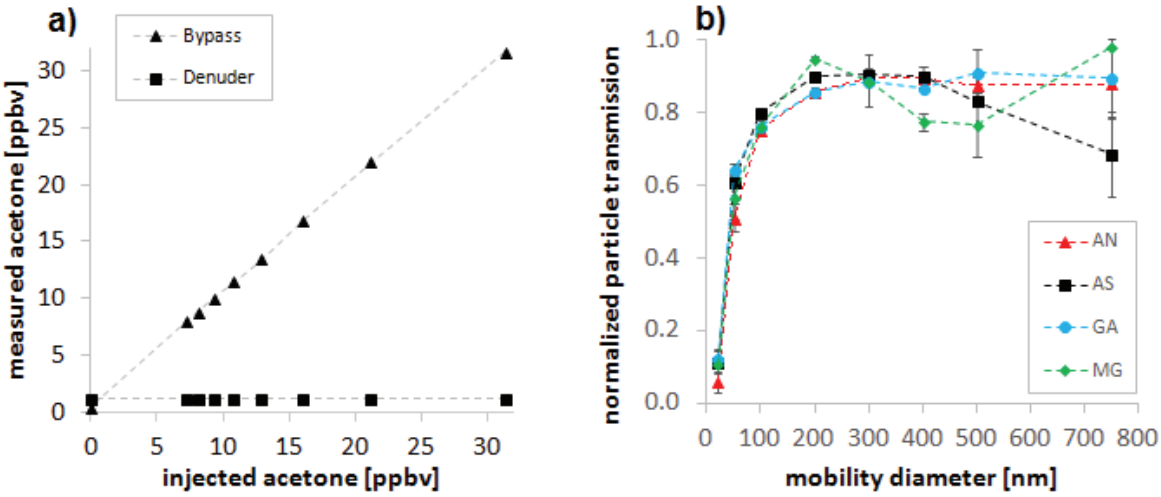

Figure 2.16. *a)Comparison of measured and injected acetone for removing efficiency of GPD. b) Transmission efficiency of the GPD for size selected particles generated from ammonium nitrate (AN), ammonium sulfate (AS), glutaric acid (GA) and methylglyoxal (MG). (Source: Eichler, 2015)*

Once the gas phase has been removed, particles analyte are guided through the aerodynamic lens (ADL) in order to focus and enrich the particle beam (see section 2.3.2.1.). At the exit of the ADL lenses a Varian TriScroll 600 pump (Agilent Inc., Santa Clara, USA) remove residual gas phase. Ratio between inlet and outlet flow determine the enrichment factor of particle sample, which theoretically has a value of 75.[58] Laboratory experiments show that the realistic enrichment factor is around 26 in the range of particles of 200-750 nm (Figure 2.17.).[58] Differences between theoretical and measured enrichment factor are likely due to particle deposition at and behind the initial critical orifice. During the experiments performed in the framework of my PhD, the enrichment factor ranged between 12 and 25 for

different experiments depending mainly on the initial seed diameter (from 113 nm up to 150 nm).

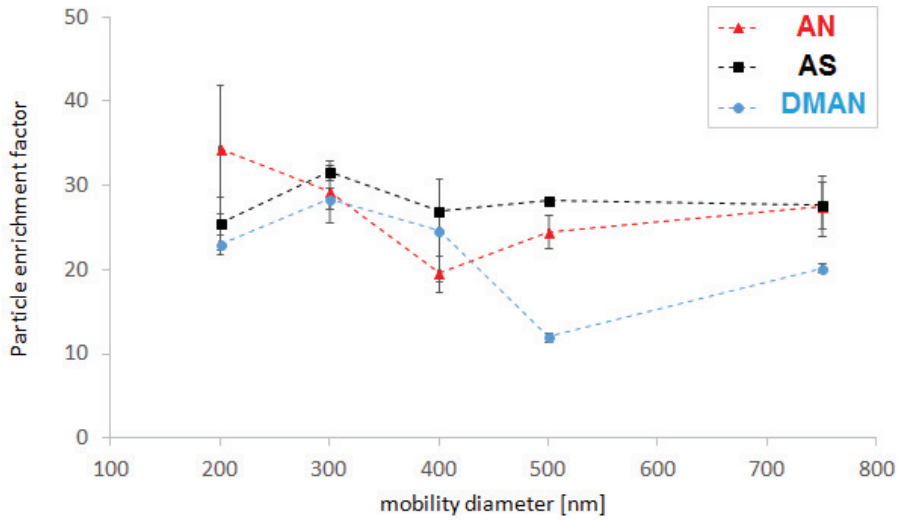

Figure 2.17. *Enrichment factor of the ADL for ammonium nitrate (AN), ammonium sulphate (AS) and dimethylaminium nitrate (DMAN) particles in the 200-750nm size range. (Source: Eichler, 2015)*

The collimated particle beam is sub-sampled into a heated passivated stainless steel tube heated at 140°C-160°C. This heated tube is herein called thermal desorption unit (TDU). An electrically insulating perfluoroalkoxy (PFA) tube was used to connect the TDU to the drift tube of the PTR-MS. Commercial PTR-MS instruments can be operated at drift tube temperatures up to 130 °C. For the measurements carried out in the frame of this dissertation, recondensation of analytes on drift tube surfaces was found to be a minor problem.

During the laboratory experiments a bypass allowed to switch between PTRMS gas phase mode to PTRMS-CHARON particle phase mode. These sampling modes were alternated every 15-20 minutes. The data were processed using Igor Pro 6.37. version (Wavemetrics, Inc.) coupled to standard PTR data analysis toolkits (Tofwerk Inc, Switzerland) version 2.5.10. and PTR-ToF-data-analyzer-toolbox v4 (Universität Innsbruck, Austria).

2.3.2.3. Transmission Electron Microscopy

Particle samples were collected on grids using a Mini Particle Sampler system developed by R'Mili et al.[59] in order to study particle morphology and elemental composition. The grids were then analysed by Transmission Electron Microscopy (TEM) technique. The grids consist of microporous amorphous carbon of small thickness (5 nm-20 nm) type Quantifoil 1.2/1.3 400 mesh (Agar Scientific®). The particles entrained by the gas flow are deposited on the grid by impaction, interception and diffusion as a function of their diameter.[59] Figure 2.18. presents the TEM grid sampling system.

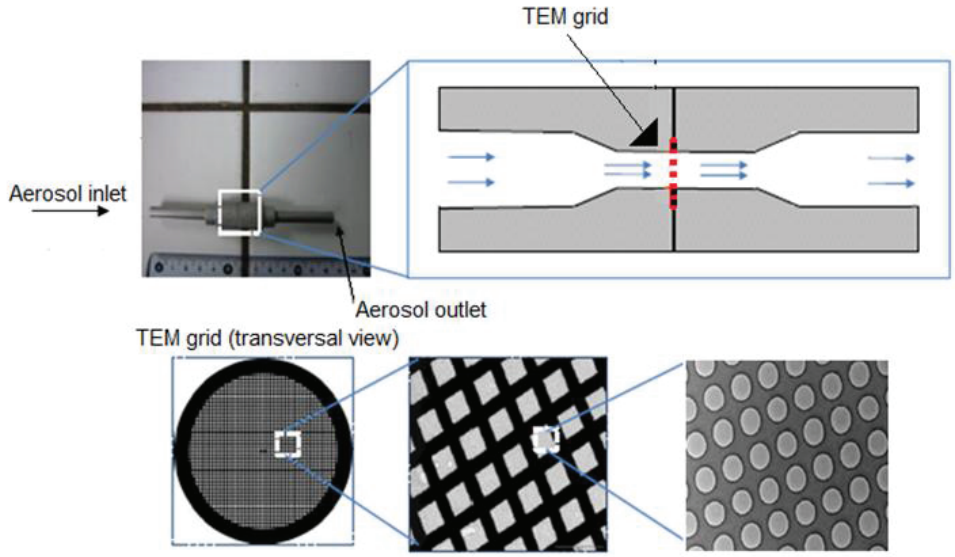

Figure 2.18. *TEM grid sampling.*

TEM is a microscopy technique that uses electrons to determine the shape and dimension of solid specimens. The image is formed from the interaction of the electrons with the sample as the beam is transmitted through the specimen.[60] The electron gun is based on a heated (up to 2500°C) tungsten filament or a LaB_6 cathode heat. The system of condenser lenses gives a demagnified image of the source on the specimen. The radiation interacts with the specimen and is scattered. The scattered radiation is brought to a focus by the objective lens, which gives a magnified image of the specimen on the image plane. Then, a system of projection lenses magnifies the intermediate image on a fluorescent screen.[61] Chemical analysis of specimen can be carried out by using TEM coupling with energy-dispersive X-ray spectroscopy (EDX). The technique relies on an interaction of X-ray excitation and a sample. At rest, an atom within the sample contains ground state (or unexcited) electrons in discrete energy levels or electron shells bound to the nucleus. The incident beam excites an electron in an inner shell, ejecting it from the shell while creating an electron hole where the electron was. An electron from an outer, higher-energy shell then fills the hole, and the difference in energy between the higher-energy shell and the lower energy shell is released in the form of an X-ray. The number and energy of the X-rays emitted from a specimen can be measured by an energy-dispersive spectrometer. As the energies of the X-rays are characteristic of the difference in energy between the two shells and of the atomic structure of the emitting element, EDX allows the elemental composition of the specimen to be measured[62]

2.3.3. Monitors

A Scanning Mobility Particle Sizer (SMPS) was used to determine particle size distribution and total particle number concentration. A schema of the SMPS principle working is shown in figure 2.19.

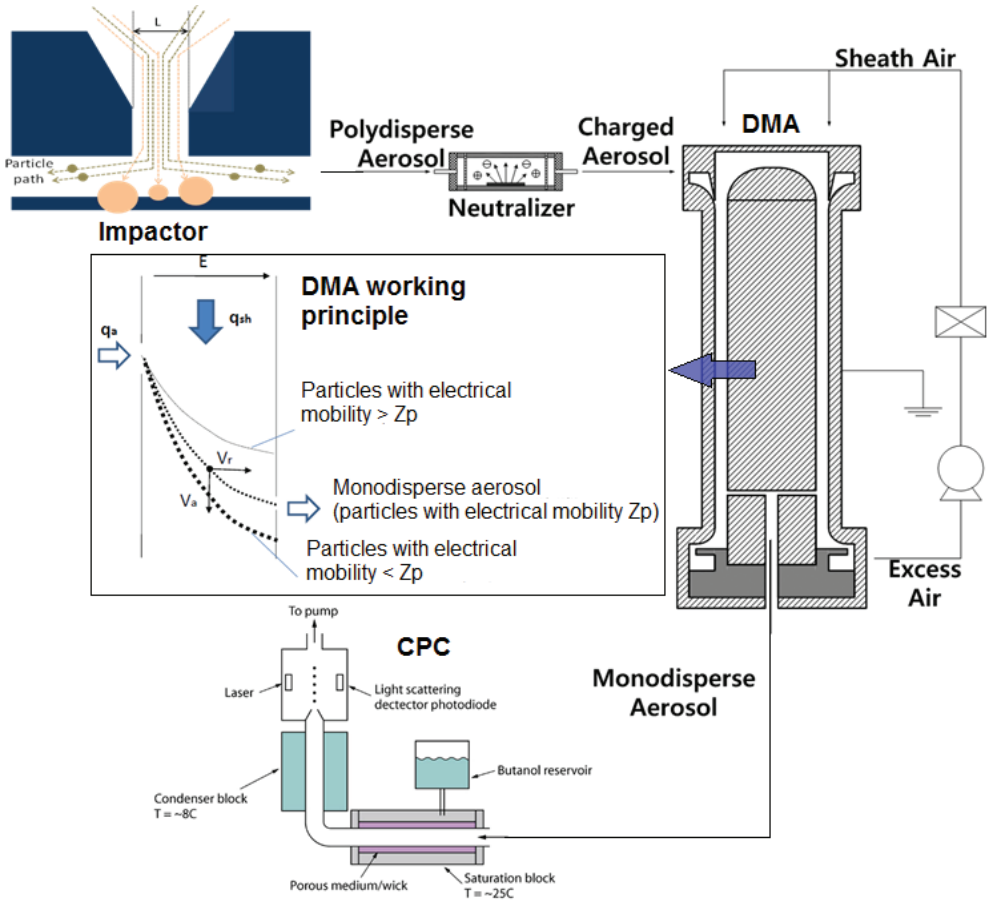

Figure 2.19. *SMPS operating principle with detail working principle of impactor, DMA and CPC. (Source: Hinds, 1999 and Kim, 2009)*

The SMPS is composed of a Differential Mobility Analyzer (DMA) and Condensation Particle Counter (CPC). Firstly, 300 ml/min aerosol flow passes through the impactor that removes large particles by forcing the flow to make 90°C direction change. Driven by their inertia, particles whose mass and speed are such that they cannot modify their trajectory are deposited on the impactor plate. Then the aerosol flow passes through a X-ray source (Kr85 source/neutralizer model TSI 3087). Particles are electrically charged in order to reach a stationary state called "Boltzmann balance".[63-66]

The particles enter into the DMA column (TSI, Shoreview, Minnesota, USA, model 3081) where they are selected according to their electrical mobility; Z_p. The DMA consists of two coaxial cylinders between which an electric field is applied. The electric field accelerates the positively charged particles and then they are precipitated along the column.[67, 68] The particle precipitation depends on their electrical mobility, Z_p.

$$Z_p = \frac{n \cdot e \cdot C_u}{3 \cdot \pi \cdot \eta \cdot D_{p,m}} \qquad [2.16]$$

Where n is the number of charge, e is the value of the charge, C_u is the Cunningham factor, η is the air viscosity and $D_{p,m}$ is the electrical mobility diameter of the particle. Thereby, electrical mobility depends on charge and particle size. Each voltage value

corresponds to a certain electrical mobility and therefore a certain particle diameter. A range of electrical voltage is thus swept over time by the central electrode in order to obtain a range of diameter. Electrical voltage can be set at one value, corresponding with a single mobility diameter. In that configuration, DMA is able to provide a monodisperse aerosol flow at the outlet from a coming polydisperse aerosol flow. This second configuration was used to generate monodisperse ammonium sulfate (AS) seeds.

Particle beam enters into the CPC (TSI, model 3776) for being counted. CPC counts particles ranging from 5 nm to 3000 nm in real time. The flow passes first through a heated tube saturated with butanol vapor. The sample stream passes then into a cooled condenser where the butanol vapors condense onto the particles, increasing their size. The particle is then detected by optical methods. When the droplets cross a laser beam, each droplet scatters light onto a photo diode. These signals are continuously counted and displayed in particles/cm^3 per second. CPC has been used in single configuration to count directly primary particle number from vehicle emissions or associated to the DMA column.

The Fast Mobility Particle Sizer (FMPS) was used for particle size distribution and particle concentration measurements during vehicle emission studies. The working principle is presented in Figure 2.20.

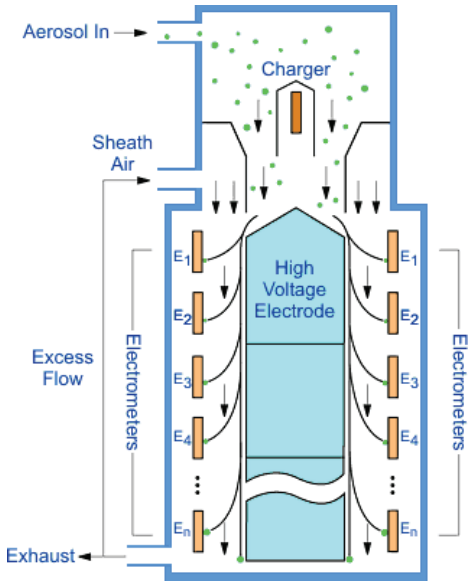

Figure 2.20. *FMPS operating principle. Source: dieselnet.com*

The FMPS (TSI, model 3091) measures particles between 6 nm to 560 nm with time resolution of one second. Large particles are removed in a cyclone. Particles are positively charged using a corona charger and injected in the column where an electrical field is applied. Particles are deposited on different electrometers corresponding to their electrical mobility. FMPS contains 22 highly sensitive electrometers that allow size segregated concentration

measurements of particles. A real-time data inversion procedure is then used to deconvolute the data.

The Scanning Mobility Particle Sizer with Faraday Cup Electrometer (SMPS+E) is a granulometer composed of a classifier (DMA) and a particle counter that uses a Faraday cavity. Figure 2.21. shows the working principle of Fadaray cup electrometer.

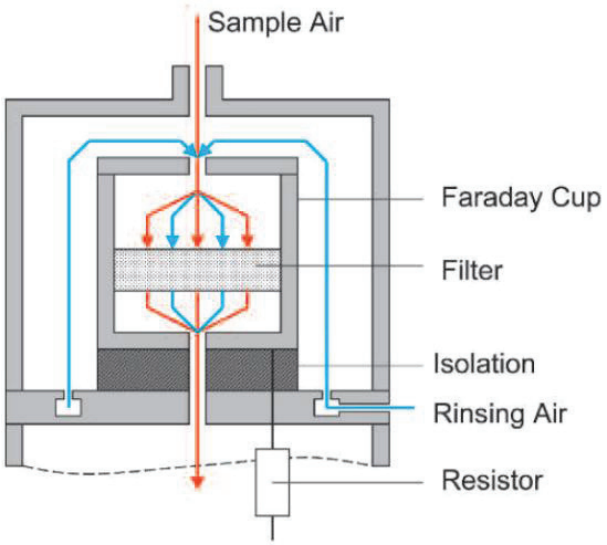

Figure 2.21. *Faraday cup electrometer operating principle. Source: grimm-aerosol.de*

The monodisperse particle beam from the DMA is sent to a metal filter in contact with the Faraday cavity. Thus, the charged particles produce an electric current, which make it possible to go back to a particle number. It provides accurate number and size of ultrafine particles. SMPS+E owns particle range from 2nm to 56nm while maximum concentration is about $1x10^8$ particles/cm^3.

The soot carbon particles were measured by an Aethalometer (AE 33-7, Magee scientific, Berkeley, CA, USA) and a Multi-Angle Absorption Photometer (MAAP 5012, Thermo Fisher Scientific, Waltham, MA, USA). Figure 2.22. shows the aethalometer working principle. The working principle of the Aethalometer is based on the optical attenuation on incident light. The aerosol flow is deposited on a filter tape where sensitive detector measure the difference on light intensity transmitted between a clean portion of tape (reference) and the collecting point. Decreasing in light intensity is interpreted as an increase of particle concentration. Thus, knowing the volumetric flow coming, concentration can be calculated. The aethalometer owns seven wavelengths ranging from ultraviolet (UV) to infrared (IR), namely: 370, 470, 525, 590, 660, 880 and 940 nm. The 880 nm wavelength corresponds to the maximum absorption of black carbon.[69, 70]

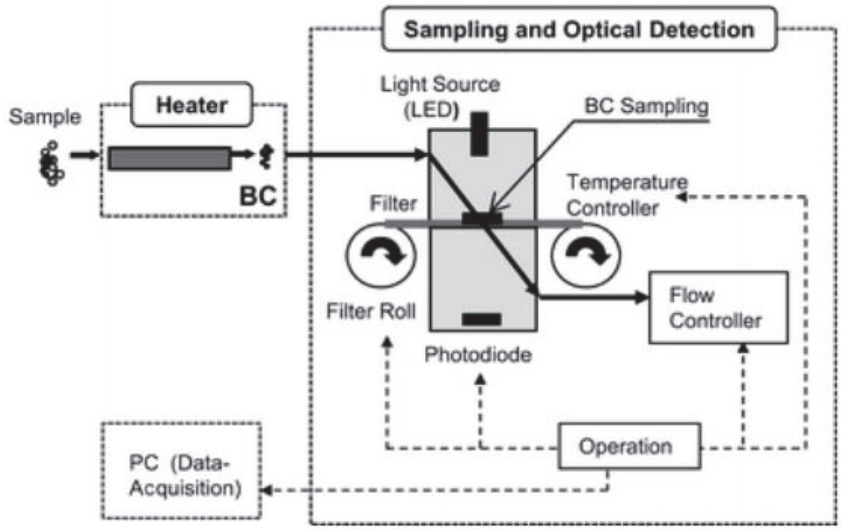

Figure 2.22. *Aethalometer working principle.*

The MAAP instrument (Thermo-Scientific model 5012) was developed to reduce the uncertainties in black carbon measurements caused by aerosol scattering and includes multiple scattering effects and absorption enhancement due to reflections from the filter. This calculation is based on the transmitted and reflected phase functions which are defined by directly measured values of transmission, direct and diffuse back scattering. Laboratory work showed that the diffuse back scatter component was a strong function of the fraction of scattering aerosol, being decreased (relative to the filter) for low scattering fractions and increased for high scattering fractions.

The NOx concentration was monitored by a CLD 88 nitrogen oxide analyzer (Eco physics, Duernten, Switzerland) during laboratory experiments. This analyzer can measure in the range 5-5000 ppbv. The working principle of the instrument is based on the chemiluminescence technique (see section 2.3.1.1.). Figure 2.23. Shows a scheme of the nitrogen oxides analyzer.

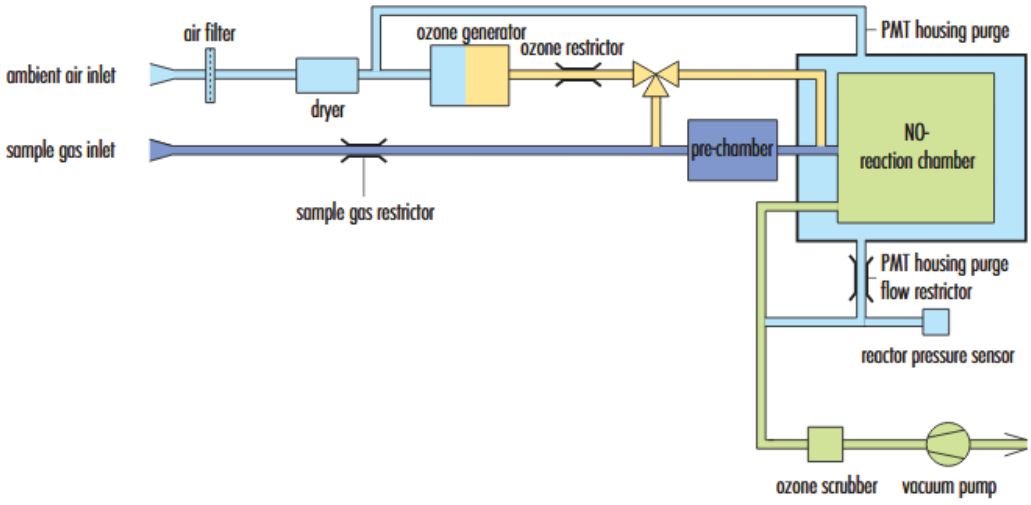

Figure 2.23. *Nitrogen oxides analyzer scheme. Source: www.Ecophysics-us.com)*

References:

1. Su D, Shiao Y, Yang J. Design and implementation of a chassis dynamometer for testing battery-powered motorcycles. In: WSEAS Transactions on Circuits and Systems; 2008.
2. Jirawattanasomkul J, Koetniyom S. Design and Development of Road Load Conditions for Chassis Dynamometer. In: International Conference on Production, Materials and Automobile Engineering (ICPMAE 2012); 2012.
3. Weiss M, Bonnel P, Kuhlwein J, Provenza A, Lambrecht U, Alessandrini S, et al. Will Euro 6 reduce the NOx emissions of new diesel cars? - Insights from on-road tests with Portable Emissions Measurement Systems (PEMS). *Atmospheric Environment* 2012; 62:657-665.
4. Ntziachristos L, Samaras Z. Speed-dependent representative emission factors for catalyst passenger cars and influencing parameters. *Atmospheric Environment* 2000; 34(27):4611-4619.
5. Tsiakmakis S, Fontaras G, Cubito C, Pavlovic J, Anagnostopoulos K, Ciuffo B. From NEDC TO WLTP: effect on the type approval CO2 emissions of light-duty vehicles. In: JRC Science for policy report; 2017.
6. Marotta A, Pavlovic J, Ciuffo B, Serra S, Fontaras G. Gaseous Emissions from Light-Duty Vehicles: Moving from NEDC to the New WLTP Test Procedure. *Environmental Science & Technology* 2015; 49(14):8315-8322.
7. Tutuianu M, Bonnel P, Ciuffo B, Haniu T, Ichikawa N, Marotta A, et al. Development of the World-wide harmonized Light duty Test Cycle (WLTC) and a possible pathway for its introduction in the European legislation. *Transportation Research Part D-Transport and Environment* 2015; 40:61-75.
8. Pavlovic J, Marotta A, Ciuffo B. CO2 emissions and energy demands of vehicles tested under the NEDC and the new WLTP type approval test procedures. *Applied Energy* 2016; 177:661-670.
9. Andre M. The ARTEMIS European driving cycles for measuring car pollutant emissions. *Science of the Total Environment* 2004; 334:73-84.
10. Andre M, Joumard R, Vidon R, Tassel P, Perret P. Real-world European driving cycles, for measuring pollutant emissions from high- and low-powered cars. *Atmospheric Environment* 2006; 40(31):5944-5953.
11. Andersson J., Clarke D. UN-GRPE PMP Phase 3: Inter-Laboratory Correlation Exercise: Framework and Laboratory Guide. In: Unece; 2004.
12. Giechaskiel B, Chirico R, DeCarlo PF, Clairotte M, Adam T, Martini G, et al. Evaluation of the particle measurement programme (PMP) protocol to remove the vehicles' exhaust aerosol volatile phase. *Science of the Total Environment* 2010; 408(21):5106-5116.
13. Kittelson DB. Engines and nanoparticles: a review. *Journal of Aerosol Science* 1998; 29(5):575-588.
14. Gidney JT, Twigg MV, Kittelson DB. Effect of Organometallic Fuel Additives on Nanoparticle Emissions from a Gasoline Passenger Car. *Environmental Science & Technology* 2010; 44(7):2562-2569.
15. Kirchner U, Scheer V, Vogt R, Kägi R. TEM study on volatility and potential presence of solid cores in nucleation mode particles from diesel powered passenger cars. *Journal of Aerosol Science* 2009; 40(1):55-64.
16. Sioutas C, Delfino RJ, Singh M. Exposure assessment for atmospheric ultrafine particles (UFPs) and implications in epidemiologic research. *Environmental health perspectives* 2005; 113(8):947-955.
17. Tobías A, Rivas I, Reche C, Alastuey A, Rodríguez S, Fernández-Camacho R, et al. Short-term effects of ultrafine particles on daily mortality by primary vehicle exhaust versus secondary origin in three Spanish cities. *Environment International* 2018; 111:144-151.
18. Yang J-Y, Kim J-Y, Jang J-Y, Lee G-W, Kim S-H, Shin D-C, et al. Exposure and toxicity assessment of ultrafine particles from nearby traffic in urban air in seoul, Korea. *Environmental health and toxicology* 2013; 28:e2013007-e2013007.
19. Louis C, Liu Y, Martinet S, D'Anna B, Valiente AM, Boreave A, et al. Dilution effects on ultrafine particles emissions from Euro 5 and Euro 6 diesel and gasoline vehicles. In. Atmospheric environment; 2017. pp. 80-88.
20. Colberg CA, Tona B, Stahel WA, Meier M, Staehelin J. Comparison of a road traffic emission model (HBEFA) with emissions derived from measurements in the Gubrist road tunnel, Switzerland. *Atmospheric Environment* 2005; 39(26):4703-4714.
21. Rossignol S, Aregahegn KZ, Tinel L, Fine L, Nozière B, George C. Glyoxal Induced Atmospheric Photosensitized Chemistry Leading to Organic Aerosol Growth. *Environmental Science & Technology* 2014; 48(6):3218-3227.
22. Aregahegn KZ, Nozière B, George C. Organic aerosol formation photo-enhanced by the formation of secondary photosensitizers in aerosols. *Faraday Discussions* 2013; 165(0):123-134.
23. Barmet P, Dommen J, DeCarlo PF, Tritscher T, Praplan AP, Platt SM, et al. OH clock determination by proton transfer reaction mass spectrometry at an environmental chamber. *Atmospheric Measurement Techniques* 2012; 5(3):647-656.
24. Li R, Palm BB, Ortega AM, Hlywiak J, Hu W, Peng Z, et al. Modeling the Radical Chemistry in an Oxidation Flow Reactor: Radical Formation and Recycling, Sensitivities, and the OH Exposure Estimation Equation. *Journal of Physical Chemistry A* 2015; 119(19):4418-4432.
25. Mao J, Ren X, Brune WH, Olson JR, Crawford JH, Fried A, et al. Airborne measurement of OH reactivity during INTEX-B. *Atmospheric Chemistry and Physics* 2009; 9(1):163-173.

26. Taylor WD, Allston TD, Moscato MJ, Fazekas GB, Kozlowski R, Takacs GA. Atmospheric photodissociation lifetimes for nitromethane, methyl nitrite, and methyl nitrate. *International Journal of Chemical Kinetics* 1980; 12(4):231-240.
27. Su Y, Chen H, Wang Z, Lv Y. Recent Advances in Chemiluminescence. *Applied Spectroscopy Reviews* 2007; 42(2):139-176.
28. Baeyens WR, Schulman SG, Calokerinos AC, Zhao Y, Garcia Campana AM, Nakashima K, et al. Chemiluminescence-based detection: principles and analytical applications in flowing streams and in immunoassays. *J Pharm Biomed Anal* 1998; 17(6-7):941-953.
29. Dewar RA. The flame ionization detector a theoretical approach. *Journal of Chromatography A* 1961; 6:312-323.
30. Hughes DEP. Flame-ionization detector for gas chromatography. *Journal of Chemical Education* 1965; 42(8):450.
31. Hansel A, Jordan A, Holzinger R, Prazeller P, Vogel W, Lindinger W. Proton transfer reaction mass spectrometry: on-line trace gas analysis at the ppb level. *International Journal of Mass Spectrometry and Ion Processes* 1995; 149-150:609-619.
32. Jordan A, Haidacher S, Hanel G, Hartungen E, Märk L, Seehauser H, et al. A high resolution and high sensitivity proton-transfer-reaction time-of-flight mass spectrometer (PTR-TOF-MS). *International Journal of Mass Spectrometry* 2009; 286(2):122-128.
33. Graus M, Müller M, Hansel A. High Resolution PTR-TOF: Quantification and Formula Confirmation of VOC in Real Time. *Journal of the American Society for Mass Spectrometry* 2010; 21(6):1037-1044.
34. Yuan B, Koss AR, Warneke C, Coggon M, Sekimoto K, de Gouw JA. Proton-Transfer-Reaction Mass Spectrometry: Applications in Atmospheric Sciences. *Chemical Reviews* 2017; 117(21):13187-13229.
35. Kohl I, Herbig J, Dunkl J, Hansel A, Daniaux M, Hubalek M. Chapter 6 - Smokers Breath as Seen by Proton-Transfer-Reaction Time-of-Flight Mass Spectrometry (PTR-TOF-MS). In: *Volatile Biomarkers*. Amann A, Smith D (editors). Boston: Elsevier; 2013. pp. 89-116.
36. Böhme DK. Ion–Molecule Reactions in Mass Spectrometry☆. In: *Encyclopedia of Spectroscopy and Spectrometry (Third Edition)*. Lindon JC, Tranter GE, Koppenaal DW (editors). Oxford: Academic Press; 2017. pp. 338-346.
37. Ellis AM, Mayhew CA. Proton Transfer Reaction Mass Spectrometry: Principle and Applications. In: WILEY; 2013.
38. Lindinger W, Jordan A. Proton-transfer-reaction mass spectrometry (PTR–MS): on-line monitoring of volatile organic compounds at pptv levels. *Chemical Society Reviews* 1998; 27(5):347-375.
39. Lindinger AHaAJaCWaRHaAWaW. Proton-transfer-reaction mass spectrometry (PTR-MS): on-line monitoring of volatile organic compounds at volume mixing ratios of a few pptv. *Plasma Sources Science and Technology* 1999; 8(2):332.
40. Blake RS, Monks PS, Ellis AM. Proton-Transfer Reaction Mass Spectrometry. *Chemical Reviews* 2009; 109(3):861-896.
41. Sémon E, Arvisenet G, Guichard E, Le Quéré J-L. Modified proton transfer reaction mass spectrometry (PTR-MS) operating conditions for in vitro and in vivo analysis of wine aroma. *Journal of Mass Spectrometry* 2017; 53(1):65-77.
42. Zhan X, Duan J, Duan Y. Recent developments of proton-transfer reaction mass spectrometry (PTR-MS) and its applications in medical research. *Mass Spectrometry Reviews* 2012; 32(2):143-165.
43. Steeghs M, Bais HP, de Gouw J, Goldan P, Kuster W, Northway M, et al. Proton-Transfer-Reaction Mass Spectrometry as a New Tool for Real Time Analysis of Root-Secreted Volatile Organic Compounds in Arabidopsis. *Plant Physiology* 2004; 135(1):47.
44. Beauchamp J, Herbig J, Dunkl J, Singer W, Hansel A. On the performance of proton-transfer-reaction mass spectrometry for breath-relevant gas matrices. *Measurement Science and Technology* 2013; 24(12):13.
45. Håkansson P. An introduction to the time-of-flight technique. *Brazilian Journal of Physics* 1999; 29:422-427.
46. DeCarlo PF, Kimmel JR, Trimborn A, Northway MJ, Jayne JT, Aiken AC, et al. Field-deployable, high-resolution, time-of-flight aerosol mass spectrometer. *Analytical Chemistry* 2006; 78(24):8281-8289.
47. Allan JD, Jimenez JL, Williams PI, Alfarra MR, Bower KN, Jayne JT, et al. Quantitative sampling using an Aerodyne aerosol mass spectrometer 1. Techniques of data interpretation and error analysis. *Journal of Geophysical Research: Atmospheres* 2003; 108(D3).
48. Cross ES, Slowik JG, Davidovits P, Allan JD, Worsnop DR, Jayne JT, et al. Laboratory and Ambient Particle Density Determinations using Light Scattering in Conjunction with Aerosol Mass Spectrometry. *Aerosol Science and Technology* 2007; 41(4):343-359.
49. Jimenez JL, Jayne JT, Shi Q, Kolb CE, Worsnop DR, Yourshaw I, et al. Ambient aerosol sampling using the Aerodyne Aerosol Mass Spectrometer. *Journal of Geophysical Research: Atmospheres* 2003; 108(D7).
50. Drewnick F, Hings SS, DeCarlo P, Jayne JT, Gonin M, Fuhrer K, et al. A new time-of-flight aerosol mass spectrometer (TOF-AMS) - Instrument description and first field deployment. *Aerosol Science and Technology* 2005; 39(7):637-658.
51. Liao J, Brock CA, Murphy DM, Sueper DT, Welti A, Middlebrook AM. Single-particle measurements of bouncing particles and in situ collection efficiency from an airborne aerosol mass spectrometer (AMS) with light-scattering detection. *Atmos Meas Tech* 2017; 10(10):3801-3820.

52. Canagaratna MR, Jayne JT, Jimenez JL, Allan JD, Alfarra MR, Zhang Q, et al. Chemical and microphysical characterization of ambient aerosols with the aerodyne aerosol mass spectrometer. *Mass Spectrometry Reviews* 2007; 26(2):185-222.
53. Alfarra MR, Coe H, Allan JD, Bower KN, Boudries H, Canagaratna MR, et al. Characterization of urban and rural organic particulate in the Lower Fraser Valley using two Aerodyne Aerosol Mass Spectrometers. *Atmospheric Environment* 2004; 38(34):5745-5758.
54. Nash DG, Baer T, Johnston MV. Aerosol mass spectrometry: An introductory review. *International Journal of Mass Spectrometry* 2006; 258(1):2-12.
55. Takegawa N, Miyakawa T, Kondo Y, Jimenez JL, Zhang Q, Worsnop DR, et al. Seasonal and diurnal variations of submicron organic aerosol in Tokyo observed using the Aerodyne aerosol mass spectrometer. *Journal of Geophysical Research: Atmospheres* 2006; 111(D11).
56. Prather KA, Nordmeyer T, Salt K. Real-time characterization of individual aerosol particles using time-of-flight mass spectrometry. *Analytical Chemistry* 1994; 66(9):1403-1407.
57. Allan JD, Alfarra MR, Bower KN, Williams PI, Gallagher MW, Jimenez JL, et al. Quantitative sampling using an Aerodyne aerosol mass spectrometer 2. Measurements of fine particulate chemical composition in two U.K. cities. *Journal of Geophysical Research: Atmospheres* 2003; 108(D3).
58. Eichler P, Muller M, D'Anna B, Wisthaler A. A novel inlet system for online chemical analysis of semi-volatile submicron particulate matter. *Atmospheric Measurement Techniques* 2015; 8(3):1353-1360.
59. R'Mili B, Le Bihan OLC, Dutouquet C, Aguerre-Charriol O, Frejafon E. Particle Sampling by TEM Grid Filtration. *Aerosol Science and Technology* 2013; 47(7):767-775.
60. Williams DB, Carter CB. The Transmission Electron Microscope. In: *Transmission Electron Microscopy: A Textbook for Materials Science*. Williams DB, Carter CB (editors). Boston, MA: Springer US; 1996. pp. 3-17.
61. Winey M, Meehl JB, O'Toole ET, Giddings TH. Conventional transmission electron microscopy. *Molecular Biology of the Cell* 2014; 25(3):319-323.
62. Wang ZL. Transmission Electron Microscopy of Shape-Controlled Nanocrystals and Their Assemblies. *The Journal of Physical Chemistry B* 2000; 104(6):1153-1175.
63. Johnson T, Caldow R, Pöcher A, Mirme A, Kittelson D. A New Electrical Mobility Particle Sizer Spectrometer for Engine Exhaust Particle Measurements. In: SAE International; 2004.
64. Shi JP, Khan AA, Harrison RM. Measurements of ultrafine particle concentration and size distribution in the urban atmosphere. *Science of The Total Environment* 1999; 235(1):51-64.
65. Greenwood SJ, Coxon JE, Biddulph T, Bennett J. An Investigation to Determine the Exhaust Particulate Size Distributions for Diesel, Petrol, and Compressed Natural Gas Fuelled Vehicles. In: SAE International; 1996.
66. Rader DJ, McMurry PH. Application of the tandem differential mobility analyzer to studies of droplet growth or evaporation. *Journal of Aerosol Science* 1986; 17(5):771-787.
67. DeCarlo PF, Slowik JG, Worsnop DR, Davidovits P, Jimenez JL. Particle Morphology and Density Characterization by Combined Mobility and Aerodynamic Diameter Measurements. Part 1: Theory. *Aerosol Science and Technology* 2004; 38(12):1185-1205.
68. Park K, Dutcher D, Emery M, Pagels J, Sakurai H, Scheckman J, et al. Tandem Measurements of Aerosol Properties—A Review of Mobility Techniques with Extensions. *Aerosol Science and Technology* 2008; 42(10):801-816.
69. Drinovec L, Močnik G, Zotter P, Prévôt ASH, Ruckstuhl C, Coz E, et al. The "dual-spot" Aethalometer: an improved measurement of aerosol black carbon with real-time loading compensation. *Atmos Meas Tech* 2015; 8(5):1965-1979.
70. Cheng YH, Yang LS. Correcting aethalometer black carbon data for measurement artifacts by using inter-comparison methodology based on two different light attenuation increasing rates. *Atmos Meas Tech Discuss* 2015; 2015:2851-2879.

CHAPTER III:

Primary emissions from diesel and gasoline light duty vehicles

In the framework of the CaPVeREA project (ADEME), the emissions of six vehicles were measured at the chassis dynamometer at the French Institute of Science and Technology for Transport, Spatial Planning, Development and Networks (IFSTTAR). Full description of the vehicles can be found in the chapter II. Briefly, three diesel vehicles (two Euro 5 and one Euro 6) and three gasoline vehicles (two Euro 5 DI and one Euro 6 DI) have been investigated. Measurements were representative of real driving conditions during Worldwide Harmonized Light Vehicles Test Cycle (WLTC) and Common Artemis Driving Cycles (CADC). Emission factors of regulated compounds and some non-regulated compounds, as well as, temperature and dilution conditions studies have been carried out by the IFSTTAR group. Most of these data can be found in the PhD thesis of Cedric Louis, in two published papers [1, 2] and in the CaPVeREA report (ADEME). Emission factors and transient profiles of regulated compounds for other two vehicles (D3 and GDI3) are reported here for the first time. Table 3.1. summarizes the measurements and the instrumentation deployed for each vehicle. My contribution to the emission studies focused on unregulated gaseous pollutants as BTEX and IVOCs as well as PM chemical composition, morphology and granulometry.

Table 3.1. *Relation of vehicles used for each study.*

	DIESEL			GASOLINE		
Vehicule	D1	D2	D3	GDI1	GDI2	GDI3
Engine	1.5 DCI	1.5 DCI	1.6 TDI	1.2TSI	1Sce	0.9 TCE
Standard	Euro 5	Euro 6b	Euro 5			
Dilution	CVS	CVS/FPS-4000	FPS-4000	CVS	CVS/FPS-4000	FPS-4000
Chemical composition (AMS)	X		X			X
Morphology (TEM)	X			X	X	
Elemental Composition (EDX)					X	
CVS vs tailpipe study					X	
Nanoparticles study			X		X	X
BC (Aethalo./MAAP)	X	X	X	X	X	X
Particle distribution (FMPS/SMPS) 6-600 nm	X		X			X
Particle distribution below 55 nm (SMPS+E)	X			X		
EF regulated compounds	X*	X*	X*	X*	X*	X*
Regulated transient			X			X
Gas phase (TD-GC-MS)			X			X
Gas phase (PTRMS)			X**			X**

* Analyzed/published by IFSTTAR. **Data provided from Prof. Wisthaler group Univ. Oslo (Norway).

3.1. Particle Emission Study

3.1.1. Impact of dilution system for particle measurements

As described in chapter II, two dilution systems were used during the emission studies: one directly at the tailpipe using a Fast Particle Sampler (FPS-4000) and a second one, a Constant Volume Sampler (CVS) system. Comparison of the two dilution systems was performed with the following conditions: FPS-4000 first dilution stage at 50°C and a second at room temperature and an average dilution ratio of 30 and the CVS with an average dilution ratio of 13 and a temperature of 25°C. Major differences in particle size distribution and number concentration are observed when comparing the two dilution systems during a WLTC cold start cycle for a gasoline DI Euro 6 vehicle (figure 3.1.).

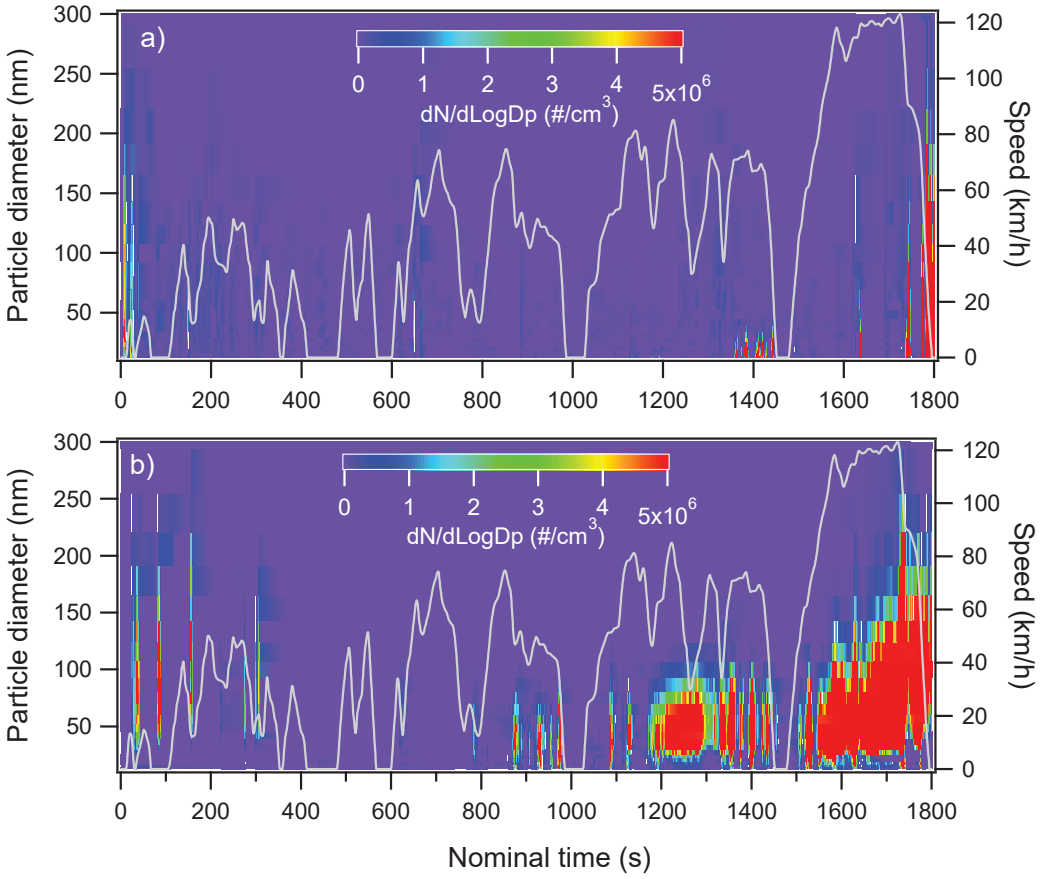

Figure 3.1. *Particle number concentration for gasoline DI Euro 6 (GDI2) vehicle during WLTC cold start cycle, sampled after tailpipe (a) and after CVS dilution system (b).*

This figure clearly shows higher PN concentration and shift of the size distribution is observed in the CVS with respect to tailpipe measurements. These observations can be explained by nucleation and condensation phenomena taking place in the CVS when semi-volatile compounds are present in the exhaust. These latter can readily condense or nucleate

during cold and weak dilution (in the CVS). Nucleation can therefore explain particle number increase after CVS dilution. This phenomenon has been previously reported as consequence of exhaust dilution.[3, 4] Condensation is also favored at low temperatures and can explain particle growth onto soot particles. Half-time coagulation was calculated by Louis et al.[2] for typical particle number concentration and particle sizes observed in this experiment and the authors reported half-time coagulation in the order of minutes, while the residence times inside the CVS ranged from 2 to 10 seconds. Thus, particle coagulation is not important inside the CVS tunnel. Other authors also reported similar bias during measurements of car emission in CVS system.[2, 5-8] In view of what observed in figure 3.1., most of the particle studies presented in this document are relative to tailpipe measurements. On the other hand, CVS results will be presented for regulated gas phase pollutants, since they were not affected by CVS dilution.

3.1.2. Gasoline Particle Emission

An extensive number of instruments have been deployed to investigate the size distribution, the morphology and the chemical composition of Euro 5 and Euro 6b GDI passenger cars. The chemical composition was investigated using an Aerosol mass spectrometer (c-ToF-AMS) and TEM grids. The particle number concentration and distribution was investigated using CPC, FMPS, SMPS and SMPS+E while BC analysis was based on Aethalometer and MAAP. Figure 3.2. presents the chemical composition of the particle phase (organics, nitrate, PAHs, water, BC) and particle number concentration and size distribution of PM emitted from an Euro 5 DI gasoline vehicle during a WLTC cold (a, b) and hot start (c, d), respectively. Relatively high concentrations of organic material, BC and nitrate are emitted during the cold start. Emission of the organic fraction reaches up to 3000 $\mu g/m^3$ during the first two minutes of the cycle then it rapidly decreases to 50-100 $\mu g/m^3$. The organic mass loading increased again to 300 $\mu g/m^3$ during acceleration and brakes episodes. Cold start period represents 57% of total organic mass emitted during the cycle. Karjalainen et al.[9] reported very similar transient profiles for organic fraction measured during the first minutes of the NEDC cycle for an Euro 5 gasoline DI vehicle.

PAHs were also measured in the particle phase during the first 2-3 minutes of the WLTC cold start. The concentration reached values of 50 $\mu g/m^3$ during warm-up periods and decreases rapidly down to instrumental detection limit. Mass loadings of nitrate, between 40-80 $\mu g/m^3$, were measured during in the first minutes of the cold start and during the fast acceleration (motorway) periods of the WLTC cycle. Cold start accounts for approximately 20 % of total nitrate concentration. Nitrate is formed through oxidation of NO to HNO_3 and it is neutralized by the ammonia present in the exhaust.[10, 11]

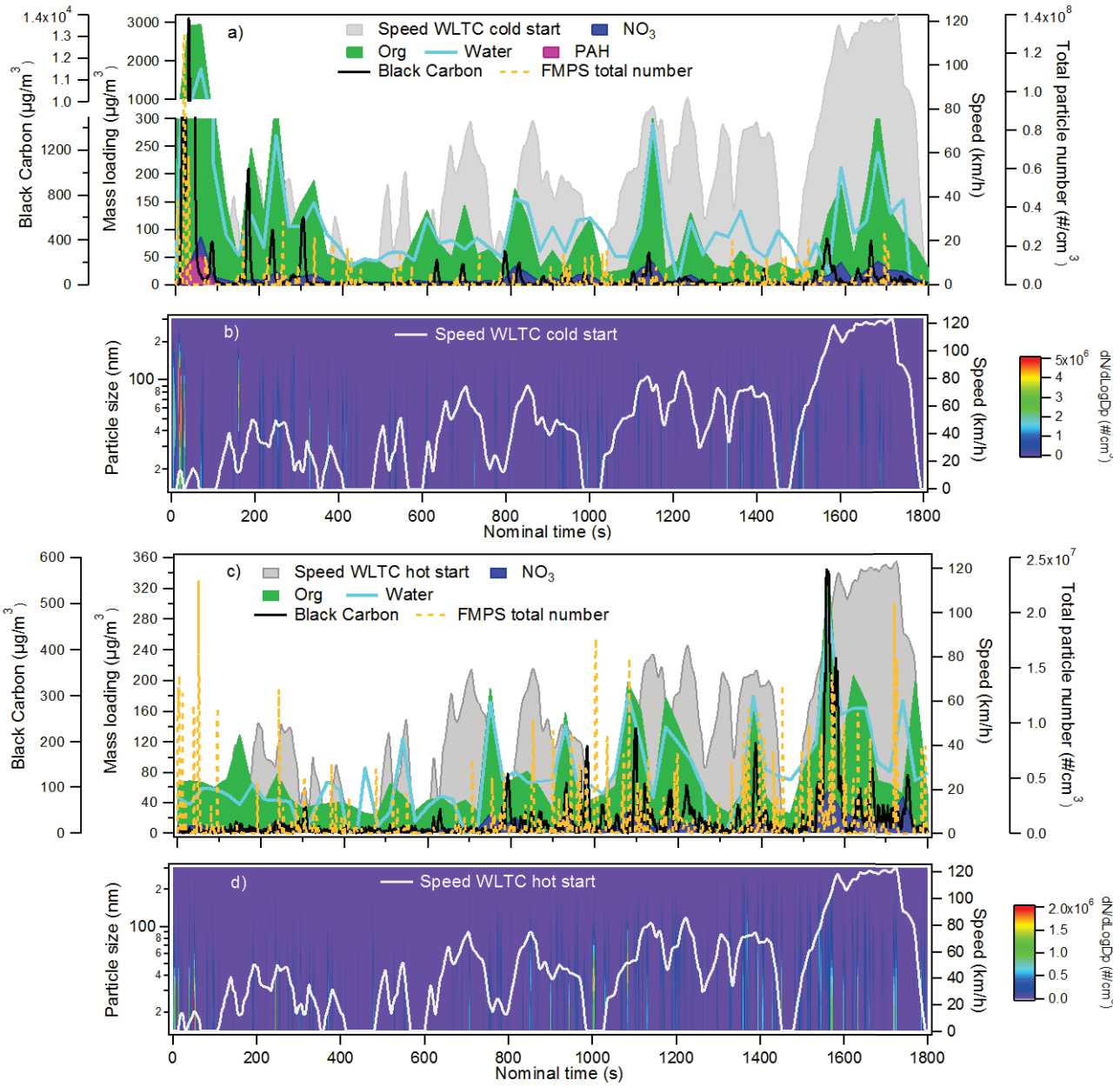

Figure 3.2. *Time series of organic, water, NO_3^-, PAHs, BC particles and particle distribution during a WLTC cold start cycle (a, b) and WLTC hot start (c, d) for GDI 3 Euro 5 gasoline vehicle.*

High loading of BC are also emitted during the first minutes of the cycle reaching concentrations of 1.4×10^4 µg/m^3. Cold start accounts for 72% of total BC emissions. The particle number concentration measured by the FMPS follows the same temporal profile than BC and organics. These results agree with several previous works that report high emissions of PM at the beginning of the cold cycle, mainly associated to BC for Euro 4 and Euro 5 GDI and PFI vehicles.[12-15] Louis et al.[13] studied cold and hot start Artemis Urban cycle for gasoline Euro 5 vehicles and found that cold start emits the double number of particles than the hot start

cycle. Chen et al.[16] indicated that cold start accounts for more than 50% and 70% of total PN for GDI and PFI vehicles, respectively.

Figure 3.3. shows the mass spectrum and size distribution of organics and PAHs during the first minutes of the WLTC cold start cycle.

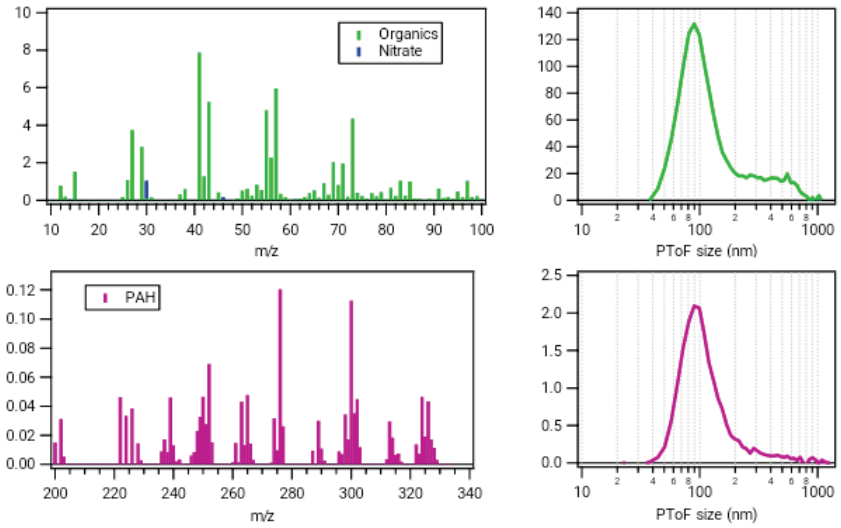

Figure 3.3. *Mass spectra of the organics and PAHs fraction and related size distribution during the first minutes of a WLTC cold start for GDI3 Euro 5 vehicle.*

The organic mass spectrum is dominated by ion fragments C_nH_{2n+1} (m/z 29, 43, 57, 71, 99...) and C_nH_{2n-3} (m/z 27, 41, 55, 69, 83, 97…), corresponding to linear and branched alkanes and cycloalkanes, respectively.[17, 18] Others groups as aromatics (m/z 77, 91, 105, 119…) are also present. The PAHs family is characterized by many compounds (from m/z 200 to 330). The most intense signals are at m/z 276, 300 and 252, corresponding to $C_{22}H_{12}$, $C_{24}H_{12}$ and $C_{20}H_{12}$ masses and have been previously associated to road transport emissions.[19-21] Literature work assigns the ion fragment at m/z 276 to anthanthrene, benzo[ghi]perylene and indeno[1,2,3-cd]pyrene; the ion fragment at m/z 300 to coronene and the ion fragment at m/z 252 to benzo[b,j,k]fluoranthene and benzo(e)pyrene.[22, 23] Recently Mueller et al.[24] reported among the most abundant PAHs found in PM from ambient measurements the ion fragments at m/z 202, 228, 252 and 276 corresponding to the $C_{16}H_{10}$, $C_{18}H_{12}$, $C_{20}H_{12}$ and $C_{22}H_{13}$.. The authors observed an increase of those signals during rush hours, and therefore suggested that these compounds were originated by road transport. PAHs have also been measured in the particle phase during tunnel experiments, the authors also reported higher PAHs EFs in wintertime rather than during summertime.[19]

Figure 3.3. also shows the size distribution measured by the AMS for organics and PAHs fractions during the first 2 minutes of the cold start. These chemical species present a mean diameter centered at 100 nm (vacuum aerodynamic diameter, Dva) during the cold start, however for the organics a second broad distribution mode is observed, spanning the 100-900

nm range (which may be explained by the agglomerates or droplets observed by the TEM images, see figure 3.6. and 3.7.). The FMPS also indicates similar size distribution. The concomitant size distribution suggests that during cold start soot particles are coated with both organics and PAHs. Figure 3.4. presents the size distribution of the organic fraction during the whole WLTC cycle. It can be observed that after the first minutes the organic particle fraction is centered on 100 nm (Dva) probably coating soot particles. Small particles can't be observed by the AMS because of the cut-off of the aerodynamic lens.

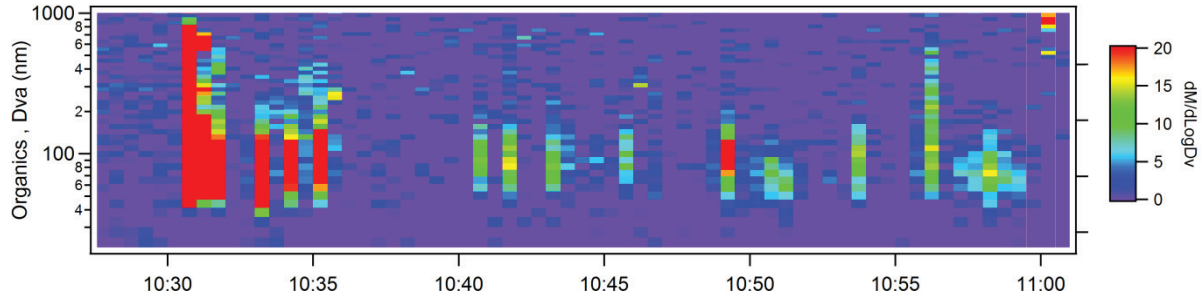

Figure 3.4. *Size distribution of the organic fraction during a WLTC cold cycle for GDI3 vehicle.*

Figure 3.5. presents black carbon and particle size distribution (5-60 nm) of PM emitted from an Euro 5 DI gasoline vehicle during Artemis Urban cold start (cycle n°1) and Artemis motorway (cycle n°2-5). AMS and FMPS instruments were not available for those experiments, hence, particle size distribution above 60 nm and time series of organic and inorganic species are not reported here.

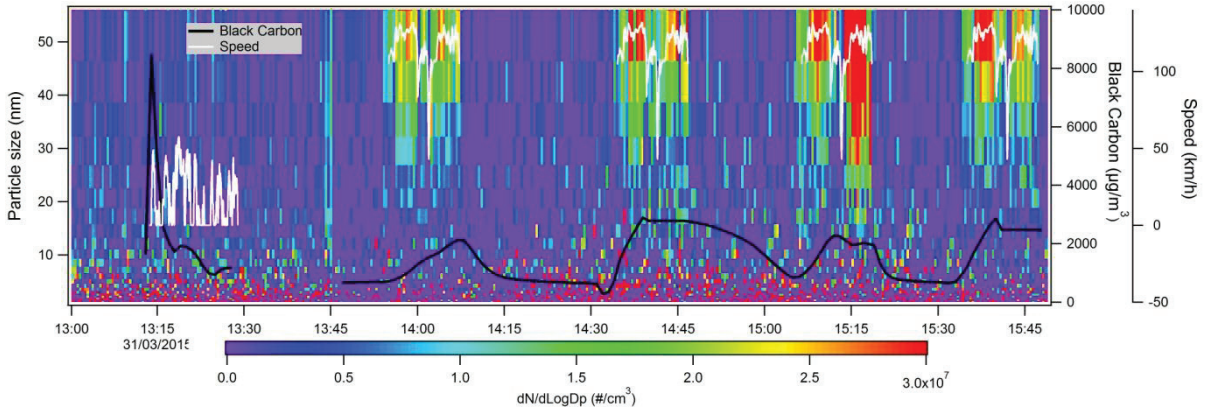

Figure 3.5. *BC concentration and particle size distribution (5-60 nm) for Euro 5 GDI1 vehicle during Artemis urban cold start (cycle n°1) and Artemis motorway (cycle n°2-5).*

Artemis urban cold start presents higher BC emissions than Artemis motorway. However, particle size distribution suggests that the emitted particles present a diameter larger than 60 nm during Artemis urban, while they are considerably smaller around 50 nm during motorway cycles. For this vehicle BC emissions during cold reach $8x10^3$ µg/m^3, slightly lower that what observed for the GD3 vehicle in figure 3.2.a-b. Artemis motorway cycle presents ultrafine particles emission (observed between 15 and 60 nm) probably due to high

temperatures and high exhaust flow. These high speed periods are characterized by BC emission in the range of 2-3x10^3 µg/m^3. Artemis motorway cycles present good repeatability, with respect to BC concentrations and particle size distribution. Particle size distribution (14-300 nm) for GDI2 vehicle during Artemis urban cold start and Artemis motorway cycles are presented in Figure AIV.2. in the annex IV.

The exhaust particle samples of a Euro 6b GDI vehicle (GDI2) were collected using a Mini Particle Sampler system (see section 2.3. in chapter II) and then analyzed using the transmission electron microscopy (TEM) and scanning electron microscopy (SEM) techniques, and by energy dispersive spectrometry (EDS) to determine the elemental chemical composition. The total flow sampling was set at 300 ml/min. PM was collected onto TEM porous grids. Figure 3.6. shows TEM images from particles sampled during the cold start of a Artemis Urban cycle (first 2 minutes only) for a Euro 6b (GDI 2) vehicle with a dilution ratio of 50.

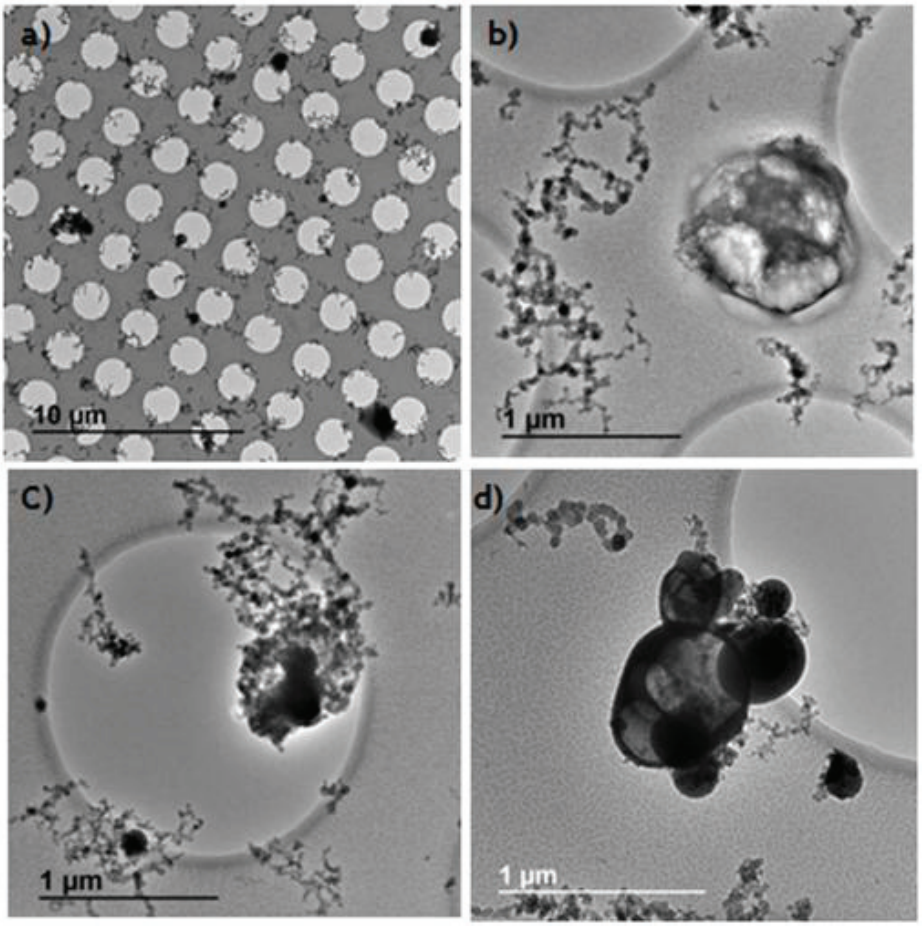

Figure 3.6. *TEM analysis during Artemis Urban cold start sampled in the first 120 seconds for GDI2 vehicle.*

The figure 3.6.a shows an overview of the sample. Figure 3.6.b, c and d show the fractal structures (chains and agglomerates) that seem to be formed by primary soot spheres of different sizes and some liquid or viscous droplets between 100 nm to 500 nm, which easily evaporate when exposed to the electron beam of the microscope. Results are in agreement

with high black carbon emissions measured by the aethalometer during cold start period for Artemis urban cycle (figure 3.5.).

Figure 3.7. shows the TEM images from particles sampled during a cold WLTC cycle for the same vehicle and for a dilution ratio of 40 at 50°C. In total two samples were collected during the cycle: one at the beginning (from 0 to 3 minutes of cycle) (a-c) and the other at the end of the cycle (from 26 to 29 minutes) (d-e).

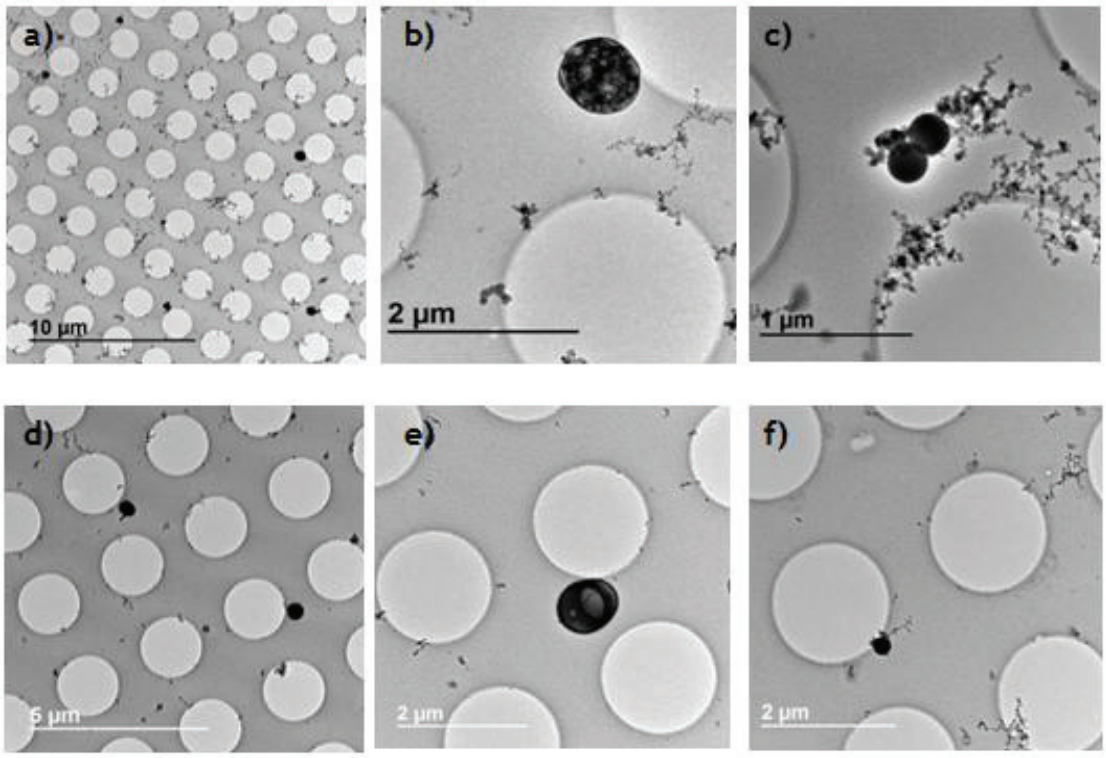

Figure 3.7. *TEM analysis during WLTC cycles for Euro 6 G-DI2 vehicle: a, b and c sampled during the first two minutes of the cycle and d, e and f sampled at the end of the cycle (from the 26th to 29th minute).*

Comparing the Artemis urban cold and the first minutes of the WLTC cold start for the same vehicle, a higher number of aggregates of fractal material is observed during the Artemis urban cold. In the last part of the WLTC cycle low fractal material is observed, according to aethalometer measurements, however the droplets are still observed (Figure 3.2.).

Emission of droplets from the GDI2 vehicle were often observed during all cycles and during lows and high speed periods, they can have variable sizes ranging from 200 nm to almost 1µm (more details about their chemical composition will be give at the end of this section). Table 3.2. shows the results from the EDX analysis of the particles shown in figures 3.6. and 3.7. On average, these droplets present C and O as major components, followed by S which was highly enriched (up to 40 wt %) in few droplets. Other minor components as sodium, calcium, potassium, manganese, phosphorous and nickel are also observed.

Table 3.2. *Particle composition by EDX in mass % analysis for GDI2 vehicle.*

% Mass	Evaporating Droplet Fig.3.6.b	Droplets Fig.3.6.c	Soot chains Fig.3.6.c	Droplet Fig.3.6.d	Droplet Fig.3.7.a	Droplet Fig.3.7.b	Empty Grid
C	20	47.7	76.6	28.6	41	68	68
O	12.6	28.5	13.4	27.6	21	18	18
Si	-			18.7		10	14
S	39.6	16	1.9	7.4	31	1.5	
K	2.8				2	0.3	
Mn	1.1		0.5	0.2	1.6	0.5	
Ni	1.3		0.6		1.7	0.7	
P	0.3	1.5	4.3	3.3		1.3	
Ca	1.2	16	0.9		1	0.9	
Na	0.9	1.5	1	8.4	1.2	1.1	
Mg	0.4	0.3			0.6	0.2	
Fe				0.5			
F		1.5		2.9			

Most of these elements seem to be associated with lubricant/oil composition and additives.[25-27] Karjalainen et al.[28] found spherical particles of variable diameter (10-200 nm) composed of oxygen, zinc, phosphorous and calcium and suggested that the metals were originated from the lubricant oil and not from fuel. Elements coming from lubricant oil as sulfur, calcium, zinc and phosphorous were also reported by Fushimi et al.[29]

Very few samples contained Fe and F. Fe has been observed in gasoline and diesel emissions [30] and has also found on used lubricant oil while it was almost absent in new lubricant oil suggesting that abrasion from engine wear was the main source of the monitored Fe. On the other hand, organics fluorine compounds have been previously reported in literature as friction modifiers additives in lubricant oils.[31] Soot chains and agglomerates have also been analyzed and of course they contain mostly C up to 76% but also O suggesting the presence of unburned organic material coating the soot particles, which was confirmed by particle mass spectrometry in figure 3.2. Additional traces of S and P are also found in those agglomerates which are mostly observed during cold start and not during high speed periods.

Samples collected after CVS from Euro 5 GDI vehicle (GDI1) for Artemis Urban cold start and Artemis Motorway cycle are presented in figure 3.8. and 3.9, respectively. The figure 3.8. presents TEM images from particles collected for the first 2 minutes of a cold start Artemis Urban cycle (average dilution of 9 m^3/min). The results are similar to those observed by TEM at the tailpipe for the Euro 6 GDI (GDI2) vehicle with two major families of particles, fractal soot

organized in chains and agglomerates and some droplets. BC profile of Euro 5 DI gasoline (figure 3.5.) is in agreement with TEM analysis. Figure 3.8.d shows the typical soot structure with a mean diameter of the primary carbon particles around 25 nm.

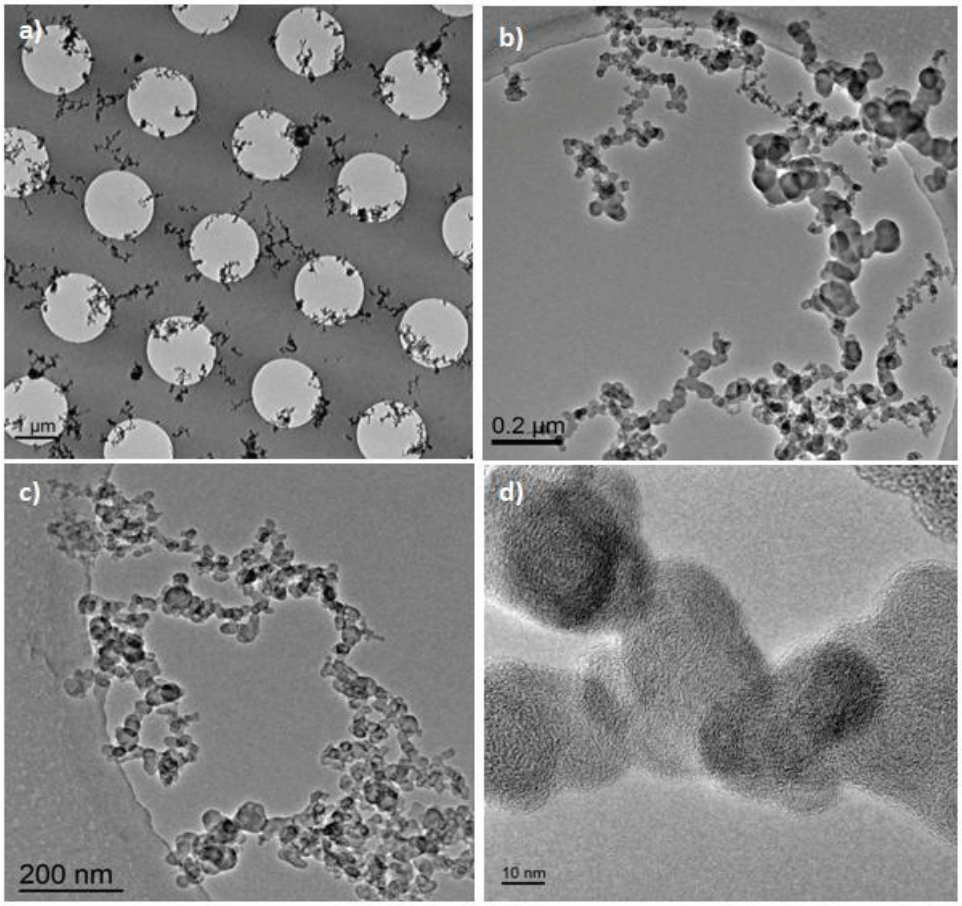

Figure 3.8. *TEM analysis during cold start Artemis Urban cycle for a Euro 5 GDI1 vehicle (sampled after CVS, first 120 seconds).*

The results are in agreement with previous literature on gasoline particles: Barone et al.[32] found primary soot particles with diameter in the range 20-25 nm and some aggregates around 200-500 nm. Gaddam and Vander Wal [33] and Mathis et al.[34] reported primary particles from 16 to 27nm. Ronkko et al.[25] and Karjalainen et al.[28] observed emission of primary particles with diameter around 15-20 nm during NEDC cycle.

A grid was also collected during an Artemis Motorway cycle (first part of cycle) for a Euro 5 (GDI1) after CVS (Figure 3.9.). TEM results show high BC emissions at the beginning of the motorway cycle. On average, the chains are slightly shorter and the agglomerates also less abundant than the one reported in Figure 3.6. and 3.7. during cold start, according to BC measurements. BC emissions of Euro 5 DI gasoline for Artemis Motorway (figure 3.5.) is in agreement with TEM analysis.

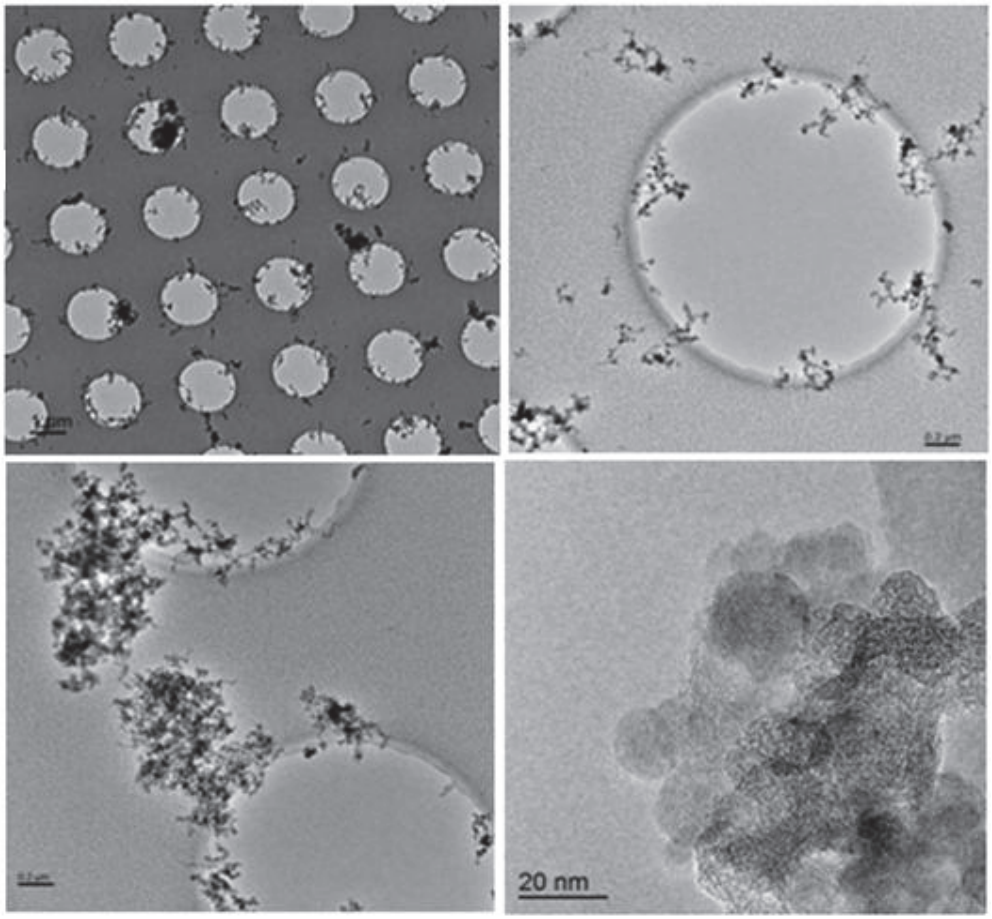

Figure 3.9. *TEM analysis during Artemis Motorway cycle for Euro 5 GDI1 vehicle (after CVS, first 7 minutes of cycle).*

3.1.3. Diesel Particle Emission

PM Emissions of a Euro 5 diesel D3 vehicle were sampled directly at tailpipe during WLTC cycle with dilution ratio in the range of 10-15. Figure 3.10. presents the chemical composition of the condensable PM fraction (organics, sulfate, nitrate and ammonium), particle number and particle size distribution under a WLTC cold start (first cycle) and hot start (second cycle). Ammonium bisulfate is emitted in appreciable concentrations during the cold WLTC cycle, reaching almost 270 $\mu g/m^3$ (calculated by the sum of sulfate and ammonium). The organic fraction is quite low around 4-5 $\mu g/m^3$ during some acceleration/decelerations of the cycle. For this vehicle BC and PAHs were close to the detection limit of the instrumentation and hence no plotted here. Some nitrate traces were also measured during the cold start cycle. Particle distribution given by FMPS indicates mean diameters around 80-100 nm. During hot start cycle, sulfate and ammonium are emitted in small concentrations compared to the cold start, reaching maximum values of 35 $\mu g/m^3$ and 6 $\mu g/m^3$, respectively. The organic fraction is low, close to background values and presents some peak reaching 5 $\mu g/m^3$, corresponding with sulfate emissions. Particle size distribution presents a mean diameter around 60 nm and little particle number emissions around $8x10^5$ particles/cm^3.

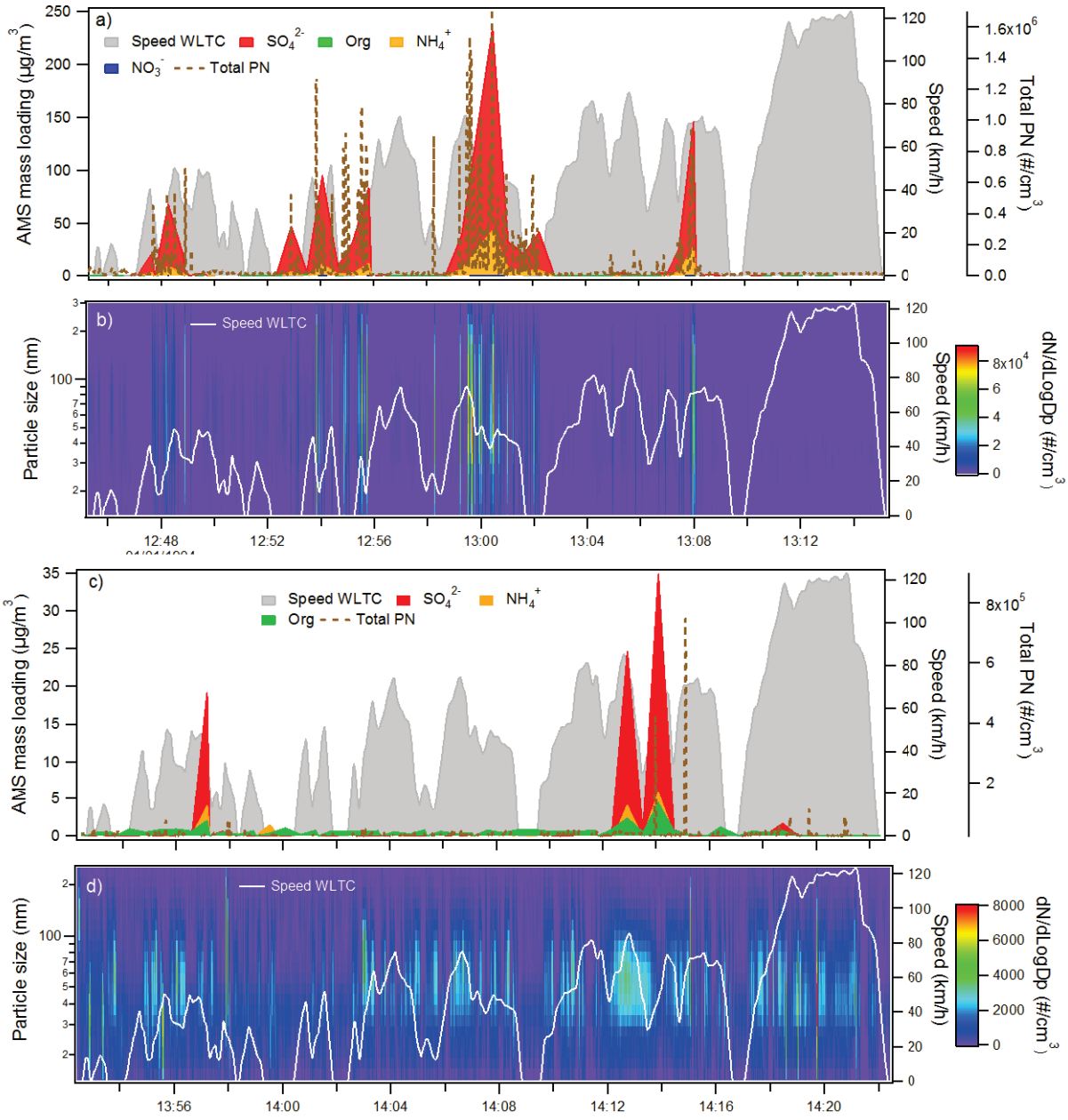

Figure 3.10. *Time series concentration of organic, SO_4^{2-}, NO_3^-, NH_4^+, PN and particle size distribution during WLTC cold/hot start for a Euro 5 D3 diesel.*

PM emissions of a Euro 5 D1 vehicle were sampled after CVS dilution system for Artemis Urban cycles. Figure 3.11. shows the chemical composition of the particle phase (organics, water) and particle number concentration.

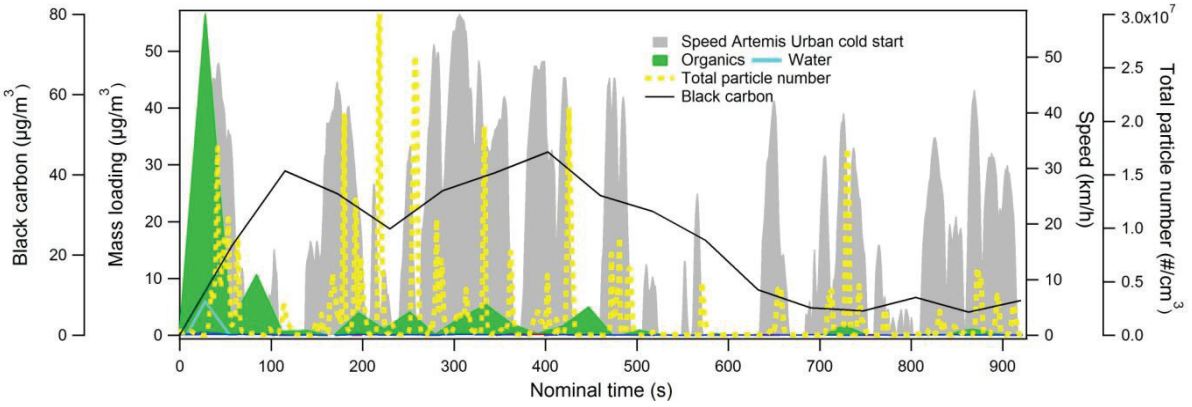

Figure 3.11. *Time series concentration of organic, water, BC and PN during Artemis urban cold start cycle for a Euro 5 D1 diesel vehicle.*

Particles are emitted at the beginning of cycle during warm-up period and are mainly composed by organic material and BC. No sulfate emissions were observed during the Artemis Urban cycle, probably due to the low speeds and low engine temperatures. The mass spectrum of the condensable species emitted during cold start can be found in annex IV (figure AIV.1.) and indicates the dominance of aliphatic compounds. Black carbon is presented together with organic particles during cold start phase but also continuously in the first half of the cycle, which is in agreement with total particle number. Due to low concentrations of BC for diesel vehicles, aethalometer presented a noisy time series. Thus MultiAngle Absorption Photometer (MAAP) was used, which has a good sensitivity but bad time resolution.

TEM grids were collected for the first 5 minutes on the Artemis Urban cold cycle (Figure 3.12.). Soot in form of fractal structure as chain or agglomerates were observed, in addition to some fine filaments of amorphous material. These structures have been related to the condensable organic fraction observed by the AMS. The amorphous carbon may be due unburned fuel that can condense upon the cold dilution occurring on the CVS and can also reorganize its structure on the TEM grid surface. The diameter of the primary soot particles was found in same range than gasoline vehicles (≈25 nm). Literature reports similar sizes for diesel emitted PM and carbon aggregates. Chain and aggregates sizes may also depend on the collection conditions (as dilution and temperature).[35-38]

EDX analysis showed that the diesel particles were mainly composed by C 80%, O 10%, 2.9% Na, 3% Si, 2% K and 0.5% S. Images were taken mainly on the soot chains or agglomerates. Unfortunately EDX analysis of the few droplets observed did not allow to determine the chemical composition because of the fast evaporation of these latter under the electron beam of the microscope.

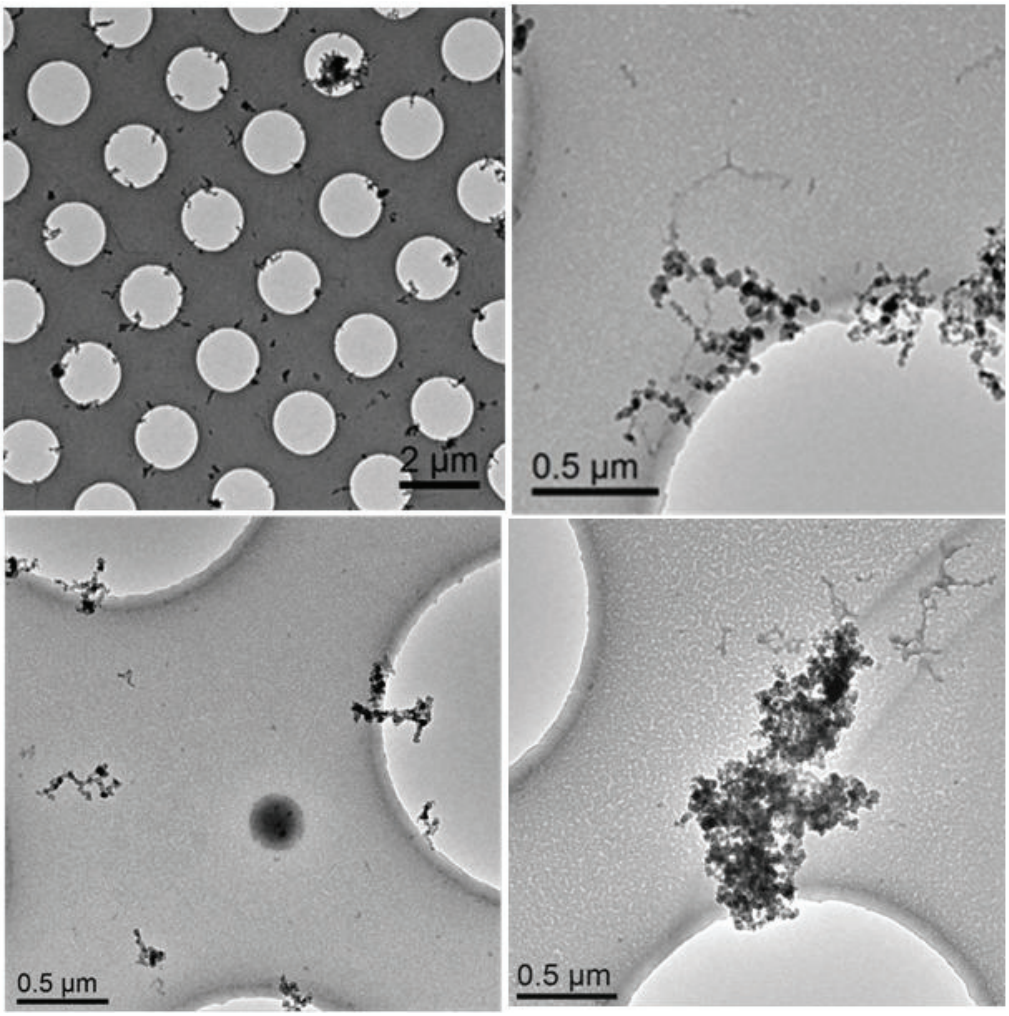

Figure 3.12. *TEM analysis during Artemis urban cold start period for Euro 5 diesel D1 vehicle*.

Figure 3.13. presents a) chemical composition of the particle (organics, sulfate, ammonium, water and BC), b) the particle size distribution by SMPS (15-450 nm) and c) by the SMPS+E (3-40 nm) and the total particle number for the Euro 5 D1 diesel vehicle during Artemis Motorway cycles at the CVS. The four motorway cycles shows a good repeatability in term of PN emitted and chemical composition. During the first two minutes of the first acceleration of the first motorway cycle high emissions of BC (up to 250 µg/m^3) and organic particles (up to 70 µg/m^3) with mean diameter around 100 nm have been observed. After approximately a couple of minutes, the chemical composition, the particle size distribution and the PN concentration radically changed.

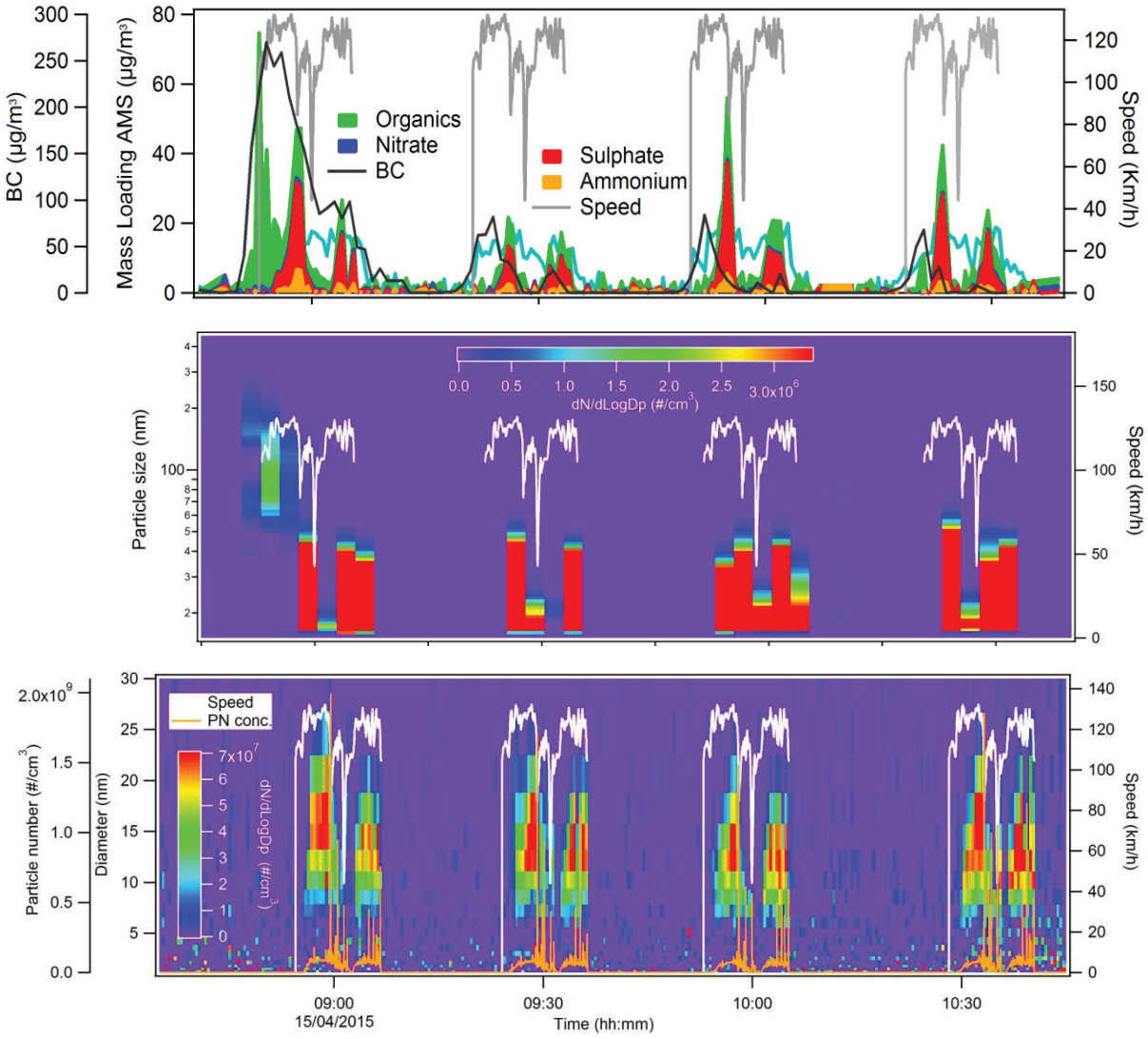

Figure 3.13. *Time series concentration of organic, water, NO_3^-, NH_4^+, BC, PN and particle distribution under Artemis Motorway cycle for Euro 5 D1 diesel vehicle.*

During high speed, emission of nucleating particles with mean diameter around 12-15 nm was observed. The chemical analysis suggested that these particles were mainly formed by ammonium bisulfate (the concentration of ammonium was relatively low and it was not able to fully neutralized the sulfate). The observed behavior was interpreted as passive DPF regeneration due to the relatively high temperatures reached and to the specific after-treatment device protocol of this vehicle. Previous literature reported both emission of gaseous sulfuric acid [39] and bisulfate particles and BC during active DPF regeneration.[17] Together with ammonium bisulfate, some traces of organic compounds were also emitted. The organic fraction could arise from the post-injection occurring during DPF regeneration. The BC profile during the four MW cycles seems to anticipate the nucleation mode burst as also confirmed the SMPS analysis.

Figure 3.14. shows the results of two samples taken during the Artemis Motorway cycles for D1 vehicle. The TEM grids were sampled at the maximum speed reached by the cycle for 5

minutes and do confirm what has been shown in figure 3.13.: little BC emissions were observed and most of the particles were composed of amorphous filaments (probably organic material) and small spherical particles (could be ammonium bisulfate). No EDX analysis was possible on those samples since the collected material rapidly evaporated under the electrons beam.

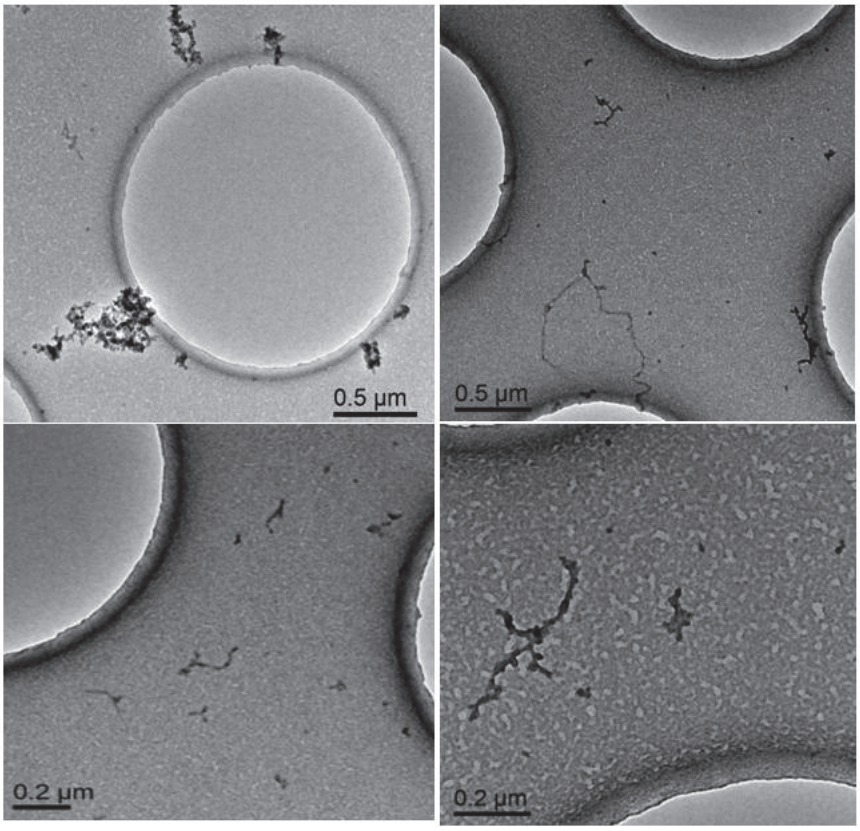

Figure 3.14. *TEM analysis during Artemis Motorway cycle for Euro 5 D1 vehicle (after CVS).*

3.1.4 Emission Factor of Particle Phase

Since one of major objectives of CaPVeREA project was to investigate unregulated compounds, which includes particle condensable material and particles below 23 nm, the PMP protocol was not applied during emission studies. For those measurements a FPS-4000 dilution system has been used. Particle size distribution and concentration have been measured using a FMPS under different dilution conditions.

Table 3.3 presents the vehicles and the sampling conditions used for the particle emission study. Figure 3.15. presents a) the total particle emission factor and b) the fraction of particles in the range 14-23 nm during the different driving cycles. The lower limit in size was fixed at 14 nm due to instrumental limitations. Indeed the FMPS shows often some measurement bias in the range 5-12 nm. Two diesel and two gasoline DI car are presented here.

As expected the GDI vehicles do emit a high number of particles and can reach values of 10^{13} #/km during WLTC cycles and Artemis Motorway. In general, the Euro 6 vehicles present

higher concentrations of PN than the respective Euro 5 cars. It is worth to note that the difference of dilution temperature (90-120 °C for Euro 5 vs. 25-50 °C for Euro 6) could be one of the factors affecting such a difference. GDI2 widely exceeds PN emission limit for WLTC, Artemis Urban cold and Artemis Motorway cycles, while it is in the limit for the urban and road cycles. GDI3 presents values close to the limitation for WLTC cycles. Both diesel vehicles are in agreement with in-force PN limitation.

Table 3.3. *Main characteristics and dilution conditions for vehicle and experiments carried out for particle number study.*

	Cycle	Aftertreatment device	Dilution ratio	Primary dilution	Dilution temperature
GDI3 Euro 5	WLTC cold	TWC	20-46	4.5-10	90
	WLTC hot		10-46	2-10	
GDI2 Euro 6b	WLTC cold	TWC	30	4	36
	WLTC hot		30	4	36
	Urban cold		50	6.7	36
	Urban hot		50	6.7	25
	Road		30	4	36
	MW		13	2.2	36
D3 Euro 5	WLTC cold	cDPF	10-15	2-3	120
	WLTC hot		7-15	1.8-3	
D2 Euro 6b	WLTC cold	cDPF + NOx trap	40-50	5-6.7	36
	WLTC hot		40	5	36
	Urban cold		10-85	2-11	36-50
	Urban hot		10-85	2-11	36-50
	Road		50	6.7	36
	MW		18	3	36

PN EFs are most of the time measured following the PMP protocol. Therefore, they presented lower EFs ($9.1x10^{11}$ to $5.8x10^{12}$ #/km) with respect to those presented here, at least for GDI vehicles.[30, 40-44] On average, cold start cycles emit between from 2.25 and 5 times more particles than hot start, for WLTC and Artemis Urban cycles, respectively. Cold start effect on PN concentration has been previously reported with reduction of PN emissions ranging from a factor 2 to 18 during hot start cycles for gasoline and diesel vehicles.[13, 16, 26, 30, 40, 45, 46]

For GDI vehicles, the PN concentration in the 14-23 nm size range represents around 20% of the total PN emitted during cold start cycles, this can be observed for WLTC cycle in figure 3.2. where particle mean diameter is around 50-60 nm. For hot cycles, the percentage of particles in 14-23 nm range increases up to 35- 40%% for Artemis motorway. Lower dilution ratio (table 3.3.) during motorway cycle can partly explain the higher emission fraction in 14-23 nm range.

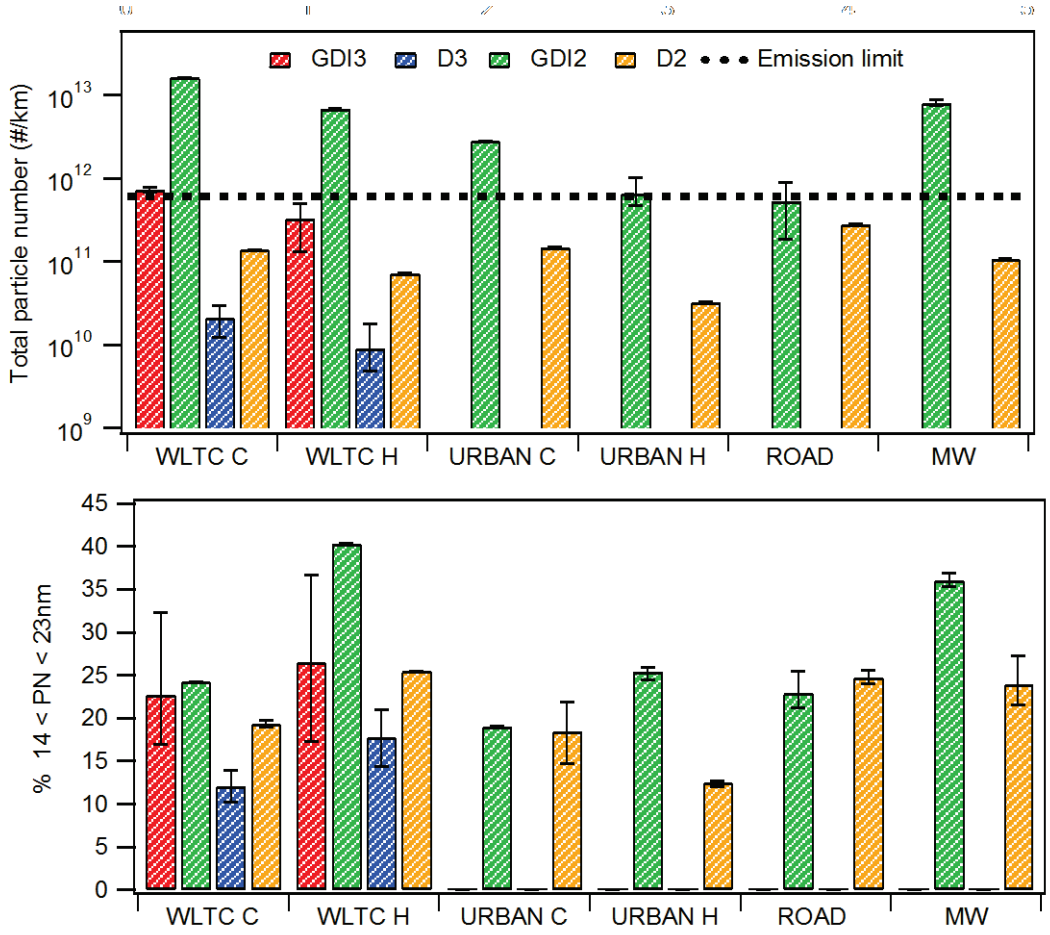

Figure 3.15. *Percentage of 14< PN ≤ 23 nm compared to total particle number emission factors for four vehicles and during different cycles. C: cold, H: hot*

Regarding diesel vehicles, during the WLTC cold, the PN concentration in the 14 -23 nm size range represents around 11% and 22% of the total PN for D2 and D3 vehicles, respectively. This percentage slightly increases to 18% and 25% for WLTC hot. In general, particles emitted during cold start present bigger diameters than those during acceleration and brakes episodes, and are considered mainly black carbon aggregates (CaPVeREA report).

Solid particles below 23 nm have been previously measured in the literature: Giechaskiel et al.[47] reported a sub-23 nm PN concentration of < 20% for diesel vehicles and 35-50% for gasoline DI vehicles. Giechaskiel and Martini[48] suggested average values of sub-23nm particles for GDI and diesel vehicles of 30-40% of the total PN concentration.

The possibility to reduce the cut-off diameter of PN concentration from 23 to 10 nm has been considered by the European Union through projects that investigated the feasibility and the accuracy of a new PMP protocol. Giechaskiel et al.[48] suggested that an implementation of PMP protocol by regulating particles in the 10-23 nm size range could be possible with actual state-of-art instrumentation technology. While lowering size below 10 nm it is thought to lead to possible sampling bias coming from re-nucleation after heating system.[49, 50] Based on the tests performed during CaPVeREA project, implementation of new PMP protocol accounting for particles range between 14 and 23 nm in future WLTC legislation would improve the total quantification of particle number.

Figure 3.16. presents EFs of BC, ammonium, nitrate, sulfate, organics and PAHs for the vehicles tested in framework of the project CaPVeREA. The AMS could be deployed only for three Euro 5 vehicles (two diesel, one gasoline). BC is mainly emitted by gasoline DI vehicles with values that range from 6 μg/km for the GDI3 during WLTC hot to 3×10^3 μg/km for GD1 during Motorway cycle. For diesel vehicles BC emission is considerable lower due to the DPF device. However, differences among the tested cars are also observed with emissions ranging from 5 μg/km for the D3 vehicle during WLTC hot to 76 μg/km for the D1 during Urban Artemis cold cycle. As a general trend, Artemis Urban and Motorway cycles do largely contribute to BC emissions. Gasoline and diesel EFs are in agreement with those previously reported by the literature, 1-$3.7\text{x}10^3$ μg/km and 22-35 μg/km, respectively.[14, 42, 51-53]

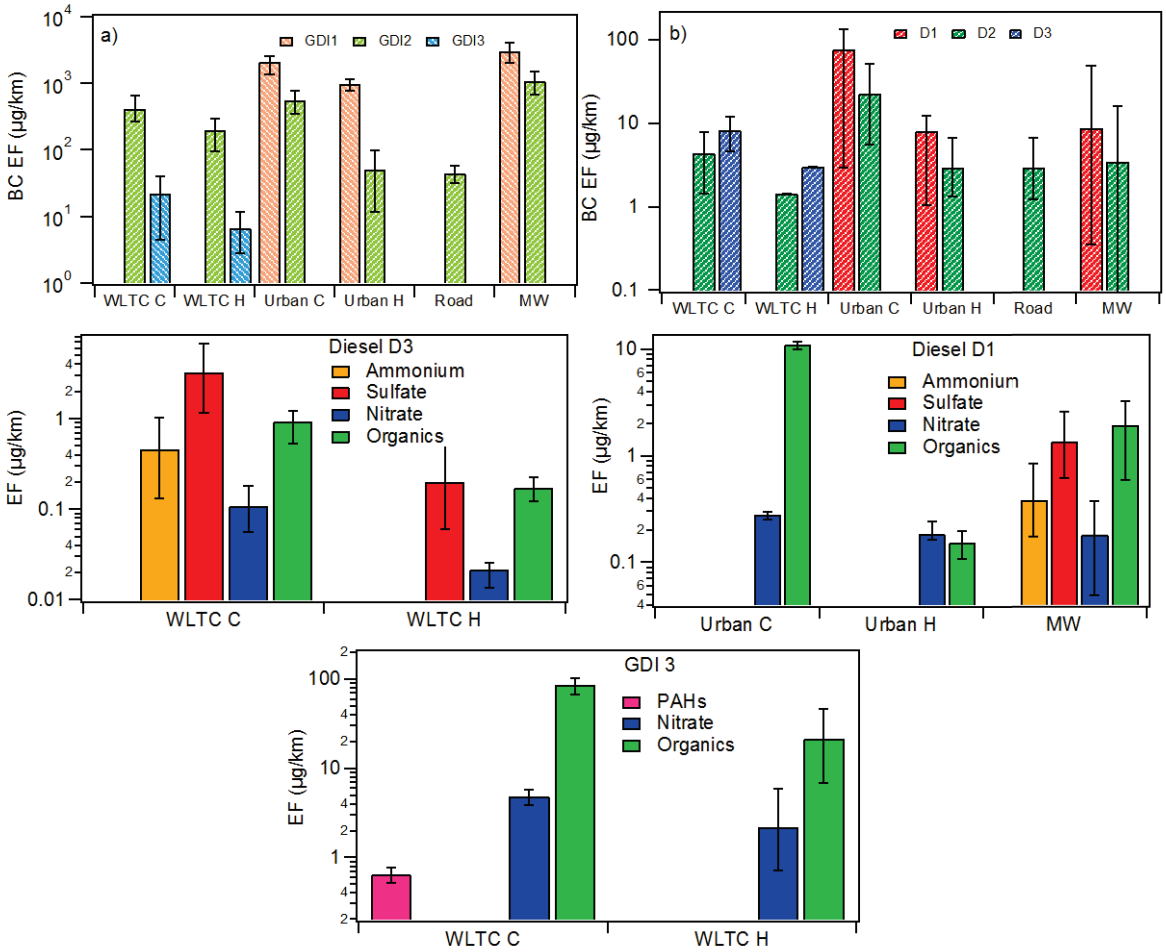

Figure 3.16. *EFs of a) BC for three GDI vehicles during Artemis and WLTC cycles, b) BC for three diesel vehicles during Artemis and WLTC cycles, c) organic and inorganic fraction for Euro 5 diesel D3 vehicle during WLTC cycle, d) organic and inorganic fraction for D1 vehicle during WLTC cycle and e) organic and inorganic fraction for GDI3 vehicle during WLTC cycle.*

The figures 3.16.c, d and e present the emission factors of sub-micrometer particles in terms of organic and inorganic fraction measured by the AMS. Generally, both diesel cars emit relatively low emissions of organic material, some ammonium bisulfate and traces of nitrate. EFs are higher during cold cycles (WLTC and Urban Artemis) but are quite variable for the two vehicles. The D3 car presented sulfate EFs in the range of 0.2-3 µg/km and organics in the range 0.2-1 µg/km, D1 showed higher EFs of organics ranging from 2 to 10 µg/km, sulfate are observed during high speed cycles (MW Artemis) and reaches 1-2 µg/km while nitrates are low around 0.2 µg/km. For the GDI vehicles EFs are much higher during the WLTC cold and the organic fraction can reach 85 µg/km, nitrate 5 µg/km and PAHs 0.6 µg/km, while during the WLTC hot organics decreased to 21 µg/km and nitrate to 2.2 µg/km. PAHs were not measured during hot cycles.

3.2. Regulated Gas Phase Pollutants

3.2.1. Transient Profiles of Gaseous Pollutants

A series of regulated compounds (CO, THC, NOx) and non regulated compounds (CO_2, benzene, NH_3) have been measured online during WLTC cycle speed profile for diesel and gasoline DI Euro 5 vehicles. The figure 3.17. presents time series emission profile of CO for a) GDI3 and b) D3 vehicles during WLTC (cold and hot) cycle.

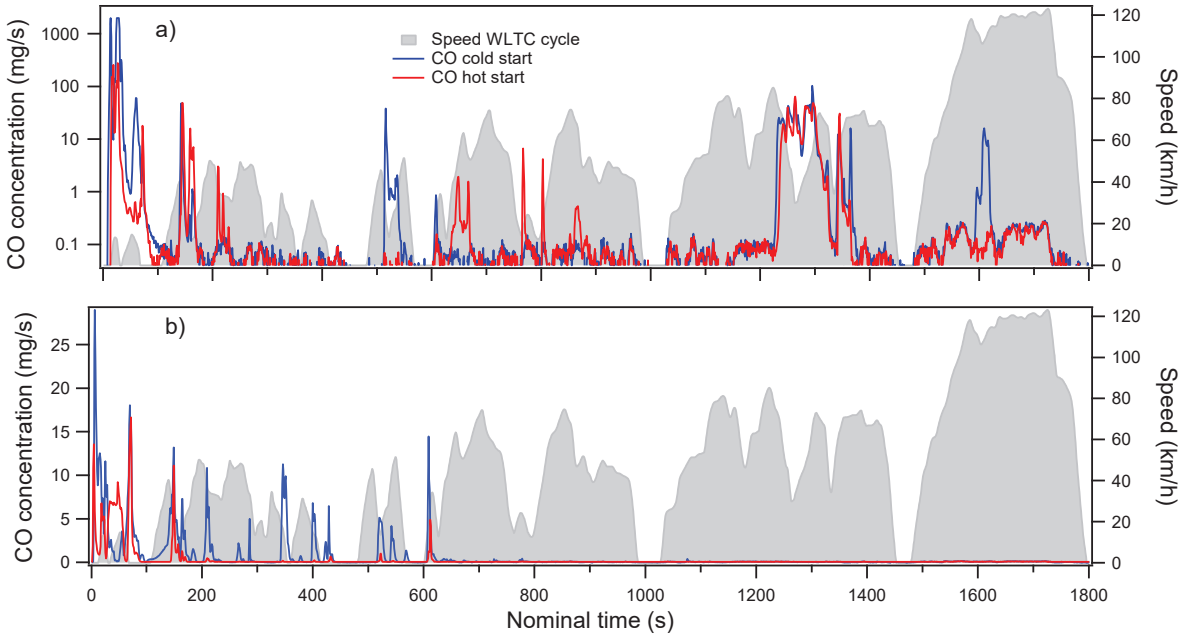

Figure 3.17. *CO time series emission during WLTC (cold and hot start) for a) GDI3 and b) D3.*

CO emissions are strongly related to cold start engine operation for both D3 and GDI3 vehicles. Almost all the CO is emitted during first 200 seconds and 600 seconds for gasoline and diesel vehicle, respectively. CO emissions are generally lower during hot cycles. Such differences between cold and hot periods have been reported previously in literature [15, 54-56] and explained by the low efficiency of catalyst converter at low temperatures. CO emissions for gasoline vehicle are much higher than diesel vehicles. For cold cycles, the difference is two orders of magnitude (3000 mg/s versus 30 mg/s). Similar results have been previously observed for recent diesel and gasoline cars.[15, 51] Such differences can arise from air/fuel ratio reached in engine or catalyst aging.

Figure 3.18. presents time series of THC emissions for a) GDI3 and (b) D3 vehicles during WLTC (cold and hot) cycle.

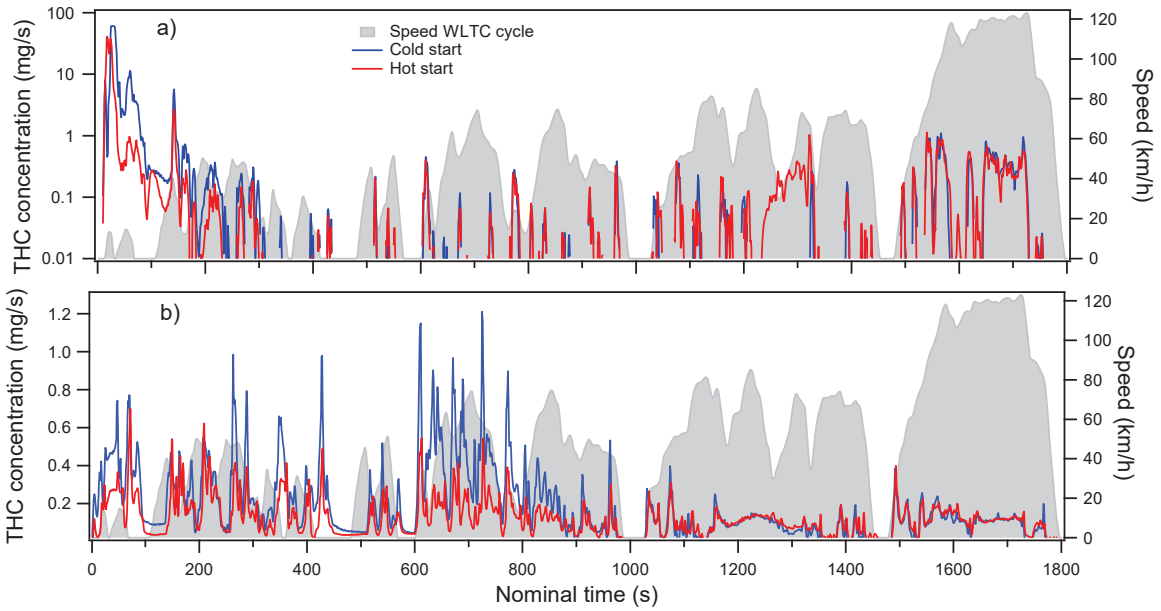

Figure 3.18. *THC time series emission during WLTC (cold and hot start) for a) Euro 5 GDI3 and b) Euro 5 D3.*

THC concentration presents a high dependence on the catalyst temperature. For the GDI3, around 90% of THCs are emitted during the first 200 seconds of the cold cycle. A similar trend was observed by Suarez-bertoa et al.[57] who reported that 85% of total THC were emitted during the first minutes of the cycle. Such high emissions in the first seconds are explained by the poor efficiency of the oxidation catalyst at low temperatures. Once catalyst warms-up, most of the HCs are efficiently oxidized.

For the diesel D3 car, the emitted concentration of THC is very low, with maximum values around 1.3 mg/s, such lower concentrations are explained by fuel composition and engine operation. Alves et al.[52], Weilenmann et al.[15], Gumus[54], Martinet et al.[1] and others authors already reported this important difference in THCs emission between gasoline and diesel cars.

Figure 3.19. presents time series profile of NOx emissions for a) GDI3 and (b) D3 vehicles under WLTC (cold and hot) cycle. Results suggest that NOx emissions are influenced by acceleration and brakes changes during high speed periods, when engine temperature and flow are high. Thus, higher NOx emissions are generally emitted during the motorway section of WLTC cycle, increasing substantially from 5 mg/s to 60-70 mg/s in case of diesel vehicle. Ko et al.[58] and Lopes et al.[53] reported similar trends under NEDC for both Euro 6 and Euro 5 Euro 6 vehicles. Karjalainen et al.[26] also reported higher NOx emissions during last part of NEDC (motorway part) for a gasoline Euro 5 vehicle. This specific gasoline vehicle (GDI3) presented an atypical high NOx concentration (saturated), due, we suppose, to a problem on the three-way-catalyst. Nevertheless, time series emissions follow similar profile for diesel and gasoline vehicle. For other gasoline vehicles, NOx emissions are considerably lower than the one presented here (see section 3.2.2.). Results are in agreement with previous literature, which

pointed out important emissions of NOx from diesel vehicles.[15, 51, 59, 60] Diesel engine works with excess of air and reaches higher temperatures in the engine, which lead to higher NOx formation.[61]

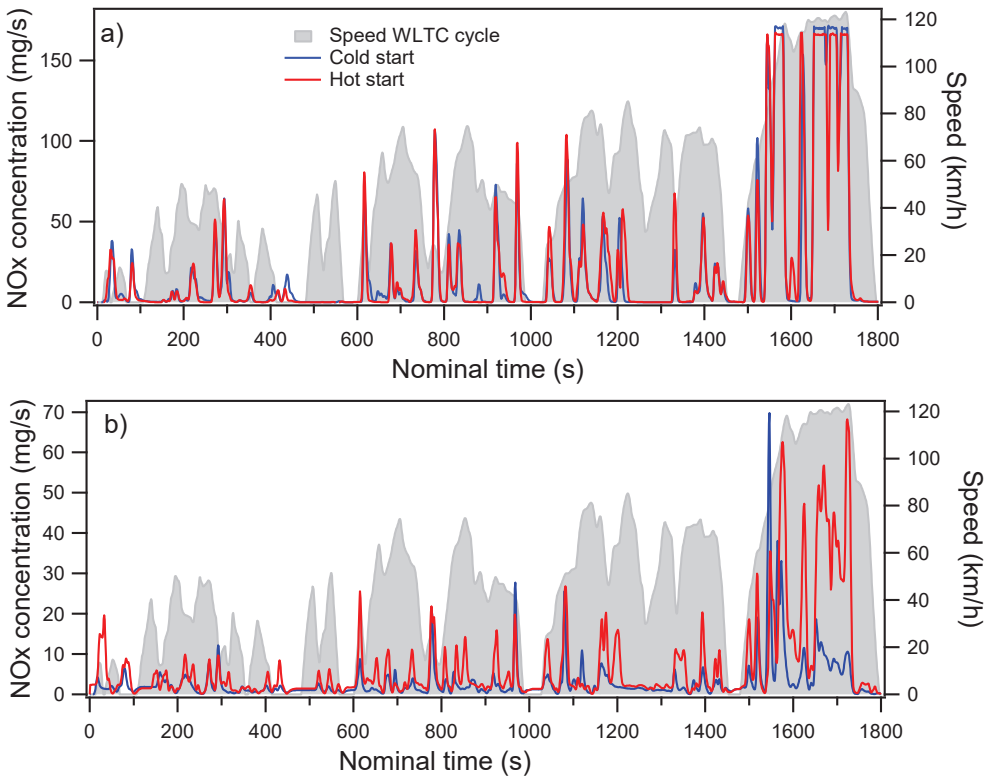

Figure 3.19. *NOx time series emission during WLTC (cold and hot start) for a) Euro 5 GDI3 and b) Euro 5 D3.*

Figure 3.20. presents time series profile of CO_2 emissions for a) GDI3 and (b) D3 vehicles under WLTC (cold and hot) cycle.

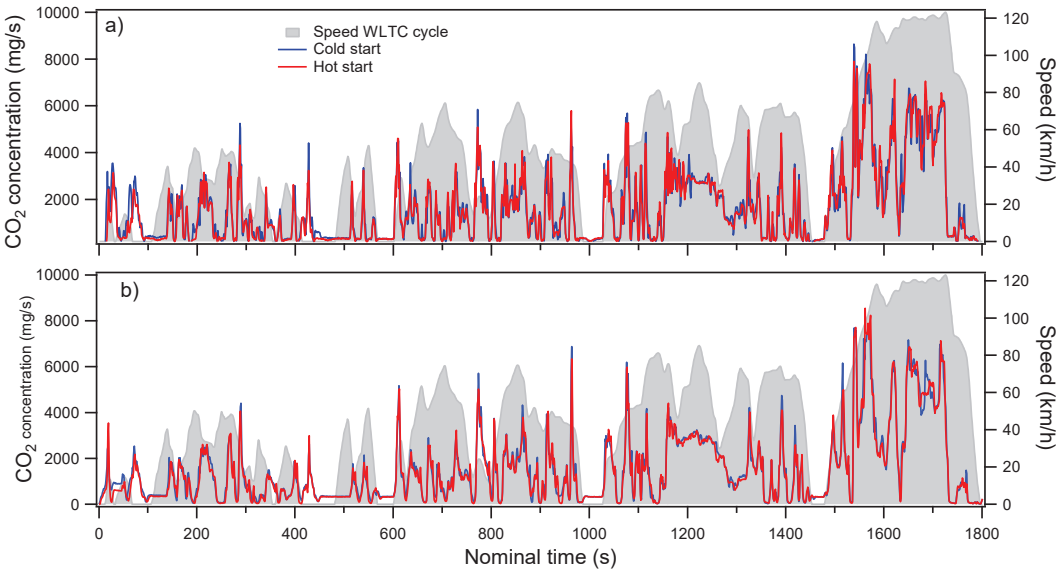

Figure 3.20. *CO_2 time series emission during WLTC (cold and hot start) for a) Euro 5 GDI3 and b) Euro 5 D3.*

The CO_2 emissions are linked with acceleration periods when the engine needs more fuel, causing higher emission of CO_2. Results are in agreement with Alves et al.[52] who also reported CO_2 emissions highly sensitive to frequency and intensity of accelerations. Thus highest emissions are therefore measured during the last part of WLTC cycle. This is in agreement with other authors [57, 62], who reported that around 60% of total CO_2 is emitted during extra-high speed period of WLTC. Both D3 and GDI3 vehicles present very similar time series profile and CO_2 concentration. Fontaras et al.[51] and Weilenmann et al.[15] found similar range of CO_2 emissions for gasoline and diesel Euro 5 vehicles among different driving cycles. No influence of cold start cycle is observed.

3.2.2. Emission Factor of Gaseous Pollutants

In this section are presented the EFs of regulated gaseous pollutants for the 6 vehicles investigated during CaPVeREA project. Four of the six vehicle have been included in previous studies published by IFSTTAR while data from the D3 vehicle and the GDI3 vehicle (both Euro 5) will be published in the future together with data on chemical composition of the particle phase and VOCs. Figure 3.21. presents emission factors of CO, CO_2, NOx and HC as for all tested cars. Note that not all vehicles have been tested during all cycles.

In general, vehicles comply the emission standards for CO with the exception of the GDI3 (Euro 6), which slightly exceed the limit. As already pointed out previously, EFs are higher for the GDI cars which can reach 1300 mg/km during MW Artemis. However the variability from one car to another is very important. Lowest EFs of 3 mg/km are measured for Urban Hot cycles. As the exhaust temperature and the flow increase with the vehicle speed, the residence time in the oxidation catalyst decreases, therefore CO emissions increase. Fontaras et al.[51] also reported for Gasoline cars highest CO emissions (EF= 2000 mg/km) during Artemis Motorway. Similar results were observed by Ghazikhani et al.[63] who showed that CO emissions are 4 times higher at 300 °C than at 200 °C. Presented EFs are in agreement with those found in literature for diesel (80-580 mg/km)[41, 51, 52, 60, 64] and gasoline (50-650 mg/km) passenger cars.[41, 42, 51]

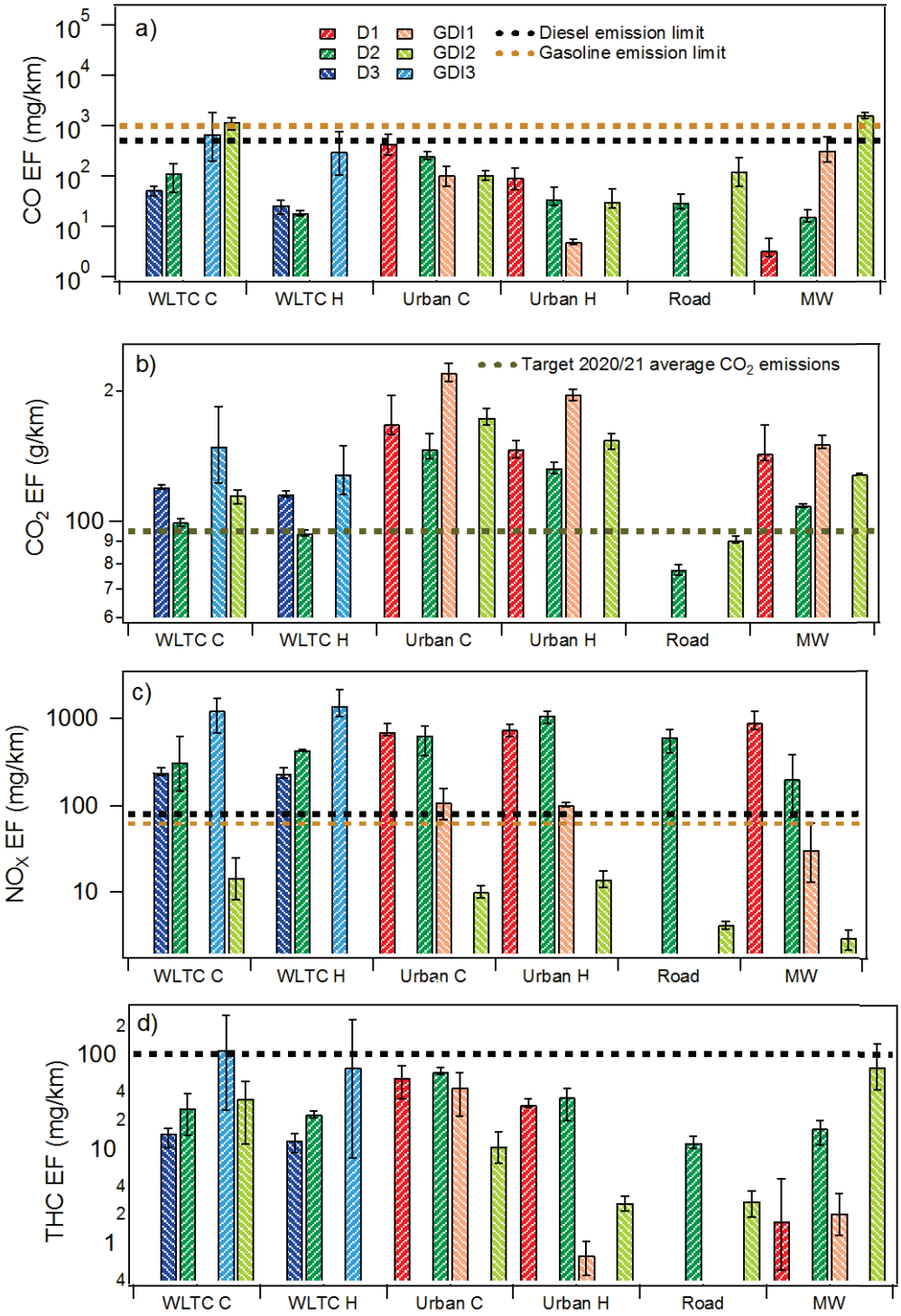

Figure 3.21. *EFs of CO, CO_2, NOx and THC for three GDI and three diesel (Euro 5 and Euro 6) vehicles. Error bars have been determinate from repeatability of EFs obtained during cycles.*

Diesel and gasoline vehicles exceed the future target of 95 g/km for CO_2 emission for most of the tested cycles. Even comparing EFs with actual CO_2 emission target of 118.5 g/km, most of the vehicles exceeded this value. Higher values are obtained for Artemis Urban cycle (cold and hot). The results are in agreement with Ntziachristos and Samaras [65] who suggest that higher EFs of CO_2 are observed for low speed cycles. In general, EFs for diesel vehicles are slightly lower than those presented for GDI vehicles. Diesel typically uses less fuel of a

comparable gasoline engine, what leads to a reduction of CO_2 per km.[66] Cold start is not a key parameter for CO_2 emissions. Results are in agreement with Alves et al.[52] who reported little differences between Artemis urban cold and hot for diesel and gasoline vehicles. Presented EFs are in agreement with those found in literature for diesel (100-300 g/km) [51, 52, 58, 60, 67] and gasoline (148-300 g/km).[41, 51]

As expected, diesel vehicles present much higher NOx emission than gasoline cars. In general, the three diesel vehicles exceed limitation for all cycles. In many cases, the EFs are up to one order of magnitude higher than what allowed by regulation. Surprisingly, the diesel Euro 6 (D2) presents values in the same order than other two Euro 5 diesel even if it was equipped with a NOx trap catalyst. The GDI2 car (Euro 6) presented the lowest NOx emissions. However, one of the gasoline cars, the GDI3 showed unusual high NOx concentrations. These unexpected high NOx values were attributed to a serious failure of the reduction catalyst in the TWC (section 3.2.1). WLTC and Artemis urban hot cycles present an increase of NOx of 17% and 25%, respectively, with respect to cold start cycles. Results are in agreement with Alves et al.[52] who studied the influence of cold start and reported 14% higher NOx emissions when engine is hot for diesel Euro 5 vehicle. Zhu et al.[42] did not report any variation of NOx emission with temperature under WLTC. In general, EFs reported here are in the agreement with previous studies, being in the order of 64-1000 mg/km for diesel [51, 52, 60, 68] (including vehicles equipped with NOx abatement technology) and 30 mg/km for gasoline, if we excluded the GD3 vehicle. [41, 51, 52]

Gasoline vehicles respect standard THCs emission limit for all cycles except the WLTC cold start, where GDI3 (Euro 5) slightly exceeds the limitation. In general, higher values are measured for gasoline vehicles rather than diesel for WLTC and Artemis Motorway cycles. However, Artemis Urban and Artemis Road present opposite trends. Fuel composition, engine working principle and different speed profiles of cycles can influence THCs concentration. As for CO, THCs concentration presents a high dependence of catalyst temperature. As seen in the previous section on transient emission profiles, THCs emissions during cold start cycles are higher than at hot start. THCs emissions are reduced by 30% in average passing from WLTC cold to WLTC hot cycle. EFs reported here are generally in agreement with those reported in literature for diesel (<100 mg/km) [51, 53, 58] and for gasoline (24-200 mg/km) vehicles. [41, 42, 51, 52]

3.3. Non Regulated Gas Phase Pollutants

3.3.1. Transient Profiles of Gaseous Pollutants

A Proton-Transfer-Reactor Time-of-Flight Mass Spectrometry was deployed in the 2017 campaign to measure organic emissions. In order to avoid losses of sticky compounds the sampling line was heated at 80°C. These data are provided by Prof. Wisthaler's group (Chemistry Department, university of Oslo, Norway). Here only some emission profiles from benzene and ammonia time series are presented. Figure 3.22. shows the time profile of benzene during WLTC cold start cycle for (a) GDI3 vehicle and (b) D3 vehicle and transient profile of ammonia during WLTC cold start cycle for (c) GDI3 vehicle and (d) D3 vehicle.

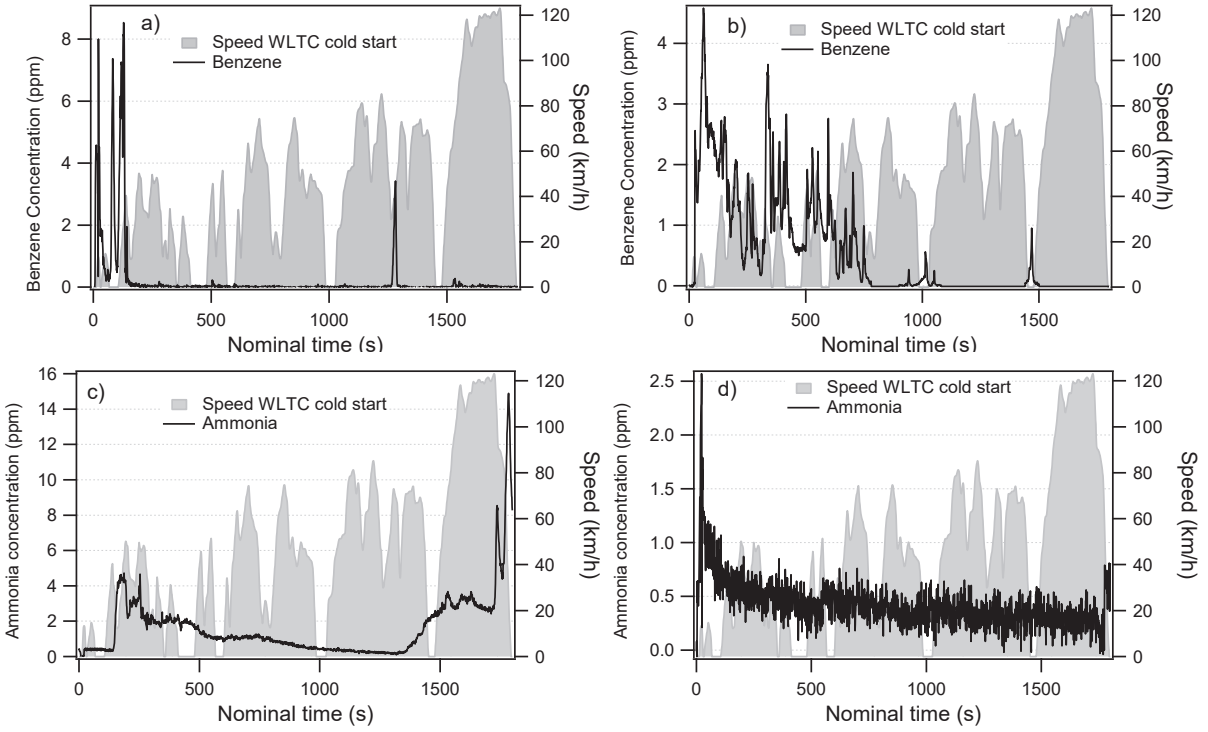

Figure 3.22. *Time series profile of benzene under WLTC cold start for Euro 5 (a) GDI3 and (b) D3 and time series profile of ammonia under WLTC cold start for Euro 5 (c) GDI3 and (d) D3.*

Benzene emissions are highly correlated to the cold start period. For the GDI3, most of the benzene is emitted in the first few minutes of the cycle, while the D3 car shows some emission for the first 900 seconds, suggesting that the two oxidation catalyst operate in different ways. Small emission spikes are observed during brakes periods (at 1350 seconds for GDI3 and at 1000 and 1500 seconds for D3 vehicles).

Emission factors of benzene measured with the PTRMS are in the order of 560 µg/km for the GDI3 and 340 µg/km for D3 car. Similar values have been measured using the

cartridges/GC-MS technique with 678 µg/km for the D3 car and 320 µg/km for the GDI3. These results are in quite a good agreement with results reported in the literature.[1, 13, 52, 69]

Gasoline NH_3 emission presents a first broad peak corresponding to the first acceleration. Its concentration then slowly decreases and increased again during high speed cycle. NH_3 has been previously reported as an important pollutant in gasoline vehicle exhaust.[70-72] Suarez-Bertoa et al.[70] tested several Euro 5 and Euro 6 gasoline vehicles and reported concentrations in the range of the ppm but the variability from one car to the other could reach an order of magnitude. The ammonia emissions measured for the GDI3 vehicle are significantly lower than those published by Suarez-bertoa et al.[70] A possible explanation can be the failure of the three way catalyst, more precisely the reduction catalyst, which was not able to reduce NOx concentrations of the vehicle. The ammonia profile presented here is in agreement with other vehicles tested in the framework of the CAPPNOR 2 project (ADEME CORTEA), which reported largest emissions during acceleration/brakes in the last part of the WLTC cycle. Heeb et al.[72] also suggested that ammonia emissions are highly correlated with acceleration and brakes during driving cycles, which is in agreement with results presented here.

Ammonia emission from the diesel D3 vehicle were very low and close to the detection limits of the instrument. These results are in agreement with Suarez-Bertoa et al.[70, 73] and Storms et al.[74] who only reported measurable ammonia emissions for SCR-equipped diesel vehicles.

3.3.2. Speciation of Organic Compounds

THCs include a myriad of compounds that are emitted from vehicles exhaust. Some of those have been identified as toxic or carcinogenic (HCHO, 1,3-butadiene, benzene, etc..) for human health and some are precursors of SOA and ozone. In this section we will present the speciation and the EFs of several HCs measured for two vehicles Euro 5 (D3 and GDI3). The HCs have been measured during WLTC cycles at the tailpipe upon FPS-4000 dilution system and collected on TENAX TA/Air toxic cartridges for further thermal desorption and analysis with GC-MS (details can be found in Chapter II). To minimize losses of organic compounds on the sampling lines the entire sampling system was maintained at 80-90°C.

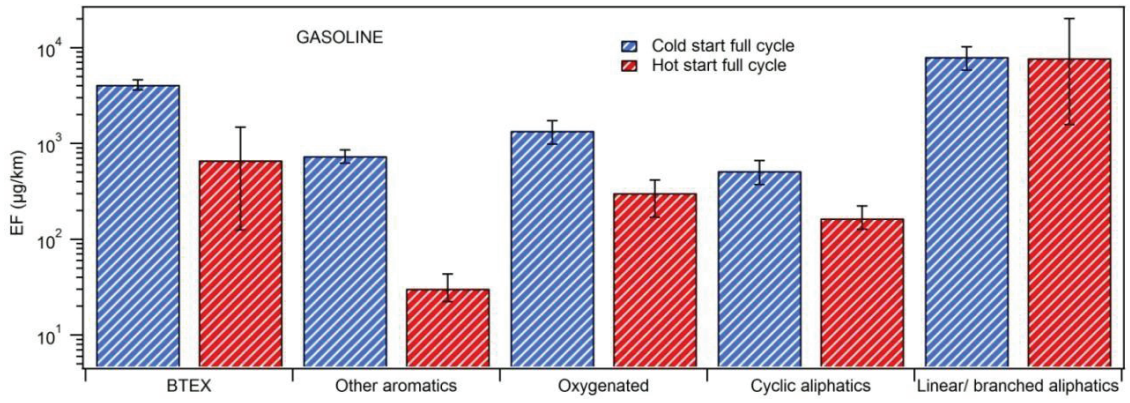

Figure 3.23. *Emission Factors of gaseous compounds for GDI3 vehicle during WLTC cycle.*

For the GDI3 vehicle, emission factors of $8x10^3$ µg/km are observed for linear/branched aliphatics (alkanes and alkenes), followed by Benzene-Toluene-Ethylbenzene-Xylene compounds (BTEX), with $4x10^3$ µg/km. The remaining aromatics compounds, which include mainly trimethyl-benzene, 1-ethyl-2-methyl-benzene, styrene, benzaldehyde, naphthalene, methyl-naphthalene and indene, together did not exceed 800 µg/km during cold starts while they were considerably lower during hot cycles. The emission factors of oxygenated compounds were in the range of 10^2-10^3 µg/km, the cyclic aliphatic compounds ranged between 1 and $5x10^2$ µg/km. Cyclopentane, cyclohexane, cyclobutane, ethyl-cyclohexane and dimethyl-cyclohexane represented the most abundant cyclic compounds. The oxygenated compounds were mainly represented by acetone, acetaldehyde, methanol, ethanol and butanol. Formaldehyde was not considered in these measurements since too light to be detected with Tenax cartridges, other methods as DNPH are more appropriate for the measurement of this compound. Differences between cartridges/GC-MS analysis and THC measured by Horiba gas analysis system (section 3.3.2.) can be explained by lack/incomplete measure of small compounds below C_3.

Figure 3.24. presents the results of VOCs/IVOCs collected during cycles for the D3 vehicle. The EFs are in the order of 10^4-10^5 µg/km for cyclic aliphatic compounds, followed by the oxygenated compounds with $3x10^4$ µg/km, linear/branched aliphatic compounds with $7x10^3$ to $1x10^4$ µg/km and finally the aromatic compounds with 1000-1500 µg/km. There is not a clear trend for cold and hot start cycle, except for cyclic compounds, which present one order of magnitude higher for hot cycles.

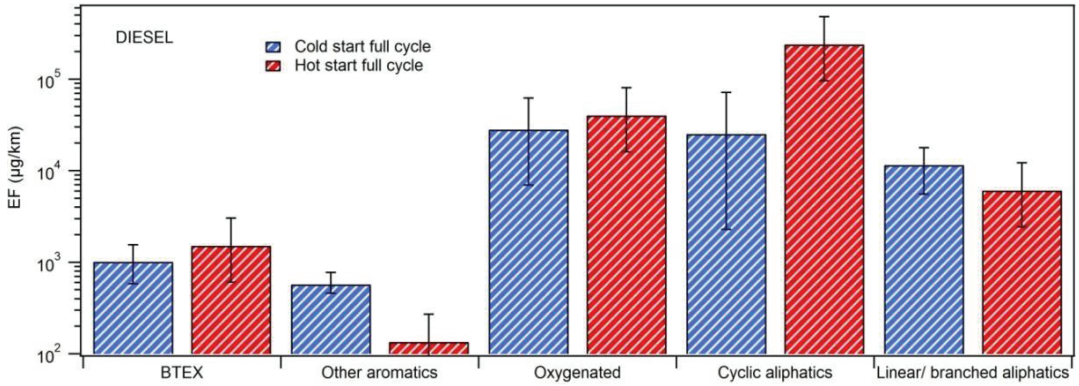

Figure 3.24. *Emission Factors of gaseous compound for D3 vehicle during WLTC cycle.*

Figure 3.25. presents the mass fraction of the measured VOCs classified in families for GDI3 and D3 vehicle during WLTC cold and hot start cycles.

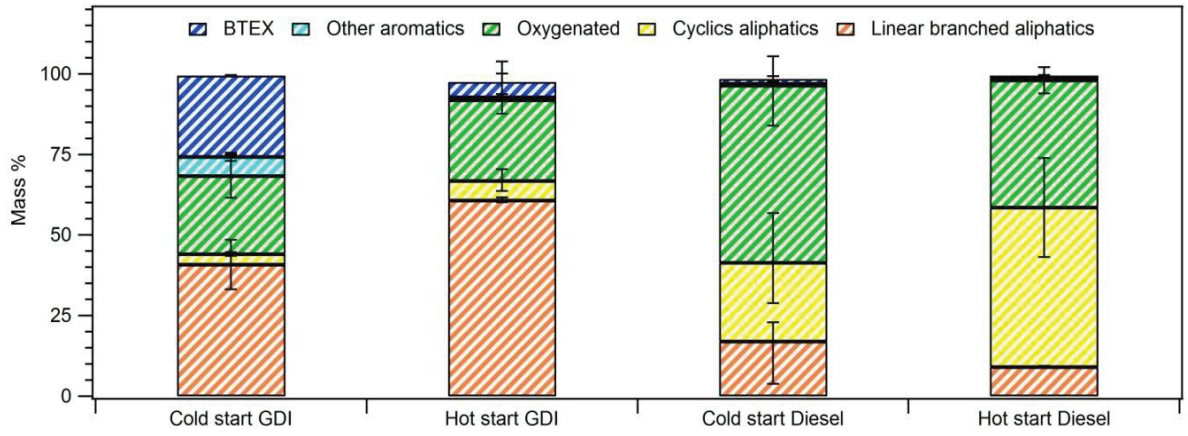

Figure 3.25. *Mass speciation of compounds based on family for GDI3 and D3vehicles during WLTC cold and hot start cycle.*

As observed, during cold start for GDI3 vehicle, aliphatic compounds contribute to 40% of the emitted organic compounds followed by the BTEX with 25% and the oxygenated compounds with 17%. The remaining aromatic compounds accounted for only 5 %. Gasoline hot start cycle showed an increase in emission of aliphatic compounds up to 68% (linear, branched and cyclic) accompanied by a decrease of the emitted aromatic compounds (15%), while oxygenated compounds did not present any important variation. Results are somehow in agreement with the literature: for gasoline DI vehicles in agreement with recent USA emission standards, Saliba et al.[46] reported average mass fraction of ≈ 61%, 23% and 14% for aliphatic, aromatics and oxygenated families, respectively. Zhao et al.[75] studied gasoline emissions and reported 57%, 3%, 7% and 21% of mass fraction for alkanes/alkenes, cyclic alkanes, oxygenated and aromatics. Liu et al.[76] reported that aromatic compounds represented 40% of the total VOC emitted by Euro 4 gasoline vehicles. Fuel composition parameters, as fraction of aromatics or presence of ethanol may strongly influence the chemical speciation.[77, 78]

Diesel cold start emissions are dominated by oxygenated compounds with 55%, followed by cyclic aliphatic with 24% and linear/branched aliphatics with 17%. The aromatic compounds present a very low fraction with only 2% (BTEX and other aromatics). Cyclic aliphatics increased during hot start cycle up to 50%, while oxygenated compounds and linear/branched aliphatics decreased to 42% and 8%, respectively.

Speciation of the measured BTEX is presented in figures 3.26. for the GDI3 vehicle.

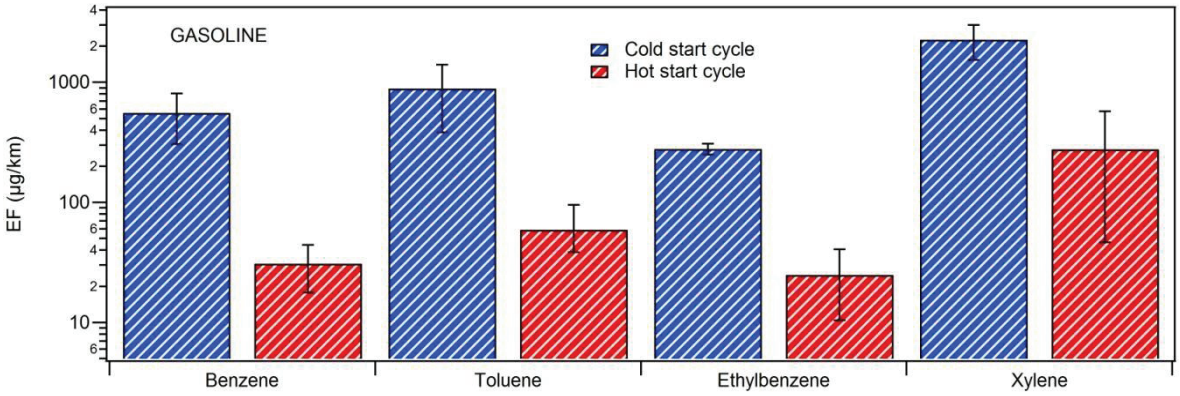

Figure 3.26. *Emission Factors of BTEX compounds for GDI3 vehicle during WLTC cycle.*

As a general trend, the BTEX emissions are considerably higher during cold cycles and then drop of one or two order of magnitude during hot cycles. Xylenes dominated the emissions with 2-3x10^3 µg/km, followed by toluene with 900 µg/km, benzene with 600 µg/km and ethylbenzene with 300 µg/km. Results are in agreement with those reported of Louis et al.[13], who reported a factor 6 for BTEX EFs between cold and hot Artemis Urban cycles. In general, EFs found here are in agreement with previous literature, which reported EFs for BTEX in the range of 100-1000 µg/km and 10-100 µg/km for cold and hot start, respectively.[52],[1, 13]

Figure 3.27. presents EFs for the individual BTEX emissions for the D3 vehicle.

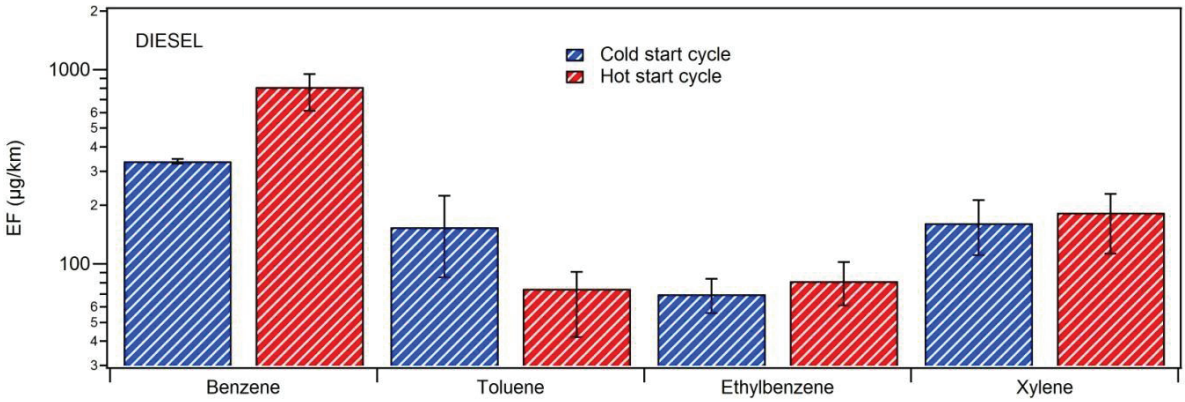

Figure 3.27. *Emission Factors of BTEX compounds for D3 vehicle.*

For the D3 vehicle, benzene largely dominate the BTEX emissions with 330-800 µg/km followed by xylene, around 200 µg/km, toluene with 70-150 µg/km and ethylbenzene with 70-

80 µg/km. Results are in agreement with those reported by other authors, which are in the range 150-600 µg/km and also reported benzene as most emitted BTEX.[1, 13]

The EFs of linear and branched aliphatic compounds with carbon number up to C_{15} are shown in figure 3.28. for gasoline DI vehicle.

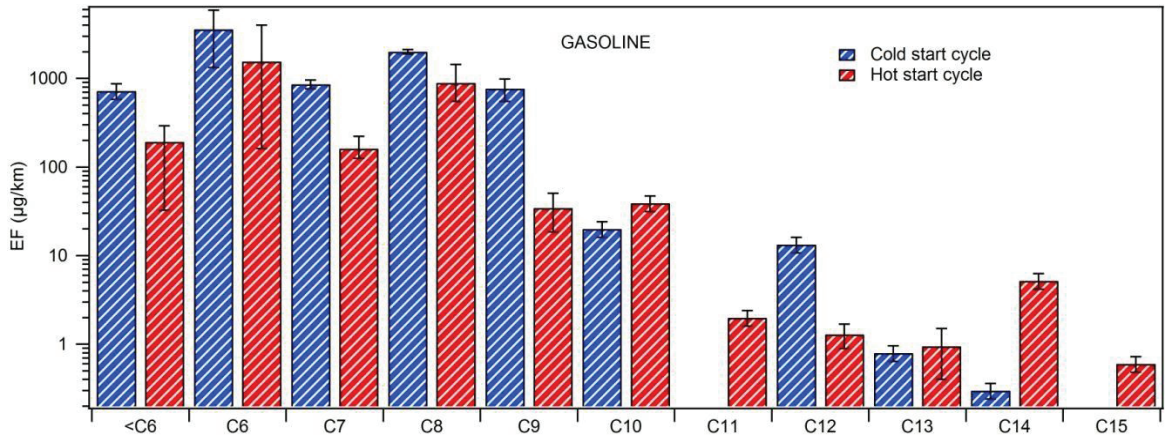

Figure 3.28. *EF for linear/branched aliphatic compounds up to C_{15} emitted for the GDI3 vehicle during WLTC cycle.*

For higher carbon number compounds (>C_{15}), the thermo desorption analysis method did not allow to ensure a quantitative assessment. For gasoline vehicle, the C_9-C_{15} compounds represent a relatively small fraction (7%) of the total linear/branched aliphatics. EFs are dominated by molecules below than C_9. What is in agreement with Lu et al.[79] Thus <C_6, C_6, C_7 and C_8 account for 15, 43, 11 and 24% of total mass, respectively. Alves et al.[52] reported highest EFs for C_6 and C_8 compounds, which presented values in the order of $3x10^3$-$3x10^4$ µg/km for C_6,C_8 and C_9 compounds, respectively, during Artemis cycles. Ensberg et al.[80] reported C_5-C_8 as the dominant group for gasoline cars. Gentner et al.[81] performed on-road tunnel emissions where gasoline vehicles dominate over diesel and reported a carbon distribution centered on C_4-C_5 for linear alkanes and C_5-C_6 for branched alkanes. They quantify compounds up to C_{11} and C_{10} for linear and branched, respectively. Regarding IVOCs compounds presented here (C_{12}-C_{15}), EFs are in the order of 1-10 µg/km. Cold start seems to have a positive influence for small aliphatic chains up to C_9, apart from that, there is not a clear trend, probably due to the low concentrations measured.

Finally, EFs of aliphatic compounds with carbon number between C_9 and C_{15} are shown in figure 3.29. for the D3 vehicle. For higher carbon number compounds (>C_{16}), the thermodesportion analysis method did not allow a quantitative analysis, nevertheless, compounds up to C_{20} have been detected.

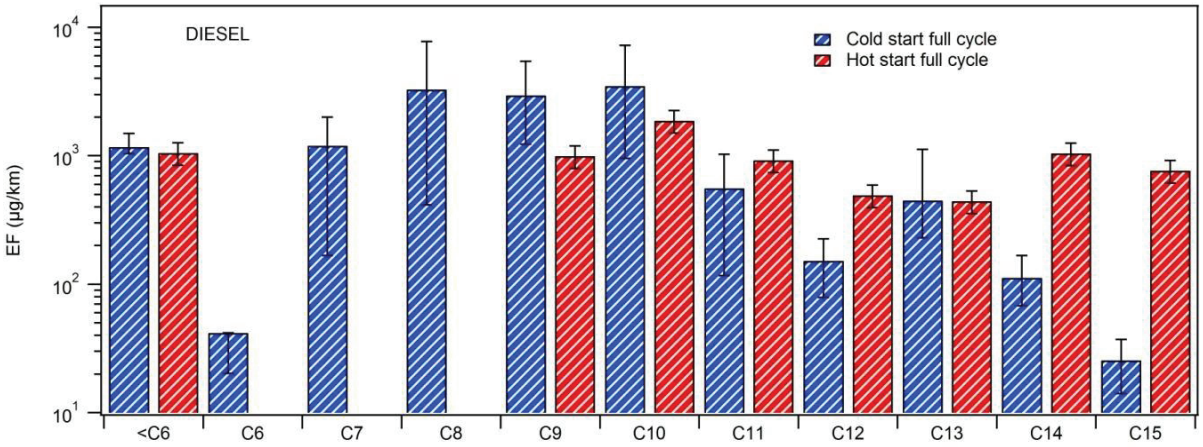

Figure 3.29. *EF for linear/branched aliphatic compounds up to C_{15} emitted for the D3 vehicle during WLTC cycle.*

The C_8-C_{15} compounds represent a relatively large fraction of the total alkanes/alkenes. The C_8, C_9 and C_{10} compounds are the most abundant and range from 1000 µg/km to 4000 µg/km. The EFs for chains larger than C_{10} range from 20 to 1000 µg/km. There is not a clear influence of cold start for this group of compounds as discussed previously. Gentner et al.[81] and Alves et al.[52] found the highest emission factors for C_9-C_{13} and C_7-C_{11} compounds, respectively. However, they report EFs in the range of $2x10^3$ to $8x10^4$ for compound between C_7-C_{11}, which are considerably higher of what found for the D3 vehicle.[52] Zhao et al.[82] presented a distribution centered around C_{12}-C_{13} compounds and progressively decreasing until C_{22}. Kim et al.[6] reported EF values between 10 µg/km and 450 µg/km for the range C_{13}-C_{21} during Artemis Urban cycle for Euro 4 diesel vehicle equipped with DPF. These EFs are at least one order of magnitude less compared to the ones obtained for the D3 diesel vehicle. However, the sampling technique as well as the target range of compounds were different for each case. Kim et al. also measured IVOCs in the range of C_{13}-C_{19} (EFs < 11 µg/km) during Artemis Urban cycle for Euro 4 diesel vehicle without DPF. Similar results are obtained by Lu et al. [79], who observed an alkane IVOCs/SVOCs distribution C_7-C_{22} centered in C_{15}-C_{15} for recent diesel vehicle equipped with DPF.

3.4. Conclusions

Three diesel vehicles (two Euro 5 and one Euro 6) and three gasoline direct injection vehicles (two Euro 5 and one Euro 6) have been tested during WLTC and Artemis driving cycles. Gas and particle phase emission studies have been carried out.

The main conclusions are presented here :

- measurements at the CVS dilution system (without the PMP method) are affected by bias due to cold dilution and low dilution ratio. Phenomena of nucleation and condensation

were observed and caused shift in particle size distribution and particle number concentration. Measurements directly at tailpipe after FPS-4000 dilution system could represent an alternative method when condensable material has to be taken into account. Unregulated sub-23 nm particles seem to account for a non negligible fraction of the emitted particles in the size range 14-23nm and represent around 20-30% of the total PN for gasoline vehicles and around 15% for diesel cars. By lowering the measurements threshold to 14 nm, improvements related to total PN quantification can be achieved.

- Gasoline DI vehicles emit a considerably amount of PM (including BC, organics, PAHs and PN concentration). Cold start accounts for an important fraction of total emitted particle concentration.
- Diesel car do emit some organic compounds (during cold start and accelerations) and sulfate mostly during acceleration and high speed cycles, suggesting passive regeneration of the DPF. These periods were associated to fast increase of particle number concentration in the nucleation mode (10-20 nm diameter).
- Particles elemental composition and morphology have been further investigated using TEM and SEM techniques. Gasoline and diesel PM are mainly formed by fractal material organized in chains or agglomerates. These structures seem to be coated by organic compounds. TEM images revealed the presence of liquid droplets. Upon chemical analysis these droplet seems to be formed by an organic matrix with inclusions of metals that suggest lubricant oil as a major source. Fe was also found and it has been mainly associated to engine wear abrasion.
- In general, Euro 5 and Euro 6 vehicles respect standard limit for CO and THCs during all cycles. NOx concentrations, however, often exceeded the limitation value for different vehicles and cycles.
- Speciation and quantification of organic compounds have been carried out for a gasoline and diesel car. Gasoline vehicle presents high emissions of BTEX and linear alkanes/alkenes while diesel vehicle emissions are dominated bycyclic, oxygenated and linear alkanes/alkenes. Among the BTEX, xylene is the most dominant compound for gasoline and benzene for diesel vehicle. Among the aliphatic compounds, gasoline presented a distribution centered around C_6-C_7 the compounds with little presence of IVOCs. Diesel car however, presented a distribution centered around the C_9-C_{10} compounds and non negligible concentrations were measured up to C_{15}compounds.

References:

1. Martinet S, Liu Y, Louis C, Tassel P, Perret P, Chaumond A, et al. Euro 6 Unregulated Pollutant Characterization and Statistical Analysis of After-Treatment Device and Driving-Condition Impact on Recent Passenger-Car Emissions. *Environmental Science & Technology* 2017; 51(10):5847-5855.
2. Louis C, Liu Y, Martinet S, D'Anna B, Valiente AM, Boreave A, et al. Dilution effects on ultrafine particles emissions from Euro 5 and Euro 6 diesel and gasoline vehicles. In. Atmospheric environment; 2017. pp. 80-88.
3. Kittelson DB. Engines and nanoparticles: a review. *Journal of Aerosol Science* 1998; 29(5):575-588.
4. Vouitsis E, Ntziachristos L, Pistikopoulos P, Samaras Z, Chrysikou L, Samara C, et al. An investigation on the physical, chemical and ecotoxicological characteristics of particulate matter emitted from light-duty vehicles. *Environ Pollut* 2009; 157(8-9):2320-2327.
5. Giechaskiel B, Chirico R, DeCarlo PF, Clairotte M, Adam T, Martini G, et al. Evaluation of the particle measurement programme (PMP) protocol to remove the vehicles' exhaust aerosol volatile phase. *Science of the Total Environment* 2010; 408(21):5106-5116.
6. Kim Y, Sartelet K, Seigneur C, Charron A, Besombes JL, Jaffrezo JL, et al. Effect of measurement protocol on organic aerosol measurements of exhaust emissions from gasoline and diesel vehicles. *Atmos Environ* 2016; 140:176-187.
7. Mathis U, Mohr M, Forss AM. Comprehensive particle characterization of modern gasoline and diesel passenger cars at low ambient temperatures. *Atmos Environ* 2005; 39(1):107-117.
8. May AA, Presto AA, Hennigan CJ, Nguyen NT, Gordon TD, Robinson AL. Gas-particle partitioning of primary organic aerosol emissions: (1) Gasoline vehicle exhaust. *Atmospheric Environment* 2013; 77:128-139.
9. Karjalainen P, Timonen H, Saukko E, Kuuluvainen H, Saarikoski S, Aakko-Saksa P, et al. Time-resolved characterization of primary particle emissions and secondary particle formation from a modern gasoline passenger car. *Atmos Chem Phys* 2016; 16(13):8559-8570.
10. Suarez-Bertoa R, Astorga C. Isocyanic acid and ammonia in vehicle emissions. *Transportation Research Part D-Transport and Environment* 2016; 49:259-270.
11. Tkacik DS, Lambe AT, Jathar S, Li X, Presto AA, Zhao Y, et al. Secondary Organic Aerosol Formation from in-Use Motor Vehicle Emissions Using a Potential Aerosol Mass Reactor. *Environmental Science & Technology* 2014; 48(19):11235-11242.
12. Clairotte M, Adam TW, Zardini AA, Manfredi U, Martini G, Krasenbrink A, et al. Effects of low temperature on the cold start gaseous emissions from light duty vehicles fuelled by ethanol-blended gasoline. *Applied Energy* 2013; 102:44-54.
13. Louis C, Liu Y, Tassel P, Perret P, Chaumond A, Andre M. PAH, BTEX, carbonyl compound, black-carbon, NO2 and ultrafine particle dynamometer bench emissions for Euro 4 and Euro 5 diesel and gasoline passenger cars. *Atmospheric Environment* 2016; 141:80-95.
14. Mamakos A, Steininger N, Martini G, Dilara P, Drossinos Y. Cost effectiveness of particulate filter installation on Direct Injection Gasoline vehicles. *Atmospheric Environment* 2013; 77:16-23.
15. Weilenmann M, Favez JY, Alvarez R. Cold-start emissions of modern passenger cars at different low ambient temperatures and their evolution over vehicle legislation categories. *Atmospheric Environment* 2009; 43(15):2419-2429.
16. Chen LF, Liang ZR, Zhang X, Shuai SJ. Characterizing particulate matter emissions from GDI and PFI vehicles under transient and cold start conditions. *Fuel* 2017; 189:131-140.
17. R'Mili B, Boréave A, Meme A, Vernoux P, Leblanc M, Noël L, et al. Physico-Chemical Characterization of Fine and Ultrafine Particles Emitted during Diesel Particulate Filter Active Regeneration of Euro5 Diesel Vehicles. *Environmental Science & Technology* 2018; 52(5):3312-3319.
18. Tobias HJ, Beving DE, Ziemann PJ, Sakurai H, Zuk M, McMurry PH, et al. Chemical analysis of diesel engine nanoparticles using a nano-DMA/thermal desorption particle beam mass spectrometer. *Environ Sci Technol* 2001; 35(11):2233-2243.
19. Chen F, Hu W, Zhong Q. Emissions of particle-phase polycyclic aromatic hydrocarbons (PAHs) in the Fu Gui-shan Tunnel of Nanjing, China. *Atmospheric Research* 2013; 124:53-60.
20. Liu Y, Gao Y, Yu N, Zhang CK, Wang SY, Ma LM, et al. Particulate matter, gaseous and particulate polycyclic aromatic hydrocarbons (PAHs) in an urban traffic tunnel of China: Emission from on-road vehicles and gas-particle partitioning. *Chemosphere* 2015; 134:52-59.
21. Marr LC, Kirchstetter TW, Harley RA, Miguel AH, Hering SV, Hammond SK. Characterization of Polycyclic Aromatic Hydrocarbons in Motor Vehicle Fuels and Exhaust Emissions. *Environmental Science & Technology* 1999; 33(18):3091-3099.
22. Bruns EA, Krapf M, Orasche J, Huang Y, Zimmermann R, Drinovec L, et al. Characterization of primary and secondary wood combustion products generated under different burner loads. *Atmos Chem Phys* 2015; 15(5):2825-2841.
23. Herring CL, Faiola CL, Massoli P, Sueper D, Erickson MH, McDonald JD, et al. New Methodology for Quantifying Polycyclic Aromatic Hydrocarbons (PAHs) Using High-Resolution Aerosol Mass Spectrometry. *Aerosol Science and Technology* 2015; 49(11):1131-1148.
24. Mueller M, Eicher P, D'Anna B, Tan W, Wisthaler A. Direct Sampling and Analysis of Atmospheric Particulate Organic Matter by Proton-Transfer-Reaction Mass Spectrometry. *Analytical Chemistry* 2017; 89(20):10889-10897.

25. Rönkkö T, Pirjola L, Ntziachristos L, Heikkilä J, Karjalainen P, Hillamo R, et al. Vehicle Engines Produce Exhaust Nanoparticles Even When Not Fueled. *Environmental Science & Technology* 2014; 48(3):2043-2050.
26. Karjalainen P, Timonen H, Saukko E, Kuuluvainen H, Saarikoski S, Aakko-Saksa P, et al. Time-resolved characterization of primary and secondary particle emissions of a modern gasoline passenger car. *Atmospheric Chemistry & Physics Discussions* 2015; 15(22):33253.
27. Amirante R, Distaso E, Napolitano M, Tamburrano P, Di Iorio S, Sementa P, et al. Effects of lubricant oil on particulate emissions from port-fuel and direct-injection spark-ignition engines. *International Journal of Engine Research* 2017; 18(5-6):606-620.
28. Karjalainen P, Pirjola L, Heikkilä J, Lähde T, Tzamkiozis T, Ntziachristos L, et al. Exhaust particles of modern gasoline vehicles: A laboratory and an on-road study. *Atmospheric Environment* 2014; 97:262-270.
29. Fushimi A, Saitoh K, Fujitani Y, Hasegawa S, Takahashi K, Tanabe K, et al. Organic-rich nanoparticles (diameter: 10–30 nm) in diesel exhaust: Fuel and oil contribution based on chemical composition. *Atmospheric Environment* 2011; 45(35):6326-6336.
30. Fu H, Wang Y, Li X, Shuai S-J. Impacts of Cold-Start and Gasoline RON on Particulate Emission from Vehicles Powered by GDI and PFI Engines. In: SAE International; 2014.
31. Mel'nikov VG. Tribological and colloid-chemical aspects of the action of organic fluorine compounds as friction modifiers in motor oils. *Chemistry and Technology of Fuels and Oils* 1997; 33(5):286-295.
32. Barone TL, Storey JME, Youngquist AD, Szybist JP. An analysis of direct-injection spark-ignition (DISI) soot morphology. *Atmospheric Environment* 2012; 49:268-274.
33. Gaddam CK, Vander Wal RL. Physical and chemical characterization of SIDI engine particulates. *Combustion and Flame* 2013; 160(11):2517-2528.
34. Mathis U, Kaegi R, Mohr M, Zenobi R. TEM analysis of volatile nanoparticles from particle trap equipped diesel and direct-injection spark-ignition vehicles. *Atmospheric Environment* 2004; 38(26):4347-4355.
35. Kocbach A, Li Y, Yttri KE, Cassee FR, Schwarze PE, Namork E. Physicochemical characterisation of combustion particles from vehicle exhaust and residential wood smoke. *Particle and fibre toxicology* 2006; 3:1-1.
36. Lapuerta M, Martos FJ, Herreros JM. Effect of engine operating conditions on the size of primary particles composing diesel soot agglomerates. *Journal of Aerosol Science* 2007; 38(4):455-466.
37. Liati A, Schreiber D, Arroyo Rojas Dasilva Y, Dimopoulos Eggenschwiler P. Ultrafine particle emissions from modern Gasoline and Diesel vehicles: An electron microscopic perspective. *Environ Pollut* 2018; 239:661-669.
38. Yang HaLXaWYaMMaLXaKG. Pyrolysis Characteristic Analysis of Particulate Matter from Diesel Engine Run on Diesel/Polyoxymethylene Dimethyl Ethers Blends Based on Nanostructure and Thermogravimetry. *Aerosol and Air Quality Research* 2016; 16(10):2560-2569.
39. Arnold F, Pirjola L, Rönkkö T, Reichl U, Schlager H, Lähde T, et al. First Online Measurements of Sulfuric Acid Gas in Modern Heavy-Duty Diesel Engine Exhaust: Implications for Nanoparticle Formation. *Environmental Science & Technology* 2012; 46(20):11227-11234.
40. Zhu R, Hu J, Bao X, He L, Zu L. Effects of aromatics, olefins and distillation temperatures (T50 & T90) on particle mass and number emissions from gasoline direct injection (GDI) vehicles. *Energy Policy* 2017; 101:185-193.
41. Köhler F. Testing of particulate emissions from positive ignition vehicles with direct fuel injection system. In. Technical Report, Institut für Fahrzeugtechnik und Mobilität; 2013.
42. Zhu RC, Hu JN, Bao XF, He LQ, Lai YT, Zu L, et al. Tailpipe emissions from gasoline direct injection (GDI) and port fuel injection (PFI) vehicles at both low and high ambient temperatures. *Environmental Pollution* 2016; 216:223-234.
43. Jang J, Lee J, Kim J, Park S. Comparisons of the nanoparticle emission characteristics between GDI and PFI vehicles. *Journal of Nanoparticle Research* 2015; 17(12).
44. TNO r. Emissions of three common GDI vehicles. In. TNO 2016 R11247 www.tno.nl; 2016.
45. Chen L, Stone R. Measurement of Enthalpies of Vaporization of Isooctane and Ethanol Blends and Their Effects on PM Emissions from a GDI Engine. *Energy & Fuels* 2011; 25(3):1254-1259.
46. Saliba G, Saleh R, Zhao YL, Presto AA, Larnbe AT, Frodin B, et al. Comparison of Gasoline Direct-Injection (GDI) and Port Fuel Injection (PFI) Vehicle Emissions: Emission Certification Standards, Cold-Start, Secondary Organic Aerosol Formation Potential, and Potential Climate Impacts. *Environmental Science & Technology* 2017; 51(11):6542-6552.
47. Giechaskiel B, Vanhanen J, Väkevä M, Martini G. Investigation of vehicle exhaust sub-23 nm particle emissions. *Aerosol Science and Technology* 2017; 51(5):626-641.
48. Giechaskiel B, Manfredi U, Martini G. Engine Exhaust Solid Sub-23 nm Particles: I. Literature Survey. *SAE Int J Fuels Lubr* 2014; 7(3):950-964.
49. Giechaskiel B, F. R, Mendoza Villafuerte P, T. G. Particle Number (PN) -Portable Emissions Measurements Systems (PEMS): Heavy Duty Vehicles Evaluation phase at the Joint Research Centre (HRC). In: EUR - Scientific and Technical Research Reports; 2016.
50. Zheng Z, Durbin TD, Karavalakis G, Johnson KC, Chaudhary A, Cocker DR, et al. Nature of Sub-23-nm Particles Downstream of the European Particle Measurement Programme (PMP)-Compliant System: A Real-Time Data Perspective. *Aerosol Science and Technology* 2012; 46(8):886-896.

51. Fontaras G, Franco V, Dilara P, Martini G, Manfredi U. Development and review of Euro 5 passenger car emission factors based on experimental results over various driving cycles. *Science of the Total Environment* 2014; 468:1034-1042.
52. Alves CA, Lopes DJ, Calvo AI, Evtyugina M, Rocha S, Nunes T. Emissions from Light-Duty Diesel and Gasoline In-Use Vehicles Measured on Chassis Dynamometer Test Cycles. *Aerosol and Air Quality Research* 2015; 15(1):99-116.
53. Lopes M, Serrano L, Ribeiro I, Cascao P, Pires N, Rafael S, et al. Emissions characterization from EURO 5 diesel/biodiesel passenger car operating under the new European driving cycle. *Atmospheric Environment* 2014; 84:339-348.
54. Gumus M. Reducing cold-start emission from internal combustion engines by means of thermal energy storage system. *Applied Thermal Engineering* 2009; 29(4):652-660.
55. Korin E, Reshef R, Tshernichovesky D, Sher E. Reducing cold-start emission from internal combustion engines by means of a catalytic converter embedded in a phase-change material. *Proceedings of the Institution of Mechanical Engineers Part D-Journal of Automobile Engineering* 1999; 213(D6):575-583.
56. Roberts A, Brooks R, Shipway P. Internal combustion engine cold-start efficiency: A review of the problem, causes and potential solutions. *Energy Conversion and Management* 2014; 82:327-350.
57. Suarez-Bertoa R, Astorga C. Impact of cold temperature on Euro 6 passenger car emissions. *Environ Pollut* 2018; 234:318-329.
58. Ko J, Jin D, Jang W, Myung CL, Kwon S, Park S. Comparative investigation of NOx emission characteristics from a Euro 6-compliant diesel passenger car over the NEDC and WLTC at various ambient temperatures. *Applied Energy* 2017; 187:652-662.
59. O'Driscoll R, ApSimon HM, Oxley T, Molden N, Stettler MEJ, Thiyagarajah A. A Portable Emissions Measurement System (PEMS) study of NOx and primary NO2 emissions from Euro 6 diesel passenger cars and comparison with COPERT emission factors. *Atmospheric Environment* 2016; 145:81-91.
60. Weiss M, Bonnel P, Kuhlwein J, Provenza A, Lambrecht U, Alessandrini S, et al. Will Euro 6 reduce the NOx emissions of new diesel cars? - Insights from on-road tests with Portable Emissions Measurement Systems (PEMS). *Atmospheric Environment* 2012; 62:657-665.
61. Heywood J. Internal Combustion Fundamentals. In: McGraw-Hill; ISBN 0-07-100499-8; 1988.
62. Pavlovic J, Marotta A, Ciuffo B. CO2 emissions and energy demands of vehicles tested under the NEDC and the new WLTP type approval test procedures. *Applied Energy* 2016; 177:661-670.
63. Ghazikhani M, Hatami M, Safari B, Domiri Ganji D. Experimental investigation of exhaust temperature and delivery ratio effect on emissions and performance of a gasoline–ethanol two-stroke engine. *Case Studies in Thermal Engineering* 2014; 2:82-90.
64. Ko J, Si W, Jin D, Myung CL, Park S. Effect of active regeneration on time-resolved characteristics of gaseous emissions and size-resolved particle emissions from light-duty diesel engine. *Journal of Aerosol Science* 2016; 91:62-77.
65. Ntziachristos L, Samaras Z. Speed-dependent representative emission factors for catalyst passenger cars and influencing parameters. *Atmospheric Environment* 2000; 34(27):4611-4619.
66. Blumberg KO, Walsh MP, Pera C. Low sulfur Gasoline & Diesel: The Key to Lower Vehicle Emissions. In. International Council on Clean Transportation, 66p; 2003.
67. (icct) Ticoct. A technical summary of Euro 6/VI vehicle emission standards. In; 2016.
68. Kwon S, Park Y, Park J, Kim J, Choi KH, Cha JS. Characteristics of on-road NO emissions from Euro 6 light-duty diesel vehicles using a portable emissions measurement system. *Science of the Total Environment* 2017; 576:70-77.
69. Gentner DR, Jathar SH, Gordon TD, Bahreini R, Day DA, El Haddad I, et al. Review of Urban Secondary Organic Aerosol Formation from Gasoline and Diesel Motor Vehicle Emissions. *Environmental Science & Technology* 2017; 51(3):1074-1093.
70. Suarez-Bertoa R, Astorga C. Isocyanic acid and ammonia in vehicle emissions. *Transportation Research Part D: Transport and Environment* 2016; 49:259-270.
71. Borsari V, Assunção JVd. Ammonia emissions from a light-duty vehicle. *Transportation Research Part D: Transport and Environment* 2017; 51:53-61.
72. Heeb NV, Saxer CJ, Forss AM, Bruhlmann S. Correlation of hydrogen, ammonia and nitrogen monoxide (nitric oxide) emissions of gasoline-fueled Euro-3 passenger cars at transient driving. *Atmospheric Environment* 2006; 40(20):3750-3763.
73. Suarez-Bertoa R, Zardini AA, Lilova V, Meyer D, Nakatani S, Hibel F, et al. Intercomparison of real-time tailpipe ammonia measurements from vehicles tested over the new world-harmonized light-duty vehicle test cycle (WLTC). *Environmental Science and Pollution Research* 2015; 22(10):7450-7460.
74. Storms W, Rateau A, Matsubara H, Lafossas FA, Mohammadi A. Clarification of NH3 Formation Mechanism on a Diesel Engine NOx Storage Reduction Catalyst Under Rich Conditions and Evaluation of the SCR Benefit at WLTC. *Topics in Catalysis* 2016; 59(10):925-930.
75. Zhao Y, Fairhurst MC, Wingen LM, Perraud V, Ezell MJ, Finlayson-Pitts BJ. New insights into atmospherically relevant reaction systems using direct analysis in real-time mass spectrometry (DART-MS). *Atmospheric Measurement Techniques* 2017; 10(4):1373-1386.
76. Liu T, Wang X, Deng W, Hu Q, Ding X, Zhang Y, et al. Secondary organic aerosol formation from photochemical aging of light-duty gasoline vehicle exhausts in a smog chamber. *Atmospheric Chemistry and Physics* 2015; 15(15):9049-9062.

77. Suarez-Bertoa R, Zardini AA, Keuken H, Astorga C. Impact of ethanol containing gasoline blends on emissions from a flex-fuel vehicle tested over the Worldwide Harmonized Light duty Test Cycle (WLTC). *Fuel* 2015; 143:173-182.
78. Gordon TD, Presto AA, Nguyen NT, Robertson WH, Na K, Sahay KN, et al. Secondary organic aerosol production from diesel vehicle exhaust: impact of aftertreatment, fuel chemistry and driving cycle. *Atmos Chem Phys* 2014; 14(9):4643-4659.
79. Lu Q, Zhao Y, Robinson AL. Comprehensive organic emission profiles for gasoline, diesel, and gas-turbine engines including intermediate and semi-volatile organic compound emissions. *Atmos Chem Phys* 2018; 18(23):17637-17654.
80. Ensberg JJ, Hayes PL, Jimenez JL, Gilman JB, Kuster WC, de Gouw JA, et al. Emission factor ratios, SOA mass yields, and the impact of vehicular emissions on SOA formation. *Atmos Chem Phys* 2014; 14(5):2383-2397.
81. Gentner DR, Worton DR, Isaacman G, Davis LC, Dallmann TR, Wood EC, et al. Chemical Composition of Gas-Phase Organic Carbon Emissions from Motor Vehicles and Implications for Ozone Production. *Environmental Science & Technology* 2013; 47(20):11837-11848.
82. Zhao Y, Nguyen NT, Presto AA, Hennigan CJ, May AA, Robinson AL. Intermediate Volatility Organic Compound Emissions from On-Road Diesel Vehicles: Chemical Composition, Emission Factors, and Estimated Secondary Organic Aerosol Production. *Environ Sci Technol* 2015; 49(19):11516-11526.

CHAPTER IV:

SOA formation and on-line chemical analysis

This second and extensive section of my PhD focused on SOA formation studies. The work is based on laboratory investigations using an aerosol flow tube (AFT). The AFT experiments intended to mimic the photo-oxidation of car exhaust in a controlled and simplified system. Since experiments were conducted in the laboratory, the strategy adopted consisted in the selection of few keys compounds found in the car exhaust. The compounds were chosen on the basis of the measured VOCs emitted by diesel and gasoline vehicles from our own studies (chapter III) and from review of the published literature. Five compounds have been selected for the laboratory investigations. Each compound is considered a "model molecule" of a family of pollutants. Among the mono-aromatic compounds, toluene was chosen since it was present in a fairly large amount and is less toxic than benzene. Among the cyclic compounds, cyclohexane (cyclic dominating diesel emissions) was chosen since was abundant in car exhaust. Among the aliphatic, nonane was selected since present in emission exhaust from both gasoline and diesel vehicles in large amount. Among the light PAHs, naphthalene was selected. The pentadecane was also tentatively tested but wall losses were so high that photoxidation experiments were not exploitable.

The aim of this work was first to determine SOA yield, and key parameters controlling SOA formation (as temperature, type and quantity of VOC, pre-existing seed particles). Additionally, thanks to the newly developed Chemical Analysis of aerosol on-line (CHARON) inlet, a much more detailed investigation on the chemical composition of both gas and particle phase has been developed.

The SOA mass was determined using the AMS and SMPS data and then were compared to the CHARON observed mass. This comparison can be found in figure 4.1. for the toluene experiments. Table AVII.1 in annex VII present the values for this intercomparison. The AMS particle density was established upon assignment of standard density to major chemical families as 1.2 g/cm^3 for the organic fraction; 1.7 g/cm^3 for ammonium sulfate (seeds); the nitrate was considered as organo-nitrate and therefore its density is considered to be 1.2 g/cm^3. The AMS collection efficiency (CE) for pure seed particles between 20 and 50% RH was around 0.5-0.55. Intercomparison with the SMPS volume was used to evaluate CE efficiency. The condensation of organic products onto ammonium sulfate seeds did only changed the CE efficiency of the aerosol to 0.6-0.65. Comparison between AMS and SMPS mass loading for two consecutive toluene experiments can be found in figure 4.2. We carried out multiple experiments on individual VOCs and then we carried out several experiments using a mixture of selected VOCs. Few and preliminary photoxidation experiments of car exhaust (GDI vehicle) were performed using an aerosol flow tube to determine major SOA constituents and SOA potential formation.

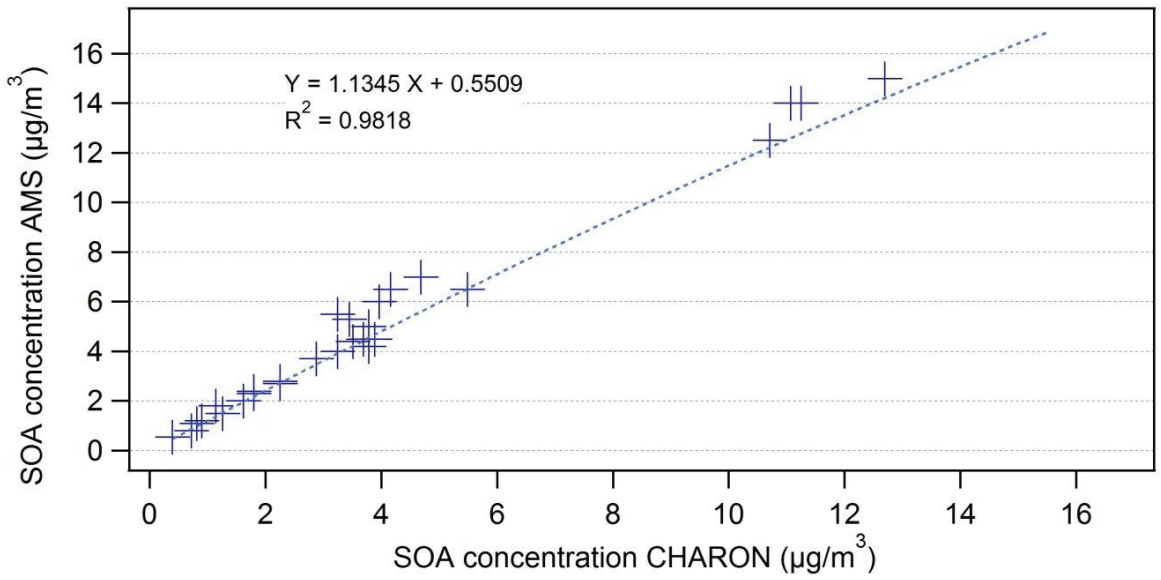

Figure 4.1. *Comparison between SOA measured using AMS and CHARON.*

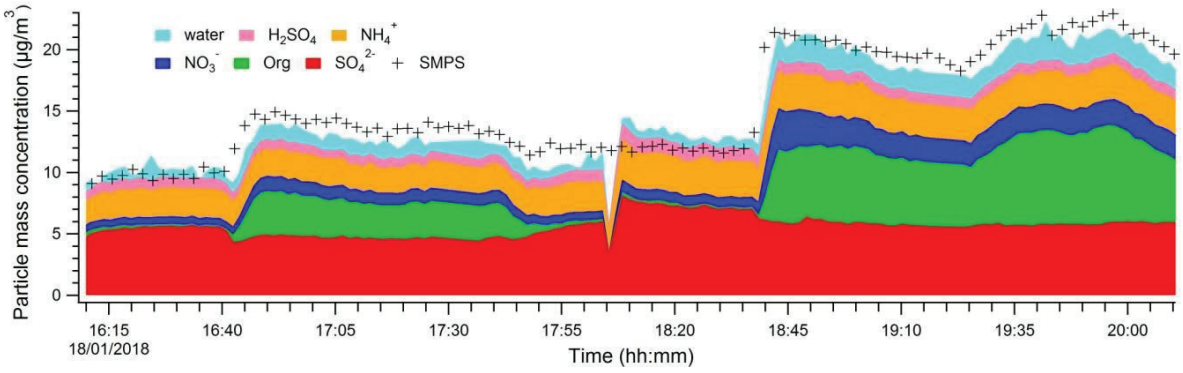

Figure 4.2. *Comparison between measured particle phase using AMS and SMPS.*

4.1. Toluene photoxidation

Toluene is one of the major monoaromatic compounds emitted in the troposphere. [1, 2] It is mainly emitted by vehicle exhausts and other combustion sources.[3]

In total, 31 experiments have been carried out in the AFT using toluene as SOA precursor. Full description of experimental setup can be found in chapter II. The particle phase was composed by ammonium sulfate (which was used as seed particles), organics and nitrate (around 8% of the produced mass).

An example of the time series mass concentration measured by the AMS and the CHARON/PTR-ToF-MS are illustrated in Figure 4.3. The produced SOA mass concentration is shown at different temperatures.

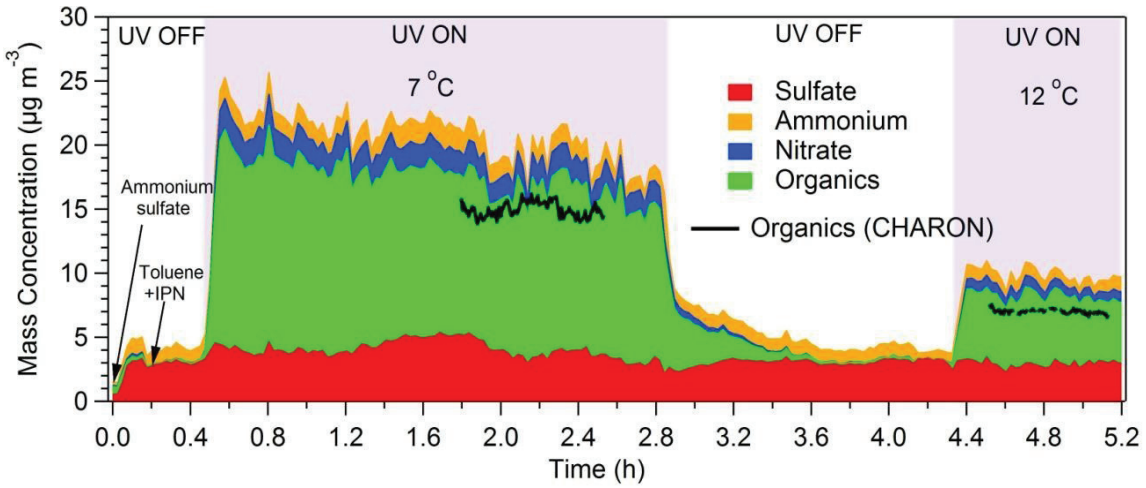

Figure 4.3. *Time series of sulfate, ammonium, nitrate, organic SOA mass concentrations as measured by the AMS and organic SOA mass concentration as sampled by CHARON-PTR-ToF-MS during two toluene photo-oxidation experiments. The AMS mass concentrations have been corrected for the CE, while the CHARON-PTR-ToF-MS organic mass concentration has been corrected for transmission efficiency. In both cases the initial toluene concentration was approximately 131 ppb and the RH was around 32%.*

The experiment starts with the introduction of 5 µg/m^3 of ammonium sulphate (red and yellow). At the same time, the precursor of the hydroxyl radical (IPN) and the toluene are introduced in the dark. After stabilization of the system, the lights are switched-on to initiate photochemistry and formation of SOA (green) and nitrate/nitro-organic (blue). Black lines indicate the amount of SOA detected by CHARON. After stabilization of the system and measurement of the gas and particulate phase the irradiation is stopped (UV off). A second experiment starts once new conditions are stable and SOA from previous experiment have disappeared.

4.1.1. Influence of parameters for SOA formation

Figure 4.4.a illustrates the SOA yield as a function of the produced SOA mass concentration at different temperatures and initial toluene concentrations. For similar initial toluene concentration and similar toluene depletion, experiments at low temperature led to higher organic concentration and hence, SOA yields. The temperature dependence over SOA yield is consistent with previous studies. For example, Takekawa et al.[4] reported almost twice higher toluene SOA yield at 10°C with respect to 30°C, and Hildebrandt et al.[5] found higher SOA yield for 11ºC compared to 32ºC. Temperature affects the gas-particle partitioning: at lower temperatures the semi-volatile species condense on the particulate phase, while at higher temperatures the same compounds evaporate and are transferred to the gas phase. Another key parameter that controls the SOA yield is the initial toluene concentration. Lower initial toluene concentrations resulted to higher SOA yield, but lower organic mass formation. The influence of seed (ammonium sulfate) concentration in SOA yield was also investigated. Figure 4.4.b shows the SOA yield as a function of the seed concentration for three temperatures. At 21°C, even if the difference on seed concentration was high (7.5 µg m^{-3}) the

increase on SOA yield was low. At 12°C, the effect of seeds particles was still limited. However at 7°C, an increase in the seed concentration from 6 μg m^{-3} to 11μg m^{-3} led to a doubled SOA yield. SOA formation ranged from 0.4 to 15.5 μg/m^3 and SOA yields ranged from 0.35% to 19.36% depending on the initial experimental conditions. The toluene walls losses were approximately 5% and were taken into account for SOA yield calculations. The toluene consumption was on average 52±7%.

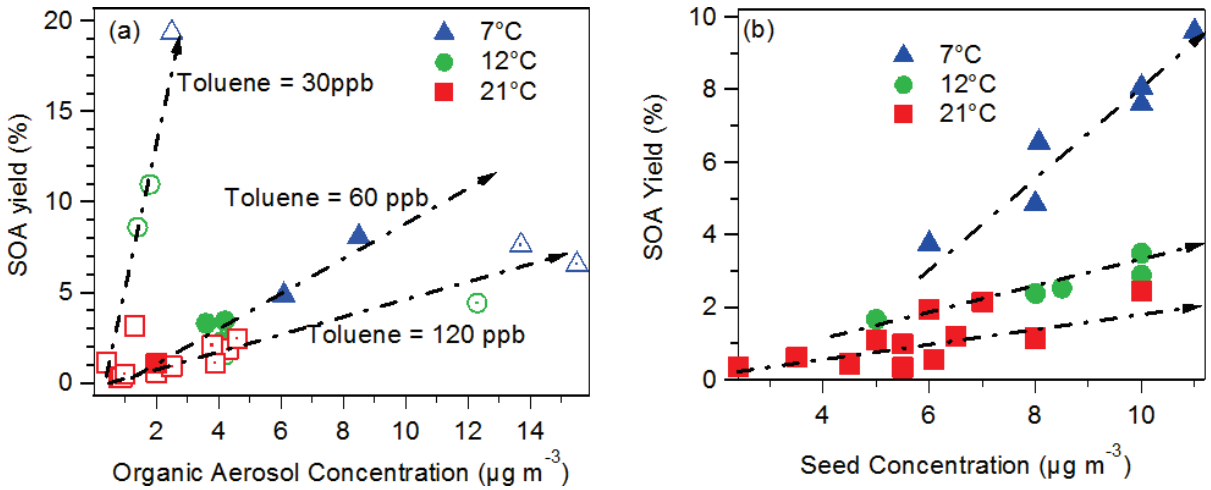

Figure 4.4. *SOA yield as a function of* **(a)** *formed organic aerosol; (b) seed concentration.*

In our experiments, VOC/NO_x ratio (ppbC/ppbv) varied between 3.28 and 7.15. Thus, we consider that the experiments were performed under relatively medium-low NO_x regime.

Figure 4.5. compares the SOA yield from this study to the yields found by Ng et al.[6] and Hildebrandt et al.[5] in smog chamber experiments. Both studies used much higher initial toluene concentrations (200-1000 ppbv) and higher NO_x conditions (300-1200 ppbv). Hildebrandt et al.[5] covered a temperature range of 11-32ºC, while Ng et al.[6] performed experiments at 25ºC.

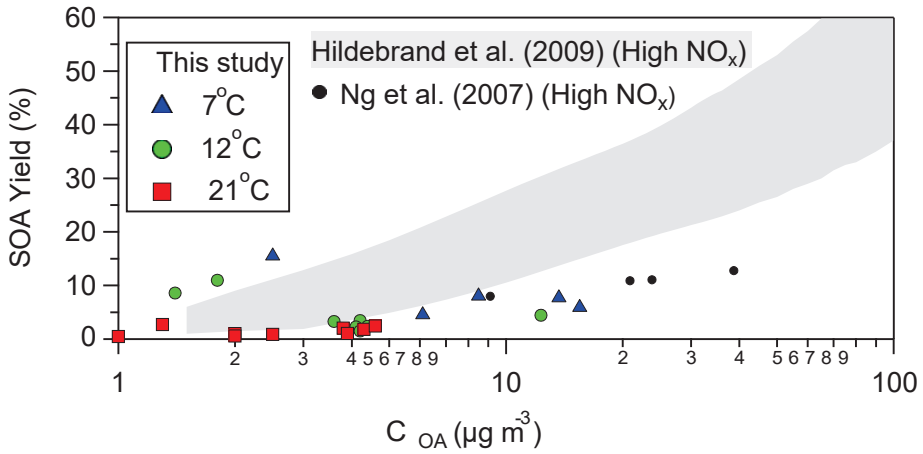

Figure 4.5. *SOA yield comparison with Ng et al. 2007 and Hildebrandt et al. 2009 toluene SOA experiments.*

Our yield is located at the lower edge of the Hildebrandt et al.[5] proposed area, and are closer to Ng et al.[6] data. One reason could be that Hildebrandt et al.[5] yields were

corrected for both organic vapors and particles losses on the chamber walls, while Ng et al.[6] applied wall losses corrections for the particulate phase only. Our SOA yields have been corrected only for toluene wall losses. SOA yield widely vary in the literature for experiments carried out in simulation chamber using toluene as VOC.[4, 7-9] In general, experiments have been done in simulation smog chamber and PAM reactors, which leads to higher •OH exposure times and hence, higher SOA loadings than the presented here.

4.1.2. Gas and particle phase carbon distribution

Figure 4.6. shows the average oxygen and nitrogen distribution as a function of the carbon number for the gas phase products of toluene photoxidation. Carbon number ranges from C_1 to C_7. At 7°C, the C_7 carbon number products account for almost 20% of the total mass. The C_7 carbon products correspond to ring retaining products including cresols and benzaldehyde and their secondary degradation products (see section 4.1.3.). The C_3-C_4 and C_2-C_5 compounds correspond to products formed upon aromatic ring cleavage. By last, the C_1 compound is formed by formic acid and formaldehyde or ion fragments corresponding to such ion fragments.

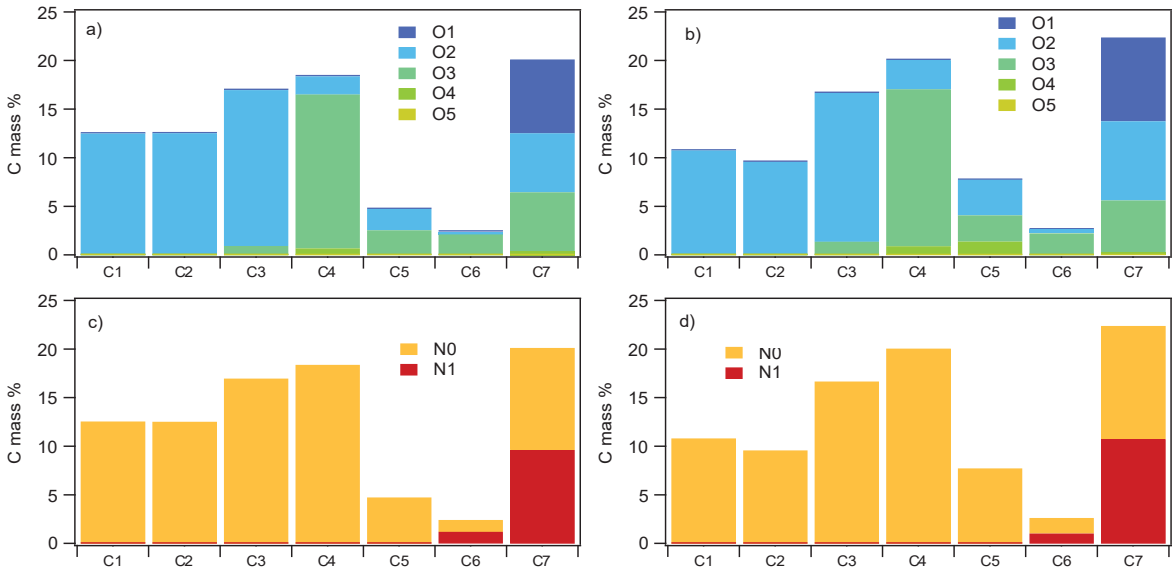

Figure 4.6. *Gas phase carbon number distribution of toluene degradation products a) as a function of oxygen at 7°C, b) as a function of oxygen at 21°C, c) as a function of nitrogen at 7°C, d) as a function of nitrogen at 21°C.*

The reaction products contain between 1 and 5 atoms of oxygen, the oxygen number increases with the carbon number of the molecule. Gas phase reaction products do also contain some nitro-compound. Nitrogen containing compounds account for 11% of total product mass in gas phase. The nitrogen containing fraction is certainly underestimated since PTRMS parameters were not optimized for linear organonitrate products measurement. Hence, only aromatic organonitrates were detected. This fraction did not show any temperature dependence in the experimental range investigated (7-22°C) which is in agreement with

Baltaretu et al.[10] who reported low temperature dependence of the primary toluene oxidation products.

Figure 4.7. shows the average oxygen and nitrogen distribution as a function of the carbon number for the particle phase products. The graphics show experiments carried out at at 7°C (a and c) and at 21°C (b and d). Carbon number ranges from 1 to 7 as for the gas phase. The mass fraction increases with the carbon number. At 7°C, the C_1 and C_2 compounds account approximately 5% each one; the C_3-C_5 compounds account for around 10-15% and the higher mass fractions corresponds to C_6 and C_7 compounds (≈23-25%). As carbon number increases, the molecules present more oxygen atoms ranging from 1 to 5 oxygen for C_7 compounds. A very small fraction of nitrogen-containing compounds is presented in particle phase (3.86% at 7°C and 2.71% at 21°C). Despite the changes in total SOA mass formed, no significant variation in the elemental composition has been observed for experiments at different temperatures.

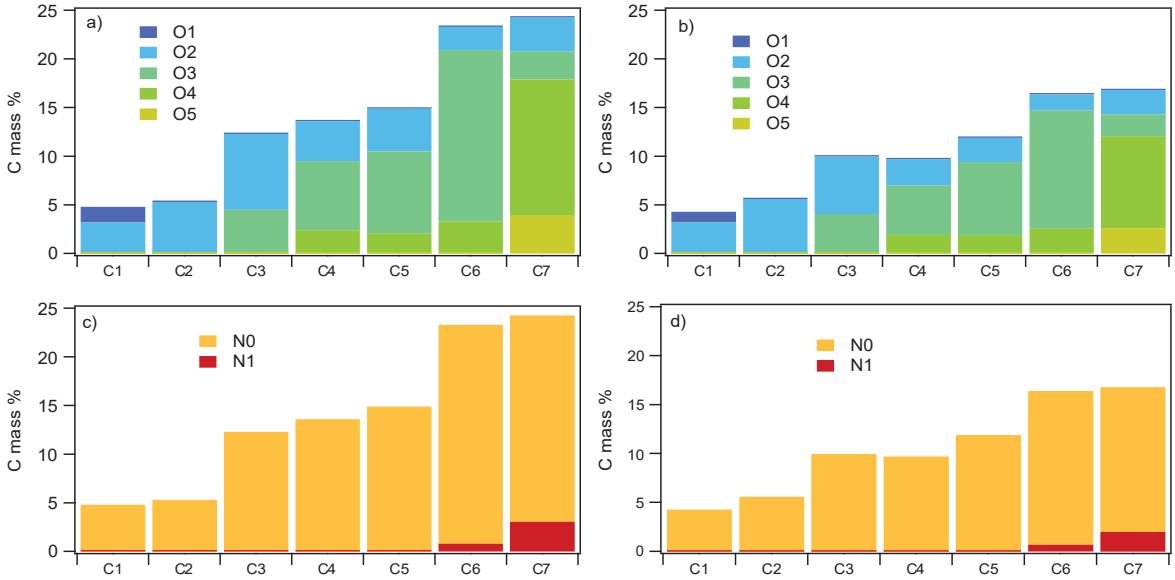

Figure 4.7. *Particle phase carbon number distribution of toluene degradation products a) as a function of oxygen at 7°C, b) as a function of oxygen at 21°C, c) as a function of nitrogen at 7°C, d) as a function of nitrogen at 21°C.*

4.1.3. Gas and particle phase analysis

A detailed chemical composition analysis of the gas and particle phase has been performed. Approximately 31 compounds were identified by the PTR-ToF-MS and the CHARON inlet in the gas and particle phase, respectively, during toluene photoxydation. Table 4.1. presents the exact mass peak, the corresponding ion molecular formula, the tentative chemical assignment (identification) and the quantification for experiments carried out at 7°C and 21°C (Exp n° 27 and 5, respectively). The gas and particle yields (in ppbC) for experiments at 21°C and 7°C can be found in tables AV.1-4 in annex V. These yields are calculated the individual formed product respect to total formed products (relative) and the individual formed product

respect to the consumed VOC (absolute). Tentative assignments are based on references taken in the laboratory of pure compounds (Table AV. 18. In the annex V) and on literature work.[11-14]

Table 4.1. *Gas and particle phase products quantification (ppbC) during the toluene photoxidation for experiments carried out at 7°C and 21°C. In bold are the identified products upon comparison with pure reference compounds.*

				Gas	Particle
n°	Possible compound(s)	Formula	Protonated m/z	7°C/21°C	7°C/21°C
1	**Methylglyoxal**	$C_3H_4O_2/C_2H_4O$	73.03/45.033	13.86/23.74	1.00/0.43
2	**Maleic anhydride**	$C_4H_2O_3/C_4H_5O_4$	99.01/ hydrate at 117.02	12.65/22.14	0.08/0.05
3	Acetic acid/Hydroxyacetaldehyde	$C_2H_4O_2$	61.028	10.84/14.89	0.68/0.40
4	**Formic acid**	CH_2O_2	47.013	10.82/16.69	0.41/0.23
5	Nitrocresols (isomers)	$C_7H_7NO_3$	154.05	5.08/8.04	0.07/0.04
6	**Benzaldehyde**	C_7H_6O	107.05/ possible contribution105.04	3.72/7.91	n.d./ n.d.
7	**Nitrotoluene**	$C_7H_7NO_2$	138.06	3.21/8.55	n.d./ n.d.
8	**Cresols (all isomers)**	C_7H_8O	109.06	2.85/5.43	n.d./ n.d.
9	Benzoic acid*	$C_7H_6O_2$ /C_7H_4O	123.04/105.04	1.99/4.03	0.13/0.07
10	4-oxo-2-pentenal*	$C_5H_6O_2/C_5H_4O$	99.046/81.035	1.90/5.66	0.56/0.18
11	methyl furandione*	$C_5H_4O_3$	113.02	1.38/2.33	0.37/0.14
12	2-butenedial	$C_4H_4O_2$	85.031	1.21/3.26	0.32/0.12
13	**Nitrophenol**	$C_6H_5NO_3$	140.04	1.04/1.61	0.10/0.05
14	2-hydroxy-1,3-propanedial*	$C_3H_4O_3/C_3H_2O_2$	89.026/71.016	0.82/2.14	0.57/0.29
15	4-Oxo-2-pentenoic acid*	$C_5H_6O_3/C_5H_4O_2$	115.04/97.032	0.78/1.86	0.70/0.4
16	4-oxo-2-butenoic-acid*	$C_4H_4O_3$ /$C_4H_2O_2$	101.03/83.012	0.78/2.48	0.43/0.19
17	2-oxo-3-hydroxybutanedial*	$C_4H_4O_4$	117.02	0.60/1.4	0.31/0.14
18	Butan-1,4-dial*	$C_4H_6O_2$	87.05	0.40/1.41	0.20/0.08
19	6-hydroxy-2-methyl, 1,4,5 trioxo-2 cyclohexene*	$C_7H_6O_4$	155.03	0.36/0.43	0.65/0.33
20	methyl-oxo-pentenoic acid*	$C_6H_8O_3/C_6H_6O_2$	129.06/ part of 111.04	0.34/0.71	0.40/0.13
21	2-hydroxy-3-oxobutanal*	$C_4H_6O_3$ /$C_4H_4O_2$	103.04/ possible contribution 85.031	0.26/0.45	0.40/0.13
22	5-Methylfurfural*	$C_6H_6O_2$	111.04 /possible contribution 97.028	0.26/0.62	0.31/0.12
23	5-Hydroxymethylfurfural*	$C_6H_6O_3/C_6H_4O_2$	127.04/109.03	0.19/0.51	0.84/0.33
24	2,3-epoxy, 2-methyl-4-hexenedial*	$C_7H_8O_3$	141.05	0.15/0.26	0.29/0.13
25	2-hydroxy-5-methyl-pentenedial*	$C_7H_8O_5$	173.04	n.d./ n.d.	0.29/0.08
26	4,5-dioxo-2-hexenoic acid*	$C_6H_6O_4$	143.03	n.d./ n.d.	0.42/0.19
27	5-hydroxy-6,4-dioxo-2-heptenal*	$C_7H_8O_4$	157.05	n.d./ n.d.	0.50/0.14

* Or isomers

Methylglyoxal is the most abundant product with an absolute yield of 5.4 % at 7°C. Methylglyoxal has been previously reported in the literature.[1, 11, 15-19] Yields widely varied depending on the experimental conditions. Baltaretu et al.[10] and Ji et al.[20] reported a yield below 4% while other studies [21-23] found methylglyoxal yields between 14-16.7%. Methylglyoxal is also the most abundant product in the particle phase accounting for 7.8% of the total SOA formation. Methylglyoxal has been previously detected in the particle phase.[11, 13, 19] The high concentrations of methylglyoxal in particle phase have been tentatively explained by bulk reaction in the particle leading to the formation of gem-diols. [11]

Glyoxal is usually reported as a main toluene photoxidation product, following the same formation route the methylglyoxal.[18, 24, 25] However, the glyoxal detection (m/z 59.013) was difficult in our system because of interferences with dominanting signal of acetone (59.049), which is formed by degradation of the IPN and because of the low sensitivity of the PTRMS for glyoxal (due to its low polarity). Other products formed upon the ring opening are the 4-oxopentenal or 2-butenedial. These compounds are co-products of glyoxal and methylglyoxal respectively. [11]

Maleic anhydride is the second most abundant gas phase product. Maleic anhydride has been previously reported in the literature.[11, 14, 26] It is formed from photolysis or •OH reaction with 2-butenenedial and further O_2 addition, ending with a ring closure.

Benzaldehyde, cresol and nitrotoluene have been previously reported as first generation product from toluene photoxydation.[10,11,16-20, 27, 28] Cresol is formed from OH-toluene adduct, product of OH-addition mechanism. H-abstraction mechanism gives rise to the benzyl radical that is rapidly converted to benzaldehyde. The ratio between H abstraction and •OH addition is well established in the literature by simulation experiments and models and it is close to 0.08.[12, 14, 21, 29-33] In this work the branching ratio of 4.3% for the benzaldehyde, without taking into account further reaction of benzaldehyde. Formation of nitrotoluene by NO_2 direct addition to the toluene molecule accounts for a 3.7% of the total products. Nitrocresol is formed by direct addition of NO_2 group to a cresol molecule and accounts for 5.9% of the total gas phase products.

The ion fragment at m/z 123.04 corresponds to the molecular formula $C_7H_6O_2$, which can be attributed to methyl benzoquinone, benzoic acid, hydroxybenzaldehyde or other isomers. Benzoic acid and methyl benzoquinone have been detected by White et al.[13] and Schwantes et al.[12] as result of the reaction of HO_2• with the peroxy radical, (formed from •OH oxidation of benzaldehyde). The methyl benzoquinone formation could be explained as a secondary product from cresol degradation. The •OH radical reaction with cresol can lead to a biclyclic intermediate compound that decomposes and produces methyl benzoquinone.[12] Hydroxy benzaldehyde was firstly reported by Borras and Totajada-Genaro [19] who proposed an •OH addition to a benzaldehyde molecule as a possible formation mechanism.

The 4-oxopentenal (m/z 99.046), the 2-oxopentenoic acid (m/z 115.04) and the hydroxymethyl trioxo cyclohexene (155.03) are major products in the particle phase. These compounds were also identified in the gas phase in smaller fractions. The 4-oxopentenal has been previously reported.[12, 14, 27] The ion fragment at m/z 115.042 has several possible isomers, literature work suggested that the aromatic ring decomposition of the bicyclic peroxy radical leads to the formation of $C_5H_6O_3$ isomers and they attributed these isomers to acetyl acrylic acid, 4-oxo-2-pentenoic acid and 2-methyl-4-oxo-2-butenoic acid.[11],[12]

The ion fragment at m/z 155.03 may have two possible isomers at least. Several previous works on toluene assigned it to hydroxymethyl trioxo cyclohexene [11, 12, 14] formed from methyl benzoquinone, which reacts with OH and after with O_2 to form its peroxy radical. Schwantes et al.[12] proposed dihydroxy methyl benzoquinone as isomer, formed by OH-degradation of the trihydroxy toluene. Degradation mechanisms for the first steps of toluene photoxidation are presented in figure AV.1. in annex V. Approximately 10-15% of the products found in the particle phase are non-volatile and are not detected in the gas phase, the remaining fraction is characterized by products that do partition between the gas and the particle phase.

4.1.4. Gas/Particle phase partitioning analysis

Using the particle and gas phase concentrations of the reaction products measured. It was possible to calculate the partitioning coefficient ($K_{p,i}$) and the saturation concentration, C_i^* using equations [1.13] and [1.17] described in chapter I. Figure 4.8. shows the $K_{p,i}$ values for three different temperatures for selected m/z's. For all compounds, the $K_{p,i}$ at 7 and 12 °C (black and green bars) are systematically higher than $K_{p,i}$ 21 °C, indicating how the volatility of these compounds is affected by relatively small changes in temperature. Figure AV.2. the in annex V contains the calculated $K_{p,i}$ values of all the m/z's.

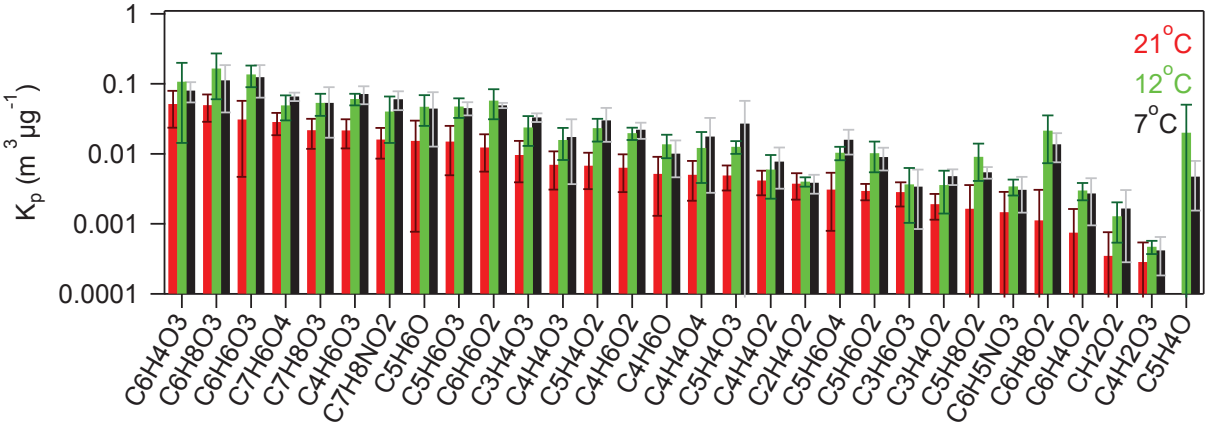

Figure 4.8. *Experimental K_p values of m/z's for toluene photoxidation, where a unique compound or a set of isomers compounds were assigned. The error bars correspond to the one standard deviation of the average.*

Figure 4.9. depicts the O:C ratio of the identified reaction products of the OH-toluene system versus the $log_{10}C_i^*$ at 21°C and 7°C as a function of the oxygen atom number. The

volatility representation into the 2D-VBS framework [34] was used in Figure 4.7. in order to facilitate the interpretation of our results. The toluene SOA products fall in the area of the semi-volatile organic compounds, SVOCs, (light green) covering also a small area of the intermediate volatile organic compounds, IVOCs (light blue). The toluene SOA saturation concentration ranged between 1 and 10^5 μg/m^3 and there was not a clear trend between the saturation concentration, O:C and oxygen number. For lower temperatures the toluene SOA saturation concentration decreased appreciably, which is indicated in figure 4.8. by the shift to the left by the gray circles (7°C date set).

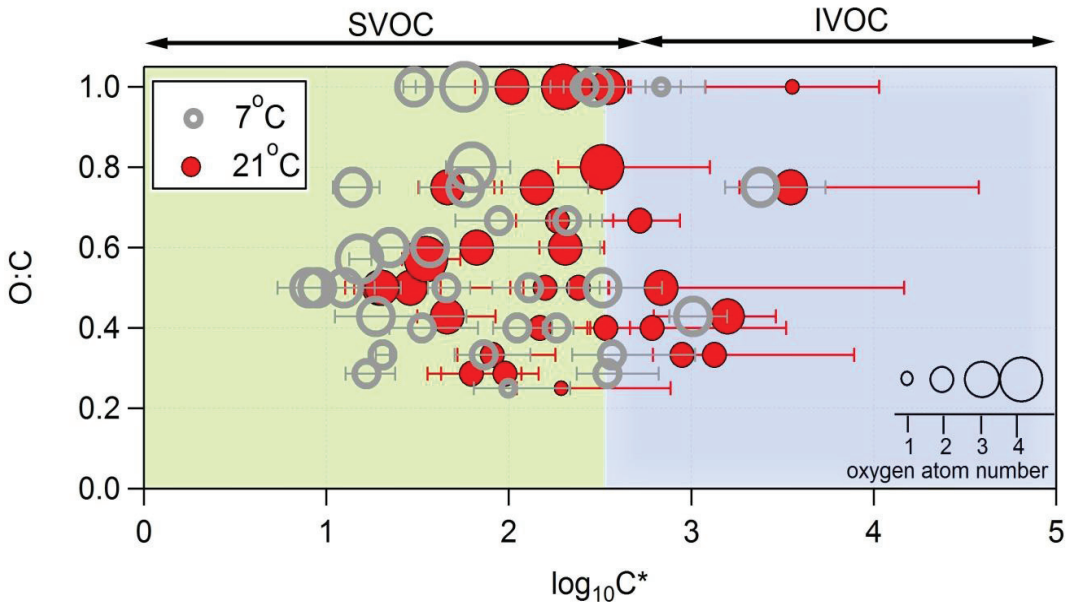

Figure 4.9. *O:C ratios versus the saturation concentration in terms of $log_{10}C^*$ for the species indentified in both gas and particle phase. The size of the dots denotes the oxygen atom number of each species. The error bars correspond to logarithmic values of the minimum and maximum K_p values shown in Figures 4.6. and AV.2.*

4.2. Naphthalene photoxidation

Naphthalene was measured in the exhaust of the tested gasoline and diesel emissions. In general, naphthalene is the most abundant PAHs in vehicle emissions.[35-38] PAHs show a very high SOA formation potential.[39-41] Thus, even if naphthalene is emitted in very small amounts in comparison to other compounds, both its contribution to SOA and its particle phase products should be investigated. In total, 7 experiments have been carried out in the AFT using naphthalene as SOA precursor. The naphthalene wall losses were approximately of 10% and were included in the SOA yield calculation.

4.2.1. Influence of parameters for SOA formation

Figure 4.10. illustrates the SOA yield as a function of the produced SOA mass concentration at different temperatures and initial naphthalene concentrations. For similar

initial VOC concentration, experiments at low temperature led to higher organic concentration and hence, SOA yields.

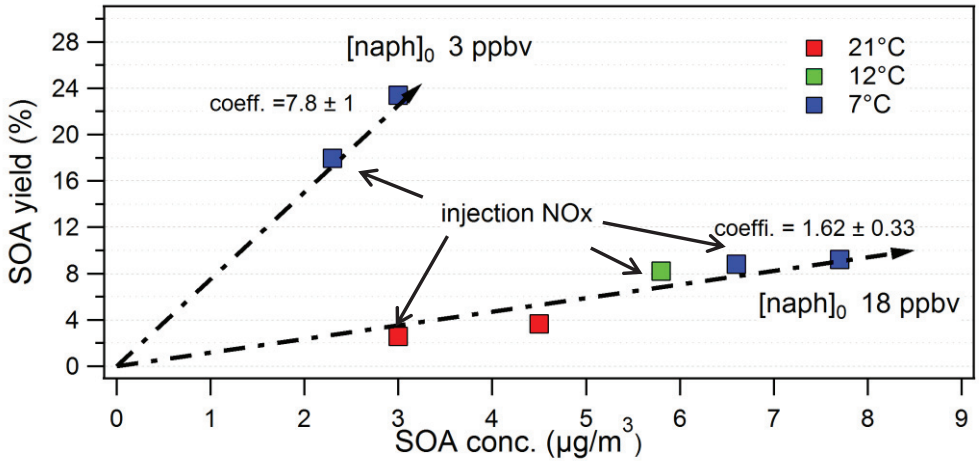

Figure 4.10. *Influence of Temperature and initial VOC concentration for naphthalene experiments.*

Others parameters as initial VOC, NOx and seeds concentration do highly influence SOA formation. For naphthalene concentrations of 3 ppbv, SOA yields are in the order of 18-23% while SOA formed is around 2-3 µg/m^3 at 7°C. SOA yield decreases to 8-9% for naphthalene concentrations of 18-25 ppbv with a formed SOA mass around 8 µg/m^3 for experiments at same temperature. Lower VOC concentration leads to higher SOA yields (as VOC consumption is low) but poor SOA mass concentration as compared to higher VOC loads. For similar initial conditions, addition of NOx (200pbbv) shows a reduction of SOA concentration from 7.7 to 6.6 µg/m^3 at 7°C and from 4.5 to 3 µg/m^3 at 21°C. NOx concentration reduce SOA formation changing the product distribution as already discussed in chapter I. This is in agreement with Chen et al.[39], who reported higher SOA yields from naphthalene and methylnaphthalene at low NOx.

To sum up the naphthalene, SOA formation ranged from 2.3 to 7.7 µg/m^3 and SOA yields from 2.6% to 23%. High variability of SOA yields is reported in the literature. Chan et al.[42] reported yields in the range of 19-30% for high NOx experiments and around 70% for low NOx regime. While Kleindienst et al.[43] reported yields between 11% and 30 % at low and high NOx regime, respectively. Shakya and Griffin [44] found reduced yield variation (8-13%) for different VOC/NOx conditions.

4.2.2. Gas and particle phase carbon distribution

Figure 4.11. shows the average oxygen and nitrogen distribution as a function of the carbon number for the gas phase products of naphthalene. The graphics show experiments carried out at 21°C (a and b) and at 7°C (c and d) with addition of 200 ppbv of NOx.

Experiments without NOx addition show almost identical product distribution and therefore are not presented here.

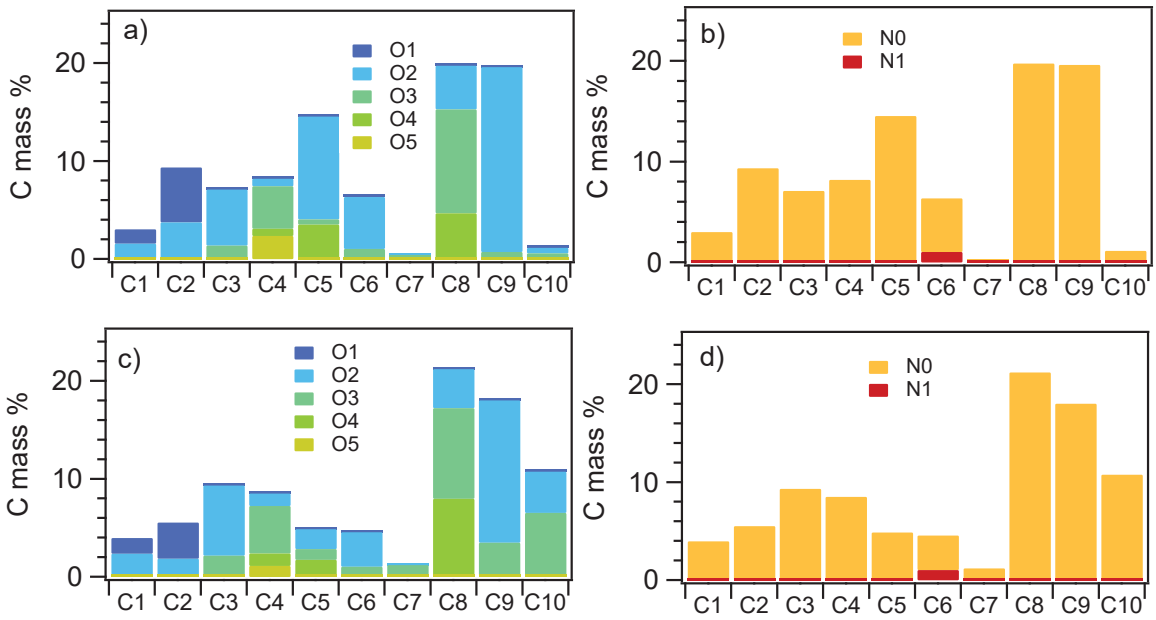

Figure 4.11. *Gas phase carbon number distribution with addition of 200 ppb of NOx a) as a function of oxygen at 21°C b) as a function of nitrogen at 21°C c) as a function of oxygen at 7°C d) as a function of nitrogen at 7°C*

Carbon number ranges from C_1 to C_{10}. Carbon distribution is dominated by C_8 (19-21%) and C_9 (14-19%) compounds, corresponding to first and second oxidation products while the C_{10} compounds (ring retaining structure) accounts for 5-10% of the total products. At room temperature Figure 4.9.(a), smaller reaction products (mainly C_5 compounds) products account for 14% of the total gas phase products. While at lower temperature (figure 4.9.c) these ccompounds account for less than 10% of the products. The C_1 and C_2 compounds present mainly one or two oxygen atoms; the C_4, C_5 and C_8 are characterized by higher oxygen content, mainly between 2 and 4 oxygen atoms. Nitrogen containing compounds account for approximately 1-2% of the gas phase products.

Figure 4.12. shows the average oxygen and nitrogen number as a function of the carbon number for the particle phase products. The graphics show experiments carried out with addition of 200ppb of NOx at 7°C. Experiments without NOx addition and experiments carried out at 21°C presented almost identical product distribution and therefore are not presented here. Particle phase products C distribution is considerably different that what observed for the gas phase (figure 4.9.). At 7°C, the C_{10} and C_8 compounds are the most abundant products, accounting for 22% and 38% of the total particle phase products, respectively. SOA composition is mainly formed by compounds containing 2, 3 and 4 oxygen atoms corresponding to 26%, 44% and 11%, respectively, of the total particle mass loading. As for carbon distribution, NOx addition to the reactants mixture has little influence in the product distribution.

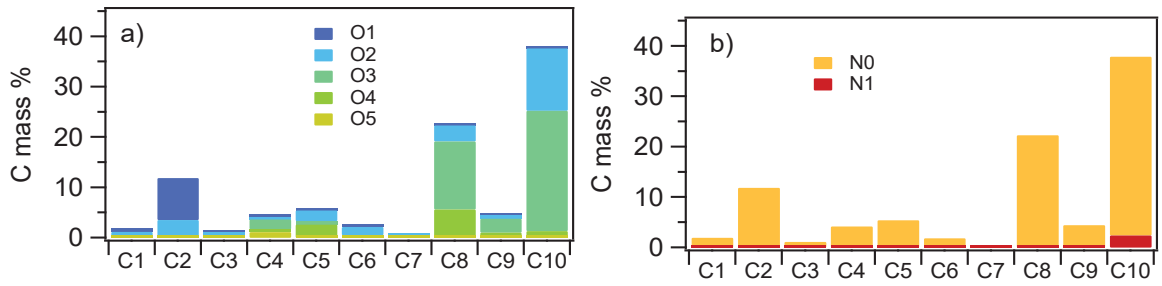

Figure 4.12. *Particle phase carbon number distribution with addition of 200 ppb of NOx at 7°C a) as a function of oxygen b) as a function of nitrogen.*

4.2.3. Gas and particle phase analysis

A detailed chemical composition analysis of the gas and particle phase has been carried out. Table 4.2. presents the exact mass peak, the corresponding ion molecular formula, the tentative chemical assignment of reaction products and quantification for experiments at 7°C and 21°C (Exp n° 5 and 2, respectively). Gas and particle yields for experiments at 21°C and 7°C can be found in tables AV.5-8 in annex V. Tentative assignments are based on references spectra of pure compounds (Table AV.18. in the annex V), toluene photoxidation products, and literature.[45-47]

In the next section only some of the major reaction products will be discussed with respect to the literature. Cinnamic acid is one of the most abundant products found in gas phase. The overall yield ranged from 19% to 14.5%. Chen et al.[39] reported cinnamic acid as a major product in the gas phase. C_9 products are secondary generation compounds formed by O_2 addition to 2-formylcinnamaldehyde to form $RO_2^{\bullet}$ radicals and further $RO^{\bullet}$ radicals. Kautzman et al.[45] proposed loss of CO_2 followed by hydride shift and O_2/HO_2 oxidation as possible explanation to form acids. The reaction mechanism can be found in figure AV.4 in the annex V.

Phthalic anhydride is a major reaction product found both in the gas and the particle phase. Gas phase yields vary from 9.9 % to 6.4% when decreasing the temperature from 21°C to 7°C. Particle phase yield are above 10%. Sasaki et al.[47] estimated yields of approximately 3% at room temperature. Phthalic anhydride is generally thought to be a second generation product, probably from first generated phthalaldehyde through further reaction with $^{\bullet}OH$ radical and isomerization process.[48]

Phthalic acid has been found the most abundant product in SOA mass in other studies [45, 48, 49] and also found in appreciable amounts here. Further oxidation of phthalic anhydride yields phthalic acid. The hydroxy phthalic anhydride is another product thought to be formed from phthalic anhydride.

Table 4.2. *Gas and particle phase products quantification (ppbC) found in naphthalene photoxidation for experiments at 7°C and 21°C.*

n°	Possible compound(s)	Formula	Protonated m/z	Gas 7°C/21°C	Particle 7°C/21°C
1	Cinnamic acid	$C_9H_8O_2$	149.059	15.00/25.38	0.18/0.02
2	Glyoxylic acid or fragment	$C_3H_6O_2$	75.044	7.41/7.72	0.15/0.06
3	Phthalic anhydride	$C_8H_4O_3/C_8H_2O_2$	149.023/131.012	6.58/13.29	2.98/0.23
4	Fragment	$C_2H_4O/C_2H_6O_2$	45.033/63.044	5.72/12.58	2.41/4.11
5	1, 4-naphthoquinone 2,3-oxide	$C_{10}H_6O_3/C_{10}H_4O_2$	175.038/157.028	5.01/0.28	1.40/0.01
6	Phthalic acid	$C_8H_6O_4$	167.033	3.80/4.75	0.61/n.d.
7	2-formylphenyl acrylic acid*	$C_{10}H_8O_3$	177.054	1.62/0.39	4.62/0.04
8	Naphtoquinone	$C_{10}H_6O_2/C_{10}H_4O$	159.044/141.033	1.36/0.46	1.35/0.07
9	Coumaric acid*	$C_9H_8O_3/C_9H_6O_2$	165.054621/147.044	3.48/0.96	0.80/0.01
10	Hydroxy phthalic anhydride	$C_8H_4O_4/C_8H_2O_3$	165.018/147.0076	3.14/0.83	0.79/0.07
11	2-formylcinnamaldehyde	$C_{10}H_8O_2/C_{10}H_6O$	161.059/143.049	2.99/0.3	1.02/0.1
12	Phthalaldehydic acid *	$C_8H_6O_3/C_8H_4O_2$	151.038/133.028	2.98/0.97	0.68/0.05
13	Formic acid	CH_2O_2	47.013	2.45/2.1	0.31/0.42
14	Phthalaldehyde	$C_8H_6O_2/C_8H_4O$	135.044/117.033	2.40/5.29	0.67/0.07
15	2-hydroxy-1,3-propanedial*	$C_3H_4O_3/C_3H_2O_2$	89.0233/71.012	2.23/1.85	0.15/0.15
16	Hexano-2,5-dione*	$C_6H_{10}O_2/C_6H_8O$	115.075/97.064	1.33/1.03	0.22/0.12
17	2-butenedial	$C_4H_4O_2$	85.028	1.32/1.02	0.14/0.1
18	Hydroxybenzoic acid*	$C_7H_6O_3/C_6H_6O$	139.038/95.049	1.24/0.52	0.09/n.d.
19	4-oxo-pentanal*	$C_5H_8O_2/C_5H_6O$	101.06/83.049	1.12/0.59	0.29/0.1
20	Nitrophenol*	$C_6H_5NO_3/C_6H_3NO_2$	140.034/122.024	1.06/1.39	0.05/n.d.
21	Nitronaphtol	$C_{10}H_7NO_3$	190.049	0.03/0.07	0.64/0.07
22	Acetic acid*	$C_2H_4O_2$	61.028	n.d/n.d.	0.73/1.28
23	Diacetylbenzene*	$C_{10}H_{10}O_2$	163.075	n.d./n.d.	0.91/0.04

* Or isomers

The phthalaldehyde yield was in the range of 2.3-3.9% for temperatures between 21°C and 7°C in gas phase. Wang et al.[48] reported phthalaldehyde as one of the most abundant gas phase product. Glyoxal is reported as co-product of phthalaldehyde as a result of loss of two carbons from naphthalene.[50] However, while glyoxal can be formed also as secondary product from other pathways, phthalaldehyde is only a first generation product.[49] Even if not measured (because of interferences with acetone), we can assume a glyoxal formation yield similar to that of phthalaldehyde.

The 2-formylcinnamaldehyde is a major ring opening reaction products. In our experiments, the 2-formylcinnamaldehyde observed in the gas phase accounts for low yields varying from 0.22% to 2.90% when decreasing the temperature from 21°C to 7°C. But

literature reported higher yields at low and high NOx regime (14-56%).[45-47, 51] Some authors suggested that 2-formylcinnamaldehyde is highly prone to photolysis.[49] Others suggested that it will be rapidly oxidized.[45] The fact that further generation products are observed in our experiments can explain the low yield measured for 2-formylcinamaldehyde which is first generation product.

The 1,4-naphthoquinone 2,3-oxide has been reported previously in literature with a yield around 5%.[47] In our study, 1,4-naphthoquinone 2,3-oxide is found in both gas and particle phase with similar yield around 5%. Zhang et al.[52] reported a formation mechanism for 1, 4-naphthoquinone 2,3-oxide starting from the peroxy hydroxynaphthalene radical followed by oxygen atom loss and isomerisation. The 1,4-naphtoquinone is another important compound in the particle phase with a yield of 5% while in the gas phase it reaches 1% at 7°C. The 1,4-naphtoquinone has been previously reported in literature in small yields, according to those presented here.[42, 45, 47, 53, 54]

A simplified naphthalene degradation mechanism for first generation product can be found in Figure AV.3 in the annex V.

4.2.4. Gas/particle phase partitioning analysis

Using the particle and gas phase concentrations of the reaction products measured it was possible to calculate the partitioning coefficient ($K_{p,i}$) and the saturation concentration, C_i^* using equations [1.13] and [1.17] described in chapter I. Figure 4.13. shows the $K_{p,i}$ values for three different temperatures, 7 , 12 and 21 °C and for selected m/z's. Figure AV.2. in the annex V contains the calculated $K_{p,i}$ values for all the m/z's measured.

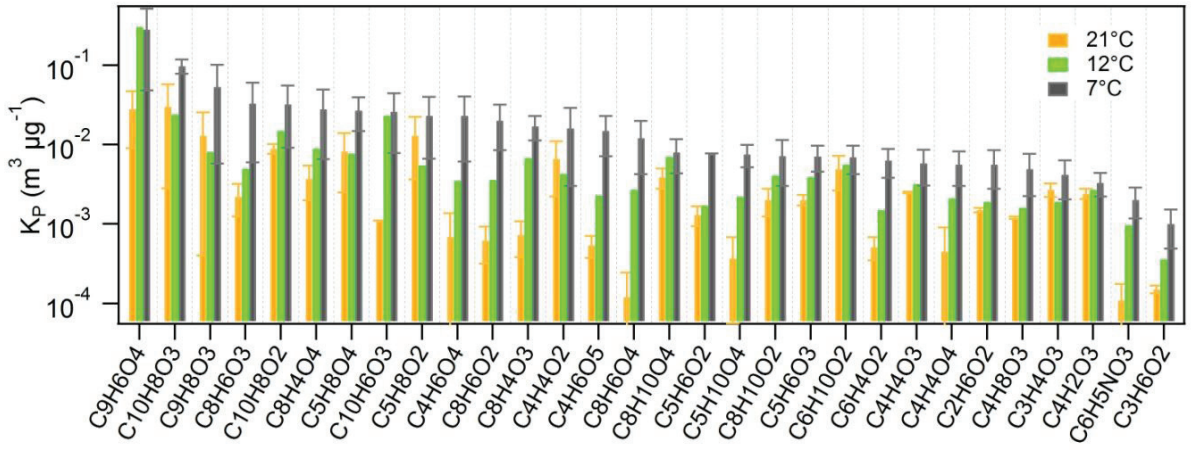

Figure 4.13. *Experimental K_p values of m/z's for naphthalene photoxidation, where a unique compound or a set of isomers compounds were assigned. The error bars correspond to the one standard deviation of the average.*

Figure 4.13. presents a wide range of partition coefficients, ranging from 0.4 to $1x10^{-4}$ $m^3/\mu g$. The $K_{p,i}$ at 21°C was clearly lower in comparison to $K_{p,i}$ at 7°C, indicating that changes in

temperature highly affect volatility of the measured species. As a trend, compounds that own higher number of carbon atoms own higher *Kp*. Figure 4.14. depicts the O:C ratio of the identified molecules i versus the $log_{10}C_i^*$ at 21°C and 7°C as a function of the oxygen atom number.

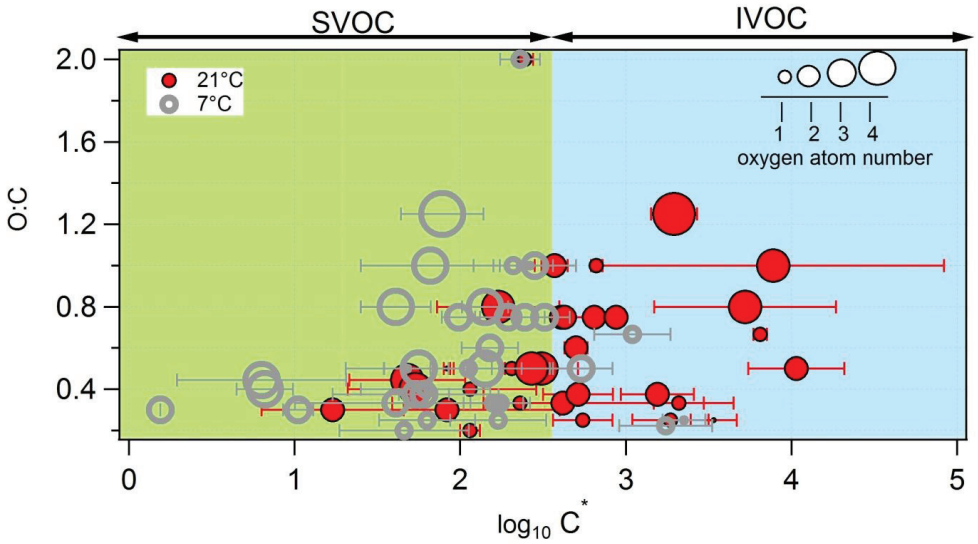

Figure 4.14. *O:C ratios versus the saturation concentration in terms of $log_{10}C^*$ for the species indentified in both gas and particle phase. The size of the dots denotes the oxygen atom number of each species. The error bars correspond to logarithmic values of the minimum and maximum K_p values shown in Figures 4.12.*

The volatility representation into the 2D-VBS framework [34] was used in Figure 4.12.. The naphthalene SOA products fall in the area of the semi-volatile organic compounds, SVOCs, (light green) covering also a small area of the intermediate volatile organic compounds, IVOCs (light blue). The SOA saturation concentration ranged between 0.2 and 10^4 μg/m^3 and there was not a clear trend between the saturation concentration and the O:C oxygen number. For lower temperatures the naphthalene SOA saturation concentration decreased appreciably, which is indicated in figure 4.14. by the shift to the left by the gray circles (7°C date set). In term of mass, for experiment at 21°C, SVOCs account for 42.7% and IVOCs for 20.14%. At 7°C, SVOCs account for 77.5% and IVOCs for 2.29%, which is in agreement with the toluene results.

4.3. Cyclohexane photoxidation

Gasoline and diesel vehicle exhaust comprises also cyclic compounds. The cycloalkanes represent a large fraction as already seen in the chapter III and in the literature.[35, 36, 55-58] Cyclohexane was chosen as model compound for the cycloalkanes family. In total, 9 experiments have been carried out in the AFT.

4.3.1. Influence of parameters for SOA formation

Figure 4.15. presents the SOA yield versus concentration of formed SOA as a function of temperature and cyclohexane initial concentration.

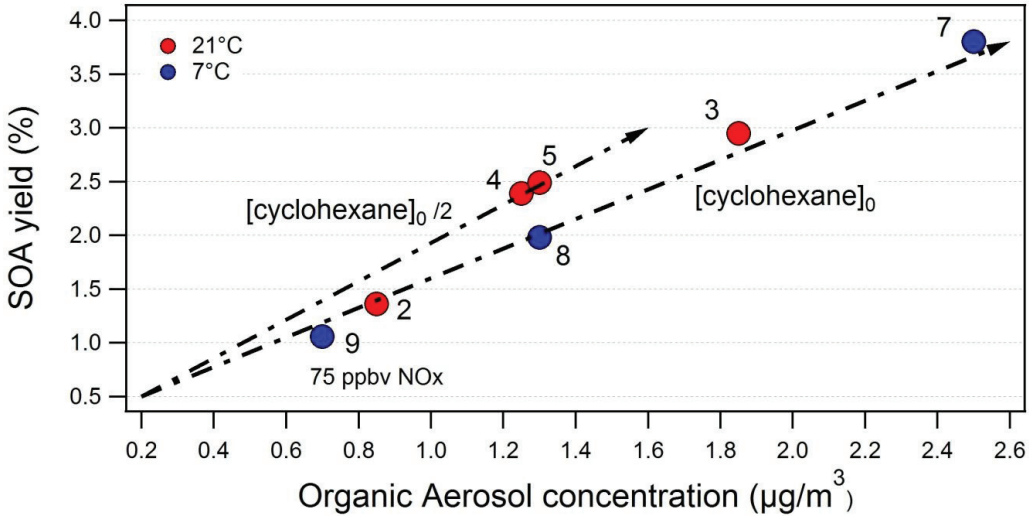

Figure 4.15. *SOA yield versus SOA concentration as a function of temperature and initial cyclohexane concentration.*

In the figure 4.15., data points 7 and 8 indicate experiment carried out under similar initial cyclohexane concentration, humidity and temperature but different OH-exposure being point 8 associated to an OH-exposure of 11 hours and point 7 to 28 hours. The enhanced OH radical exposure induces an increase in SOA mass concentration from 1.3 µg /m^3 to 2.5 µg /m^3. While points 8 and 9 show, under identical experimental conditions, a reduction of a factor two in the formation of the SOA (from 1.3 µg/m^3 to 0.7µg/m^3) when 75 ppbv of NOx are added. Points 3, 4 and 5 show the effect of the initial concentration of cyclohexane for experiments at 21 °C. Thus, doubling initial concentration of cyclohexane (from 25 to 50 ppbv), an increase of 0.6µg/m^3 of SOA mass is observed.

To sum up the cyclohexane, SOA formation ranged from 0.7 to 1.85 µg/m^3 and SOA yields from 1.06 % to 3.8 %. Experiments without preexisting AS seed did not produce any SOA mass. Lim and Ziemann [59] reported a yield of 4% for cyclohexane studies at room temperature in smog chamber in presence of NOx using much higher concentrations of precursor and seeds.

4.3.2. Gas and particle phase carbon distribution

Figure 4.16. shows the average oxygen number distribution as a function of the carbon number for the reaction products of cyclohexane. The graphics show (a) gas phase products, (b) particle phase products, (c) gas phase product when 75 ppbv NOx are added and (d) particle phase products when 75 ppbv NOx are added for experiments at 7°C.

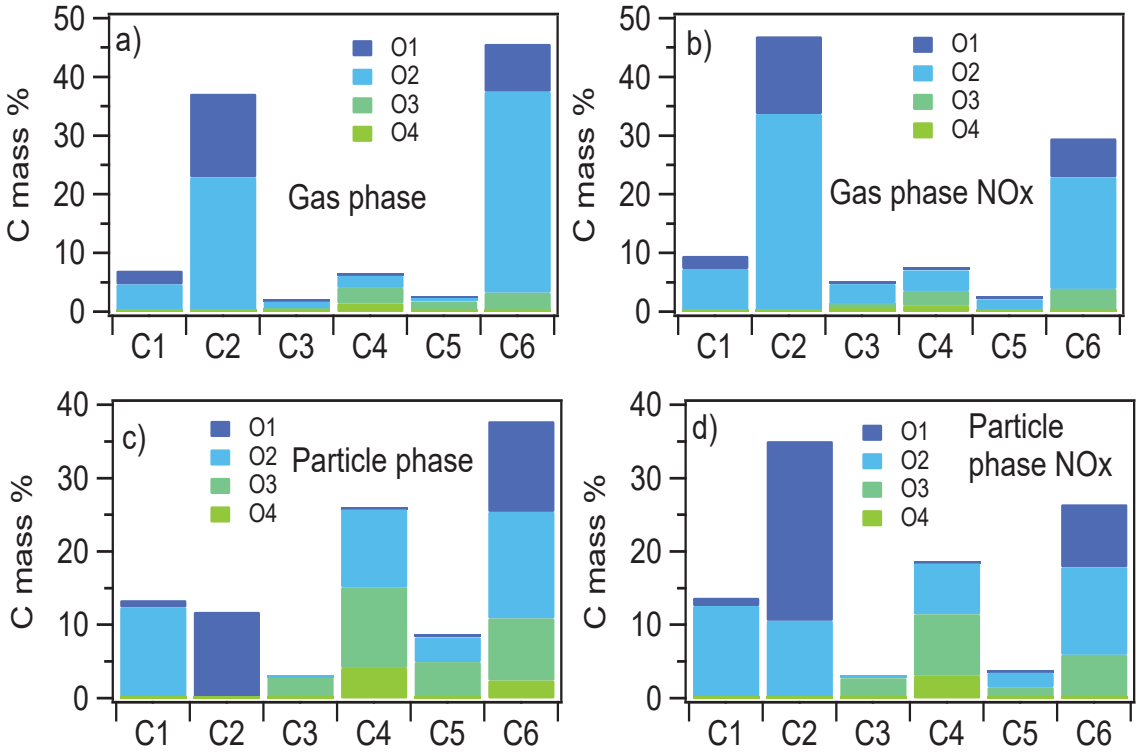

Figure 4.16. Average oxygen number as a function of carbon number product distribution at 7°C for: gas phase experiment (a), gas phase experiment with NOx addition (b), particle phase experiment (c), particle phase experiment with NOx addition(d).

Cyclohexane reaction products range from C_1 to C_6 compounds in both phases. The carbon distribution is always dominated by C_2 (37-47%) and C_6 (30-46%) compounds, corresponding to first and second oxidation and ring retaining products, respectively. As observed, addition NOx and hence, a reduction of VOC/NOx ratio from 3.7 to 3.2 (plot b and d) leaded to an increase of the C_2 mass fraction and decreased of C_6 mass fraction. Results suggest that pathways corresponding to ring retained products formation (cyclohexanone, cyclohexanedione, cyclohexanol...) are favoured at low NOx regimes while ring cleavage is more likely at high NOx values. In the particle phase, the C_4 compounds account for approximately 18-24% of the total mass fraction. This group can be formed from fragmentation of C_6 compounds.

Nitrogen containing compounds were not detected in the cyclohexane experiments but it has to be noted that aliphatic nitro-compounds would be readily decomposed in the PTR-MS loosing HNO_2 or HNO_3 and giving rise to oxygenated ion fragments. Therefore we are almost blind with respect to these compounds with the used instrumental parameters.

4.3.3. Gas and particle phase analysis

A detailed chemical composition analysis of the gas and particle phase was carried out using PTR-MS and CHARON inlet. Table 4.3. presents the exact mass peak, the corresponding ion molecular formula, the tentative chemical assignment of reaction products and the

quantification for experiments at 7°C with and without NOx addition (Experiments n° 9 and 8, respectively).

The gas and particle yields for the experiments at 7°C with and without NOx addition can be found in tables AV.9-12 in the annex V. Tentative product assignment was based on references spectra of pure compounds (Table AV. 18. in the annex V) and previous literature. [60-64] In the next section only some of the major reaction products will be discussed with respect to the literature.

Table 4.3. *Gas and particle phase products quantification (ppbC) found in cyclohexane photoxidation for experiments at 7°C without and with NOx addition.*

n°	Possible compound(s)	Formula	Protonated m/z	Gas	Particle
				W NOx/w/o NOx	W NOx/w/o NOx
1	Cyclohexanedione	$C_6H_8O_2$	113.06	14.51/20.28	0.06/0.07
2	Acetic acid/fragment	$C_2H_4O_2$	61.028	27.85/13.25	0.08/n.d.
3	Acetaldehyde /fragment	$C_2H_4O/C_2H_6O_2$	45.033/63.044	13.61/10.51	0.26/0.14
4	Cyclohexanone	$C_6H_{10}O$	99.080	5.00/4.11	0.01/0.03
5	Formic acid	CH_2O_2/CH_4O_3	47.012/65.022	6.44/2.98	0.12/0.15
6	Cyclohexanol	$C_6H_{12}O$	101.097	0.81/1.08	0.07/0.13
7	hexan-1,6-dial/hydroxy cyclohexanone	$C_6H_{10}O_2/C_6H_8O$	115.07/97.062	0.90/1.35	0.05/0.10
8	2,4-dihydroxybutanal*	$C_4H_6O_2/C_4H_4O$	87.044/69.031	2.24/0.87	0.03/0.06
9	pentan-1,5-dial	$C_4H_4O_3/C_4H_2O_2$	101.02/83.012	0.84/0.73	0.04/0.06
10	2-hydroxy-1,3-propanedial*	$C_4H_8O_2/C_4H_6O$	89.059/71.049	0.84/0.43	0.03/0.07
11	2-hydroxy-3-oxobutanal*	$C_4H_6O_3/C_4H_4O_2$	103.04/85.028	0.86/0.64	0.03/0.05
12	methyl-oxo-pentenoic acid*	$C_6H_8O_3/C_5H_8O$	129.05/85.064	0.74/0.41	0.03/0.05
13	3-hydroxypentane-1,5-dial	$C_5H_6O_3/C_5H_4O_2$	115.04/97.028	0.09/0.95	0.01/0.05
14	Formaldehyde /fragment	CH_2O	31.018	1.99/1.50	0.01/0.01
15	4-oxo-pentanal	$C_5H_8O_2/C_5H_6O$	101.06/83.049	1.48/0.26	0.02/0.03

* Or isomers

Cyclohexanone is a well-known gas phase reaction product of cyclohexane.[63] Its degradation by OH radicals can give rise to the cyclohexanedione, one of the most abundant products in the gas phase. The overall yield ranged from 16% to 32%. Its formation can be explained by the $^{\bullet}OH$ reaction with cyclohexanone. The high yield of cyclohexanedione may explain the small yield of cyclohexanone reported here (5-6%), compared to literature (9-21%).[62, 65-67] First generation ring retaining products as cyclohexanol and hydroxy cyclohexanone do present an important fraction of the gas products reaching 2 % in the gas phase and 10% in the particle phase. These products were also reported in previous literature. [63, 67] Figure AV.4. in the annex V presents a simplified cyclohexane degradation mechanism and first generation products formation.

Ring cleavage pathway forms dialdehydes and carboxylic acids.[58, 64] Acetic acid, acetaldehyde, formic acid, formaldehyde, glyoxylic acid and butan-1,4-dial can be explained by open ring followed by further decomposition of the C_6 atom molecules. Formaldehyde, hexanedial and formic acid have been reported in literature [61, 65, 66] and are also reported here for both phases. Formic acid is one of the major products in particle phase (12.3%). Formation mechanism for formic acid is presented in figure AV.5 in the annex V. During the present experiments average ratio between ring retaining and ring cleavage reaction products was approximately of 0.66 for the gas phase, while for the particle phase this value is approximately 0.23.

Figure 4.17. depicts the O:C ratio of the identified molecules i versus the $log_{10}C_i^*$ for experiment as a function of the oxygen atom number. The volatility representation into the 2D-VBS framework was used in Figure 4.15. in order to facilitate the interpretation of our results. The cyclohexane SOA products fall in the area of the semi-volatile organic compounds, SVOCs, (light green) covering also a small area of the intermediate volatile organic compounds, IVOCs (light blue). The cyclohexane SOA saturation concentration ranged between 10 and 10^3 μg/m^3. Compounds with higher O:C ratio showed in general lower volatility even though some exception is observed. In term of mass, for experiments without NOx injection, SVOCs account for 65% and IVOCs for 9% of the total SOA mass.

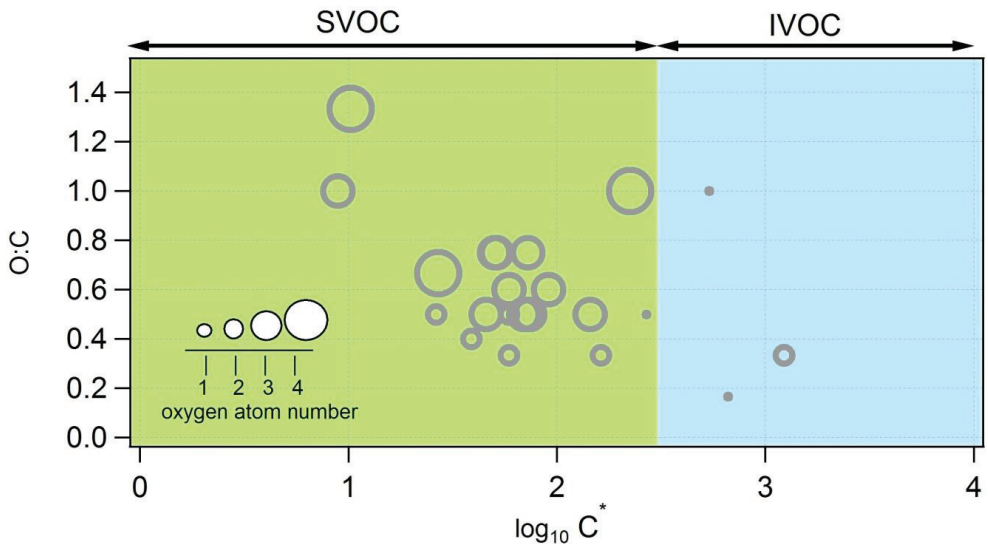

Figure 4.17. *O:C ratios versus the saturation concentration in terms of $log_{10}C^*$ for the species indentified in particle phase. The size of the dots denotes the oxygen atom number of each species.*

4.4. Nonane photoxidation

Linear alkanes have been measured in both gasoline and diesel tailpipe emissions. Alkanes have reported as major VOCs in the vehicles exhaust.[36, 55, 68, 69] It was recently shown that low volatility alkanes (IVOCs…), may highly contribute to SOA formation.[70-73] Nonane was

found in both diesel and gasoline measured emissions and since alkanes distribution is not the same for diesel and gasoline vehicles, we found nonane as appropriate compound for represent both emissions. In total, 7 experiments have been carried out in the AFT using nonane as SOA precursor. The nonane wall losses were evaluated (10-15%) and were considered in the SOA yield calculation. Experiments with long linear alkanes have been carried out using the pentadecane, a good proxy for diesel emissions. However, wall losses of this compound were too high in our experimental set-up.

4.4.1. Influence of parameters for SOA formation

Figure 4.18. shows the SOA yield as a function of the final OA concentration at different temperatures. SOA formation ranges from 1.85 to 4.3 µg/m^3 and SOA yields ranged from 0.24% to 1.64%. When temperature increases from 7°C to 21°C, the amount of SOA formed is reduced by half. This can be observed comparing the blue and red points (7°C and 21°C) plotted for the same initial VOC concentration. Takekawa et al.[4] studied the influence of the temperature for linear alkanes. On average, an increment of SOA yield of 2.7% was reported for a temperature change from 30 °C to 10 °C, what is in agreement with results presented here. Other parameters as initial VOC concentration do influence SOA formation. For nonane concentrations of 73 ppbv (nonane$_0$/2.5), SOA yield was in the approximately 1.6% and decreased to 0.5% when the nonane concentration was193 ppbv.

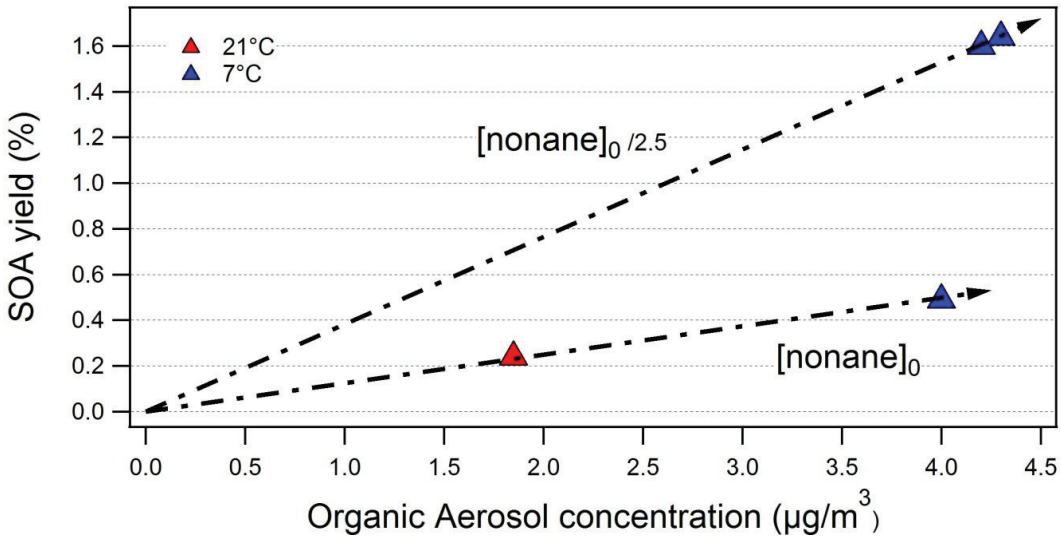

Figure 4.18. SOA *yield versus SOA formation as a function of different temperatures and initial concentrations of nonane.*

The photo-oxidation of nonane has been investigated in simulation chambers experiments which reported higher SOA yields (8-10%). [63, 74] Our results indicate yields around 2% at low temperature and 1% at room temperature. This difference has been mainly attributed to several experimental parameters: initial precursors and seeds concentrations

were much higher in the chamber experiments and also the experiments presented longer oxidation time (days).

4.4.2. Gas and particle phase carbon distribution

Figure 4.19. shows the average oxygen and nitrogen distribution as a function of the carbon number for both the gas and the particle phase reaction products. The graphics show the product C distribution for experiments carried out at 21°C (a and c) and at 7°C (b and d).

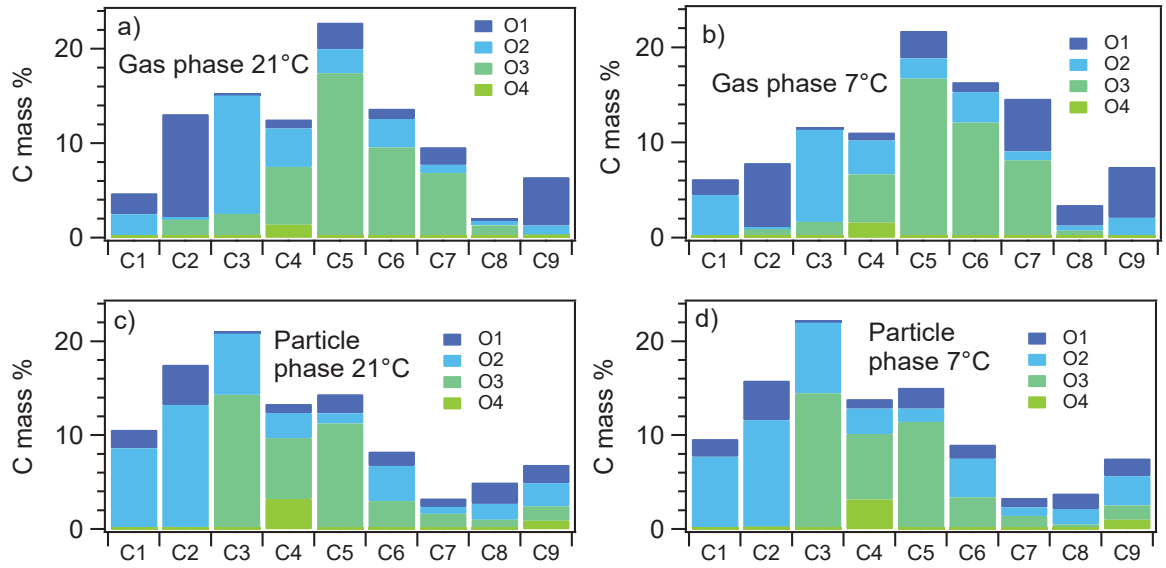

Figure 4.19. *Average oxygen number as a function of carbon number product distribution for: gas phase experiment at 21°C (a) , for gas phase experiment at 7°C (b) for particle phase experiment at 21°C (c) and for particle phase experiment at 7°C (d).*

The carbon number of the reaction products ranges from C_1 to C_9. The gas phase carbon distribution is dominated by the C_5 (22-23%) compounds but the C distribution is slightly different at the two experimental temperatures. At room temperature most of the gas phase products are distributed around C_2 and C_6 compound, while at lower temperature the distribution shift towards larger product (C_5-C_7). In the particle phase, the carbon distribution is dominated by small compounds, namely C_2 and C_3 groups (16-18% and 21-22%, respectively). It has to be noted that nonane reaction products highly fragment in the PTR-MS and therefore many of the ion fragments could also belong to larger molecules. The oxygen distribution is dominated by compounds containing three oxygens in both phases, while the C_4 and C_9 compounds do contain the most oxidized compounds with molecules having four oxygens.

4.4.3. Gas and particle phase analysis

A chemical composition analysis of the gas and particle phase has been carried out. Table 4.4. presents the exact mass peak, the corresponding ion molecular formula, the tentative assignment for reaction products and quantification for experiments under low NOx

conditions at 7°C and 21°C (experiments n° 5 and 2, respectively). Gas and particle yields for experiments at 21°C and 7°C can be found in tables AV.13-16 in annex V. Tentative assignments are based on references spectra of pure compounds (the major reaction products for experiments Table AV.18. In the annex V) and literature.[63, 74-78]

Reaction products of nonane are highly fragmented in the PTR-MS. The fragmentation patterns of aldehydes and acids have been investigated in dedicated experiments using pure reference compounds. For the most oxidized and functionalized we did not have references and therefore the assignment is very preliminary and uncertain. Nonane reaction products are mainly aldehydes, peroxy acids, carboxylic acids, nonanone and dihydrofurans (DHFs). Figure 4.20. shows the degradation mechanism from linear alkanes at low NOx regime.[75]

Table 4.4. *Gas and particle phase products quantification (ppbC) found in nonane photoxidation for experiments at 7°C and 21°C.*

n°	Possible compound(s)	Formula	Protonated m/z	Gas	Particle
				7°C/21°C	7°C/21°C
1	Propanoic acid	$C_3H_6O_2/C_3H_4O$	75.044/57.033	19.90/15.90	0.30/0.23
2	Pentaneperoxoic acid	$C_5H_{10}O_3/C_5H_8O_2$	119.07/101.06	30.51/16.30	0.18/0.15
3	Acetaldehyde	$C_2H_4O/C_2H_6O_2$	45.033/63.044	14.86/15.20	0.13/0.12
4	Heptanal	$C_7H_{14}O/C_7H_{12}$	115.11/97.101	11.80/2.55	0.04/0.03
5	Hexaneperoxoic acid	$C_6H_{12}O_3/C_6H_{10}O_2$	133.08/115.07	25.88/13.00	0.11/0.08
6	Formic acid	CH_2O_2	47.01	9.63/3.41	0.26/0.26
7	Butaneperoxoic acid	$C_4H_8O_3/C_4H_6O_2$	105.05/87.044	9.40/6.91	0.19/0.16
8	Butanoic acid	$C_4H_8O_2/C_4H_6O$	89.059/71.049	7.59/5.55	0.11/0.09
9	Nonanone	$C_9H_{18}O/C_9H_{16}$	143.14/125.13	6.65/4.64	0.06/0.05
10	Pentanal	$C_5H_{10}O/C_5H_8$	87.08/69.069	6.14/3.81	0.09/0.08
11	1-ethyl, 4-propyl dihydrofuran	$C_9H_{16}O$	141.13	4.86/2.36	0.01/0.01
12	Octanal	$C_8H_{16}O/C_8H_{14}$	129.13/111.12	4.65/0.54	0.06/0.07
13	Pentanoic acid	$C_5H_{10}O_2/C_5H_8O$	103.07/85.064	4.57/3.49	0.06/0.04
14	Heptaneperoxoic acid	$C_7H_{14}O_3/C_7H_{12}O_2$	147.10/129.09	17.49/9.33	0.06/0.06
15	Formaldehyde	CH_2O	31.02	3.57/3.01	0.06/0.06
16	Propaneperoxoic acid	$C_3H_6O_3/C_2H_6O/C_3H_4O_2$	91.038/73.028	3.26/3.20	0.59/0.51
17	Hexanal	$C_6H_{12}O/C_6H_{10}$	101.10/83.085	2.25/1.47	0.06/0.05
18	4-oxo-2-pentenal*	$C_5H_6O_2/C_5H_4O$	99.044/81.033	1.95/5.39	0.17/0.15
19	Acetic acid/fragment	$C_2H_4O_2$	61.03	n.d./n.d.	0.38/0.39

* Or isomers

The nonane degradation products identified in our experiments are in good agreement with the work reported in the literature.[63, 74] Following the scheme proposed by Yee et al. (Figure 4.20.) [75] the formation of carbonyl products such as nonanone (channel 1), and dihydrofuran (channel 3) can be explained. In our case, acetaldehydes, heptanal and pentanal are the most abundant aldehydes. Aldehydes are formed following channel 1 in the scheme. The observed peroxy acids and carboxylic acids are second or third generation products.

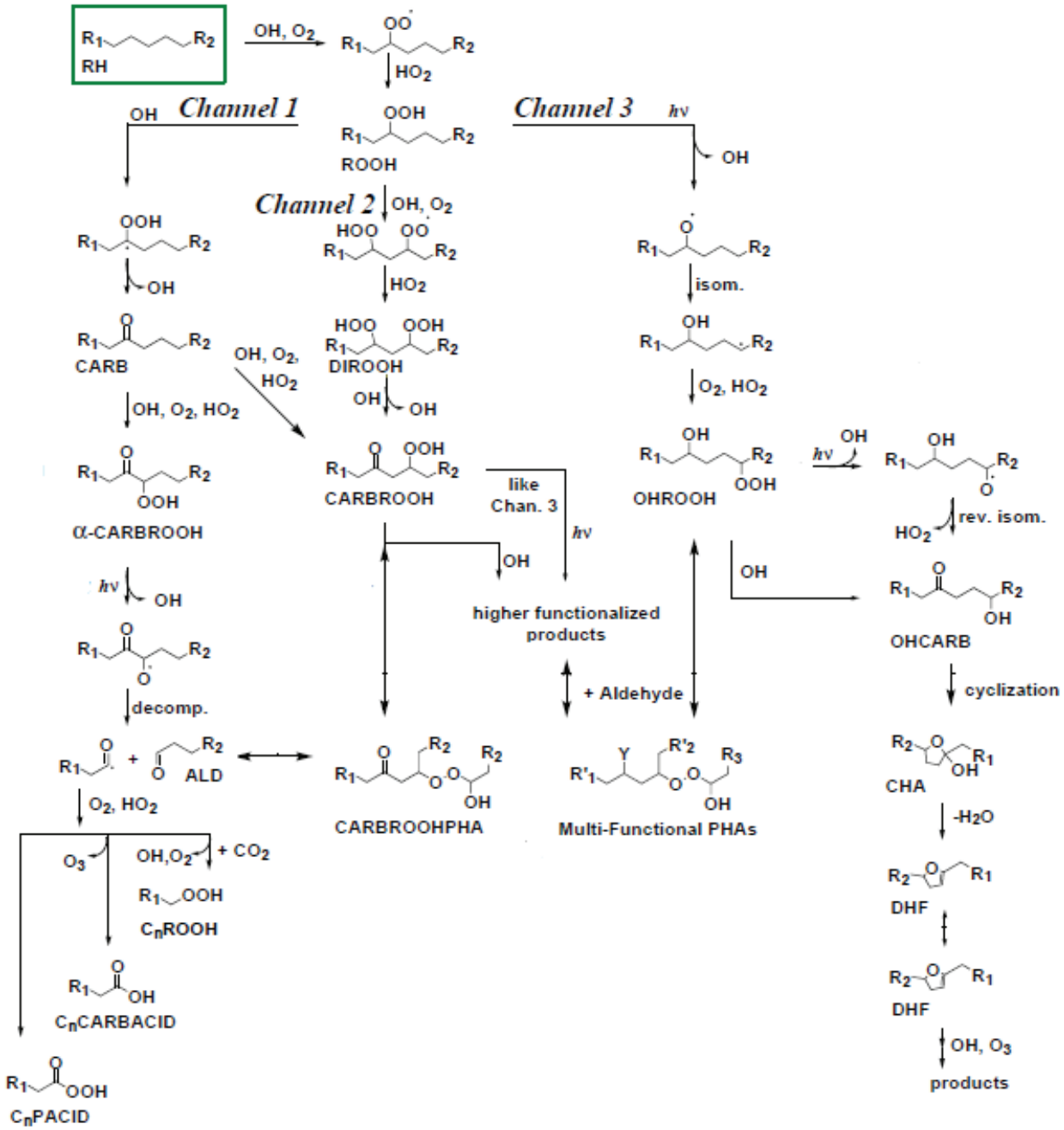

Figure 4.20. *Simplified linear alkane degradation mechanism at low NOx regime, adapted from Yee et al, 2013*

Due to high functionalized reaction products, high fragmentation and large uncertainties on the chemical assignment, the gas/particle partitioning investigation has been not developed yet.

4.5. SOA from nonane-toluene

Figure 4.21. presents the SOA yield versus concentration of formed SOA for a mixture of toluene-nonane for experiments carried out at different temperatures. The black line indicates how a temperature drop from 21 to 7° C causes an increase in the SOA yield from 0.38 % to 1.6 % and on SOA mass concentration from 1.8 to 4.8 μg/m^3. The red line shows how the NOx addition (200 ppbv) to the reactants mixture causes a drop of the SOA yield and SOA mass concentration of almost of a factor 2.

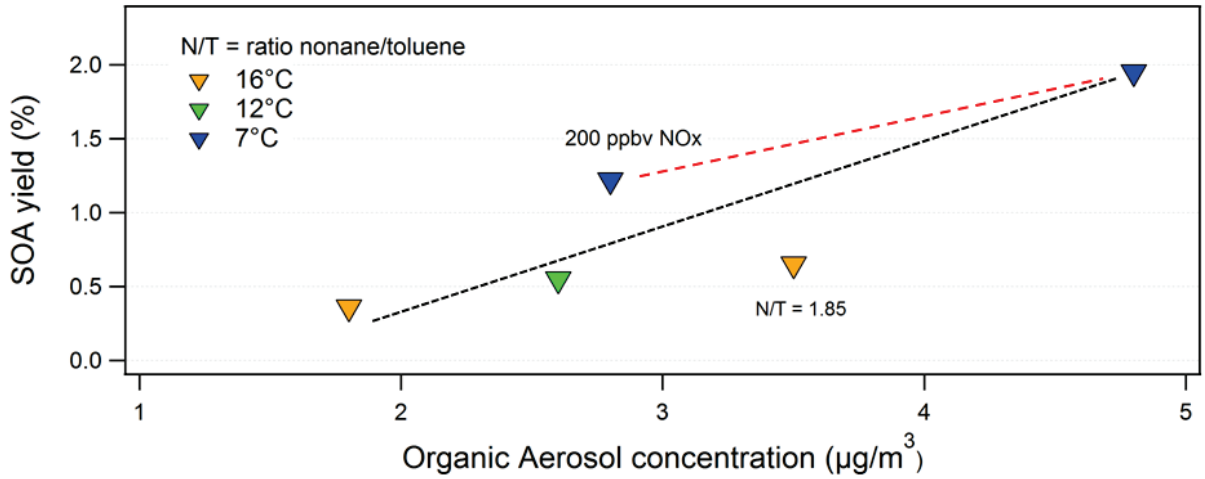

Figure 4.21. SOA *yield versus SOA formation as a function of different temperatures, VOC concentrations and NOx concentrations.*

All experiences are characterized by a nonane/toluene ratio of 4, only one has been carried out at the nonane/toluene ratio of 1.85. The increment of the toluene fraction in the reaction mixture double the SOA formed (from 1.8 to 3.5 μg/m^3). The oxidation times in these experiences correspond to 5-6 hours of atmospheric OH exposure.

Figure 4.22. presents the carbon number distribution as a function of oxygen number distribution for experiments carried out at 16° and 7° C. The reaction products carbon number ranges from C_1 to C_9. The gas phase carbon distribution is dominated by the C_7 (20-23%), C_4 (14-20%) and C_2 (15-23%) but the C distribution is slightly different at the two temperatures. In the particle phase the carbon distribution is dominated by C_2 group (20-25%) followed to C_7 (15%) and C_5 (10-18%). There is an important increase of C_8 and C_9 group compared to gas phase.

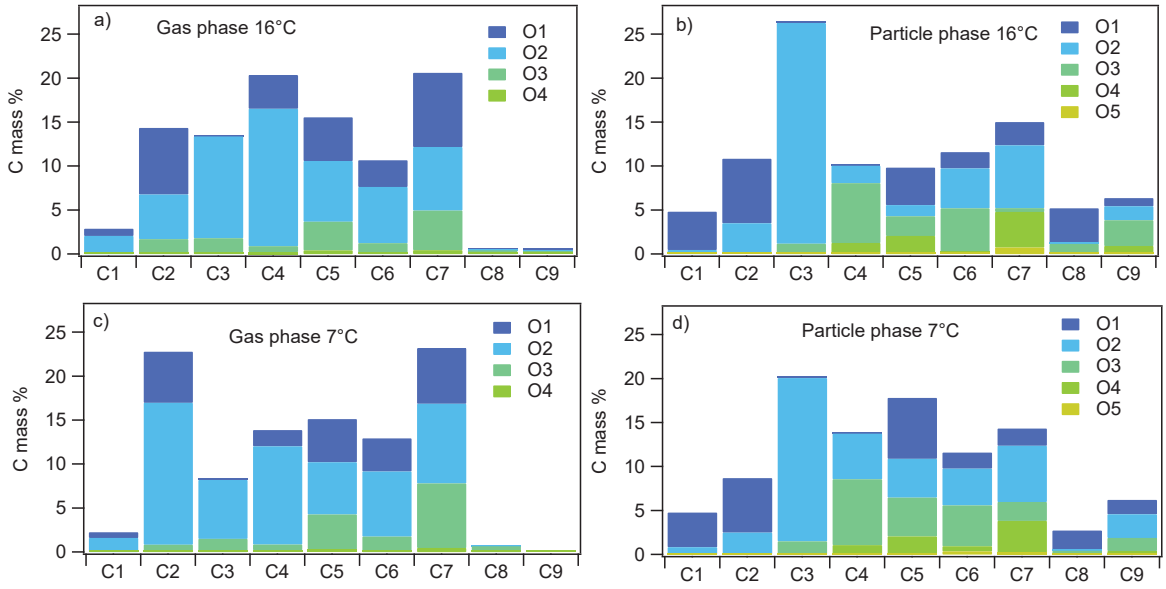

Figure 4.22. carbon number distribution as a function of oxygen number distribution for: gas phase experiments at 16°C (a), particle phase experiments at 7°C (b), gas phase experiments at 16°C (c) and particle phase experiments at 7° C (d).

The oxygen distribution is dominated by compounds containing two oxygen in gas phase, while in the particle phase compounds with two and three oxygen represent the largest fraction of the products. Some particle phase products contain five oxygen atoms while they are not present in the gas phase.

By comparing the reaction products for the mixture with the individual experiments it is possible to apportion the sources in terms of fraction of aliphatic vs. aromatic reaction products (table 4.5.).

Table 4.5. Gas and particle mass fraction of product regarding parent VOC.

	Gas Phase (mass %)		Particle Phase (mass %)	
	21° C	7° C	21° C	7° C
Aliphatic	53	55	22	23
Aromatic	32	33	62	57
Both	15	11	16	20

The gas phase products are dominated by nonane products (53-55%) while toluene products account for 31-33% only, and approximately 15 % of the compounds identified are common to both reactants. In the particle phase the reaction products from toluene degradation dominated with 57-61% of the particle phase followed by products from nonane (21-22%). These results further support was observed previously about the higher potential of SOA formation of toluene with respect to nonane.

4.6. General trends in SOA formation

The next section will present a general discussion about the results on the SOA formation in the AFT set-up. The figure 4.23. presents the SOA formed with respect to the concentration of preexisting ammonium sulphate particles between 3 and 13 µg/m^3. In general, SOA from aromatic compounds seems to be more sensitive to changes in seed concentration, while for nonane, cyclohexane and nonane/toluene (ratio 4) there is a very low dependence on the seeds concentration. These differences can be explained by the volatility of the reaction products generated by the SOA precursor and will be discussed after figure 4.24.

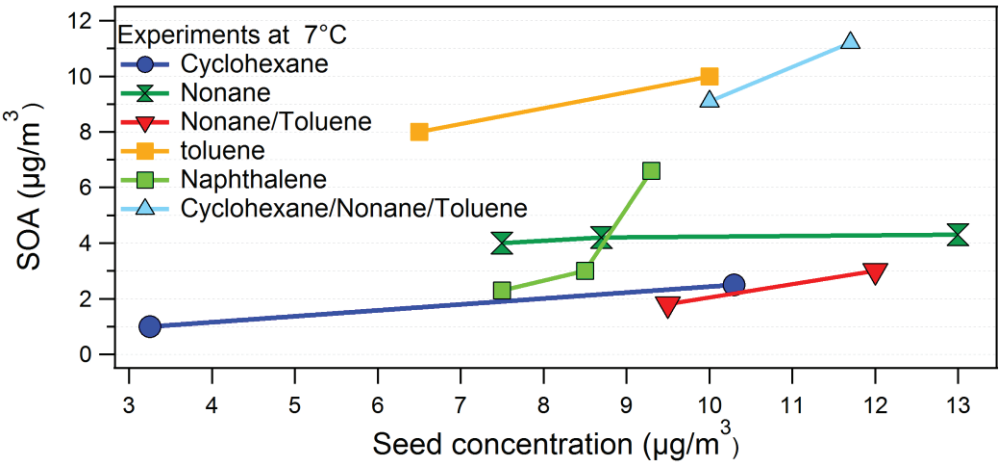

Figure 4.23. *SOA formed as a function of ammonium sulfate seed for individual VOC and mixtures.*

The Figure 4.24. shows the amount of SOA formed for the tested compounds as a function of temperature. The experimental conditions chosen are comparable (except the initial concentration of the VOC).

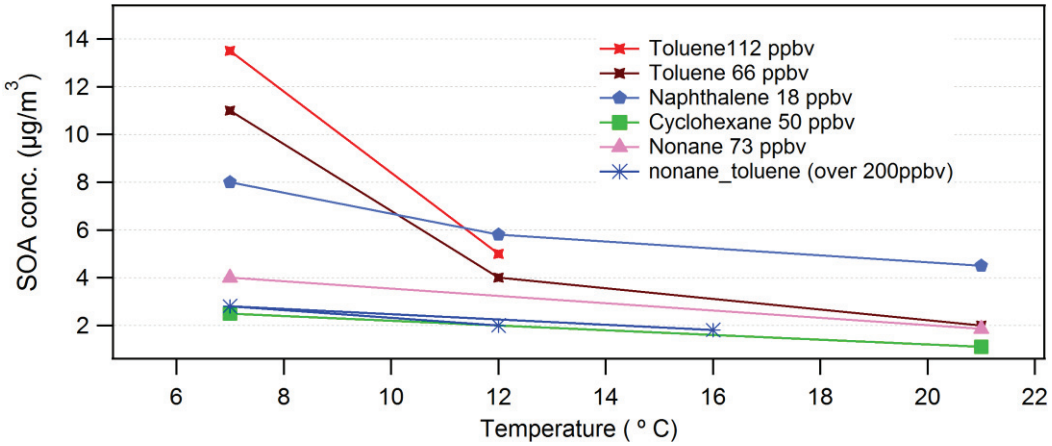

Figure 4.24. *SOA formed as a function of temperature for individual VOC and mixtures.*

The figure clearly shows as the temperature differently affects the SOA mass loading for the different VOC precursors. To our knowledge, relatively few works investigated

systematically SOA formation at different temperatures. The results show that the SOA mass loading can almost increase by a factor 5 when temperature decreases from 21°C to 7°C (brown data set) for the toluene SOA. For naphthalene, the temperature dependence is quite flat and the SOA concentration double when passing from 21°C to 7°C. These differences have been explained in term of the volatility of the reaction products formed during photoxidation. The naphthalene particle composition is dominated by oxygenated C_8-C_{10} compounds of low volatility (evaluation using the partitioning coefficients). We therefore suggest that these compounds can readily partition to the particle phase at room temperature. It has to be noted that the initial concentration of naphthalene was only 18 ppbv. The toluene particle composition is dominated by oxygenated by C_6-C_7 compounds, having slighter higher volatility, and therefore can condense onto the seeds particle only at lower temperature. For nonane and cyclohexane the situation is different: the reaction products are in general quite volatile and low condensation is observed at all temperatures.

Figure 4.25. shows the normalized SOA yield for different VOCs and mixture at 7 °C. The results are presented in terms of SOA yield normalized by the OH radical exposure. This normalization was needed since the experiments were carried out with different OH concentrations and a direct comparison was not possible while the VOC concentrations was high and ranged in the order of 130-250 ppbv.

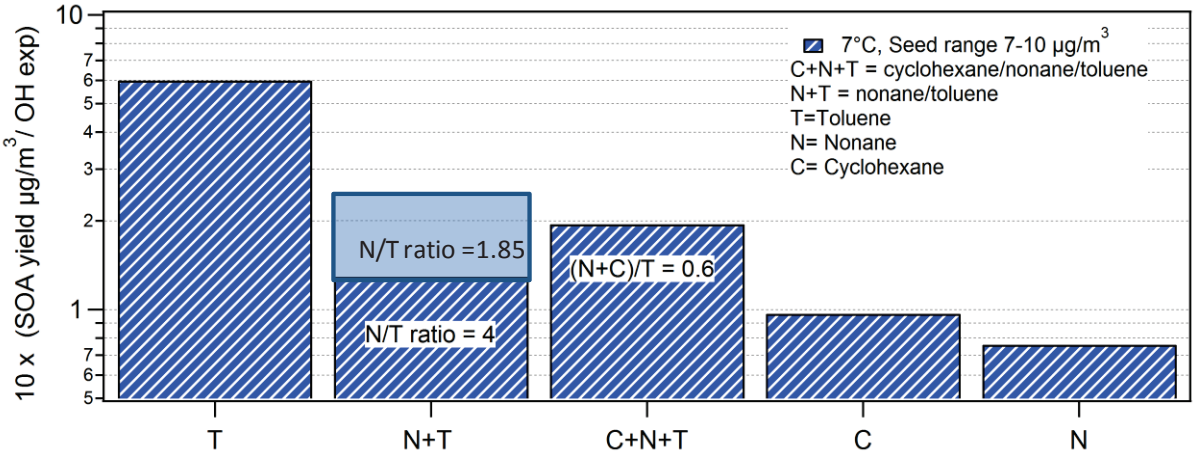

Figure 4.25. *Normalized SOA for some VOC and mixtures.*

For the nonane-toluene mixture with N/T ratio of 4, the normalized yield is around 0.13%/h (dark blue histogram) and increased to 0.22%/h (light blue histogram) when N/T becomes 1.85. For the cyclohexane-nonane-toluene system, a ratio of aliphatic to aromatics of 0.6 was used. Toluene clearly exhibit the highest SOA yield, followed by the mixture of VOCs (that contained toluene) then follow cyclohexane and toluene.

Figure 4.26. shows the effect of NOx addition to the normalized SOA yield for the different experiments. The amount of NOx added is indicated for each experiment.

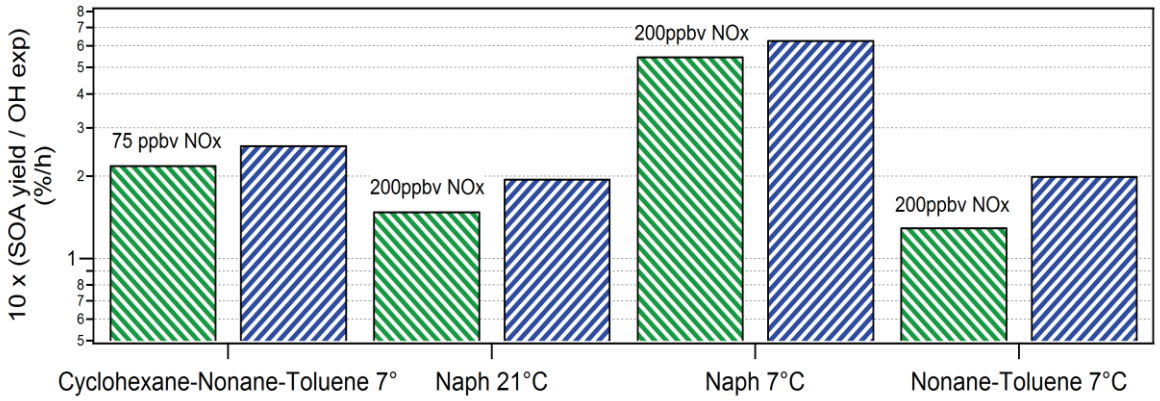

Figure 4.26. *Comparison of normalized SOA yield for experiment with/without addition of NOx.*

As a general trend a reduction in SOA concentration of 30% was observed when NOx is added to the reaction mixture. However the VOC/NOx ratio did not change significantly in all experiments because the isopropyl nitrite used as a precursor of the hydroxyl radicals produces itself quite a lot of NO_2. Therefore most of the experiments were already in a low NOx regime and the addition of NOx did not drastically change the regime.

4.7. Photoxidation of real vehicle emissions

Few SOA experiments were carried out using exhaust emissions from GDI3 Euro 5. These experiments have to be considered a preliminary work to optimize the experimental set-up for future application and coupling of the AFT and the CHARON inlet on complex system as a car generated SOA. The car exhaust was collected at the tailpipe during a cold WLTC cycle and introduced into temporary reservoir (60 liters, Pyrex) through a 80-90°C heated line. The reservoir allowed achieving a desired emission dilution and prevented the injection of flow turbulences due to speed cycle changes into the AFT which operates under steady-state conditions. After collection, the reservoir was connected to the AFT and the experiment started. A C-ToF-AMS and a HR-PTR-ToF coupled with CHARON inlet were used to characterize primary emission and aging products in both gas and particle phase, respectively. The AFT temperature was set at 25°C and the RH was 37% during the experiments.

4.7.1 Primary VOC emissions speciation

Before starting the photoxidation the car emission were investigated by sampling directly from the reservoir. Figure 4.27. presents the averaged VOC concentration and carbon distribution for aromatics, aliphatics and oxygenated compounds emitted by the gasoline vehicle. Mass assignment follow the procedure proposed by Erickson et al. [79]

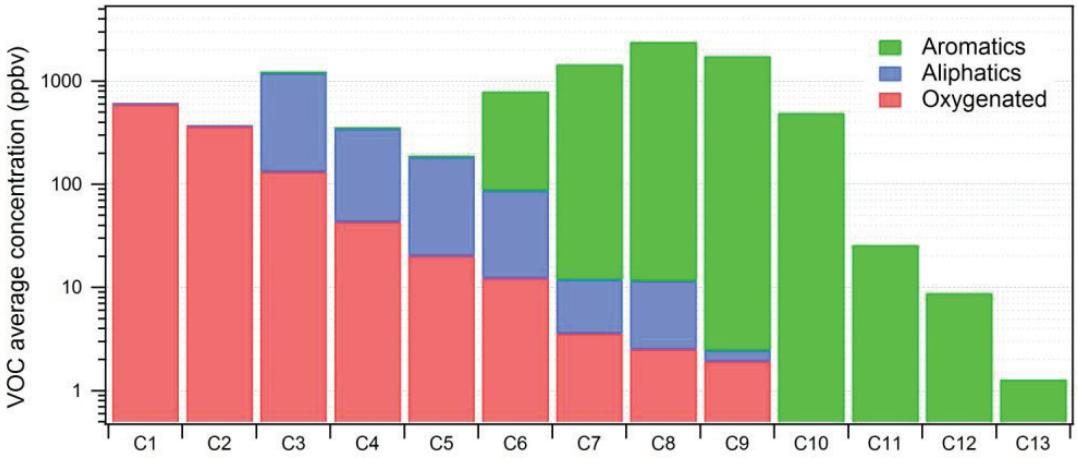

Figure 4.27. *Averaged primary VOC concentration as a function of carbon number for different families of compounds.*

As expected, the aromatic compounds represent the largest fraction of the emitted VOC, dominating the range C_6-C_{13}. Aliphatic compounds have been measured up to C_9 ,which is in quite good agreement with the tenax cartridges results (chapter III) and with the typical gasoline VOCs carbon distribution based on direct sampling or fuel analysis observed in literature (chapter I). Gas phase compounds with carbon atom above C_{13} have been not detected in gas phase of the reservoir. Possible bias may occur during sampling and during the reaction process. During exhaust transfer in the reservoir (at room temperature) many aliphatic compounds are lost by condensation on the tubing lines and reservoir walls. The second is that PTR-MS has low sensitivity towards aliphatic alkane/alkenes.

Figure 4.28. presents the average mass spectrum of the car emissions organized by chemical families.

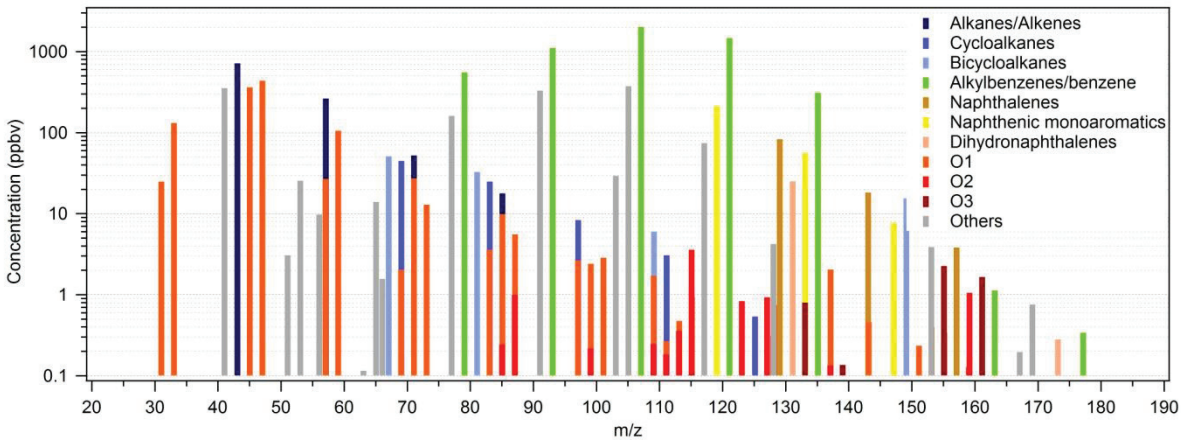

Figure 4.28. *Averaged VOC concentration over mass spectrum distributed by families for GDI Euro 5 vehicle for first 7 minutes of WLTC cold cycle.*

Among the aromatics (green lines) that account for almost 70% of the measured mass fraction the most abundant are xylene, trimethylbenzene, toluene, benzene and durene.

Aliphatic and oxygenated compounds represent 18% and 12% of total emitted VOC mass. Aliphatics are represented by alkanes/alkenes (mostly m/z 43, 57, 71), bicycloalkanes (mostly m/z 67, 81, 109) and cycloalkanes (mostly m/z 69, 83, 97). The oxygenated compounds present a large fraction of VOCs with one single oxygen (99%), being ethanol, acetaldehyde, methanol and acetone the main species.

4.7.2. SOA formation from VOC photoxidation

The Figure 4.29. presents the time series of the condensable fraction of the aerosol during the photoxidation experiment measured by the c-ToF-AMS. The particles were composed by organics, nitrate and small traces of sulfates and PAHs. The organic fraction (green) represents the ensemble of the POA and the SOA fraction. In two periods of the experiment, the AMS measured before the AFT, allowing to determine the POA mass loading. By subtracting the POA from (POA+SOA) mass, the SOA fraction can be evaluated. These two periods correspond to 11:52-12:00 and 12:49-12:55 AMS time and are shown in the figure 4.27. in pale yellow. The SOA formation is therefore 3.4 µg/m^3 in the first part of the experiment and 1.7µg/m^3 at the end, respectively, which corresponds to 27% of total OA in first period and 50% in second period. The SOA/POA ratio is 0.53 for first period and 1 for second period. These experiments correspond to an initial photoxidation process and cannot be directly compared to chamber studies where SOA/POA ratios are much higher. Secondary nitrates are also formed through photoxidation (≈0.9 and 0.3 µg/m^3 for first and second period, respectively). Sulfate arises from the car emissions.

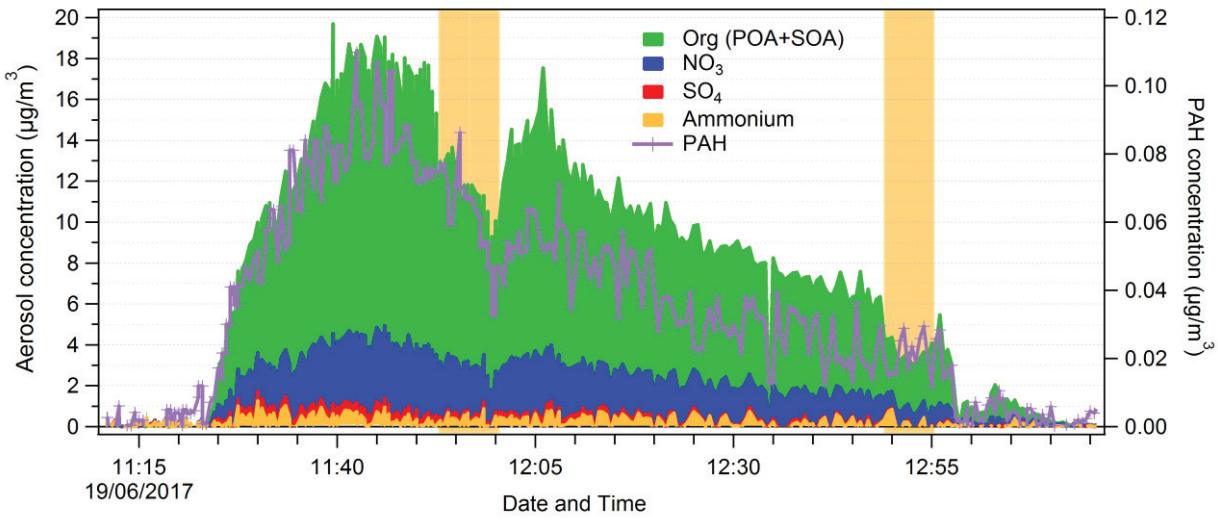

Figure 4.29. *Organic, nitrate, sulfate and PAHs time series profiles for AFT photoxidation of GDI emissions.*

4.7.3. Gas and particle phase carbon distribution

The analysis of the gas phase was very complicated by the myriad of organic compounds found in the exhaust. Figure 4.30. shows the carbon distribution of the GDI exhaust reaction products in the gas phase as a function of oxygen (a) and nitrogen (b) number.

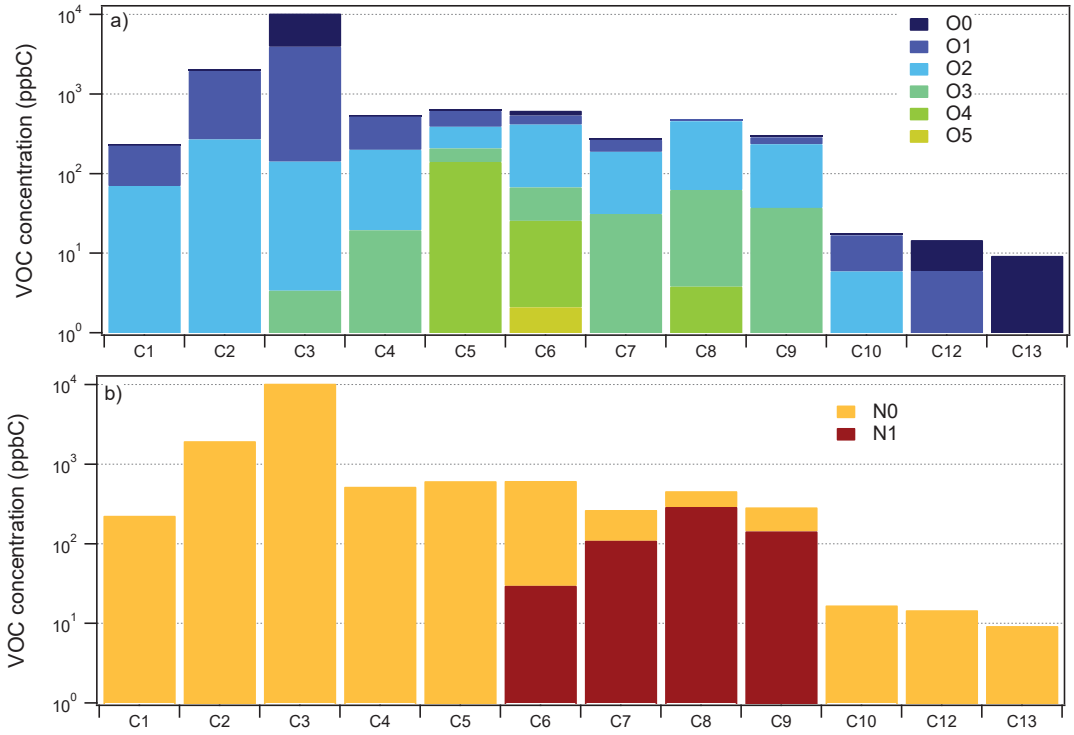

Figure 4.30. *Gas phase carbon number distribution as a function of oxygen (a) and nitrogen (b) for GDI exhaust photoxidation.*

The carbon number distribution of the gas phase product is very broad and ranges from C_1 to C_{13} compounds. The mass fraction of the gas phase products is dominated by C_2-C_3 (75-80%) molecules due to high concentration of small oxygenated compounds and fragments of aliphatic compounds, followed by the C_1 and C_4-C_9 compounds. The number of the oxygen atoms in the degradation products range from zero (which are just aliphatic fragments of a reaction product) to five oxygen (in a C_6 compound). One and two oxygen atoms are dominant in the C_1-C_3 reaction products, while three and four oxygen are dominant in the C_5-C_9 reaction products. The nitrogen containing compounds represent a small fraction of total products (1.48%), even at high NOx regime. However, this fraction is highly underestimated due to fragmentation of these compounds in the PTRMS.

Figure 4.31. shows the carbon distribution of the GDI exhaust reaction products in the particle phase as a function of oxygen (a) and nitrogen (b) number. The particle phase has a quite different chemical composition with respect the gas phase. The carbon number distribution of the particle phase products is very broad and ranges from C_1 to C_{19} compounds.

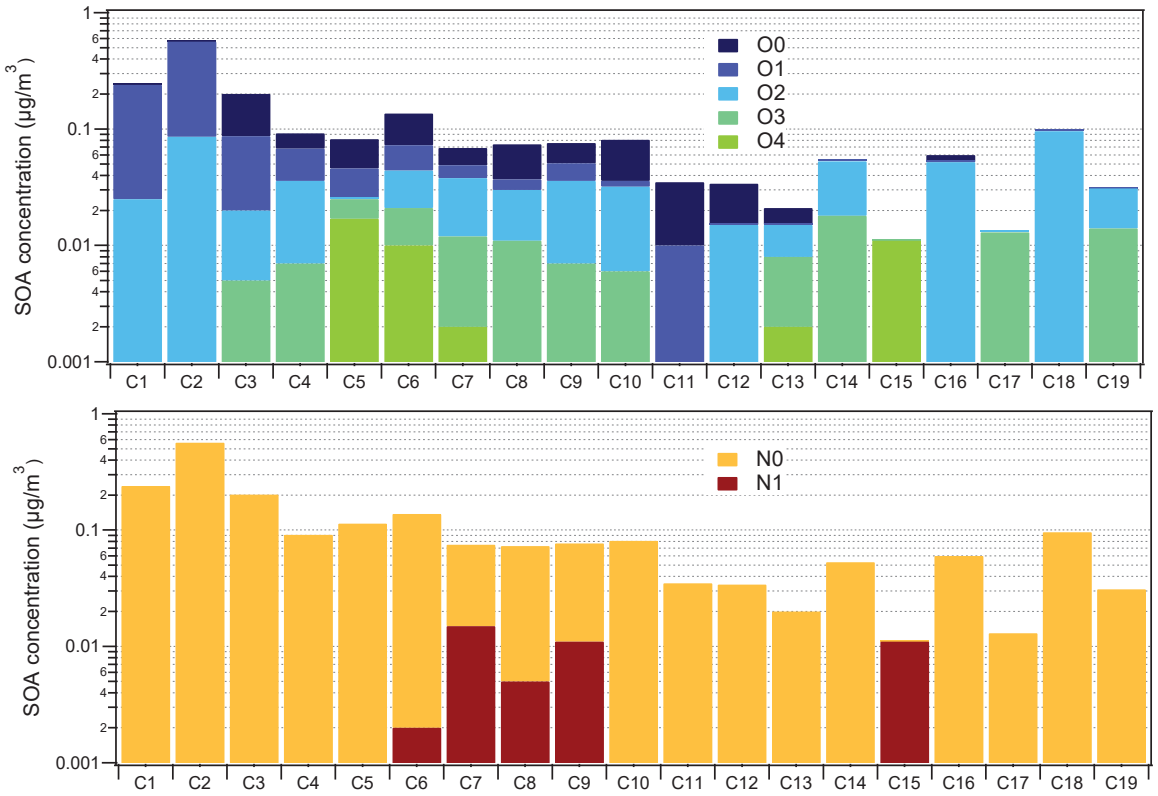

Figure 4.31. *Particle phase carbon number distribution as a function of oxygen (a) and nitrogen (b) for GDI exhaust photoxidation.*

The particle phase carbon distribution is dominated by the C_1-C_3 compounds (51%) which are most likely fragments of larger molecules. The oxygen distribution does not follow a clear trend. Highly oxygenated products are observed for compounds with more than three C atoms. The C_3-C_{10} product distribution is characterized by compounds with three or four oxygen atoms, from C_{11} to C_{19} the particle phase products are characterized by less oxygenated compounds with the exception of the C_{15} and C_{17} compounds.

The particle phase is also characterized by the presence of some nitro-compounds. Since the aromatic nitro compounds can be detected by our PTR-MS, a list of these products is represented in Table 4.6. for both the gas and the particle phase. The most abundant compounds are the nitroxylene, nitrotoluene, nitrotrimethylbenzene). A detailed chemical composition analysis of the gas and particle phase was not possible in the case of this complex mixture of precursors and reaction products. More analytical work is needed to achieve this difficult task of identification and quantification of the major reaction products.

Table 4.6. *Nitro-products found in gas and particle phase of GDI exhaust photoxidation.*

n°	Protonated m/z	Formula	Possible compound(s)	% gas phase	% particle phase
1	Nitroxylene	$C_8H_9NO_2$	152.07	0.33	nd
2	Nitrostyrene	$C_8H_7NO_2$	150.05	0.29	0.21
3	Nitrotoluene	$C_7H_7NO_2$	138.06	0.24	0.30
4	Nitro trimethylbenzene	$C_9H_{11}NO_2$	166.08	0.18	0.28
5	Nitrophenylethanol	$C_8H_9NO_3$	168.06	0.12	0.04
6	Nitroindane	$C_9H_9NO_2$	164.07	0.11	nd
7	Hydroxy nitrotoluene	$C_7H_7NO_3$	154.05	0.08	0.39
8	nitrophenol	$C_6H_5NO_3$	140.03	0.06	0.09
9	Nitrobenzene	$C_6H_5NO_2$	124.03	0.04	nd
10	Nitrophenylpropanol	$C_9H_{11}NO_3$	182.08	0.04	0.25

4.8. Conclusions

Photoxidation experiments of different VOC precursors has been carried out using an AFT. The study aimed at determining: 1) the influence of atmospheric key parameters on SOA formation (as temperature, VOC concentration, seeds); 2) the identification and quantification of the major gas phase degradation products; 3) the identification and quantification of the major particle phase degradation products using the new developed tool for online characterization of submicron particles, CHARON. Few additional experiments were carried on the photoxidation of a Euro 5 GDI vehicle exhaust.

The main conclusions of this work on SOA formation are presented below:

- the investigation of the model compounds allowed the determination of quantitative relationships between the SOA yield and SOA concentration with respect to the temperature in the range 21-7°C, the initial VOC and hydroxyl radical concentration and the presence of pre-existing particle seeds. Highest SOA yield have been measured for aromatic compounds (24 % for naphthalene and 16 % for toluene) at low temperature and low VOC concentrations. The temperature was clearly a sensitive parameter: changing from 21 to 7°C induced a SOA increase of a factor 2 for SOA derived from naphthalene, nonane and cyclohexane; and up to a factor 4 for toluene generated SOA. These differences were explained in terms of the volatility of the reaction products formed during photoxidation process. The initial VOC concentration is another important parameter and tends positively to affect the final SOA concentration. The presence of preexisting particles tends to favor SOA formation, especially for aromatic compounds. While NOx concentration negatively affects SOA formation for all tested VOCs.

- the SOA photoxidation study of individual VOC and their mixture present for the first time results from the newly developed CHARON-inlet coupled to HR-PTR-MS for on-line analysis of organic aerosol. In the framework of this PhD thesis, we demonstrated that the instrument is an efficient tool able to chemically characterize a high fraction of the formed SOA. For the toluene experiments a more complete products analysis was achieved and a paper is now in preparation. For the other VOCs, more analytical work is clearly needed. Nevertheless, the CHARON inlet was able to identify a considerable fraction of the particle phase mass (much more that what is normally feasible using collection on filters followed by extraction and traditional chemical analysis). Table 4.7. summarizes the consumed VOC fraction, SOA yield, identified gas phase fraction and fraction of speciated mass using CHARON. For all the investigated systems, it was possible to determine the products raw formula both in the gas and the particle phase. As a result, a partition coefficient was calculated for each mass at a given temperature. The determination of partitioning coefficients allow us to have a better view on the aerosol properties and is an important step forwards in order to fully understand the formation and evolution of SOA under atmospheric conditions.

Table 4. 7. *Maximun and minimum consumed VOC fraction (%) and identified product fractions (%) in gas and particle phase for tested VOCs at different temperatures.*

	Consumed VOC (% ppbC/ppbC)	SOA Yield (%(µg/m^3) / (µg/m^3))*, **	Total identified mass in gas phase (% ppbC/ ppbC)*	Fraction of speciated mass in CHARON (%)**
Toluene 21°C	43 – 62	1 -4	21 – 51	86 – 92
Toluene 12°C	47.- 57	2 – 11	26 – 59	
Toluene 7°C	46 -57	4 – 19	25 – 45	
Naphthalene 21°C	86 – 91	5	50 – 61	97-99
Naphthalene 12° C	76	8	83	
Naphthalene 7°C	80 – 84	9 – 24	36 – 77	
Nonane 21°C	76	1	10	88-90
Nonane 7°C	76	1-2	16	
Cyclohexane 21° C	25	1 - 3		95- 96
Cyclohexane 7°C	25	1 – 4	71 – 98	

* respect to VOC consumption; ** calculated using AMS SOA mass in µg/m^3; *** respect to total measured mass in CHARON in µg/m^3.

- During the photoxidation of aromatic compounds nitrotoluene, nitrocresol, nitronaphthol, nitronaphthalene, nitrophenol or nitrochatechol have been identified both the gas and the particle phase. These compounds are well known to be more harmful than the parent aromatic compound.

References:

1. Hu D, Tolocka M, Li Q, KamenS RM. A kinetic mechanism for predicting secondary organic aerosol formation from toluene oxidation in the presence of NOx and natural sunlight. *Atmospheric Environment* 2007; 41(31):6478-6496.
2. Cabrera-Perez D, Taraborrelli, D., Sander, R., and Pozzer, A. Global atmospheric budget of simple monocyclic aromatic compounds. In. https://doi.org/10.5194/acp-16-6931-2016 ed. Atmos. Chem. Phys.; 2016. pp. 6931-6947.
3. Skorokhod AI, Berezina, E. V., Moiseenko, K. B., Elansky, N. F., and Belikov, I. B. Benzene and toluene in the surface air of northern Eurasia from TROICA-12 campaign along the Trans-Siberian Railway. In. https://doi.org/10.5194/acp-17-5501-2017 ed: Atmos. Chem. Phys.; 2017. pp. 5501-5514.
4. Takekawa H, Minoura H, Yamazaki S. Temperature dependence of secondary organic aerosol formation by photo-oxidation of hydrocarbons. *Atmospheric Environment* 2003; 37(24):3413-3424.
5. Hildebrandt L, Donahue NM, Pandis SN. High formation of secondary organic aerosol from the photo-oxidation of toluene. *Atmos Chem Phys* 2009; 9(9):2973-2986.
6. Ng NL, Kroll JH, Chan AWH, Chhabra PS, Flagan RC, Seinfeld JH. Secondary organic aerosol formation from m-xylene, toluene, and benzene. *Atmos Chem Phys* 2007; 7(14):3909-3922.
7. Ng NL, Kroll JH, Chan AWH, Chhabra PS, Flagan RC, Seinfeld JH. Secondary organic aerosol formation from m-xylene, toluene, and benzene. *Atmospheric Chemistry and Physics* 2007; 7(14):3909-3922.
8. Hildebrandt L, Donahue NM, Pandis SN. High formation of secondary organic aerosol from the photo-oxidation of toluene. *Atmospheric Chemistry and Physics* 2009; 9(9):2973-2986.
9. Hildebrandt Ruiz L, Paciga AL, Cerully KM, Nenes A, Donahue NM, Pandis SN. Formation and aging of secondary organic aerosol from toluene: changes in chemical composition, volatility, and hygroscopicity. *Atmospheric Chemistry and Physics* 2015; 15(14):8301-8313.
10. Baltaretu CO, Lichtman EI, Hadler AB, Elrod MJ. Primary Atmospheric Oxidation Mechanism for Toluene. *Journal of Physical Chemistry A* 2009; 113(1):221-230.
11. Jang MS, Kamens RM. Characterization of secondary aerosol from the photooxidation of toluene in the presence of NOx and 1-propene. *Environmental Science & Technology* 2001; 35(18):3626-3639.
12. Schwantes RH, Schilling KA, McVay RC, Lignell H, Coggon MM, Zhang X, et al. Formation of highly oxygenated low-volatility products from cresol oxidation. *Atmospheric Chemistry and Physics* 2017; 17(5):3453-3474.
13. White SJ, Jamie IM, Angove DE. Chemical characterisation of semi-volatile and aerosol compounds from the photooxidation of toluene and NOx. *Atmospheric Environment* 2014; 83:237-244.
14. Hamilton JF, Webb PJ, Lewis AC, Reviejo MM. Quantifying small molecules in secondary organic aerosol formed during the photo-oxidation of toluene with hydroxyl radicals. *Atmospheric Environment* 2005; 39(38):7263-7275.
15. Hurley MD, Sokolov O, Wallington TJ, Takekawa H, Karasawa M, Klotz B, et al. Organic aerosol formation during the atmospheric degradation of toluene. *Environmental Science & Technology* 2001; 35(7):1358-1366.
16. Hamilton JF, Lewis AC, Bloss C, Wagner V, Henderson AP, Golding BT, et al. Measurements of photo-oxidation products from the reaction of a series of alkyl-benzenes with hydroxyl radicals during EXACT using comprehensive gas chromatography. *Atmospheric Chemistry and Physics* 2003; 3:1999-2014.
17. Kleindienst TE, Conver TS, McIver CD, Edney EO. Determination of secondary organic aerosol products from the photooxidation of toluene and their implications in ambient PM2.5. *Journal of Atmospheric Chemistry* 2004; 47(1):79-100.
18. Arey J, Obermeyer G, Aschmann SM, Chattopadhyay S, Cusick RD, Atkinson R. Dicarbonyl Products of the OH Radical-Initiated Reaction of a Series of Aromatic Hydrocarbons. *Environmental Science & Technology* 2009; 43(3):683-689.
19. Borras E, Tortajada-Genaro LA. Determination of oxygenated compounds in secondary organic aerosol from isoprene and toluene smog chamber experiments. *International Journal of Environmental Analytical Chemistry* 2012; 92(1):110-124.
20. Ji YM, Zhao J, Terazono H, Misawa K, Levitt NP, Li YX, et al. Reassessing the atmospheric oxidation mechanism of toluene. *Proceedings of the National Academy of Sciences of the United States of America* 2017; 114(31):8169-8174.
21. Smith DF, McIver CD, Kleindienst TE. Primary product distribution from the reaction of hydroxyl radicals with toluene at ppb NOX mixing ratios (vol 30, pg 209, 1998). *Journal of Atmospheric Chemistry* 1998; 31(3):349-350.
22. Dumdei BE, Kenny DV, Shepson PB, Kleindienst TE, Nero CM, Cupitt LT, et al. MS MS ANALYSIS OF THE PRODUCTS OF TOLUENE PHOTOOXIDATION AND MEASUREMENT OF THEIR MUTAGENIC ACTIVITY. *Environmental Science & Technology* 1988; 22(12):1493-1498.
23. Tuazon EC, Macleod H, Atkinson R, Carter WPL. ALPHA-DICARBONYL YIELDS FROM THE NOX-AIR PHOTOOXIDATIONS OF A SERIES OF AROMATIC-HYDROCARBONS IN AIR. *Environmental Science & Technology* 1986; 20(4):383-387.
24. Nishino N, Arey J, Atkinson R. Formation Yields of Glyoxal and Methylglyoxal from the Gas-Phase OH Radical-Initiated Reactions of Toluene, Xylenes, and Trimethylbenzenes as a Function of NO2 Concentration. *Journal of Physical Chemistry A* 2010; 114(37):10140-10147.

25. Gomez Alvarez E, Viidanoja J, Munoz A, Wirtz K, Hjorth J. Experimental confirmation of the dicarbonyl route in the photo-oxidation of toluene and benzene. *Environmental Science & Technology* 2007; 41(24):8362-8369.
26. Forstner HJL, Flagan RC, Seinfeld JH. Secondary organic aerosol from the photooxidation of aromatic hydrocarbons: Molecular composition. *Environmental Science & Technology* 1997; 31(5):1345-1358.
27. Sato K, Hatakeyama S, Imamura T. Secondary organic aerosol formation during the photooxidation of toluene: NOx dependence of chemical composition. *Journal of Physical Chemistry A* 2007; 111(39):9796-9808.
28. Xu JL, Griffin RJ, Liu Y, Nakao S, Cocker DR. Simulated impact of NOx on SOA formation from oxidation of toluene and m-xylene. *Atmospheric Environment* 2015; 101:217-225.
29. Seuwen R, Warneck P. Oxidation of toluene in NO chi free air: Product distribution and mechanism. *International Journal of Chemical Kinetics* 1996; 28(5):315-332.
30. Klotz B, Sorensen S, Barnes I, Becker KH, Etzkorn T, Volkamer R, et al. Atmospheric oxidation of toluene in a large-volume outdoor photoreactor: In situ determination of ring-retaining product yields. *Journal of Physical Chemistry A* 1998; 102(50):10289-10299.
31. Wu RR, Pan SS, Li Y, Wang LM. Atmospheric Oxidation Mechanism of Toluene. *Journal of Physical Chemistry A* 2014; 118(25):4533-4547.
32. Wagner V, Jenkin ME, Saunders SM, Stanton J, Wirtz K, Pilling MJ. Modelling of the photooxidation of toluene: conceptual ideas for validating detailed mechanisms. *Atmospheric Chemistry and Physics* 2003; 3:89-106.
33. Birdsall AW, Elrod MJ. Comprehensive NO-Dependent Study of the Products of the Oxidation of Atmospherically Relevant Aromatic Compounds. *Journal of Physical Chemistry A* 2011; 115(21):5397-5407.
34. Donahue NM, Epstein SA, Pandis SN, Robinson AL. A two-dimensional volatility basis set: 1. organic-aerosol mixing thermodynamics. *Atmos Chem Phys* 2011; 11(7):3303-3318.
35. Martinet S, Liu Y, Louis C, Tassel P, Perret P, Chaumond A, et al. Euro 6 Unregulated Pollutant Characterization and Statistical Analysis of After-Treatment Device and Driving-Condition Impact on Recent Passenger-Car Emissions. *Environmental Science & Technology* 2017; 51(10):5847-5855.
36. Ensberg JJ, Hayes PL, Jimenez JL, Gilman JB, Kuster WC, de Gouw JA, et al. Emission factor ratios, SOA mass yields, and the impact of vehicular emissions on SOA formation. *Atmos Chem Phys* 2014; 14(5):2383-2397.
37. Keyte IJ, Albinet A, Harrison RM. On-road traffic emissions of polycyclic aromatic hydrocarbons and their oxy- and nitro- derivative compounds measured in road tunnel environments. *Science of The Total Environment* 2016; 566-567:1131-1142.
38. Munoz M, Haag R, Zeyer K, Mohn J, Comte P, Czerwinski J, et al. Effects of Four Prototype Gasoline Particle Filters (GPFs) on Nanoparticle and Genotoxic PAH Emissions of a Gasoline Direct Injection (GDI) Vehicle. *Environ Sci Technol* 2018; 52(18):10709-10718.
39. Chen C-L, Kacarab M, Tang P, Cocker DR. SOA formation from naphthalene, 1-methylnaphthalene, and 2-methylnaphthalene photooxidation. *Atmospheric Environment* 2016; 131:424-433.
40. Yuan B, Hu WW, Shao M, Wang M, Chen WT, Lu SH, et al. VOC emissions, evolutions and contributions to SOA formation at a receptor site in eastern China. *Atmos Chem Phys* 2013; 13(17):8815-8832.
41. Wang S, Ye J, Soong R, Wu B, Yu L, Simpson AJ, et al. Relationship between chemical composition and oxidative potential of secondary organic aerosol from polycyclic aromatic hydrocarbons. *Atmos Chem Phys* 2018; 18(6):3987-4003.
42. Chan AWH, Kautzman KE, Chhabra PS, Surratt JD, Chan MN, Crounse JD, et al. Secondary organic aerosol formation from photooxidation of naphthalene and alkylnaphthalenes: implications for oxidation of intermediate volatility organic compounds (IVOCs). *Atmos Chem Phys* 2009; 9(9):3049-3060.
43. Kleindienst TE, Jaoui M, Lewandowski M, Offenberg JH, Docherty KS. The formation of SOA and chemical tracer compounds from the photooxidation of naphthalene and its methyl analogs in the presence and absence of nitrogen oxides. *Atmos Chem Phys* 2012; 12(18):8711-8726.
44. Shakya KM, Griffin RJ. Secondary organic aerosol from photooxidation of polycyclic aromatic hydrocarbons. *Environ Sci Technol* 2010; 44(21):8134-8139.
45. Kautzman K, Surratt J, Chan M, W H Chan A, Hersey S, Chhabra P, et al. Chemical Composition of Gas- and Aerosol-Phase Products from the Photooxidation of Naphthalene. In: The journal of physical chemistry. A. 114. 913-34. 10.1021/jp908530s; 2009.
46. Nichipor GV, Gerasimov GY. Gas-phase radiation-chemical oxidation of naphthalene. *High Energy Chemistry* 2008; 42(5):335-341.
47. Sasaki J, Aschmann SM, Kwok ESC, Atkinson R, Arey J. Products of the Gas-Phase OH and NO3 Radical-Initiated Reactions of Naphthalene. *Environmental Science & Technology* 1997; 31(11):3173-3179.
48. Wang L, Atkinson R, Arey J. Dicarbonyl Products of the OH Radical-Initiated Reactions of Naphthalene and the C1- and C2-Alkylnaphthalenes. *Environmental Science & Technology* 2007; 41(8):2803-2810.
49. Kleindienst TE, Jaoui M, Lewandowski M, Offenberg JH, Docherty KS. The formation of SOA and chemical tracer compounds from the photooxidation of naphthalene and its methyl analogs in the presence and absence of nitrogen oxides. *Atmospheric Chemistry and Physics* 2012; 12(18):8711-8726.
50. Nishino N, Arey J, Atkinson R. Yields of glyoxal and ring-cleavage co-products from the OH radical-initiated reactions of naphthalene and selected alkylnaphthalenes. *Environ Sci Technol* 2009; 43(22):8554-8560.

51. Nishino N, Arey J, Atkinson R. 2-Formylcinnamaldehyde Formation Yield from the OH Radical-Initiated Reaction of Naphthalene: Effect of NO2 Concentration. *Environmental Science & Technology* 2012; 46(15):8198-8204.
52. Zhang Z, Lin L, Wang L. Atmospheric oxidation mechanism of naphthalene initiated by OH radical. A theoretical study. *Physical Chemistry Chemical Physics* 2012; 14(8):2645-2650.
53. Atkinson R, Aschmann SM. Kinetics of the gas-phase reactions of alkylnaphthalenes with O3, N2O5 and OH radicals at 298 ± 2 K. *Atmospheric Environment (1967)* 1987; 21(11):2323-2326.
54. Bunce NJ, Liu L, Zhu J, Lane DA. Reaction of Naphthalene and Its Derivatives with Hydroxyl Radicals in the Gas Phase. *Environmental Science & Technology* 1997; 31(8):2252-2259.
55. Alves CA, Lopes DJ, Calvo AI, Evtyugina M, Rocha S, Nunes T. Emissions from Light-Duty Diesel and Gasoline In-Use Vehicles Measured on Chassis Dynamometer Test Cycles. *Aerosol and Air Quality Research* 2015; 15(1):99-116.
56. Gentner DR, Worton DR, Isaacman G, Davis LC, Dallmann TR, Wood EC, et al. Chemical Composition of Gas-Phase Organic Carbon Emissions from Motor Vehicles and Implications for Ozone Production. *Environmental Science & Technology* 2013; 47(20):11837-11848.
57. Roy A, Sonntag D, Cook R, Yanca C, Schenk C, Choi Y. Effect of Ambient Temperature on Total Organic Gas Speciation Profiles from Light-Duty Gasoline Vehicle Exhaust. *Environmental Science & Technology* 2016; 50(12):6565-6573.
58. Hunter JF, Carrasquillo AJ, Daumit KE, Kroll JH. Secondary Organic Aerosol Formation from Acyclic, Monocyclic, and Polycyclic Alkanes. *Environmental Science & Technology* 2014; 48(17):10227-10234.
59. Lim YB, Ziemann PJ. Effects of Molecular Structure on Aerosol Yields from OH Radical-Initiated Reactions of Linear, Branched, and Cyclic Alkanes in the Presence of NOx. *Environmental Science & Technology* 2009; 43(7):2328-2334.
60. Alam MS, Camredon M, Rickard AR, Carr T, Wyche KP, Hornsby KE, et al. Total radical yields from tropospheric ethene ozonolysis. *Physical Chemistry Chemical Physics* 2011; 13(23):11002-11015.
61. Orlando JJ, Iraci LT, Tyndall GS. Chemistry of the Cyclopentoxy and Cyclohexoxy Radicals at Subambient Temperatures. *The Journal of Physical Chemistry A* 2000; 104(21):5072-5079.
62. Aschmann SM, Arey J, Atkinson R. Reactions of OH radicals with C6-C10 cycloalkanes in the presence of NO: isomerization of C7-C10 cycloalkoxy radicals. *J Phys Chem A* 2011; 115(50):14452-14461.
63. Lim YB, Ziemann PJ. Chemistry of Secondary Organic Aerosol Formation from OH Radical-Initiated Reactions of Linear, Branched, and Cyclic Alkanes in the Presence of NOx. *Aerosol Science and Technology* 2009; 43(6):604-619.
64. D'Anna B, Wisthaler A, Andreasen O, Hansel A, Hjorth J, Jensen NR, et al. Atmospheric chemistry of C3-C6 cycloalkanecarbaldehydes. *J Phys Chem A* 2005; 109(23):5104-5118.
65. Aschmann SM, Chew AA, Arey J, Atkinson R. Products of the Gas-Phase Reaction of OH Radicals with Cyclohexane: Reactions of the Cyclohexoxy Radical. *The Journal of Physical Chemistry A* 1997; 101(43):8042-8048.
66. Takagi H, Washida N, Bandow H, Akimoto H, Okuda M. Photooxidation of C5-C7 cycloalkanes in the nitric oxide-water-air system. *The Journal of Physical Chemistry* 1981; 85(18):2701-2705.
67. Atkinson R, Aschmann SM, Carter WPL, Winer AM, Pitts JN. Formation of alkyl nitrates from the reaction of branched and cyclic alkyl peroxy radicals with NOx. In: Int. J. Chem. Kinet; 1984.
68. Gentner DR, Isaacman G, Worton DR, Chan AWH, Dallmann TR, Davis L, et al. Elucidating secondary organic aerosol from diesel and gasoline vehicles through detailed characterization of organic carbon emissions. *Proceedings of the National Academy of Sciences* 2012; 109(45):18318.
69. Schauer JJ, Kleeman MJ, Cass GR, Simoneit BRT. Measurement of Emissions from Air Pollution Sources. 5. C1−C32 Organic Compounds from Gasoline-Powered Motor Vehicles. *Environmental Science & Technology* 2002; 36(6):1169-1180.
70. Zhao YL, Nguyen NT, Presto AA, Hennigan CJ, May AA, Robinson AL. Intermediate Volatility Organic Compound Emissions from On-Road Gasoline Vehicles and Small Off-Road Gasoline Engines. *Environmental Science & Technology* 2016; 50(8):4554-4563.
71. Zhao Y, Lambe AT, Saleh R, Saliba G, Robinson AL. Secondary Organic Aerosol Production from Gasoline Vehicle Exhaust: Effects of Engine Technology, Cold Start, and Emission Certification Standard. *Environmental Science & Technology* 2018; 52(3):1253-1261.
72. Sartelet K, Zhu S, Moukhtar S, André M, André JM, Gros V, et al. Emission of intermediate, semi and low volatile organic compounds from traffic and their impact on secondary organic aerosol concentrations over Greater Paris. *Atmospheric Environment* 2018; 180:126-137.
73. Robinson AL, Donahue NM, Shrivastava MK, Weitkamp EA, Sage AM, Grieshop AP, et al. Rethinking organic aerosols: semivolatile emissions and photochemical aging. *Science* 2007; 315(5816):1259-1262.
74. Lim YB, Ziemann PJ. Products and mechanism of secondary organic aerosol formation from reactions of n-alkanes with OH radicals in the presence of NOx. *Environmental Science & Technology* 2005; 39(23):9229-9236.
75. Yee LD, Craven JS, Loza CL, Schilling KA, Ng NL, Canagaratna MR, et al. Secondary Organic Aerosol Formation from Low-NOx Photooxidation of Dodecane: Evolution of Multigeneration Gas-Phase Chemistry and Aerosol Composition. *Journal of Physical Chemistry A* 2012; 116(24):6211-6230.
76. Cappa CD, Zhang X, Loza CL, Craven JS, Yee LD, Seinfeld JH. Application of the Statistical Oxidation Model (SOM) to Secondary Organic Aerosol formation from photooxidation of C-12 alkanes. *Atmospheric Chemistry and Physics* 2013; 13(3):1591-1606.

77. Yee LD, Craven JS, Loza CL, Schilling KA, Ng NL, Canagaratna MR, et al. Effect of chemical structure on secondary organic aerosol formation from C-12 alkanes. *Atmospheric Chemistry and Physics* 2013; 13(21):11121-11140.
78. Fahnestock KAS, Yee LD, Loza CL, Coggon MM, Schwantes R, Zhang X, et al. Secondary Organic Aerosol Composition from C-12 Alkanes. *Journal of Physical Chemistry A* 2015; 119(19):4281-4297.
79. Erickson MH, Gueneron M, Jobson BT. Measuring long chain alkanes in diesel engine exhaust by thermal desorption PTR-MS. *Atmos Meas Tech* 2014; 7(1):225-239.

CHAPTER V:

General conclusions and perspectives

This chapter summarizes the main conclusions from the two research axis investigate in the framework of my PhD thesis: the evaluation of modern diesel and gasoline DI vehicle emissions and the SOA formation from traffic related VOCs.

Transport sector is, nowadays, fundamental to the economic development of a country and also allows a better communication between people, favoring their quality of life. However, transport plays a key role in climate change and air pollution. This contribution is expected to increase since demand for urban mobility as well as vehicle number in cities is increasing among Europe and other countries. Transport accounts for a third of energy consumption in the EU members and around a fifth of the total greenhouse gases emitted. Thus, road transport is considered as one of the main contributor to global warming and air pollution. Among all pollutants in the urban environments, particulate matter (PM), particularly the fine and ultrafine PM (below 10 and 2.5µm, respectively) present potential toxicity.

The reduction of emissions from road transport is clearly one of the priorities for governments that progressively introduced more restrictive regulations for vehicle emissions. Car manufacturers have responded by introducing a series of in-engine modifications and exhaust after treatment technologies, e.g. the Diesel Particulate Filter (DPF) or Selective Catalytic Reduction (SCR) of NOx and NOx trap devices. However, modern cars are still poorly characterized.

A first objective of this research work was to assess the emissions from modern (Euro 5 and Euro 6) vehicles. The regulated and un-regulated emissions from six vehicles (3 diesel and 3 gasoline DI) have been evaluated during Artemis and WLTC cycles. An original set of analytical instruments has been deployed to allow a comprehensive study of the emitted PM and the identification of VOCs. Main outputs suggest that: (1) sampling at tailpipe resulted to be a more a suitable approach for PN measurements than the CVS dilution system. Cold dilution in the CVS induced nucleation and condensation phenomena of the semi-volatile compounds present in the exhaust. (2) PMP protocol is based on PN measurements with 23 nm cut-off. However, particles in the 14-23 nm range can account for approximately 20-30% of total PN for GDI and around 10-15% for diesel cars. By downsizing particle counters cut-off threshold to 14 nm, an improvement of PN quantification would be achieved for tested cycles. (3) As general trends, gasoline DI vehicles showed highest EFs of PM (organics, PAHs and BC) mostly during cold start cycles. (4) In diesel vehicles, ammonium bisulfate was mainly emitted during passive regeneration of the DPF during high speed cycles (WLTC and mainly Motorway). Such process leads to high emission of particles in the ultrafine mode.TEM analysis of the collected particles indicated two types of particles: soot in form of fractal material or agglomerates and a second type of particles mostly liquid droplets likely coming from lubricants oils.

EFs of regulated pollutants have been firstly reported here for two Euro 5 vehicles (GDI3 and D3) during WLTC cycle and compared together with EFs reported by IFSTTAR vehicles. The GDI3 and D3 vehicles do not exceed standard limits for CO and HC. NOx concentrations, however, often exceeds limitation value for both vehicles. The GDI3 vehicle presents the highest NOx EFs, probably due to a failure of the reduction catalyst. Analysis of emitted compounds as a function of cycle speed suggests that CO_2 and NOx emissions depend mainly of speed profile of the cycle (acceleration and brakes) while CO or THC are mainly emitted during cold start periods of cycle.

In the line of improve air quality by reducing vehicle emissions, the EU commission progressively introduced stringent regulations which comprise lower emission limits. Study of non regulated gaseous pollutants was another important axis during vehicle characterization emission experiments at IFSTTAR. Thus, species as benzene or ammonia have been measured by PTRMS for Euro 5 diesel and gasoline vehicles. In general, benzene is emitted during first part of cycle, corresponding to light-off catalyst period. Benzene is emitted in around the same concentrations for tested GDI and diesel vehicles. Results are consistent with those reported by GC-MS analysis. Ammonia is emitted during the last part of the WLTC for GDI vehicle, corresponding to high speed regime. Reported emissions are somewhere lower that those found in literature. NH_3 is emitted in very low concentration for diesel vehicle, which is in agreement with previous literature, where ammonia emissions had only been reported for diesel vehicles equipped with SCR NOx abatement technology.

Gas phase sampling on TENAX Cartridges and further thermal desorption followed by chromatography analysis by ATD-GC-MS methodology has been carried out to characterize VOCs emissions. The emissions of VOCs have been classified in five families: BTEX, others aromatics, oxygenated compounds, cyclic aliphatics and linear/branched aliphatics. For gasoline DI vehicle BTEX and linear/branched aliphatic were the most abundant compounds with EFs in the range 10^3-10^4 µg/km. While for diesel vehicles cyclic aliphatic and oxygenated compounds were the most abundant with EFs up to 10^4 µg/km. Among the BTEX, xylene and benzene are the dominant compounds for gasoline and diesel vehicles, respectively. Gasoline aliphatic distribution is centered on C_6-C_7 compounds, with negligible emissions beyond C_{12}. While diesel emissions presents a carbon distribution centered on C_9-C_{10} compounds with non negligible concentrations up to C_{16} compounds. Higher carbon number products (up to C_{20}) have been detected for diesel emissions. VOCs analysis suggests diesel vehicle is an important source of IVOCs, which are considered as good SOA precursors.

Contrary to what was thought a couple of decades ago secondary particles formed in the atmosphere through physical and chemical processes dominated the fine fraction of the aerosol in urban and polluted environments. While the conceptual picture appears to be reasonably well established, the most efficient SOA precursors in modern vehicular exhaust and

the main atmospheric photochemical pathways for SOA formation are still under debate. Research efforts are currently focusing on SOA formation in urban environments where population and traffic densities are highest and where poor air quality and detrimental health effects are evident.

Thus, in order to establish the contribution of SOA from primary car emission, detailed investigation of individual/family precursors is vital. The AFT experiments intended to mimic the photo-oxidation of car exhaust in a controlled and simplified system. Experiments were conducted in the laboratory and the strategy adopted consisted in the selection of few key compounds found in the car exhaust. The compounds were chosen on the basis of the measured VOCs emitted by diesel and gasoline vehicles from our own studies (chapter III) and from published literature. Five compounds have been selected for the laboratory investigations (toluene, nonane, cyclohexane and naphthalene). The aim of this work was to determine SOA yield, chemical composition of both gas and particle phase, key parameters controlling SOA formation (as temperature, type and quantity of VOC, pre-existing seed particles). Experiments were then repeated using a mixture of the selected VOCs. The new developed Chemical Analysis of aerosol on-line (CHARON) inlet coupled to PTRMS was deployed for the speciation of the organics in the particle phase. Few and preliminary photoxidation experiments of car exhaust (GDI vehicle) were performed using an aerosol flow tube to determine major SOA constituents and SOA potential formation.

These investigations allowed the determination of quantitative relationships between the SOA yield and SOA concentration with respect to the temperature in the range 21-7°C, the initial VOC and hydroxyl radical concentration and the presence of pre-existing particle seeds. Highest SOA yield have been measured for aromatic compounds (24 % for naphthalene and 16 % for toluene) at low temperature and low VOC concentrations. The temperature was clearly a sensitive parameter: a decrease from 21 to 7°C induced a SOA increase of a factor 2 for SOA derived from naphthalene, nonane and cyclohexane and up to a factor 4 for toluene generated SOA. These differences were explained in term of the volatility of the reaction products formed during photoxidation process. The initial VOC concentration is another important parameter and tend positively affect the final SOA concentration. The presence of preexisting particles tends to favor SOA formation, especially for aromatic compounds. While NOx concentration negatively affects SOA formation for all tested VOCs.

In the framework of this experimental work we deployed for the first time the newly developed the Chemical Analysis of Aerosol Online" (CHARON) coupled to the PTRMS. This system enables to sample and analyze submicron particle matter in-situ and with real time resolution. The SOA photoxidation experiments suggest that the instrument is able to chemically characterize a high fraction of the formed SOA. This result is in itself quite promising since traditional off-line methods as filters collection followed by extraction and

chemical analysis often can identify and quantify no more than 30-40% of the organic mass. For some VOCs degradation experiments, as toluene and naphthalene, the chemical analysis of both the gas and particle phases is quite complete and satisfactory while for nonane and cyclohexane more analytical work is needed mainly due to high fragmentation of the reaction products in the PTR-MS. For all the investigated systems during laboratory experiments, it was possible to determine the products raw formula both in the gas and the particle phase. As a result, the partition coefficients for all products were calculated. Determination of partitioning coefficients for each reaction product provides key information on the volatility of individual compounds, and by extension, on the volatility of the total SOA bulk. This is an important step forwards in order to fully understand the formation and evolution of SOA under atmospheric conditions.

Identification and quantification of individual compounds allows also to assess the potential toxicity of both gas and particle phase reaction products. In the framework of this work we could measure the formation of potentially toxic and harmful compounds to human health, as nitrotoluene, nitrocresol, nitronaphthol, nitronaphthalene, nitrophenol or nitrocatechol. Nitrogen containing products were also detected in the real gasoline exhaust photoxidation experiments.

A very preliminary set of experiments on photoxidation of Euro 5 gasoline direct injection was carried out. The test was developed as a first essay for further research projects, where real vehicles exhaust will be photoxidized using both smog chambers and AFT systems. Results strengthen the feasibility of CHARON to measure and identify degradation products of very complex mixtures.

Future perspectives

A comprehensive assessment of the real impact of vehicular emissions should consider both primary emissions and secondary pollutants formed in the atmosphere via physico-chemical processes. The rapid development of engine technologies, aftertreatment devices and new standards requires to keep updated the emission factors database for regulated compounds. Future studies should focus on Euro 6b-c passenger cars and vehicles equipped with modern aftertreatment devices as NOx trap, SCR and possibly gasoline vehicles equipped with GPF technology. It would be very useful to extend the database to non-regulated pollutants as particle condensable fraction (organics, PAHs, nitrate and sulfate), PN concentration below 23nm, and to gaseous pollutants as reduced nitrogen species as ammonia or amines which could highly influence the formation of new particle in the atmosphere.

To better assess SOA formation from vehicle exhaust it is mandatory to better quantify pollutants as IVOCs or SVOCs. These compounds are difficult to quantify correctly because of

their low volatility and thus, can easily be lost in lines before sampling. The development of a standard methodology able to accurately quantify IVOCs and SVOCs emission is important for modelers in order to understand contribution of these pollutants to the SOA budget. Nowadays, emissions of IVOCs and SVOCs are calculated as fraction of primary pollutants, as POA or VOCs, what leads to a considerable level of uncertainty in SOA models.

A better comprehension of the main mechanisms leading to SOA formation is also needed for an accurate estimation of the SOA budget. In this context, it would be useful to combine smog chamber (longer oxidation times) and aerosol flow tubes (temperature dependence studies) in order mimic in a more realistic way atmospheric processes.

Identification of toxic degradation products in the gas and the particle phase is vital for the assessment of car pollutants on human health. Particulate matter (PM) is a complex, heterogeneous mixture that changes in time and space. It encompasses many different chemical components and physical characteristics, which are potential contributors to toxicity. Nowadays there is growing evidence that particles toxicity differs depending on their chemical composition. Further effort should be therefore devoted in combining detailed PM chemical analysis and toxicity studies.

Future experiments on SOA derived from real vehicle emissions will be carried out in the consortium established CaPVeREA project. The research activity will continue therefore the work started during this PhD thesis and will focus on aging processes of car emissions using simulation chambers.

ANNEXES

Annex I

Table AI.1. *Fuel composition for tested vehicles.*

	Diesel		Gasoline	
	Euro 5	Euro 6b	Euro 5	Euro 6b
Density at 15°C (kg/m^3)	829	835	726	742
Sulfur content (mg/kg)	8.8	8.8	7.4	6.7
Water content (mg/km)	60.0	70.0	-	-
Total contamination (mg/kg)	12	12	-	-
Total AH (% m)	23.2	27.3	-	-
PAHs (%)	3.0	3.3	-	-
BTEX (%)	1.2	-	-	-
Lead content (mg/L)	-	-	< 2.5	< 2.5
Benzene content (% m)	-	-	0.36	0.44
Ethanol content (% vol)	-	-	7.5	7.4
ETBE content (% vol)	-	-	5.1	4.9
Total oxygenated (% vol)	-	-	12.7	17.6
Oxygen content (% m)	-	-	3.7	3.6
Aromatic content (% m)	-	-	19.3	26.2
Olefin content (% vol)	-	-	15.3	13.8
Saturates content (% vol)	-	-	52.6	-

Annex II

Table AII.1. *Experiment conditions using for D1 Euro 5 diesel vehicle.*

n°	Cycle	Start	CVS Flow (m^3/min)	Dilution Ratio (FPS)	Primary dilution (FPS)	Dilution Temperature (FPS)
1	Urban	Cold	9	100	16.4	50
2	Urban	Cold	9	100	16.4	50
3	Urban	Cold	9	1000	22.0	50
4	Urban	Cold	9	100	16.4	100
5	Urban	Cold	9	1000	22.0	100
6	Motorway	Hot	13	8	1.5	50
7	Motorway	Hot	13	8	1.5	50
8	Motorway	Hot	13	12	1.9	50
9	Motorway	Hot	13	12	1.9	50
10	Motorway	Hot	13	16	2.6	50
11	Motorway	Hot	13	16	2.6	50
12	Motorway	Hot	13	30	4.5	50
13	Motorway	Hot	13	30	4.5	50
14	Motorway	Hot	13	30	4.5	50
15	Motorway	Hot	13	30	4.5	50
16	Motorway	Hot	13	56	6.8	50
17	Motorway	Hot	13	56	6.8	50
18	Motorway	Hot	13	100	16.4	50
19	Motorway	Hot	13	100	16.4	50
20	Motorway	Hot	13	1000	22.0	50
21	Motorway	Hot	13	1000	22.0	50

Table AII.2. *Experiment conditions using for D3 Euro 5 diesel vehicle.*

n°	Cycle	Start	CVS Flow (m^3/min)	Dilution Ratio (FPS)	Primary dilutin (FPS)	Dilution Temperature (FPS)
1	WLTC	Cold	13	15	2.8	130
2	WLTC	Hot	13	15	2.8	130
3	WLTC	Hot	13	15	2.8	130
4	WLTC	Cold	13	15	2.8	120
5	WLTC	Hot	13	7	1.2	120
6	WLTC	Hot	13	10	1.8	120
7	WLTC	Cold	13	46	9.7	120
8	WLTC	Hot	13	10	1.8	120
9	WLTC	cold	13	46	9.7	120
10	WLTC	Hot	13	46	9.7	120

Table AII.3. *Experiment conditions using D2 Euro 6b diesel vehicle.*

n°	Cycle	Start	CVS Flow (m^3/min)	Dilution Ratio (FPS)	Primary dilution (FPS)	Dilution Temperature (FPS)
1	WLTC	Cold	13	10	1.8	50
2	WLTC	hot	13	10	1.8	50
3	WLTC	Cold	13	36	5.0	50
4	WLTC	hot	13	36	5.0	50
5	WLTC	Cold	13	10	1.8	50
6	WLTC	Cold	13	10	1.8	50
7	Urban	Cold	9	20	3.0	50
8	Urban	semi cold	9	10	1.8	50
9	Urban	Cold	9	85	13.0	36
10	Urban	hot	9	85	13.0	36
11	Urban	hot	9	85	13.0	36
12	Urban	semi cold	9	85	13.0	36
13	Urban	hot	9	85	13.0	36
14	Urban	hot	9	85	13.0	36
15	Urban	Cold	9	10	1.8	50
16	Urban	Cold	9	10	1.8	50
17	Urban	hot	9	10	1.8	50
18	Urban	hot	9	10	1.8	50
19	Urban	semi cold	9	10	1.8	50
20	Urban	hot	9	10	1.8	50
21	Urban	hot	9	10	1.8	50
22	Road	hot	9	50	6.7	30
23	Road	hot	9	50	6.7	30
24	Road	hot	9	50	6.7	30
25	Road	hot	9	30	4.5	50
26	Road	hot	9	30	4.5	50
27	Road	hot	9	30	4.5	50
28	Motorway	hot	13	10	1.8	50
29	Motorway	hot	13	10	1.8	50
30	Motorway	hot	13	10	1.8	50
31	Motorway	hot	13	18	2.9	50
32	Motorway	hot	13	18	2.9	50
33	Motorway	hot	13	18	2.9	50

Table AII.4. *Experiment conditions using for GDI1 Euro 5 gasoline vehicle.*

n°	Cycle	Start	CVS Flow (m^3/min)	Dilution Ratio (FPS)	Primary dilution (FPS)	Dilution Temperature (FPS)
1	Urban	Cold	9	100	16.4	50
2	Urban	Cold	9	1000	22.0	50
3	Urban	Cold	9	100	16.4	100
4	Urban	Cold	9	1000	22.0	100
5	Urban	Cold	9	100	16.4	150
6	Urban	Cold	9	1000	22.0	150
7	Motorway	Hot	13	30	4.5	50
8	Motorway	Hot	13	30	4.5	50
9	Motorway	Hot	13	30	4.5	50
10	Motorway	Hot	13	100	16.4	50
11	Motorway	Hot	13	100	16.4	50
12	Motorway	Hot	13	400	5.5	50
13	Motorway	Hot	13	400	5.5	50
14	Motorway	Hot	13	400	5.5	50
15	Motorway	Hot	13	1000	22.0	50
16	Motorway	Hot	13	1000	22.0	50
17	Motorway	Hot	13	1000	22.0	50

Table AII.5. *Experiment conditions using for GDI3 Euro 5 gasoline vehicle.*

n°	Cycle	Start	CVS Flow (m^3/min)	Dilution Ratio (FPS)	Primary dilution (FPS)	Dilution Temperature (FPS)
1	WLTC	Cold	13	20	3.0	90
2	WLTC	Hot	13	46	9.7	90
3	WLTC	Hot	13	46	9.7	90
4	WLTC	Cold	13	46	9.7	90
5	WLTC	Hot	13	10	1.8	90
6	WLTC	Hot	13	10	1.8	90
7	WLTC	Cold	13	46	9.7	90
8	WLTC	Hot	13	46	9.7	90
9	WLTC	Hot	13	10	1.8	90
10	WLTC	Cold	13	46	9.7	90
11	WLTC	Hot	13	10	1.8	75
12	WLTC	Cold	13	46	9.7	75
13	WLTC	Cold	13	46	9.7	90
14	WLTC	Hot	13	10	1.8	80

Table AII.6. *Experiment conditions using for GDI2 Euro 6b gasoline vehicle.*

n°	Cycle	Start	CVS Flow (m^3/min)	Dilution Ratio (FPS)	Primary dilution (FPS)	Dilution Temperature (FPS)
1	WLTC	Cold	13	30	5.0	36
2	WLTC	hot	13	30	5.0	36
3	WLTC	Cold	13	20	3.0	50
4	WLTC	hot	13	20	3.0	50
5	WLTC	Cold	13	20	3.0	50
6	WLTC	Cold	13	40	5.7	36
7	Urban	Cold	9	10	1.8	150
8	Urban	hot	9	10	1.8	150
9	Urban	hot	9	10	1.8	150
10	Urban	semi cold	9	10	1.8	50
11	Urban	hot	9	10	1.8	150
12	Urban	hot	9	10	1.8	150
13	Urban	Cold	9	10	1.8	150
14	Urban	hot	9	10	1.8	150
15	Urban	hot	9	10	1.8	150
16	Urban	semi cold	9	10	1.8	150
17	Urban	hot	9	10	1.8	150
18	Urban	hot	9	10	1.8	150
19	Urban	Cold	9	50	6.7	36
20	Road	hot	9	100	17.0	150
21	Road	hot	9	100	17.0	150
22	Road	hot	9	100	17.0	150
23	Road	hot	9	10	1.8	150
24	Road	hot	9	10	1.8	150
25	Road	hot	9	10	1.8	150
26	Road	hot	9	36	5.0	36
27	Road	hot	9	36	5.0	36
28	Road	hot	9	36	5.0	36
29	Motorway	hot	13	13	1.7	36
30	Motorway	hot	13	13	1.7	36
31	Motorway	hot	13	13	1.7	36
32	Motorway	hot	13	20	3.0	50
33	Motorway	hot	13	20	3.0	50
34	Motorway	hot	13	10	1.8	50
35	Motorway	hot	13	20	3.0	50

Annex III

Table AIII.1. *Experimental conditions for toluene experiments.*

n°	T (°C)	VOC_0 (ppbv)	VOC_{end} (ppbv)	RH (%)	NOx (ppb)	AS Seed ($\mu g/m^3$)	Seed size (nm)	$^{\bullet}OH$ ($molec/cm^3$)	VOC/NOx (ppbC/ppbv)
1	21	112	48.2	30	542	6.0	150	$1.17x10^8$	4.45
2	21	23	11.3	30	566	7.5	150	$1.04x10^8$	3.28
3	21	23	12.0	30	570	8.0	150	$9.46x10^7$	3.28
4	21	112	59.4	30	204	7.0	150	$9.32x10^7$	6.84
5	21	112	58.2	24	302	10.0	150	$9.40x10^7$	5.60
6	21	159	89.0	39	481	2.4	113	$8.03x10^7$	5.31
7	21	159	84.2	33	494	5.5	113	$8.79x10^7$	5.25
8	21	124	70.4	38	470	6.1	113	$9.07x10^7$	4.84
9	21	161	69.2	41	436	3.5	113	$9.18x10^7$	5.58
10	21	161	67.6	41	426	6.5	113	$9.49x10^8$	5.64
11	21	84	31.8	35	424	5.0	113	$1.23x10^8$	4.38
12	21	127	53.4	43	801	5.5	113	$1.04x10^8$	4.11
13	16	128	56.3	37	746	5.0	113	$1.18x10^8$	4.20
14	16	128	61.4	37	746	8.0	113	$1.07x10^8$	4.20
15	12	66	31.5	30	551	10.0	150	$1.08x10^8$	3.83
16	12	112	67.9	24	225	7.0	150	$8.13x10^7$	6.48
17	12	112	59.4	24	189	8.0	150	$9.12x10^7$	7.15
18	12	32	4.3	24	200	8.0	150	$1.22x10^8$	3.16
19	12	8	3.4	24	200	8.0	150	$1.22x10^8$	3.28
20	12	112	52.6	24	346	10.0	150	$1.09x10^8$	5.27
21	12	112	60.5	50	322	8.0	150	$9.07x10^7$	5.43
22	12	66	35.0	50	329	8.0	150	$9.22x10^7$	4.40
23	12	80	34.4	28	409	8.5	113	$1.04x10^8$	4.37
24	12	132	60.7	36	442	6.7	113	$1.17x10^8$	5.09
25	12	125	53.7	33	736	5.0	113	$1.36x10^8$	4.19
26	7	66	36.3	24	376	10	150	$8.81x10^7$	4.23
27	7	112	61.6	24	361	10	150	$8.69x10^7$	5.17
28	7	62	27.2	32	446	8.0	113	$9.83x10^7$	3.97
29	7	128	62.9	31	423	8.1	113	$7.35x10^7$	5.12
30	7	44	20.0	41	760	6.0	131	$8.45x10^7$	3.58
31	7	8	4.4	24	361	8.0	131	$1.074x10^8$	4.20

Table AIII.2. Experimental conditions for nonane experiments.

n°	T (°C)	VOC_0 (ppbv)	VOC_{end} (ppbv)	RH (%)	NOx (ppb)	AS Seed ($\mu g/m^3$)	Seed size (nm)	$^{\bullet}OH$ ($molec/cm^3$)	VOC/NOx (ppbC/ppbv)
1	21	193	47	35	427	NO	NO	$1.69x10^8$	7.1
2	21	193	47	43	499	8.5	113	$1.69x10^8$	6.5
3	12	193	47	33	430	NO	NO	$1.69x10^8$	7.0
4	7	193	47	29	459	NO	NO	$1.69x10^8$	6.8
5	7	193	47	25	480	7.5	113	$1.69x10^8$	6.6
6	7	73	26	40	760	13.0	113	$1.46x10^8$	3.9
7	7	73	26	39	760	8.7	113	$1.46x10^8$	3.9

Table AIII.3. Experimental conditions for cyclohexane experiments.

n°	T (°C)	VOC_0 (ppbv)	VOC_{end} (ppbv)	RH (%)	NOx (ppb)	AS Seed ($\mu g/m^3$)	Seed size (nm)	$^{\bullet}OH$ ($molec/cm^3$)	VOC/NOx (ppbC/ppbv)
1	21	50	32	44	533	NO	NO	$1.96w10^8$	3.6
2	21	50	32	42	505	6.5	113	$1.96w10^8$	3.6
3	21	50	32	41	508	5	113	$1.96x10^8$	3.6
4	21	25	10	35	508	6	113	$1.96x10^8$	3.3
5	21	25	10	35	508	6	113	$1.96x10^8$	3.3
6	7	50	30	30	519	NO	NO	$1.96x10^8$	3.6
7	7	50	28	32	325	10.3	117	$1.96x10^8$	3.9
8	7	60	42	42	497	3	113	$7.62x10^7$	3.7
9	7	60	42	42	547*	3.5	113	$7.62x10^7$	3.2

* Injection of 75 ppb of NOx.

Table AIII.4. Experimental conditions for naphthalene experiments.

n°	T (°C)	VOC_0 (ppbv)	VOC_{end} (ppbv)	RH (%)	NOx (ppb)	AS Seed ($\mu g/m^3$)	Seed size (nm)	$^{\bullet}OH$ ($molec/cm^3$)	VOC/NOx (ppbC/ppbv)
1	21	25	2.3	55	689	9.0	113	$1.57x10^8$	3.4
2	21	25	3.5	53	870*	9.5	113	$1.30x10^8$	2.6
3	12	17	4.0	35	745*	10.0	131	$9.53x10^7$	2.4
4	7	18	3.0	41	571	5.2	131	$1.22x10^8$	3.3
5	7	17	3.4	37	726*	9.3	131	$1.06x10^8$	2.4
6	7	3	0.7	40	760	7.5	117	$9.59x10^7$	3.0
7	7	3	0.7	40	760	8.5	117	$9.59x10^7$	3.0

* Injection of 200 ppb of NOx.

Table AIII.5. Experimental conditions for naphthalene experiments.

n°	T (°C)	VOC_0 (ppbv)	VOC_{end} (ppbv)	RH (%)	Nox (ppb)	AS Seed ($\mu g/m^3$)	Seed size (nm)	$^{\bullet}OH$ ($molec/cm^3$)	VOC/NOx (ppbC/ppbv)
1	16	58	7	42	805*	7.5	126	$9.71x10^7$	2.7
2	12	102	13	35	770*	7.0	126	$9.46x10^7$	3.0
3	7	102	15	40	750*	7.5	126	$8.80x10^7$	3.0

* Injection of 200 ppb of NOx.

Table AIII.6. Experimental conditions for naphthalene experiments.

n°	VOC	T (°C)	VOC_0 ppb	VOC_{end} ppb	RH (%)	Nox ppb	Seed $\mu g/m^3$	Seed size (nm)	$^{\bullet}OH$ $molec/cm^3$	VOC/NOx ppbC/ppb
1	N T	16	230 124	157 81	50	484*	12.0	146	$7.50X10^7$	7.6
2	N T	16	230 76	157 63	50	480*	12.0	146	$7.50X10^7$	7.6
3	N T	16	230 76	157 63	44	480*	9.5	146	$7.50X10^7$	7.0
4	N T	12	230 57	143 50	42	522*	11.0	146	$6.73X10^7$	6.5
5	N T	7	230 57	198 44	37	461*	9.5	146	$6.73X10^7$	6.9
6	N T	7	230 57	198 40	37	255	9.5	146	$6.73X10^7$	12.5
7	C N T	7	60 38 166	42 11 114	36	548**	10.0	113	$7.62X10^7$	6.0
8	C N T	7	60 38 166	42 11 109	34	481	11.7	113	$7.62X10^7$	6.8
9	P T Naph	16	4 42 3	3 30 1	50	760	7.0	113	$5.93X10^7$	3.4
10	P T Naph	12	6 40 2	3 31 1	38	745*	7.0	131	$5.93X10^7$	2.6
11	P T Naph	7	4 41 3	3 30 1	38	950*	8.5	131	$5.93X10^7$	2.7
12	P T Naph	7	4 42 3	3 30 1	38	775	8.5	131	$5.93X10^7$	3.4
13	P T Naph	7	4 42 3	3 30 1	35	760	8.0	113	$5.93X10^7$	3.4
14	N T Naph	7	230 57 12	126 46 8	35	478	9.5	131	$6.73X10^7$	5.1
15	N T Naph P	7	73 42 3 4	26 30 1 3	42	760	8.7	113	$1.46X10^8$	4.3

* Injection of 200 ppb of NOx, ** Injection of 75 ppb of NOx. N=nonane, T=Toluene, C=cyclohexane, Naph= Naphthalene, P= Phenol

Annex IV

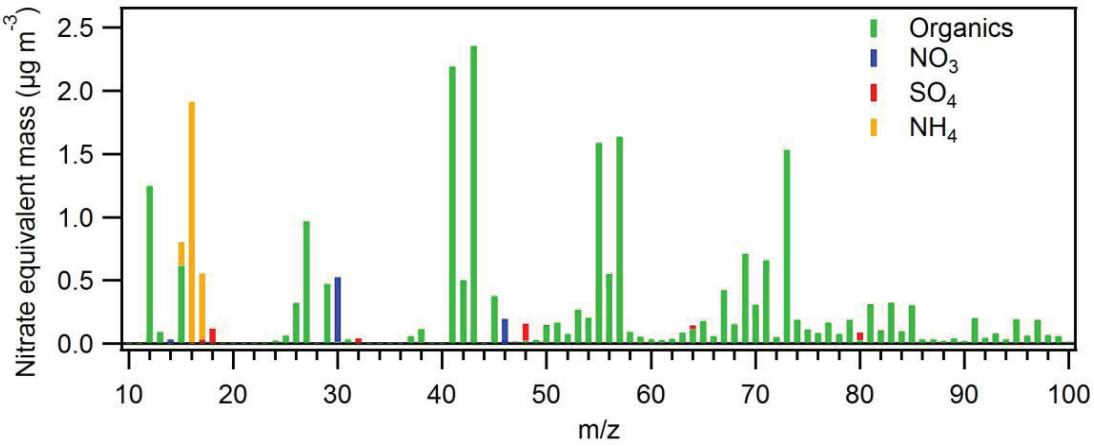

Figure AIV.1. *m/z for first minute of Artemis urban cold start cycle for D1 diesel Euro 5 vehicle.*

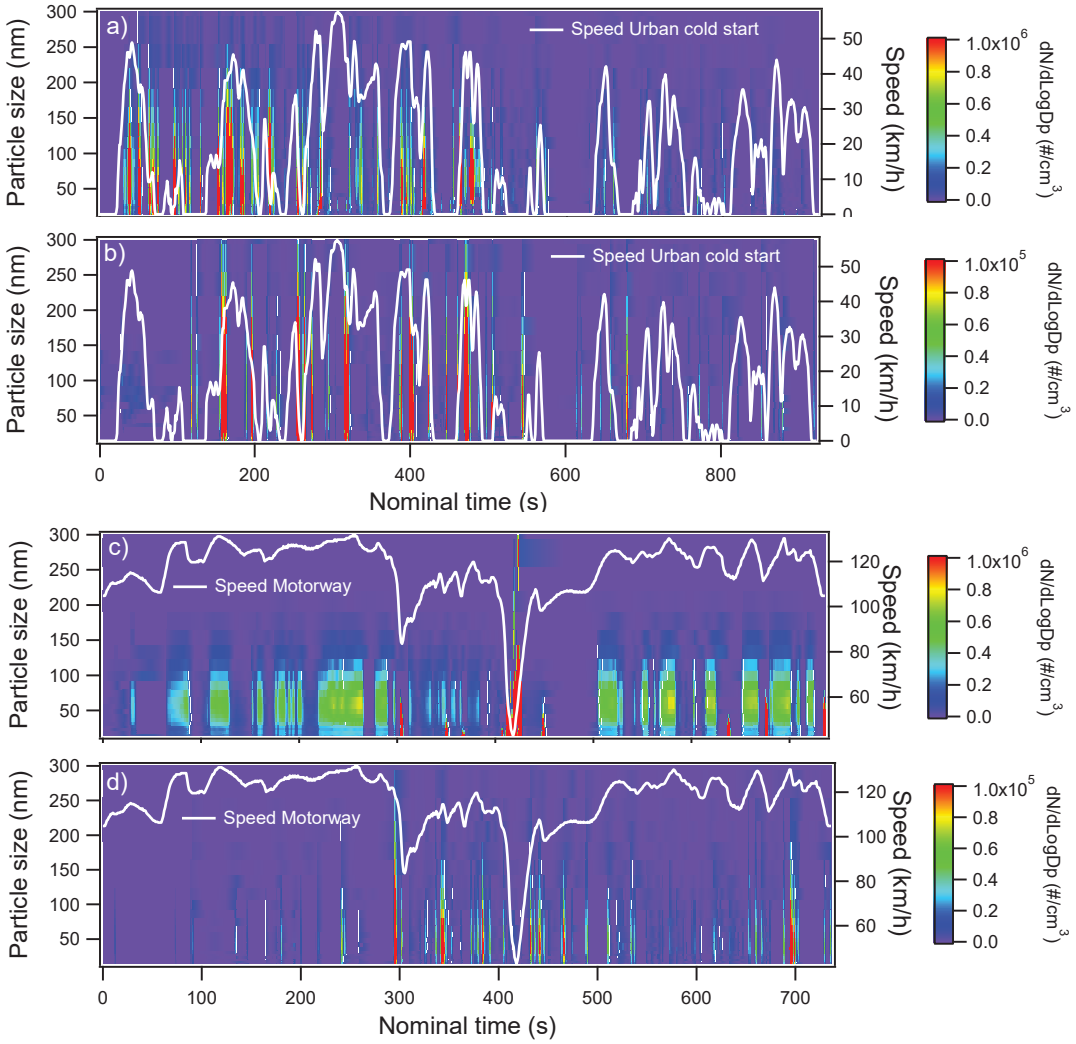

Figure AIV.2. *Particle size distribution for a) GDI2 during Artemis urban cold start cycle, b) Diesel D2 during Artemis urban cold start cycle , c) GDI2 during Artemis Motorway cycle and d) Diesel D2 during Artemis Motorway cycle.*

Annex V

Table AV.1. *Gas and particle phase main products (concentration of product/concentration total product (ppbC/ppbC)) found in toluene photoxidation for experiments at 21°C.*

n°	Possible compound(s)	Formula	Protonated m/z	% gas phase	% particle phase
1	Methylglyoxal	$C_3H_4O_2/C_2H_4O$	73.028/45.033	15.3	5.9
2	Maleic anhydride	$C_4H_2O_3/C_4H_5O_4$	99.010/ hydrate at 117.02	14.3	0.7
3	Acetic acid/Hydroxyacetaldehyde	$C_2H_4O_2$	61.028	9.6	5.6
4	Formic acid	CH_2O_2	47.013	10.8	3.2
5	Nitrocresols (structural isomers)	$C_7H_7NO_3$	154.05	5.2	0.5
6	Benzaldehyde	C_7H_6O	107.05	5.1	n.d
7	Nitrotoluene	$C_7H_7NO_2$	138.06	5.5	n.d
8	Cresols (all isomers)	C_7H_8O	109.06	3.5	n.d
9	Benzoic acid*	$C_7H_6O_2$ /C_7H_4O	123.04 /105.04	2.6	1.0
10	4-oxo-2-pentenal*	$C_5H_6O_2/C_5H_4O$	99.046/81.035	3.7	2.5
11	methyl furandione*	$C_5H_4O_3$	113.02	1.5	1.9
12	2-butenedial	$C_4H_4O_2$	85.031	2.1	1.6
13	Nitrophenol	$C_6H_5NO_3$	140.04	1.0	0.7
14	2-hydroxy-1,3-propanedial*	$C_3H_4O_3/C_3H_2O_2$	89.026/71.016	1.4	4.1
15	4-Oxo-2-pentenoic acid*	$C_5H_6O_3/C_5H_4O_2$	115.04/97.032	1.2	5.6
16	4-oxo-2-butenoic-acid*	$C_4H_4O_3$ /$C_4H_2O_2$	101.03/83.012	1.6	2.6
17	2-oxo-3-hydroxybutanedial*	$C_4H_4O_4$	117.02	0.9	1.9
18	Butan-1,4-dial*	$C_4H_6O_2$	87.046	0.9	1.1
19	6-hydroxy-2-methyl, 1,4,5 trioxo-2 cyclohexene*	$C_7H_6O_4$	155.03	0.3	4.6
20	methyl-oxo-pentenoic acid*	$C_6H_8O_3/C_6H_6O_2$	129.06/ part of 111.04	0.5	1.8
21	2-hydroxy-3-oxobutanal*	$C_4H_6O_3$ /$C_4H_4O_2$	103.04/ possible contribution 85.031	0.3	1.8
22	5-Methylfurfural*	$C_6H_6O_2$	111.04	0.4	1.7
23	5-Hydroxymethylfurfural*	$C_6H_6O_3/C_6H_4O_2$	127.04/109.03	0.3	4.6
24	2,3-epoxy, 2-methyl-4-hexenedial*	$C_7H_8O_3$	141.05	0.2	1.7
25	2-hydroxy-5-methyl-pentenedial*	$C_7H_8O_5$	173.04	n.d.	1.1
26	4,5-dioxo-2-hexenoic acid*	$C_6H_6O_4$	143.03	n.d.	3.0
27	5-hydroxy-6,4-dioxo-2-heptenal*	$C_7H_8O_4$	157.05	n.d.	1.5

Table AV.2. *Gas and particle phase main products (concentration of product/concentration total product found (ppbC/ppbC)) found in toluene photoxidation for experiments at 7°C.*

n°	Possible compound(s)	Formula	Protonated m/z	% gas phase	% particle phase
1	Methylglyoxal	$C_3H_4O_2/C_2H_4O$	73.030/45.033	16.0	7.8
2	Maleic anhydride	$C_4H_2O_3/C_4H_5O_4$	99.010/ hydrate at 117.02	14.6	0.6
3	Acetic acid/Hydroxyacetaldehyde	$C_2H_4O_2$	61.028	12.5	5.3
4	Formic acid	CH_2O_2	47.013	12.5	3.2
5	Nitrocresols (structural isomers)	$C_7H_7NO_3$	154.05	5.9	0.6
6	Benzaldehyde	C_7H_6O	107.05/ possible contribution 105.04	4.3	nd
7	Nitrotoluene	$C_7H_7NO_2$	138.06	3.7	nd
8	Cresols (all isomers)	C_7H_8O	109.06	3.3	nd
9	Benzoic acid*	$C_7H_6O_2$ /C_7H_4O	123.04/105.04	2.3	1.0
10	4-oxo-2-pentenal*	$C_5H_6O_2/C_5H_4O$	99.046/81.035	2.2	4.4
11	methyl furandione*	$C_5H_4O_3$	113.02	1.6	2.9
12	2-butenedial	$C_4H_4O_2$	85.031	1.4	2.5
13	Nitrophenol	$C_6H_5NO_3$	140.04	1.2	0.8
14	2-hydroxy-1,3-propanedial*	$C_3H_4O_3/C_3H_2O_2$	89.026/71.016	0.9	4.5
15	4-Oxo-2-pentenoic acid*	$C_5H_6O_3/C_5H_4O_2$	115.04/97.032	0.9	5.5
16	4-oxo-2-butenoic-acid*	$C_4H_4O_3$ /$C_4H_2O_2$	101.03/83.012	0.9	3.4
17	2-oxo-3-hydroxybutanedial*	$C_4H_4O_4$	117.02	0.7	2.4
18	Butan-1,4-dial*	$C_4H_6O_2$	87.05	0.5	1.6
19	6-hydroxy-2-methyl, 1,4,5 trioxo-2 cyclohexene*	$C_7H_6O_4$	155.03	0.4	5.1
20	methyl-oxo-pentenoic acid*	$C_6H_8O_3/C_6H_6O_2$	129.06/ part of 111.04	0.4	3.1
21	2-hydroxy-3-oxobutanal*	$C_4H_6O_3$ /$C_4H_4O_2$	103.04/ possible contribution 85.031	0.3	3.1
22	5-Methylfurfural*	$C_6H_6O_2$	111.04 /possible contribution 97.028	0.3	2.4
23	5-Hydroxymethylfurfural*	$C_6H_6O_3/C_6H_4O_2$	127.04/109.03	0.2	6.6
24	2,3-epoxy, 2-methyl-4-hexenedial*	$C_7H_8O_3$	141.05	0.2	2.3
25	2-hydroxy-5-methyl-pentenedial*	$C_7H_8O_5$	173.04	n.d.	2.3
26	4,5-dioxo-2-hexenoic acid*	$C_6H_6O_4$	143.03	n.d.	3.3
27	5-hydroxy-6,4-dioxo-2-heptenal*	$C_7H_8O_4$	157.05	n.d.	3.9

Table AV.3. *Gas and particle phase main products (concentration of product/consumed VOC (ppbC/ppbC)) found in toluene photoxidation for experiments at 7°C.*

n°	Possible compound(s)	Formula	Protonated m/z	% gas phase	% particle phase
1	Methylglyoxal	$C_3H_4O_2/C_2H_4O$	73.028/45.033	6.2	0.6
2	Maleic anhydride	$C_4H_2O_3/C_4H_5O_4$	99.01/ hydrate at 117.02	4.3	0.1
3	Acetic acid/Hydroxyacetaldehyde	$C_2H_4O_2$	61.028	2.6	0.4
4	Formic acid	CH_2O_2	47.013	1.6	0.2
5	Nitrocresols (structural isomers)	$C_7H_7NO_3$	154.05	1.6	0.1
6	Benzaldehyde	C_7H_6O	107.05	3.3	nd
7	Nitrotoluene	$C_7H_7NO_2$	138.06	1.3	nd
8	Cresols (all isomers)	C_7H_8O	109.06	1.6	Nd
9	Benzoic acid*	$C_7H_6O_2$ /C_7H_4O	123.04 /105.04	1.0	0.1
10	4-oxo-2-pentenal*	$C_5H_6O_2/C_5H_4O$	99.046/81.035	1.1	0.3
11	methyl furandione*	$C_5H_4O_3$	113.02	0.4	0.2
12	2-butenedial	$C_4H_4O_2$	85.031	0.5	0.2
13	Nitrophenol	$C_6H_5NO_3$	140.04	0.4	0.1
14	2-hydroxy-1,3-propanedial*	$C_3H_4O_3/C_3H_2O_2$	89.026/71.016	0.2	0.3
15	4-Oxo-2-pentenoic acid*	$C_5H_6O_3/C_5H_4O_2$	115.04/97.032	0.3	0.3
16	4-oxo-2-butenoic-acid*	$C_4H_4O_3$ /$C_4H_2O_2$	101.03/83.012	0.2	0.2
17	2-oxo-3-hydroxybutanedial*	$C_4H_4O_4$	117.02	0.2	0.1
18	Butan-1,4-dial*	$C_4H_6O_2$	87.046	0.1	0.1
19	6-hydroxy-2-methyl, 1,4,5 trioxo-2 cyclohexene*	$C_7H_6O_4$	155.03	0.2	0.3
20	methyl-oxo-pentenoic acid*	$C_6H_8O_3/C_6H_6O_2$	129.06/ part of 111.04	0.1	0.3
21	2-hydroxy-3-oxobutanal*	$C_4H_6O_3$ /$C_4H_4O_2$	103.04/ possible contribution 85.031	0.1	0.2
22	5-Methylfurfural*	$C_6H_6O_2$	111.04	0.1	0.2
23	5-Hydroxymethylfurfural*	$C_6H_6O_3/C_6H_4O_2$	127.04/109.03	0.1	0.4
24	2,3-epoxy, 2-methyl-4-hexenedial*	$C_7H_8O_3$	141.05	0.1	0.2
25	2-hydroxy-5-methyl-pentenedial*	$C_7H_8O_5$	173.04	nd	0.2
26	4,5-dioxo-2-hexenoic acid*	$C_6H_6O_4$	143.03	nd	0.2
27	5-hydroxy-6,4-dioxo-2-heptenal*	$C_7H_8O_4$	157.05	nd	0.3

Table AV.4. *Gas and particle phase main products (concentration of product/consumed VOC (ppbC/ppbC)) found in toluene photoxidation for experiments at 21°C.*

n°	Possible compound(s)	Formula	Protonated m/z	% gas phase	% particle phase
1	Methylglyoxal	$C_3H_4O_2/C_2H_4O$	73.028/45.033	5.4	0.1
2	Maleic anhydride	$C_4H_2O_3/C_4H_5O_4$	99.01/ hydrate at 117.02	6.3	<0.1
3	Acetic acid/Hydroxyacetaldehyde	$C_2H_4O_2$	61.028	3.5	0.1
4	Formic acid	CH_2O_2	47.013	2.5	< 0.1
5	Nitrocresols (structural isomers)	$C_7H_7NO_3$	154.05	1.7	<0.1
6	Benzaldehyde	C_7H_6O	107.05	3.7	nd
7	Nitrotoluene	$C_7H_7NO_2$	138.06	3.0	Nd
8	Cresols (all isomers)	C_7H_8O	109.06	2.4	nd
9	Benzoic acid*	$C_7H_6O_2$ /C_7H_4O	123.04 /105.04	1.7	<0.1
10	4-oxo-2-pentenal*	$C_5H_6O_2/C_5H_4O$	99.046/81.035	2.0	0.1
11	methyl furandione*	$C_5H_4O_3$	113.02	0.7	<0.1
12	2-butenedial	$C_4H_4O_2$	85.031	1.1	<0.1
13	Nitrophenol	$C_6H_5NO_3$	140.04	0.4	<0.1
14	2-hydroxy-1,3-propanedial*	$C_3H_4O_3/C_3H_2O_2$	89.026/71.016	0.5	0.1
15	4-Oxo-2-pentenoic acid*	$C_5H_6O_3/C_5H_4O_2$	115.04/97.032	0.9	0.1
16	4-oxo-2-butenoic-acid*	$C_4H_4O_3$ /$C_4H_2O_2$	101.03/83.012	0.7	<0.1
17	2-oxo-3-hydroxybutanedial*	$C_4H_4O_4$	117.02	0.4	<0.1
18	Butan-1,4-dial*	$C_4H_6O_2$	87.046	0.5	<0.1
19	6-hydroxy-2-methyl, 1,4,5 trioxo-2 cyclohexene*	$C_7H_6O_4$	155.03	0.1	0.1
20	methyl-oxo-pentenoic acid*	$C_6H_8O_3/C_6H_6O_2$	129.06/ part of 111.04	0.3	<0.1
21	2-hydroxy-3-oxobutanal*	$C_4H_6O_3$ /$C_4H_4O_2$	103.04/ possible contribution 85.031	1.2	0.1
22	5-Methylfurfural*	$C_6H_6O_2$	111.04	0.3	<0.1
23	5-Hydroxymethylfurfural*	$C_6H_6O_3/C_6H_4O_2$	127.04/109.03	0.2	0.1
24	2,3-epoxy, 2-methyl-4-hexenedial*	$C_7H_8O_3$	141.05	0.1	<0.1
25	2-hydroxy-5-methyl-pentenedial*	$C_7H_8O_5$	173.04	nd	<0.1
26	4,5-dioxo-2-hexenoic acid*	$C_6H_6O_4$	143.03	Nd	<0.1
27	5-hydroxy-6,4-dioxo-2-heptenal*	$C_7H_8O_4$	157.05	nd	<0.1

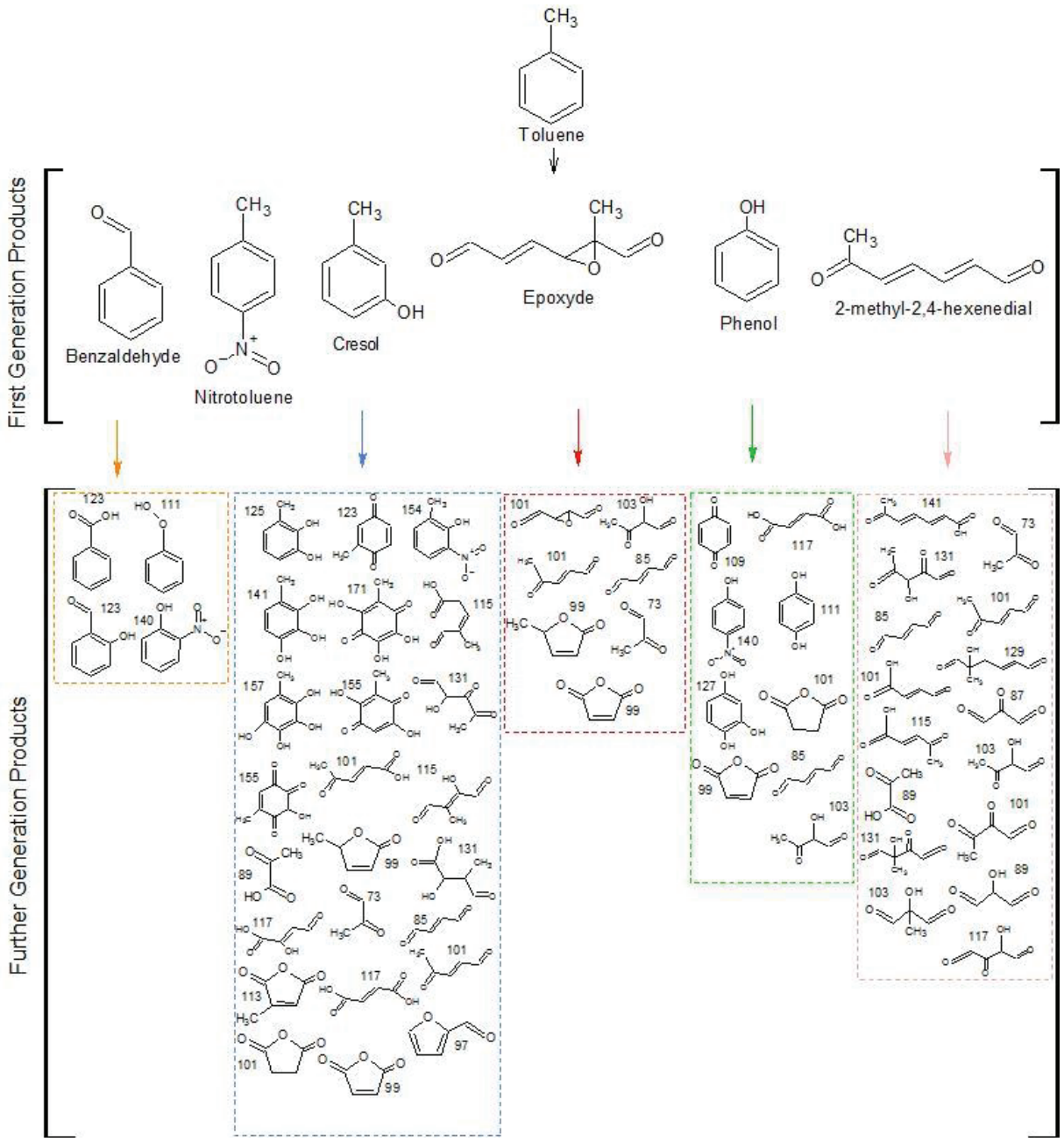

Figure AV.1. *Proposed first generation products and tentative further products for toluene photoxidation based on experimental analysis and previous literature.*

Table AV.5. *Gas and particle phase products (concentration of product/concentration total product formed (ppbC/ppbC)) found in naphthalene photoxidation for experiments at 7°C.*

n°	Possible compound(s)	Formula	Protonated m/z	% gas phase	% particle phase
1	Cinnamic acid	$C_9H_8O_2$	149.06	14.5	0.7
2	Glyoxylic acid or fragment	$C_3H_6O_2$	75.044	7.2	0.6
3	Phthalic anhydride	$C_8H_4O_3/C_8H_2O_2$	149.02/131.01	6.4	11.2
4	Fragment	$C_2H_4O/C_2H_6O_2$	45.033/63.044	5.5	9.1
5	1, 4-naphthoquinone 2,3-oxide	$C_{10}H_6O_3/C_{10}H_4O_2$	175.04/157.03	4.9	5.3
6	Phthalic acid	$C_8H_6O_4$	167.03	3.7	2.3
7	2-formylphenyl acrylic acid*	$C_{10}H_8O_3$	177.05	1.6	17.4
8	Naphtoquinone	$C_{10}H_6O_2/C_{10}H_4O$	159.04/141.03	1.3	5.1
9	Coumaric acid*	$C_9H_8O_3/C_9H_6O_2$	165.05/147.04	3.4	3.0
10	Hydroxy phthalic anhydride	$C_8H_4O_4/C_8H_2O_3$	165.02/147.01	3.1	3.0
11	2-formylcinnamaldehyde	$C_{10}H_8O_2/C_{10}H_6O$	161.06/143.05	2.9	3.9
12	Phthalaldehydic acid *	$C_8H_6O_3/C_8H_4O_2$	151.04/133.03	2.9	2.6
13	Formic acid	CH_2O_2	47.013	2.4	1.2
14	Phthalaldehyde	$C_8H_6O_2/C_8H_4O$	135.04/117.03	2.3	2.5
15	2-hydroxy-1,3-propanedial*	$C_3H_4O_3/C_3H_2O_2$	89.023/71.012	2.2	0.6
16	Hexano-2,5-dione*	$C_6H_{10}O_2/C_6H_8O$	115.08/97.064	1.3	0.8
17	2-butenedial	$C_4H_4O_2$	85.028	1.3	0.5
18	Hydroxybenzoic acid*	$C_7H_6O_3/C_6H_6O$	139.04/95.049	1.20	0.4
19	4-oxo-pentanal*	$C_5H_8O_2/C_5H_6O$	101.06/83.049	1.1	1.1
20	Nitrophenol*	$C_6H_5NO_3/C_6H_3NO_2$	140.03/122.02	1.0	0.2
21	Nitronaphtol	$C_{10}H_7NO_3$	190.05	nd	2.4
22	Acetic acid*	$C_2H_4O_2$	61.028	nd	2.8
23	Diacetylbenzene*	$C_{10}H_{10}O_2$	163.08	nd	3.4

Table AV.6. *Gas phase main products (concentration of product/concentration total product (ppbC/ppbC)) found in naphthalene photoxidation for experiments at 21°C.*

n°	Possible compound(s)	Formula	Protonated m/z	% gas phase
1	Cinnamic acid	$C_9H_8O_2$	149.06	18.9
2	Glyoxylic acid or fragment	$C_3H_6O_2$	75.044	5.7
3	Phthalic anhydride	$C_8H_4O_3/C_8H_2O_2$	149.02/131.01	9.9
4	Fragment	$C_2H_4O/C_2H_6O_2$	45.033/63.044	9.4
5	1, 4-naphthoquinone 2,3-oxide	$C_{10}H_6O_3/C_{10}H_4O_2$	175.04/157.03	0.2
6	Phthalic acid	$C_8H_6O_4$	167.03	3.5
7	2-formylphenyl acrylic acid*	$C_{10}H_8O_3$	177.05	0.3
8	Naphtoquinone	$C_{10}H_6O_2/C_{10}H_4O$	159.04/141.03	0.3
9	Coumaric acid*	$C_9H_8O_3/C_9H_6O_2$	165.05/147.04	0.7
10	Hydroxy phthalic anhydride	$C_8H_4O_4/C_8H_2O_3$	165.02/147.01	0.6
11	2-formylcinnamaldehyde	$C_{10}H_8O_2/C_{10}H_6O$	161.06/143.05	0.2
12	Phthalaldehydic acid *	$C_8H_6O_3/C_8H_4O_2$	151.04/133.03	0.7
13	Formic acid	CH_2O_2	47.013	1.6
14	Phthalaldehyde	$C_8H_6O_2/C_8H_4O$	135.04/117.03	3.9
15	2-hydroxy-1,3-propanedial*	$C_3H_4O_3/C_3H_2O_2$	89.023/71.012	1.4
16	Hexano-2,5-dione*	$C_6H_{10}O_2/C_6H_8O$	115.08/97.064	0.8
17	2-butenedial	$C_4H_4O_2$	85.028	0.8
18	Hydroxybenzoic acid*	$C_7H_6O_3/C_6H_6O$	139.04/95.049	0.4
19	4-oxo-pentanal*	$C_5H_8O_2/C_5H_6O$	101.06/83.049	0.4
20	Nitrophenol*	$C_6H_5NO_3/C_6H_3NO_2$	140.03/122.02	1.0
21	Nitronaphtol	$C_{10}H_7NO_3$	190.05	1.0
22	Acetic acid*	$C_2H_4O_2$	61.028	Nd
23	Diacetylbenzene*	$C_{10}H_{10}O_2$	163.08	Nd

Table AV.7. *Gas phase main products (concentration of product/consumed VOC (ppbC/ppbC)) found in naphthalene photoxidation for experiments at 7°C.*

n°	Possible compound(s)	Formula	Protonated m/z	% gas phase	% particle phase
1	Cinnamic acid	$C_9H_8O_2$	149.06	11.1	0.1
2	Glyoxylic acid or fragment	$C_3H_6O_2$	75.044	5.5	0.1
3	Phthalic anhydride	$C_8H_4O_3/C_8H_2O_2$	149.02/131.01	5.0	2.3
4	Fragment	$C_2H_4O/C_2H_6O_2$	45.033/63.044	4.3	1.8
5	1, 4-naphthoquinone 2,3-oxide	$C_{10}H_6O_3/C_{10}H_4O_2$	175.04/157.03	3.7	1.0
6	Phthalic acid	$C_8H_6O_4$	167.03	2.8	0.4
7	2-formylphenyl acrylic acid*	$C_{10}H_8O_3$	177.05	1.2	3.2
8	Naphtoquinone	$C_{10}H_6O_2/C_{10}H_4O$	159.04/141.03	1.0	1.0
9	Coumaric acid*	$C_9H_8O_3/C_9H_6O_2$	165.05/147.04	2.6	0.5
10	Hydroxy phthalic anhydride	$C_8H_4O_4/C_8H_2O_3$	165.02/147.01	2.3	0.5
11	2-formylcinnamaldehyde	$C_{10}H_8O_2/C_{10}H_6O$	161.06/143.05	2.2	0.8
12	Phthalaldehydic acid *	$C_8H_6O_3/C_8H_4O_2$	151.04/133.03	2.2	0.5
13	Formic acid	CH_2O_2	47.013	1.8	0.2
14	Phthalaldehyde	$C_8H_6O_2/C_8H_4O$	135.04/117.03	0.9	0.2
15	2-hydroxy-1,3-propanedial*	$C_3H_4O_3/C_3H_2O_2$	89.023/71.012	1.7	0.1
16	Hexano-2,5-dione*	$C_6H_{10}O_2/C_6H_8O$	115.08/97.064	1.0	0.2
17	2-butenedial	$C_4H_4O_2$	85.028	1.0	0.1
18	Hydroxybenzoic acid*	$C_7H_6O_3/C_6H_6O$	139.04/95.049	0.9	0.1
19	4-oxo-pentanal*	$C_5H_8O_2/C_5H_6O$	101.06/83.049	0.8	0.2
20	Nitrophenol*	$C_6H_5NO_3/C_6H_3NO_2$	140.03/122.02	0.8	<0.1
21	Nitronaphtol	$C_{10}H_7NO_3$	190.05	<0.1	0.5
22	Acetic acid*	$C_2H_4O_2$	61.028	nd	0.6
23	Diacetylbenzene*	$C_{10}H_{10}O_2$	163.08	nd	0.7

Table AV.8. *Gas phase main products (concentration of product/consumed VOC (ppbC/ppbC)) found in naphthalene photoxidation for experiments at 21°C.*

n°	Possible compound(s)	Formula	Protonated m/z	% gas phase
1	Cinnamic acid	$C_9H_8O_2$	149.06	11.5
2	Glyoxylic acid or fragment	$C_3H_6O_2$	75.044	3.5
3	Phthalic anhydride	$C_8H_4O_3/C_8H_2O_2$	149.02/131.01	6.4
4	Fragment	$C_2H_4O/C_2H_6O_2$	45.033/63.044	5.7
5	1, 4-naphthoquinone 2,3-oxide	$C_{10}H_6O_3/C_{10}H_4O_2$	175.04/157.03	0.1
6	Phthalic acid	$C_8H_6O_4$	167.03	2 .1
7	2-formylphenyl acrylic acid*	$C_{10}H_8O_3$	177.05	0.2
8	Naphtoquinone	$C_{10}H_6O_2/C_{10}H_4O$	159.04/141.03	0.2
9	Coumaric acid*	$C_9H_8O_3/C_9H_6O_2$	165.05/147.04	0.4
10	Hydroxy phthalic anhydride	$C_8H_4O_4/C_8H_2O_3$	165.02/147.01	0.4
11	2-formylcinnamaldehyde	$C_{10}H_8O_2/C_{10}H_6O$	161.06/143.05	0.1
12	Phthalaldehydic acid *	$C_8H_6O_3/C_8H_4O_2$	151.04/133.03	0.4
13	Formic acid	CH_2O_2	47.013	1.0
14	Phthalaldehyde	$C_8H_6O_2/C_8H_4O$	135.04/117.03	1.5
15	2-hydroxy-1,3-propanedial*	$C_3H_4O_3/C_3H_2O_2$	89.023/71.012	0.8
16	Hexano-2,5-dione*	$C_6H_{10}O_2/C_6H_8O$	115.08/97.064	0.5
17	2-butenedial	$C_4H_4O_2$	85.028	0.5
18	Hydroxybenzoic acid*	$C_7H_6O_3/C_6H_6O$	139.04/95.049	0.2
19	4-oxo-pentanal*	$C_5H_8O_2/C_5H_6O$	101.06/83.049	0.3
20	Nitrophenol*	$C_6H_5NO_3/C_6H_3NO_2$	140.03/122.02	0.6
21	Nitronaphtol	$C_{10}H_7NO_3$	190.05	<0.1
22	Acetic acid*	$C_2H_4O_2$	61.028	nd
23	Diacetylbenzene*	$C_{10}H_{10}O_2$	163.08	nd

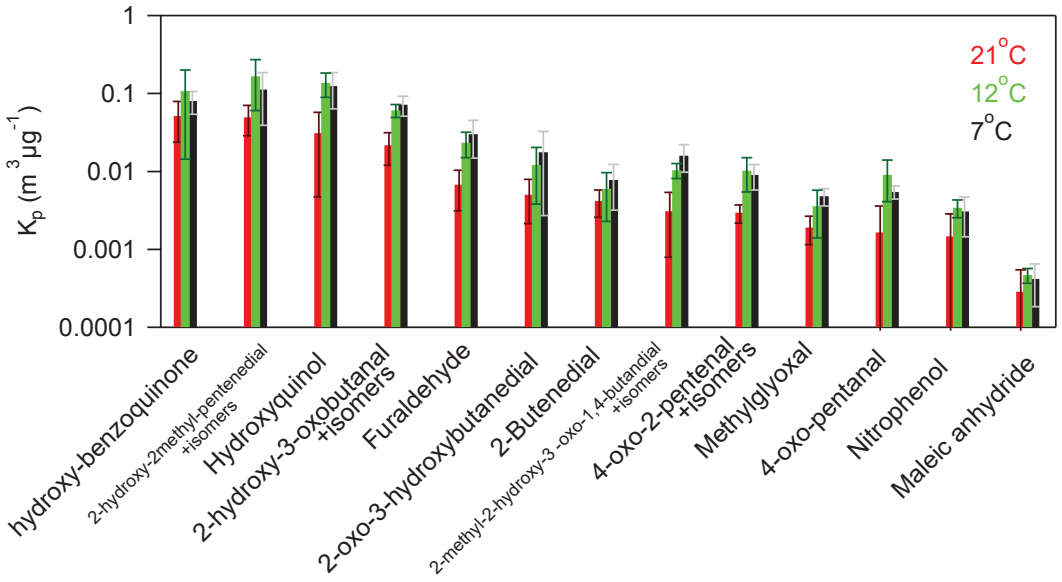

Figure AV.2. Experimental K_p values of m/z's, where a unique compound or a set of isomers compounds were assigned. The error bars correspond to the one standard deviation of the average.

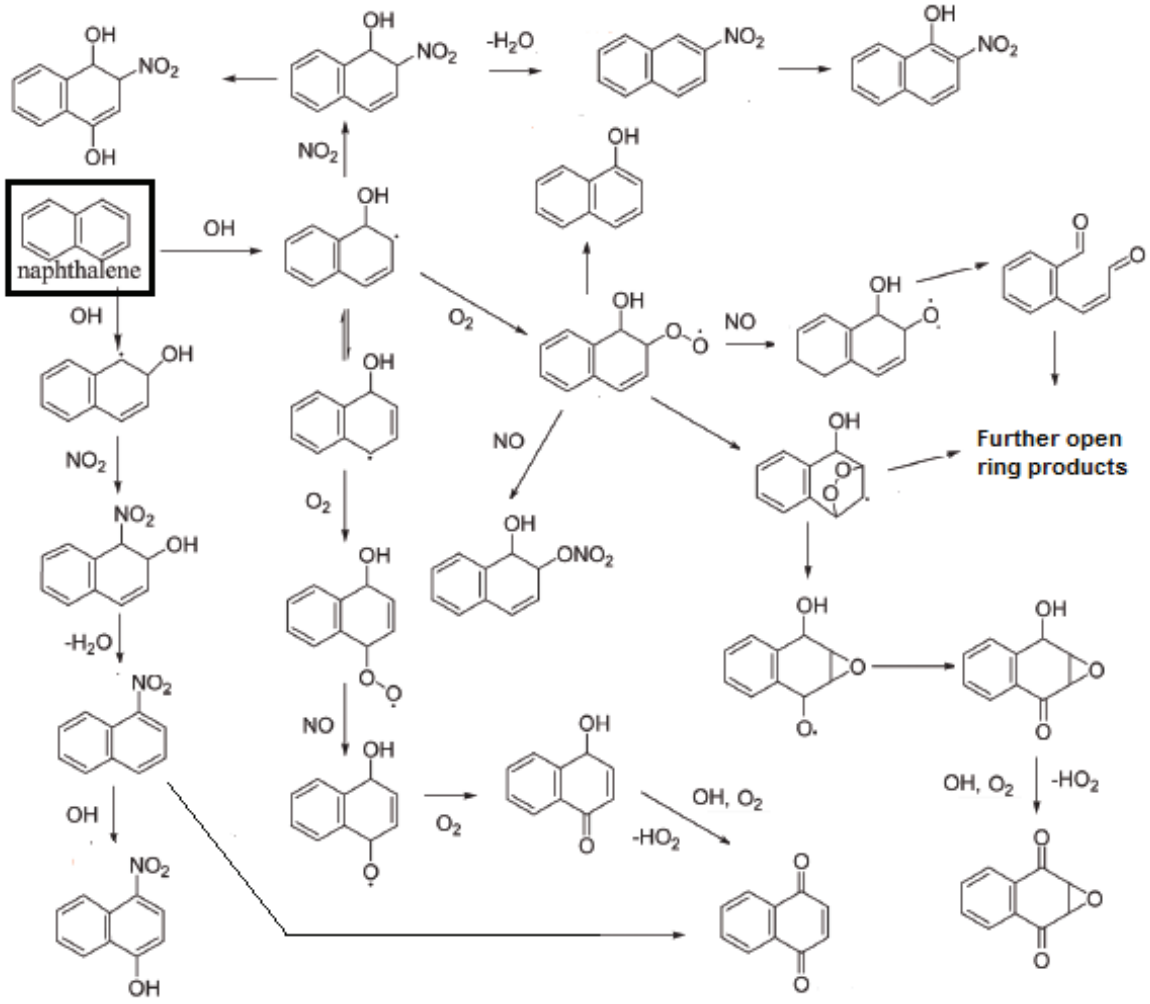

Figure AV.3. *Simplified naphthalene degradation mechanism, adapted from Kautzman et al.2010.*

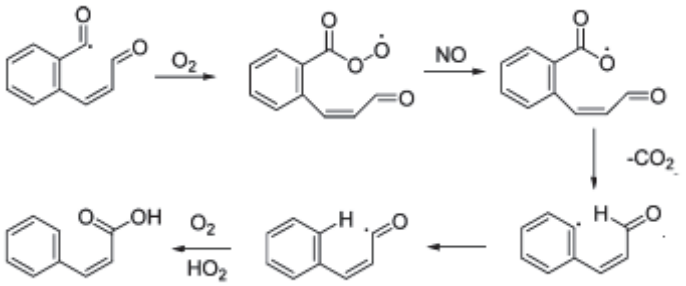

Figure AV.4. Possible mechanism for the formation of C_7 and C_9 compounds. Source: Kautzman et al. 2010.

Table AV.9. *Gas and particle phase products (concentration of product/concentration total product formed (ppbC/ppbC)) found in cyclohexane photoxidation for experiments at 7°C without NOx addition.*

n°	Possible compound(s)	Formula	Protonated m/z	% gas phase	% particle phase
1	Cyclohexanedione	$C_6H_8O_2$	113.06	31.7	5.8
2	Acetic acid/fragment	$C_2H_4O_2$	61.028	20.7	nd
3	Acetaldehyde /fragment	$C_2H_4O/C_2H_6O_2$	45.033/63.044	16.4	11.8
4	Cyclohexanone	$C_6H_{10}O$	99.080	6.4	2.2
5	Formic acid	CH_2O_2/CH_4O_3	47.012/65.022	4.7	12.4
6	Cyclohexanol	$C_6H_{12}O$	101.10	1.7	10.2
7	hexan-1,6-dial/hydroxy cyclohexanone	$C_6H_{10}O_2/C_6H_8O$	115.07/97.062	2.1	8.0
8	2,4-dihydroxybutanal*	$C_4H_6O_2/C_4H_4O$	87.044/69.031	1.4	5.2
9	pentan-1,5-dial	$C_4H_4O_3/C_4H_2O_2$	101.02/83.012	1.1	5.0
10	2-hydroxy-1,3-propanedial*	$C_4H_8O_2/C_4H_6O$	89.059/71.049	0.7	5.3
11	2-hydroxy-3-oxobutanal*	$C_4H_6O_3/C_4H_4O_2$	103.04/85.028	1.0	4.4
12	methyl-oxo-pentenoic acid*	$C_6H_8O_3/C_5H_8O$	129.05/85.064	0.6	3.8
13	3-hydroxypentane-1,5-dial	$C_5H_6O_3/C_5H_4O_2$	115.04/97.028	1.5	3.7
14	Formaldehyde /fragment	CH_2O	31.018	2.4	1.0
15	4-oxo-pentanal	$C_5H_8O_2/C_5H_6O$	101.06/83.049	0.40	2.2

Table AV.10. *Gas and particle phase main products (concentration of product/concentration total product (ppbC/ppbC)) found in cyclohexane photoxidation for experiments at 7°C with NOx addition.*

n°	Possible compound(s)	Formula	Protonated m/z	% gas phase	% particle phase
1	Cyclohexanedione	$C_6H_8O_2$	113.06	16.4	5.8
2	Acetic acid/fragment	$C_2H_4O_2$	61.028	31.5	8.2
3	Acetaldehyde /fragment	$C_2H_4O/C_2H_6O_2$	45.033/63.044	15.4	26.8
4	Cyclohexanone	$C_6H_{10}O$	99.080	5.7	1.4
5	Formic acid	CH_2O_2/CH_4O_3	47.012/65.022	7.3	12.6
6	Cyclohexanol	$C_6H_{12}O$	101.10	0.9	7.2
7	hexan-1,6-dial/hydroxy cyclohexanone	$C_6H_{10}O_2/C_6H_8O$	115.07/97.062	1.0	5.6
8	2,4-dihydroxybutanal*	$C_4H_6O_2/C_4H_4O$	87.044/69.031	2.5	3.4
9	pentan-1,5-dial	$C_4H_4O_3/C_4H_2O_2$	101.02/83.012	0.9	4.0
10	2-hydroxy-1,3-propanedial*	$C_4H_8O_2/C_4H_6O$	89.059/71.049	0.9	3.5
11	2-hydroxy-3-oxobutanal*	$C_4H_6O_3/C_4H_4O_2$	103.04/85.028	1.0	3.1
12	methyl-oxo-pentenoic acid*	$C_6H_8O_3/C_5H_8O$	129.05/85.064	0.8	3.2
13	3-hydroxypentane-1,5-dial	$C_5H_6O_3/C_5H_4O_2$	115.04/97.028	0.10	0.8
14	Formaldehyde /fragment	CH_2O	31.018	2.2	1.1
15	4-oxo-pentanal	$C_5H_8O_2/C_5H_6O$	101.06/83.049	1.7	1.9

Table AV.11. *Gas and particle phase main products (concentration of product/consumed VOC (ppbC/ppbC)) found in cyclohexane photoxidation for experiments at 7°C without NOx addition.*

n°	Possible compound(s)	Formula	Protonated m/z	% gas phase	% particle phase
1	Cyclohexanedione	$C_6H_8O_2$	113.06	22.6	0.1
2	Acetic acid/fragment	$C_2H_4O_2$	61.028	14.7	nd
3	Acetaldehyde /fragment	$C_2H_4O/C_2H_6O_2$	45.033/63.044	11.7	0.2
4	Cyclohexanone	$C_6H_{10}O$	99.080	4.6	<0.1
5	Formic acid	CH_2O_2/CH_4O_3	47.012/65.022	3.3	0.2
6	Cyclohexanol	$C_6H_{12}O$	101.10	1.2	0.1
7	hexan-1,6-dial/hydroxy cyclohexanone	$C_6H_{10}O_2/C_6H_8O$	115.07/97.062	1.5	0.1
8	2,4-dihydroxybutanal*	$C_4H_6O_2/C_4H_4O$	87.044/69.031	1.0	0.1
9	pentan-1,5-dial	$C_4H_4O_3/C_4H_2O_2$	101.02/83.012	0.8	0.1
10	2-hydroxy-1,3-propanedial*	$C_4H_8O_2/C_4H_6O$	89.059/71.049	0.5	0.1
11	2-hydroxy-3-oxobutanal*	$C_4H_6O_3/C_4H_4O_2$	103.04/85.028	0.7	0.1
12	methyl-oxo-pentenoic acid*	$C_6H_8O_3/C_5H_8O$	129.05/85.064	0.6	0.1
13	3-hydroxypentane-1,5-dial	$C_5H_6O_3/C_5H_4O_2$	115.04/97.028	1.0	0.1
14	Formaldehyde /fragment	CH_2O	31.018	1.7	<0.1
15	4-oxo-pentanal	$C_5H_8O_2/C_5H_6O$	101.06/83.049	0.3	<0.1

Table AV.12. *Gas and particle phase main products (concentration of product/consumed VOC (ppbC/ppbC)) found in cyclohexane photoxidation for experiments at 7°C with NOx addition.*

n°	Possible compound(s)	Formula	Protonated m/z	% gas phase	% particle phase
1	Cyclohexanedione	$C_6H_8O_2$	113.06	16.0	0.1
2	Acetic acid/fragment	$C_2H_4O_2$	61.028	31.0	0.1
3	Acetaldehyde /fragment	$C_2H_4O/C_2H_6O_2$	45.033/63.044	15.2	0.3
4	Cyclohexanone	$C_6H_{10}O$	99.080	5.6	<0.1
5	Formic acid	CH_2O_2/CH_4O_3	47.012/65.022	7.2	0.1
6	Cyclohexanol	$C_6H_{12}O$	101.10	0.9	0.1
7	hexan-1,6-dial/hydroxy cyclohexanone	$C_6H_{10}O_2/C_6H_8O$	115.07/97.062	1.0	0.1
8	2,4-dihydroxybutanal*	$C_4H_6O_2/C_4H_4O$	87.044/69.031	2.5	<0.1
9	pentan-1,5-dial	$C_4H_4O_3/C_4H_2O_2$	101.02/83.012	0.9	<0.1
10	2-hydroxy-1,3-propanedial*	$C_4H_8O_2/C_4H_6O$	89.059/71.049	1.0	<0.1
11	2-hydroxy-3-oxobutanal*	$C_4H_6O_3/C_4H_4O_2$	103.04/85.028	1.0	<0.1
12	methyl-oxo-pentenoic acid*	$C_6H_8O_3/C_5H_8O$	129.05/85.064	1.2	<0.1
13	3-hydroxypentane-1,5-dial	$C_5H_6O_3/C_5H_4O_2$	115.04/97.028	0.1	<0.1
14	Formaldehyde /fragment	CH_2O	31.018	2.2	<0.1
15	4-oxo-pentanal	$C_5H_8O_2/C_5H_6O$	101.06/83.049	1.7	<0.1

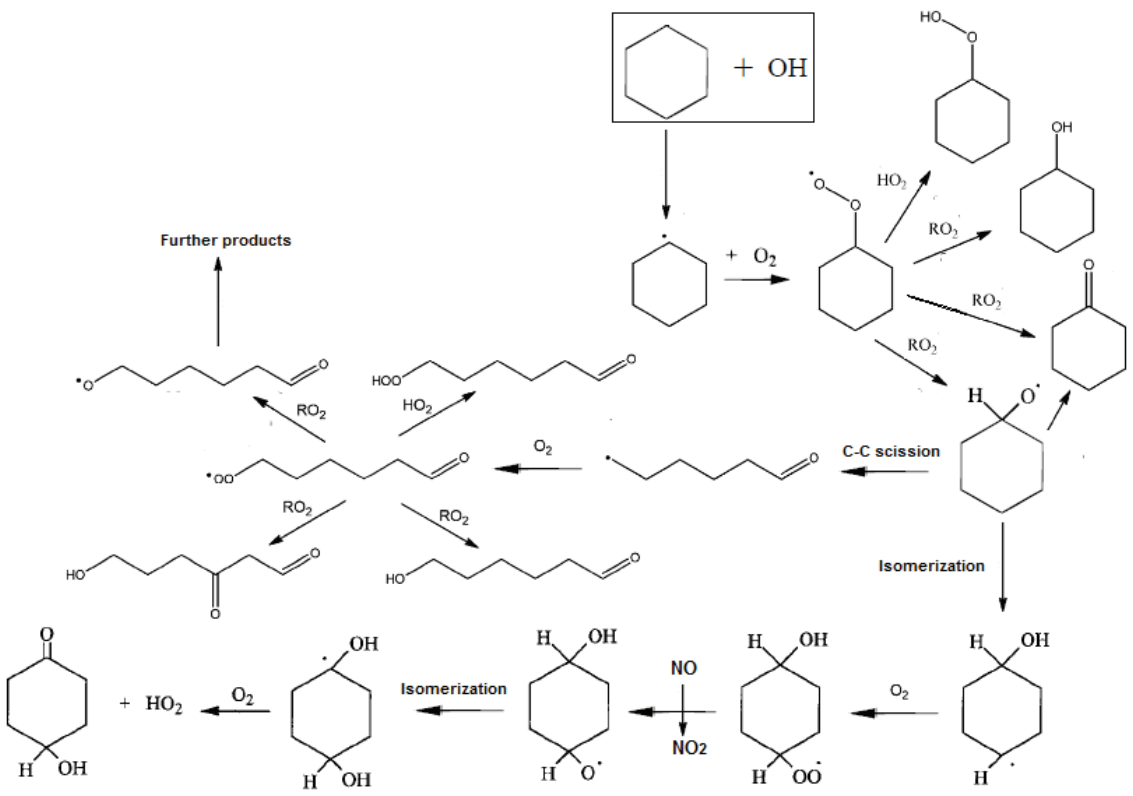

Figure AV.5. Simplified cyclohexane degradation mechanism and first generation product formation, adapted from Alam et al., 2011 and Lim and Ziemann, 2009

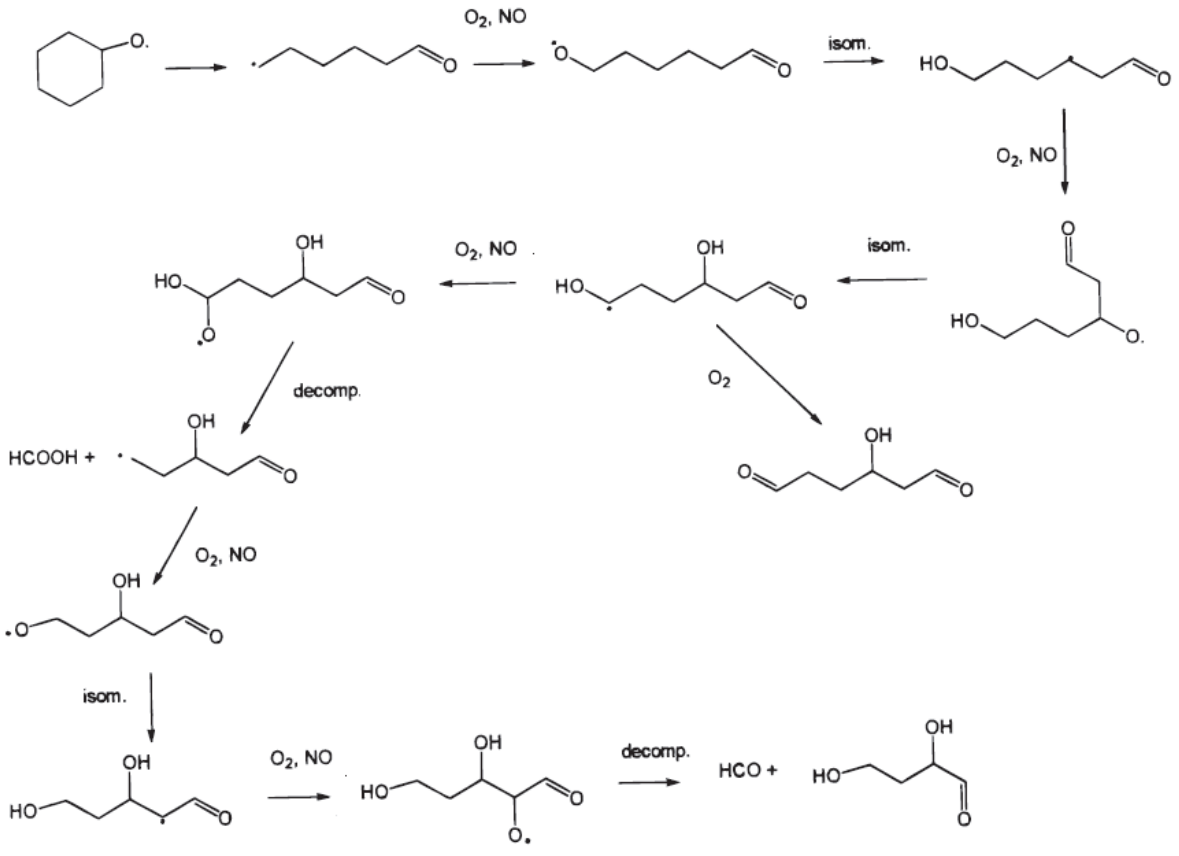

Figure AV.6. Possible route to formic acid formation from cyclohexoxy radical. Source: Orlando et al.,2000

Table AV.13. Gas and *particle phase main products (concentration of product/concentration total product (ppbC/ppbC)) found in nonane photoxidation for experiments at 7°C.*

n°	Possible compound(s)	Formula	Protonated m/z	% gas phase	% particle phase
1	Propanoic acid	$C_3H_6O_2/C_3H_4O$	75.044/57.033	9.3	7.9
2	Pentaneperoxoic acid	$C_5H_{10}O_3/C_5H_8O_2$	119.07/101.06	7.3	1.4
3	Acetaldehyde	$C_2H_4O/C_2H_6O_2$	45.033/63.044	6.9	3.5
4	Heptanal	$C_7H_{14}O/C_7H_{12}$	115.11/97.101	5.5	1.1
5	Hexaneperoxoic acid	$C_6H_{12}O_3/C_6H_{10}O_2$	133.08/115.07	5.3	1.3
6	Formic acid	CH_2O_2	47.01	4.5	6.9
7	Butaneperoxoic acid	$C_4H_8O_3/C_4H_6O_2$	105.05/87.044	3.5	4.5
8	Butanoic acid	$C_4H_8O_2/C_4H_6O$	89.059/71.049	3.5	2.8
9	Nonanone	$C_9H_{18}O/C_9H_{16}$	143.14/125.10	3.1	1.5
10	Pentanal	$C_5H_{10}O/C_5H_8$	87.08/69.069	2.9	2.5
11	1-ethyl, 4-propyl dihydrofuran	$C_9H_{16}O$	141.13	2.3	0.3
12	Octanal	$C_8H_{16}O/C_8H_{14}$	129.13/111.12	2.2	1.6
13	Pentanoic acid	$C_5H_{10}O_2/C_5H_8O$	103.07/85.064	2.1	1.5
14	Heptaneperoxoic acid	$C_7H_{14}O_3/C_7H_{12}O_2$	147.10/129.09	1.8	0.5
15	Formaldehyde	CH_2O	31.02	1.7	1.7
16	Propaneperoxoic acid	$C_3H_6O_3/C_2H_6O/C_3H_4O_2$	91.038/73.028	1.5	2.7
17	Hexanal	$C_6H_{12}O/C_6H_{10}$	101.10/83.085	1.1	1.6
18	4-oxo-2-pentenal*	$C_5H_6O_2/C_5H_4O$	99.044/81.033	0.9	4.4
19	Acetic acid/fragment	$C_2H_4O_2$	61.030	nd	10.1

Table AV.14. Gas and *particle phase main products (concentration of product/concentration total product (ppbC/ppbC)) found in nonane photoxidation for experiments at 21°C.*

n°	Possible compound(s)	Formula	Protonated m/z	% gas phase	% particle phase
1	Propanoic acid	$C_3H_6O_2/C_3H_4O$	75.044/57.033	11.7	6.9
2	Pentaneperoxoic acid	$C_5H_{10}O_3/C_5H_8O_2$	119.07/101.06	4.6	1.0
3	Acetaldehyde	$C_2H_4O/C_2H_6O_2$	45.033/63.044	11.2	3.6
4	Heptanal	$C_7H_{14}O/C_7H_{12}$	115.11/97.101	1.9	0.9
5	Hexaneperoxoic acid	$C_6H_{12}O_3/C_6H_{10}O_2$	133.08/115.07	1.8	1.2
6	Formic acid	CH_2O_2	47.01	2.5	7.7
7	Butaneperoxoic acid	$C_4H_8O_3/C_4H_6O_2$	105.05/87.044	4.3	4.2
8	Butanoic acid	$C_4H_8O_2/C_4H_6O$	89.059/71.049	4.1	2.8
9	Nonanone	$C_9H_{18}O/C_9H_{16}$	143.14/125.10	3.4	1.4
10	Pentanal	$C_5H_{10}O/C_5H_8$	87.08/69.069	2.8	2.3
11	1-ethyl, 4-propyl dihydrofuran	$C_9H_{16}O$	141.13	1.7	0.4
12	Octanal	$C_8H_{16}O/C_8H_{14}$	129.13/111.12	0.4	2.2
13	Pentanoic acid	$C_5H_{10}O_2/C_5H_8O$	103.07/85.064	2.6	1.1
14	Heptaneperoxoic acid	$C_7H_{14}O_3/C_7H_{12}O_2$	147.10/129.09	0.3	0.8
15	Formaldehyde	CH_2O	31.02	2.2	1.7
16	Propaneperoxoic acid	$C_3H_6O_3/C_2H_6O/C_3H_4O_2$	91.038/73.028	2.4	2.6
17	Hexanal	$C_6H_{12}O/C_6H_{10}$	101.10/83.085	1.1	1.6
18	4-oxo-2-pentenal*	$C_5H_6O_2/C_5H_4O/C_5H_2$	99.044/81.033	4.0	4.4
19	Butanal	C_4H_8O	61.030	0.9	0.8
20	Acetic acid/fragment	$C_2H_4O_2$	75.044/57.033	nd	11.6

* Or isomers

Table AV.15. Gas and *particle phase main products (concentration of product/consumed VOC (ppbC/ppbC)) found in nonane photoxidation for experiments at 7°C.*

n°	Possible compound(s)	Formula	Protonated m/z	% gas phase	% particle phase
1	Propanoic acid	$C_3H_6O_2/C_3H_4O$	75.044/57.033	1.5	<0.1
2	Pentaneperoxoic acid	$C_5H_{10}O_3/C_5H_8O_2$	119.07/101.06	2.3	<0.1
3	Acetaldehyde	$C_2H_4O/C_2H_6O_2$	45.033/63.044	1.1	<0.1
4	Heptanal	$C_7H_{14}O/C_7H_{12}$	115.11/97.101	0.9	<0.1
5	Hexaneperoxoic acid	$C_6H_{12}O_3/C_6H_{10}O_2$	133.08/115.07	2.0	<0.1
6	Formic acid	CH_2O_2	47.01	0.7	<0.1
7	Butaneperoxoic acid	$C_4H_8O_3/C_4H_6O_2$	105.05/87.044	0.7	<0.1
8	Butanoic acid	$C_4H_8O_2/C_4H_6O$	89.059/71.049	0.4	<0.1
9	Nonanone	$C_9H_{18}O/C_9H_{16}$	143.14/125.10	0.5	<0.1
10	Pentanal	$C_5H_{10}O/C_5H_8$	87.08/69.069	0.3	<0.1
11	1-ethyl, 4-propyl dihydrofuran	$C_9H_{16}O$	141.13	0.4	<0.1
12	Octanal	$C_8H_{16}O/C_8H_{14}$	129.13/111.12	0.4	<0.1
13	Pentanoic acid	$C_5H_{10}O_2/C_5H_8O$	103.07/85.064	0.4	<0.1
14	Heptaneperoxoic acid	$C_7H_{14}O_3/C_7H_{12}O_2$	147.10/129.09	1.3	<0.1
15	Formaldehyde	CH_2O	31.02	0.3	<0.1
16	Propaneperoxoic acid	$C_3H_6O_3/C_2H_6O/C_3H_4O_2$	91.038/73.028	0.2	<0.1
17	Hexanal	$C_6H_{12}O/C_6H_{10}$	101.10/83.085	0.2	<0.1
18	4-oxo-2-pentenal*	$C_5H_6O_2/C_5H_4O/C_5H_2$	99.044/81.033	<0.1	<0.1
19	Butanal	C_4H_8O	61.030	0.1	<0.1
20	Acetic acid/fragment	$C_2H_4O_2$	75.044/57.033	<0.1	<0.1

* Or isomers

Table AV.16. Gas and *particle phase main products (concentration of product/consumed VOC (ppbC/ppbC)) found in nonane photoxidation for experiments at 21°C.*

n°	Possible compound(s)	Formula	Protonated m/z	% gas phase	% particle phase
1	Propanoic acid	$C_3H_6O_2/C_3H_4O$	75.044/57.033	1.2	<0.1
2	Pentaneperoxoic acid	$C_5H_{10}O_3/C_5H_8O_2$	119.07/101.06	1.2	<0.1
3	Acetaldehyde	$C_2H_4O/C_2H_6O_2$	45.033/63.044	1.1	<0.1
4	Heptanal	$C_7H_{14}O/C_7H_{12}$	115.11/97.101	0.2	<0.1
5	Hexaneperoxoic acid	$C_6H_{12}O_3/C_6H_{10}O_2$	133.08/115.07	1.0	<0.1
6	Formic acid	CH_2O_2	47.01	0.3	<0.1
7	Butaneperoxoic acid	$C_4H_8O_3/C_4H_6O_2$	105.05/87.044	0.5	<0.1
8	Butanoic acid	$C_4H_8O_2/C_4H_6O$	89.059/71.049	0.6	<0.1
9	Nonanone	$C_9H_{18}O/C_9H_{16}$	143.14/125.10	0.4	<0.1
10	Pentanal	$C_5H_{10}O/C_5H_8$	87.08/69.069	0.5	<0.1
11	1-ethyl, 4-propyl dihydrofuran	$C_9H_{16}O$	141.13	0.2	<0.1
12	Octanal	$C_8H_{16}O/C_8H_{14}$	129.13/111.12	<0.1	<0.1
13	Pentanoic acid	$C_5H_{10}O_2/C_5H_8O$	103.07/85.064	0.3	<0.1
14	Heptaneperoxoic acid	$C_7H_{14}O_3/C_7H_{12}O_2$	147.10/129.09	0.7	<0.1
15	Formaldehyde	CH_2O	31.02	0.2	<0.1
16	Propaneperoxoic acid	$C_3H_6O_3/C_2H_6O/C_3H_4O_2$	91.038/73.028	0.2	<0.1
17	Hexanal	$C_6H_{12}O/C_6H_{10}$	101.10/83.085	0.1	<0.1
18	4-oxo-2-pentenal*	$C_5H_6O_2/C_5H_4O/C_5H_2$	99.044/81.033	<0.1	<0.1
19	Butanal	C_4H_8O	61.030	0.1	<0.1
20	Acetic acid/fragment	$C_2H_4O_2$	75.044/57.033	<0.1	<0.1

* Or isomers

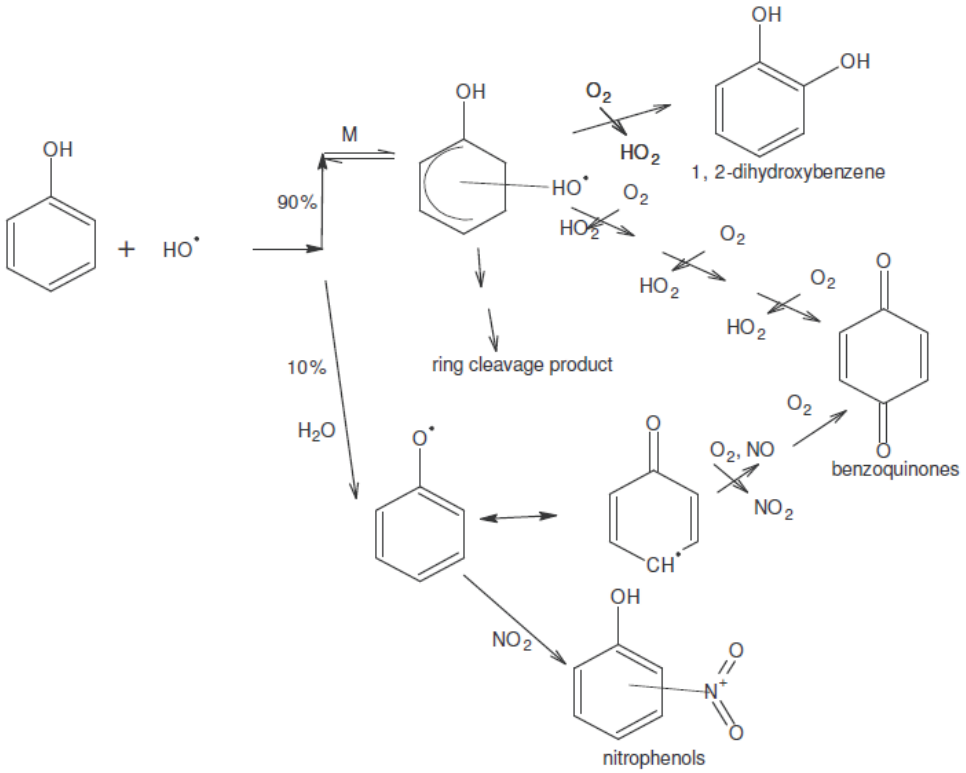

***Figure AV.7**. Proposed mechanism for first generation product formation from phenol photoxidation. Source: Olariu et al., 2002*

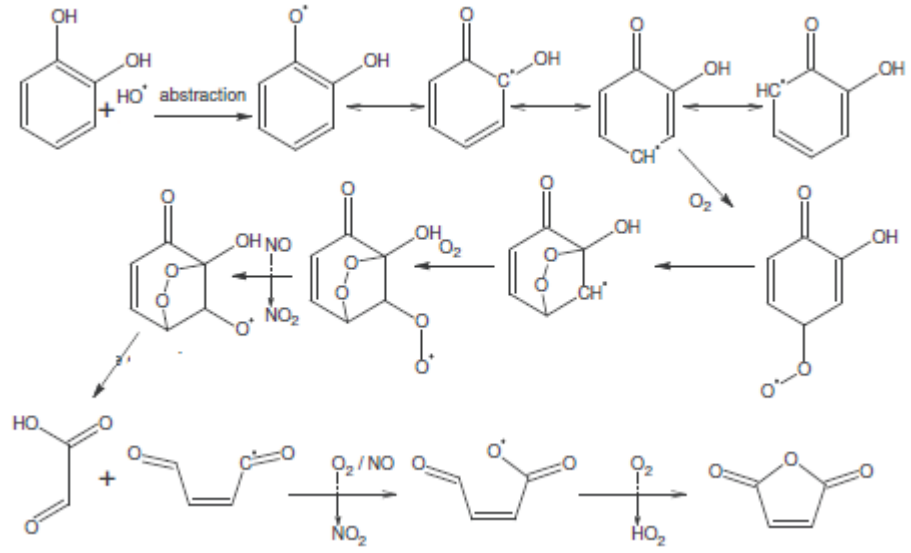

Figure AV.8. Formation mechanism of maleic anhydride from catechol. Source: Turpin et al., 2005

Table AV.17. *K rate (x10^{-9} cm s^{-1}) used for detected mass during PTRMS/CHARON analysis. Rests of masses have a k rate of 3.2 by default.*

m/z	k rate	m/z	k rate	m/z	k rate
18.034	3.270	**81.071**	1.952	**115.04**	3.222
31.018	3.027	**83.016**	3.108	**115.07**	3.325
32.996	2.742	**83.050**	3.241	**115.11**	3.417
33.034	3.039	**83.087**	1.972	**117.02**	3.128
41.038	1.563	**85.031**	3.130	**117.03**	3.403
43.019	3.047	**85.065**	3.259	**122.06**	3.395
43.054	1.583	**87.046**	3.152	**123.04**	3.358
44.024	3.035	**87.081**	3.277	**125.03**	3.279
44.058	1.593	**89.026**	3.035	**125.06**	3.373
45.034	3.064	**89.060**	3.173	**127.0**	3.185
47.013	2.892	**91.040**	3.059	**127.04**	3.287
47.050	3.082	**91.057**	2.049	**129.06**	3.304
48.014	2.883	**93.072**	2.068	**129.09**	3.392
51.009	2.692	**95.034**	2.963	**129.12**	3.472
57.070	1.719	**95.052**	3.310	**136.04**	3.326
59.049	3.117	**97.017**	2.832	**138.06**	3.342
61.030	2.972	**97.032**	3.213	**139.05**	3.353
61.065	3.137	**97.064**	3.327	**139.06**	3.340
63.026	3.180	**97.103**	2.108	**139.08**	3.434
63.045	2.996	**99.010**	3.108	**140.04**	3.316
63.056	2.994	**99.046**	3.233	**141.02**	3.279
71.016	3.040	**101.03**	3.119	**141.07**	2.534
71.050	3.191	**101.06**	3.239	**143.04**	3.296
71.087	1.855	**103.04**	3.140	**143.15**	3.532
73.030	3.064	**103.07**	3.257	**154.05**	3.382
73.063	3.211	**105.03**	3.343	**154.06**	3.568
74.029	3.059	**107.05**	3.359	**155.03**	3.350
75.026	1.893	**109.07**	3.374	**155.08**	2.670
75.046	3.087	**111.05**	3.292	**157.06**	3.365
77.026	2.931	**111.11**	2.244	**168.03**	3.377
77.058	3.087	**113.02**	3.203	**171.02**	3.361
77.070	3.085	**113.06**	3.309	**171.04**	3.360
79.054	1.932	**115.01**	3.106	**199.05**	3.097
81.035	3.222	**115.02**	3.388	**199.11**	3.679

Table AV.18. *References of pure compounds (>99 %, Sigma-Aldrich) for PTRMS gas phase and CHARON particulate phase. PTRMS configuration was: Pdrift 2.075 mbar; Tdrift= 120°C; Udrift= 395 V; E/N= 114 Td (PTRMS) ; E/N =108 Td (CHARON). For CHARON references, pure compound were used. The compounds were dissolved in water (if soluble). Some compounds was not detected in the particle phase probably for the reduced solubility.*

	Formula	m/z	Intensity PTRMS	Intensity CHARON
Methylglyoxal	$C_3H_5O_2$	74.029		3.6
	$C_3H_4O_2$	73.028		100.0
	C_2H_4O	45.045		13.1
5-Methylfurfural	$C_6H_6O_2$	111.04	100.0	100.0
	$C_6H_7O_2$	112.05		
	$C_6H_8O_2$	113.06		
	$C_6H_5O_2$	110.06	1.5	
	C_5H_6O	83.049	3.1	
	$C_5H_4O_2$	97.028	3.1	13.8
Catechol	$C_6H_4O_2$	109.03	100.0	100
	$C_6H_6O_2$	111.04	11.1	12.5
5-Hydroxymethylfurfural	$C_6H_7O_3$	128.04	6.5	
	$C_6H_6O_3$	127.04	100.0	
	$C_6H_5O_3$	126.02	3.3	
	$C_6H_4O_3$	125.02	58.0	
	$C_6H_4O_2$	109.03	29.2	
Hydroxyquinol	$C_6H_4O_3$	125.02		100.0
	$C_6H_5O_3$	126.02		7.0
	$C_6H_6O_3$	127.04		2.8
Benzaldehyde	C_7H_6O	107.05	100.0	
	C_7H_7O	108.05	7.50	
	C_7H_4O	105.03	12.0	
	C_6H_6	79.05	2.6	
Furaldehyde	$C_5H_4O_2$	97.028	100.0	
	$C_5H_5O_2$	98.03		
Maleic anhydride	$C_4H_2O_3$	99.007	100.0	100.0
	$C_4H_3O_3$	100.01	3.8	3.3
	$C_4H_4O_3$	101.02	0.5	1.1
	$C_4H_4O_4$	117.08		5.5
Benzoquinone	$C_6H_4O_2$	109.03	100.0	100.0
	$C_6H_5O_2$	110.06	3.0	
	$C_5H_4O_2$	97.03	9.1	
Cresol	C_7H_8O	109.06	100.0	
	C_7H_9O	110.06	7.1	
Crotonic acid	$C_4H_6O_2$	87.044	17.6	
	$C_4H_7O_2$	88.047		
	C_2H_4O	45.033	82.4	
Benzoic acid	$C_7H_6O_2$	123.04	100.0	
	$C_7H_5O_2$	122.03	3.8	
	C_7H_4O	105.04	17.5	

	C_7H_5O	106.03	1.3	
4-Nitrotoluene	$C_7H_7NO_2$	138.06	100.0	
	$C_7H_8NO_2$	139.06		
4-Nitrophenol	$C_6H_5NO_3$	140.03	100.0	100.0
	$C_6H_6NO_3$	141.04	7.0	7.1
Nitrocatechol	$C_6H_5NO_2$	124.03		2.0
	$C_6H_4O_3$	125.03		10.2
	$C_6H_5O_3$	126.02		5.4
	$C_6H_3NO_4$	154.007		5.2
	$C_6H_4NO_4$	155.018		5.8
	$C_6H_5NO_4$	156.03		100.0
	$C_6H_6NO_4$	157.028		6.1
nonanal gas	$C_9H_{18}O$	143.14	50.8	51.9
	C_9H_{17}	125.13	21.3	19.9
	C_5H_9	69.07	27.8	28.2
Heptanal	$C_7H_{14}O$	115.11	15.7	21.8
	C_7H_{13}	97.10	77.6	78.2
	C_7H_{14}	98.10	6.7	
hexanal	$C_6H_{12}O$	101.10	11.9	15.6
	C_6H_{11}	83.085	82.4	84.4
	C_6H_{12}	84.08	5.7	
pentanal	$C_5H_{10}O$	87.08	12.2	16.0
	C_5H_9	69.07	83.1	84.0
	C_5H_{10}	70.07	4.7	
butanal	C_4H_8O	73.06	16.0	
	C_4H_7	55.05	80.3	
	C_4H_8	56.05	3.7	

Annex VI

Table VI.1. *Response factors (counts/ng) for VOCs used for ATD-GC-MS calibration*

Compound	Reponse factor (counts/ng)
Benzene	115012
Toluene	110870
Ethylbenzene	106035
m-Xylene	100546
1,3,5 TMB	95126
Naphthalene	112040
1-Butanol	21625
Propan-2-ol	11680
Heptanol	75230
Cyclohexane	55564
Dimethylpentane	30744
Nonane	105802
Decane	108205
Undecane	133206
Dodecane	168320
Tridecane	204011
Tetradecane	235869
Pentadecane	267445
Hexadecane	291719
Heptadecane	317998
Octadecane	304698
Nonadecane	240568

Annex VII

Table AVII.1. *AMS and CHARON SOA formed intercomparison.*

Experiment n°	SOA CHARON (µg/m^3)	SOA AMS (µg/m^3)
1	3.9	4.5
2	1.1	1.8
3	0.4	0.6
4	3.5	5.3
5	4.2	6.5
6	0.7	0.8
7	0.8	1.1
8	0.9	1.2
9	1.8	2.4
10	3.5	4.4
11	1.8	2.3
12	2.3	2.7
13	2.9	3.7
14	3.2	4.0
15	3.8	5.0
16	3.2	5.5
17	34	6.0
18	1.3	1.5
19	1.6	2.0
20	4.7	7.0
21	12.7	15.0
22	10.7	12.5
23	3.7	4.5
24	11.1	14.0
25	3.8	4.2
26	11.2	14.0
27	18.9	20.0
28	5.5	6.5
29	13.9	17.3
31	2.3	2.8